



UNIONE EUROPEA  
Fondo Sociale Europeo



**UNIVERSITÀ DEGLI STUDI DELL'AQUILA**  
**DIPARTIMENTO DI INGEGNERIA CIVILE, EDILE-ARCHITETTURA, AMBIENTALE**

Dottorato di Ricerca in  
INGEGNERIA CIVILE, EDILE-ARCHITETTURA, AMBIENTALE

Curriculum INGEGNERIA CIVILE

XXXII ciclo

Titolo della tesi

SVILUPPO DI NUOVI MATERIALI, MODELLI E TECNICHE INNOVATIVE PER LA  
CONSERVAZIONE E IL RAFFORZAMENTO SISMICO DEL PATRIMONIO EDILIZIO  
MONUMENTALE STORICO

SSD AREA 08 – ICAR 09

Dottorando

MICHELE ANGIOLILLI

Coordinatore del corso

Prof. Marcello Di Riso

Tutor

Prof. Amedeo Gregori

Correlatore

Prof. Gianluca Cusatis

A.A. 2018/2019





UNIVERSITÀ DEGLI STUDI DELL'AQUILA

Department of Civil, Construction and Environmental  
Engineering

**DOCTORAL THESIS**

---

**Development of new materials,  
models and techniques for the  
conservation and seismic  
reinforcement of the historical  
heritage**

---

Ph.D Course in Civil, Construction and Environmental  
Engineering

XXXII cycle

Candidate

**Michele Angiolilli**

Thesis Tutors

**Prof. Amedeo Gregori**  
**Prof. Gianluca Cusatis**

Coordinator

**Prof. Marcello Di Risio**



December, 2020



---

DEVELOPMENT OF NEW  
MATERIALS, MODELS AND  
TECHNIQUES FOR THE  
CONSERVATION AND SEISMIC  
REINFORCEMENT OF  
THE HISTORICAL HERITAGE

Michele Angiolilli

Prof. Amedeo Gregori  
Prof. Gianluca Cusatis

---

Reviewers:

Prof. Erez Gal     *Ben-Gurion University of The Negev, Beer Sheva, Israel*

Prof. Mohammed Alnaggar     *University of Rensselaer Polytechnic Institute,  
Troy, New York*

---

**Development of new materials, models and techniques for the conservation and seismic reinforcement of the historical heritage**

Michele Angiolilli

Candidate ID number: 251772

Department of Civil, Construction and Environmental Engineering- DICEAA  
University of L'Aquila

Copyright © 2020, Michele Angiolilli. All rights reserved.

Material for which the author is the copyright owner cannot be used without the written permission of the author. The permission to reproduce copyright protected material does not extend to any material that is copyright of a third party; authorization to reproduce such material must be obtained from the copyright owners concerned. This thesis has been typeset by L<sup>A</sup>T<sub>E</sub>X and phdiceaa class.

Version: R01-18<sup>th</sup> November 2020

Website: <http://diceaa.univaq.it/>

# Table of contents

<b>Foreword</b>	<b>21</b>
<b>Research Plan</b>	<b>23</b>
State of the art . . . . .	25
Degree of innovation . . . . .	27
Interdisciplinarity of the research . . . . .	29
Methodology . . . . .	30
<b>Structure of the thesis</b>	<b>33</b>
<b>Abstract in italian</b>	<b>35</b>
<b>1 The preservation issue for historical masonries</b>	<b>43</b>
1.1 Introduction . . . . .	44
1.2 Description of the historical stone masonry of central Italy . . . . .	48
1.3 Classic strengthening system . . . . .	52
1.4 The classic fiber-based strengthening system . . . . .	56
1.5 The newly short fiber-based strengthening system . . . . .	65
<b>2 Experiments</b>	<b>71</b>
2.1 Investigation on the FRCM system . . . . .	72
2.1.1 Diagonal tests carried out in situ . . . . .	72
2.1.2 Diagonal tests carried out in laboratory . . . . .	95
2.2 Investigation on the fibrous lime-mortar material . . . . .	109
2.2.1 Optimization of the mix design . . . . .	110
2.2.2 Mechanical characterization of the product . . . . .	115
2.3 Chapter conclusions . . . . .	138
<b>3 Computational modeling</b>	<b>143</b>
3.1 Overview of the modeling technique employed for stone masonries	144
3.1.1 The macro-modeling . . . . .	146
3.1.2 The micro-modeling . . . . .	150
3.2 The Lattice Discrete Particle Model . . . . .	153
3.2.1 Geometrical characterization . . . . .	156
3.2.2 Governing equations . . . . .	160
3.3 Simulation of unreinforced stone masonry walls . . . . .	163
3.3.1 Investigation of the stone and size distribution . . . . .	163
3.3.2 Size-effect of the wall . . . . .	173
3.3.3 Effect of the configuration test . . . . .	182
3.4 Simulation of stone masonry walls reinforced by FRCM system . .	187

3.4.1	Mortar thickness effect . . . . .	193
3.4.2	Bond behavior at the masonry-mortar interfaces . . . . .	195
3.4.3	Fiber grid effect . . . . .	197
3.4.4	Fiber anchor effect . . . . .	206
3.5	Simulation of the innovative fibrous-mortar . . . . .	207
3.5.1	Governing equation of the fiber-mortar interaction . . . . .	209
3.5.2	Calibration procedure . . . . .	214
3.6	Comparison between the FRCM and the newly systems . . . . .	228
3.7	Chapter conclusions . . . . .	237
<b>4</b>	<b>Technical direction</b>	<b>243</b>
<b>5</b>	<b>Conclusions</b>	<b>255</b>
	<b>Bibliography</b>	<b>263</b>
	<b>Appendix A</b>	<b>283</b>
A1	List of publications during the PhD . . . . .	283
A2	International and national conference papers . . . . .	284
	<b>Appendix B</b>	<b>285</b>
B1	Nomenclature . . . . .	285

# List of Figures

1.1	Medium-high seismic risk areas in the world [1]. . . . .	44
1.2	Influence of the masonry types on the suitability of the buildings set in Norcia after the 2016 earthquake. . . . .	46
1.3	The “Venice Charter for the Conservation and Restoration of Monuments and Sites” is a set of guidelines, drawn up in 1964 by a group of conservation professionals in Venice, that provides an international framework for the conservation and restoration of historic buildings. . . . .	47
1.4	Different masonry types of the historical building of L’Aquila. . . .	49
1.5	The FRP system consisting of the application of fiber laminates on the surface of stone masonry wall. . . . .	57
1.6	The FRCM system applied as a coating to the stone masonry surface. . . . .	59
1.7	The newly strengthening system, based on a lime-based mortar with short fibers chaotically embedded in the matrix, applied as coating to the masonry surface. . . . .	68
1.8	The newly strengthening system applied for the structural repointing of the old and damaged mortar joints. . . . .	68
2.1	The monumental masonry building “Margherita Palace” standing in the city of L’Aquila, almost at the center of the old fortified town. (photo taken from [2]). . . . .	72
2.2	a,b) Chaotic masonry texture made of irregular stone units, poor lime-clay mortar and inclusions of bricks. . . . .	75
2.3	Geometrical characterization of the glass fiber grid. . . . .	76
2.4	a) Particular of the disposition of the fiber grids: a square glass fabric grid of 1 m is placed on fabric stripes placed at the edges of the specimen; b) Details of the anchors. . . . .	76
2.5	a) Masonry specimen isolated from a wall of “Margherita Palace” (L’Aquila); b) Detail of the upper apparatus: 1) Masonry specimen; 2) Steel confinement corner plate closed on the lateral surfaces; 3) HEA180 steel beam; 4) Load cell; 5) Hydraulic jack compresses; 6) Apparatus of contrast; 7) Steel nut; 8) Threaded bar. . . . .	78
2.6	Configuration of the diagonal compression test. The LVDT <sub>v1</sub> and the LVDT <sub>v2</sub> transducers measured the compressive shortening whereas the LVDT <sub>h1</sub> and the LVDT <sub>h1</sub> ones measured the tensile elongation. . . . .	79
2.7	Graphical procedure for the computation of: a) the secant shear modulus $G_{30\%}$ . . . . .	80

2.8	Graphical procedure for the computation of the cyclic shear modulus $G_i$ . . . . .	81
2.9	Measurement of the compressive load $P$ during the time $t$ of the experimental tests. . . . .	82
2.10	Measurement of the displacements $d_v1$ and $d_v2$ recorded during the time $t$ of the tests. The achievement of maximum shear stress is represented by asterisk markers. . . . .	84
2.11	Shear stress $\tau$ computed for the four specimens and related to the compressive and tensile strains, $\varepsilon_v$ and $\varepsilon_h$ , respectively . . . . .	85
2.12	Shear stress $\tau$ computed for the four specimens and related to the the shear strain $\gamma$ . . . . .	85
2.13	Backbone curves obtained for the unreinforced (URM) and the reinforced (RM) panels. . . . .	86
2.14	Cyclic shear modulus $G_i$ as a function of $\gamma$ . . . . .	87
2.15	a,b) Dimensionless shear modulus and shear strain ( $G_{i,ND}$ and $\gamma_{ND}$ ) as a function of the load cycles; c,d) $G_{i,ND}$ and $\gamma_{ND}$ related to the dimensionless load cycles. . . . .	88
2.16	Multilinear fit of the $\tau_{0,ND}-\gamma_{0,ND}$ backbone curves of the URM and RM cases. . . . .	89
2.17	Total strain energy $U$ as a function of $\gamma_{ND}$ for the unreinforced (URM) and the reinforced (RM) panels. . . . .	90
2.18	Cracking opening on the unreinforced masonry specimen during the 1URM test. . . . .	90
2.19	Cracking opening on the reinforced masonry specimen during the 2RM test. . . . .	91
2.20	Cracking opening on the reinforced masonry specimen during the 3RM test. . . . .	91
2.21	Cracking opening on the unreinforced masonry specimen during the 4URM test. . . . .	92
2.22	Cracking propagation through the thickness of the 3RM specimen; . . . . .	93
2.23	Particular of the undamaged fiber grid at the end of the test. The external layer of the reinforcement mortar was previously removed. . . . .	94
2.24	Carbon fiber anchor (a) and steel bar anchor (b) extracted from the specimen at the end of the test 3RM to investigate their damage. . . . .	94
2.25	Schematic of the layers constituting the FRCM system applied on the masonry wall specimens: 1 and 3 are NHL mortar layers with a thickness of about 10 mm each; 2 is the glass fiber grid embedded in the mortar; b) Picture of the glass fiber grid used in the experiments. . . . .	96
2.26	a) First layer of mortar applied on the panel surface using a metal trowel; b) and application of the fiber grid slightly pressing it into the mortar layer. . . . .	96
2.27	a)Insertion the fiber anchors into the holes positioned in correspondence of the corners; b) filling the vacuum between the connectors and the masonry with lime-based mortar; c) refolding of the fiber anchors on the fiber grid with an angle splay of $360^\circ$ . . . . .	97
2.28	Picture of stone masonry specimen of dimension 1.2 m x 1.2 m x 0.34 m. . . . .	97

2.29 a) Configuration of the diagonal compression test; c) details of the upper apparatus: (1) masonry sample; (2) steel confinement corner plate closed on the lateral surfaces; (3) “L-shape” steel element ; (4) load cell; (5) hydraulic jack compresses; (6) apparatus of contrast; (7) UPN180 beam connection. . . . .	98
2.30 Compressive strain $\varepsilon_v$ (a) and tensile strain $\varepsilon_h$ (b) measured on the specimens during the time of the tests. . . . .	102
2.31 Shear stress $\tau$ computed for the specimens related to the duration of the tests (a) and the shear strain $\gamma$ of the panels. . . . .	102
2.32 Axial strain $\varepsilon_s$ measured for the vertical stands of the fiber grids during the 1RM- $\overline{GC}$ (a) and the 2RM- $\overline{G}$ tests (b). . . . .	103
2.33 Maximum values of the axial strain measured from the 16 gauges applied on the vertical stands of the fiber grids during the 1RM- $\overline{GC}$ and the 2RM- $\overline{G}$ tests . . . . .	104
2.34 a) Axial strain measured along the connectors $\varepsilon_a$ during the tests; b) zoom-in of the $\varepsilon_a-t$ plot; c) position of the four fiber anchors; d) scheme of the deformation of the specimen at the failure. . . . .	104
2.35 crack propagation along the compressed diagonal of the unreinforced masonry specimen. . . . .	106
2.36 Damage along the compresses diagonal observed for the reinforced panel. . . . .	106
2.37 Concentration of the damage in the top corner of the reinforced specimen. . . . .	107
2.38 Out of plane failure observed for the reinforced masonry specimens.	107
2.39 Failure of the glass fiber anchor. . . . .	108
2.40 Test machine of the Aquilaprem company used in the first part of the experimental campaign. . . . .	111
2.41 Compressive strength and tensile strength obtained for the Compression Test (CT) and the 3 Point Bending Test (3PBT) for two different type of fiber by varying the fiber content. . . . .	112
2.42 Compressive and tensile strengths obtained for two different type of fiber by varying the fiber content. . . . .	112
2.43 Compressive and tensile strengths obtained for two different type of fiber by varying the fiber content. . . . .	113
2.44 Compressive and tensile strengths obtained for the FGCS HP24 by varying the fiber content. . . . .	113
2.45 Two fiber types used in the experimental campaign: the 950Y (a) and the HP24 (b). . . . .	115
2.46 Slump test procedure: a) casting of the mortar therein the mould; b) raising of the mould from the mortar; c) Slump measurement in terms of the mean of two diameter values of the mortar after 20 strokes. . . . .	118
2.47 Slump measured for the HP24 and the 950Y cases by varying the fiber content F. . . . .	118
2.48 Notched beam adopted for the 3PBT. . . . .	121
2.49 Variation of the fracture energy of notched specimens in terms of the un-notched ligament $d - a$ , where $d$ is the depth and $a$ is the notch depth. . . . .	122

2.50	a) Displacement controlled hydraulic testing machine of the LPMS of L'Aquila; b) details of the test apparatus; c) detail of the rigid box, obtained by a 3D printer, for the allocation of the LVDT across the notch of the beam. . . . .	123
2.51	Flexural stress $\sigma_f$ related to the vertical displacement $\delta$ measured in the 3PBT for the unreinforced case (NF). . . . .	124
2.52	Flexural stress $\sigma_f$ related to the vertical displacement $\delta$ measured in the 3PBT for the HP24 with different fiber content. . . . .	124
2.53	Flexural stress $\sigma_f$ related to the vertical displacement $\delta$ measured in the 3PBT for the 950Y with different fiber content. . . . .	125
2.54	Flexural strength $\sigma_f$ (a) and fracture energy $G_f$ (b) measured in the 3PBT for two fiber type (HP24 and 950Y) with different fiber content. . . . .	126
2.55	a) Scheme employed for the Brazilian test (BT); b) Picture of the test carried out at the LPMS of L'Aquila. . . . .	128
2.56	Tensile strength $f_t$ Vs vertical displacement $\delta$ measured in the BT for the unreinforced case (NF). . . . .	129
2.57	Tensile strength $f_t$ Vs vertical displacement $\delta$ measured in the BT for the HP24 fiber with different fiber content: a) 1.5%, b) 2.0%, c) 2.5%. . . . .	130
2.58	Tensile strength $f_t$ Vs vertical displacement $\delta$ measured in the BT for the 950Y fiber with different fiber content: a) 1.5%, b) 2.0%, c) 2.5%. . . . .	130
2.59	Tensile strength $f_t$ measured in the BT for two fiber type (HP24 and 950Y) with different fiber content. . . . .	131
2.60	Scheme employed for the Compression Test (CT); b) Picture of the test carried out at the LPMS of L'Aquila. . . . .	132
2.61	Compressive strength $f_c$ Vs vertical deformation $\varepsilon_v$ measured in the CT for the HP24 fiber with different fiber content: a) 1.5%, b) 2.0%, c) 2.5%. . . . .	133
2.62	Compressive strength $f_c$ Vs vertical deformation $\varepsilon_v$ measured in the CT for the HP24 fiber with different fiber content: a) 1.5%, b) 2.0%, c) 2.5%. . . . .	133
2.63	Compressive strength $f_c$ Vs vertical deformation $\varepsilon_v$ measured in the CT for the 950Y fiber with different fiber content: a) 1.5%, b) 2.0%, c) 2.5%. . . . .	134
2.64	Compressive strength $f_c$ measured in the CT for two fiber type (HP24 and 950Y) with different fiber content. . . . .	135
2.65	Increasing of the mechanical properties (flexural strength $\sigma_f$ , fracture energy $G_f$ , tensile strength $f_t$ and compressive strength $f_c$ ) respect to the unreinforced case by varying the fiber content. Figure also shows the comparison between the two fiber type (the HP24 and the 950Y). . . . .	136
2.66	a) Fiber-reinforced mortar specimen after the 3PBT; b) Cracking propagation on some specimens at the end of the 3PBT; c,d) failure of the fiber-reinforced specimen after the execution of the CT. . .	137
3.1	The discrete-element model therein the Macro-Modeling approach developed by Calio [3]. . . . .	147

3.2	The discrete-element model therein the Macro-Modeling approach developed by Casolo [4]. . . . .	148
3.3	The FEM macro-model model of an existing historical stone building, the municipal seat called “Palazzo Margherita” [5]. On the left, the cracking pattern on the masonry walls obtained in the pushover analysis. . . . .	149
3.4	Simplified micro-modeling (two-phase material) and detailed micro-modeling (three-phase material). . . . .	150
3.5	The LDPM geometry in 2D. In particular, one can have a first simplification in the geometry passing from the coarse irregular aggregates to the spherical particles. Then, a Delaunay tetrahedralization on the centre of the spheres is carried out to obtain the Domain Tessellation. . . . .	154
3.6	Similarity between concrete and stone masonry materials at different observation scales. . . . .	155
3.7	a) Point Gaussian view of sphere distribution, randomly generated into a masonry specimen; b) Comparison between experimental and numerical sieve curves. . . . .	156
3.8	a) Delaunay tetrahedralization and domain tessellation; b) single stone unit represented by a polyhedral cell and its triangular facets, enclosing a spherical particle. . . . .	157
3.9	a) Cell outline generated around the spheres; b) possible failure layers generated around the spherical particles. . . . .	157
3.10	Visualization of the masonry panel surface. The LDPM cells generated by the standard procedure and the newly developed procedure (using for both the cases $d_0=80$ mm, $d_a=220$ mm, and $n_F=0.5$ ). . . . .	158
3.11	Sectional views of the masonry specimen. Stone particles generated by employing: a) the standard procedure; b) the newly procedure developed for disordered masonries. . . . .	159
3.12	Sectional views of masonry specimens characterized by different sets of particle distribution, by varying stone dimension $d$ (in the range of $50 \div 150$ mm, $100 \div 150$ mm, $50 \div 250$ mm, $100 \div 250$ mm) and by assuming two specimen thickness values equal to: a) 500 mm; b) 700 mm. . . . .	164
3.13	Diagonal compression tests carried out by LDPM using two of the eight different granulometric distribution assumed: t500-D50÷150 and t500-D50÷250. Each graph represents 50 simulations by varying the stone arrangements. . . . .	167
3.14	Diagonal compression tests carried out by LDPM for the t700-D50÷150 and t700-D50÷250 cases. . . . .	167
3.15	Diagonal compression tests carried out by LDPM for the t500-D100÷150 and t500-D100÷250 cases. . . . .	167
3.16	Diagonal compression tests carried out by LDPM for the t700-D100÷150 and t700-D100÷250 cases. . . . .	167
3.17	Probability Density Function - PDF (a) and Cumulative Density Function - CDF (b) obtained by employing 8 different grain size distribution and assuming a Gaussian distribution for the maximum stress $\tau_0$ . . . . .	169

3.18	PDF (a) and CDF (b) obtained for the shear modulus $G$ . . . . .	169
3.19	PDF (a) and CDF (b) obtained for the the ductility $\mu_{80\%}$ . . . . .	169
3.20	Probability density function obtained by assuming Gaussian distribution for the ductility capacity $\mu_{80\%}$ , $\mu_{70\%}$ , and $\mu_{60\%}$ estimated in correspondence of the 80%, 70%, and 60% of the maximum shear stress $\tau_0$ , respectively. Results are referred to the $t500 - D50 \div 150$ case. . . . .	171
3.21	Coefficient of variation $CV$ related to the ratio $d_m/t$ . $CV$ is computed for: (a) the maximum stress $\tau_0$ ; (b) the shear modulus $G$ . . . . .	171
3.22	Coefficient of variation $CV$ related to the ratio $d_m/t$ . $CV$ is computed for the ductility $\mu_{80\%}$ . . . . .	172
3.23	Size effect scheme adopted in the LDPM simulation. . . . .	175
3.24	Mechanical response computed by varying the size specimens. . . . .	176
3.25	a) Representation of the maximum shear stress $\tau_0$ as function of specimen size $D$ ; b) log-log scale representation for $\tau_0$ as function of $D$ . . . . .	177
3.26	Size effect on ductility parameter, $\mu_{80\%}$ . . . . .	177
3.27	Contours of crack opening at failure $w$ of the D0.6, D1.2, D2.4, D4.8, and D9.6 specimens. . . . .	178
3.28	Zoom in of the crack opening at failure on the central part of the specimen (Figure 3.27) concerned the D0.6 case. . . . .	179
3.29	Zoom in of the crack opening at failure on the central part of the specimen (Figure 3.27) concerned the D1.2 case. . . . .	179
3.30	Zoom in of the crack opening at failure on the central part of the specimen (Figure 3.27) concerned the D2.4 case. . . . .	179
3.31	Zoom in of the crack opening at failure on the central part of the specimen (Figure 3.27) concerned the D4.8 case. . . . .	179
3.32	Zoom in of the crack opening at failure on the central part of the specimen (Figure 3.27) concerned the D9.6 case. . . . .	180
3.33	Correlation between the measure of the Fracture Process Zone FPZ (normalized respect of the specimen dimension $D$ ) as function of $D/D_0$ . . . . .	180
3.34	Apparatus for determination of the shear strength of masonry specimen, according to ASTM code. . . . .	182
3.35	Two different test configurations (S1 and S2) adopted for the characterization of shear parameters of the masonry wall. . . . .	183
3.36	a) Numerical responses carried out for the configurations S1 and S2; b) zoom in of the results to better observe the difference in terms of stiffness between S1 and S2. . . . .	184
3.37	Contours of meso-scale crack opening at failure for three unreinforced masonry specimens at $\gamma=0.01$ , by adopting the S1 configuration ( $w$ is the crack opening). . . . .	185
3.38	Contours of meso-scale crack opening at failure for three unreinforced masonry specimens at $\gamma=0.01$ , by adopting the S2 configuration ( $w$ is the crack opening). . . . .	186

3.39	Numerical response of the UnReinforced Masonry (URM) specimens under diagonal compression test (on the left). Cracking evolution on the specimen for different values of the shear strain $\gamma$ (on the right). . . . .	188
3.40	Numerical responses computed for the mortar samples under the three-point bending test (3PBT) and the compression test (CT) .	189
3.41	contours of meso-scale crack opening at failure for mortar samples at strain value equal to 0.0025 in the compression test (a) and the three-point bending test (b). . . . .	189
3.42	Numerical responses and crack opening at failure computed for both the masonry and mortar material under diagonal test. . . . .	190
3.43	Stone masonry specimen reinforced with fiber grids and fiber anchors (both embedded in external mortar layers). On the right is illustrated in detail the fiber anchor modeled with hexahedral solid elements; the geometrical properties of the 16 anchor ends (14.7 mm in width, 0.2 mm in thickness and 150 mm in length) are equivalent to an ideal circular configuration (0.1 mm in thickness and 150 mm in radius). . . . .	191
3.44	a) Comparison between unreinforced panels (URM) and panels reinforced by only mortar layer (without both fiber grid and anchors) having different values of thickness $t$ : 10 mm, 15 mm, 20 mm, 25 mm and 30 mm; b) reinforcement coefficients $k_G$ , $k_{\tau_0}$ , and $k_\mu$ function of $t$ . . . . .	193
3.45	Crack opening at failure on both the masonry and the mortar layer for $\gamma=0.01$ , by assuming a thickness $t$ of the strengthening mortar equal to 10 mm. . . . .	194
3.46	Crack opening at failure on both the masonry and the mortar layer for $\gamma=0.01$ , by assuming a thickness $t$ of the strengthening mortar equal to 15 mm. . . . .	194
3.47	Crack opening at failure on both the masonry and the mortar layer for $\gamma=0.01$ , by assuming a thickness $t$ of the strengthening mortar equal to 20 mm. . . . .	194
3.48	a) Comparison between Perfect Bond (PB) and Weak Bond (WB) hypotheses at the masonry-mortar interfaces in the case of masonry strengthened only by mortar layers; b) bond stress measured on the three external areas "a", "b" and "c" of the specimen. . . . .	195
3.49	Crack opening at failure (masonry on the left and mortar on the right) for $\gamma=0.005$ , by assuming the PB hypotheses. . . . .	196
3.50	Crack opening at failure (masonry on the left and mortar on the right) for $\gamma=0.005$ , by assuming the WB hypotheses. . . . .	196
3.51	a) LDPM responses obtained for the URM case, the RM-M case, and the RM-G case (masonry sample strengthened by fiber grids embedded in the mortar layers); b) axial strain of both the vertical and the horizontal gauges Vs shear strain of the masonry panel of the RM-G test. . . . .	197
3.52	Maximum values of the axial strain measured along: the vertical fiber strands (a) and the horizontal fiber strands (b). . . . .	198

3.53	a,b) Axial strain measured for the vertical stands of the fiber grids during the experimental tests carried out on two masonry panels strengthened by the FRCM. . . . .	199
3.54	Crack opening at failure on both the masonry and the mortar layer for $\gamma=0.01$ , by employing the glass fiber grids embedded in the mortar layers. . . . .	199
3.55	Axial strain of the glass fiber grid measured at $\gamma=0.005$ (on the left) and $\gamma=0.01$ (on the right). . . . .	200
3.56	Simulation of the diagonal compression test for the mortar specimen. . . . .	201
3.57	Mortar square specimen of 250 mm in size and 20 mm in thickness reinforced by fiber grid with different geometrical features: a) Space gap of 25 mm; b) space gap of 25 mm and fiber width of 5 mm; c) space gap of 50 mm; d) space gap of 100. For the cases a, b and c, the fiber width is equal to 10 mm. . . . .	201
3.58	a) Shear stress–shear strain plot of fiber-reinforced mortar panels with different geometric features of the fiber strands; b) Zoom in of the (a) plot. . . . .	202
3.59	Axial force measured of the fiber strands as a function of the shear strain of the panel for different cases: (a) RP-grid25; (b) RP-grid25s; (c) RP-grid50; (d) RP-grid100. . . . .	203
3.60	Axial strain measured of the fiber strands as a function of the shear strain of the panel for different cases: (a) RP-grid25; (b) RP-grid25s; (c) RP-grid50; (d) RP-grid100. . . . .	203
3.61	Crack opening at the failure of the mortar panel by assuming different geometric feature of the fiber strands: (a) RP-grid25 case; (b) RP-grid25s case; (c) RP-grid50 case; (d) RP-grid100 case. . . . .	204
3.62	Axial force of the fiber strands under different geometric feature assumptions: (a) RP-grid25 case; (b) RP-grid25s case; (c) RP-grid50 case; (d) RP-grid100 case. . . . .	205
3.63	Axial strain of the fiber strands under different geometric feature assumptions: (a) RP-grid25 case; (b) RP-grid25s case; (c) RP-grid50 case; (d) RP-grid100 case. . . . .	205
3.64	a) Comparison between unreinforced specimens (URM), reinforced panels by both the fiber grids and anchors embedded in the mortar layers (RM-GC), and reinforced panels without fiber anchors (RM-G); b) axial strain of the glass fiber grid and the fiber anchor measured at $\gamma=0.005$ . . . . .	206
3.65	Single fiber pullout: a) partial debonding; b) full debonding with consequent to frictional slip. . . . .	210
3.66	Typical load versus slippage relationships for the single fiber pullout.	210
3.67	Single fiber pullout: a) initial condition; b) spalling. . . . .	211
3.68	Crack-bridging fiber with random crack opening orientation. . . . .	213
3.69	Notched mortar specimen modeled by using LDPM for the simulation of the experiments performed under 3PBT configuration. . . . .	215
3.70	The HP24 fiber type is chaotically distributed through the mortar matrix by LDPM to simulate the experimental 3PBTs. The fiber content was assumed equal to 1.5%, 2.0% and 2.5%. . . . .	217

3.71	The 950Y fiber type is chaotically distributed through the mortar matrix by LDPM to simulate the experimental 3PBTS. The fiber content was assumed equal to 1.5%, 2.0% and 2.5%. . . . .	217
3.72	Effect of the debonding fracture energy $G_d$ (assumed equal to 0 N/m and 10 N/m) on the mechanical response of the fibrous mortar specimen by assuming: (a) $\beta = 0$ ; (b) $\beta = -0.2$ . . . . .	218
3.73	Effect of the slip-hardening/softening parameter $\beta$ (a) and the bond friction stress $\tau_b$ (b) on the mechanical response of the fiber reinforced mortar specimen. . . . .	219
3.74	Effect of the fiber content F on the mechanical response of the fibrous mortar specimen for: (a) the HP24; (b) the 950Y. . . . .	220
3.75	Variation of the responses due to the the distribution of the fiber through the mortar matrix. Five random distributions of the HP24 fiber for each fiber content (F=1.5%, 2.0% and 2.5%) are considered.	221
3.76	Variation of the responses due to the the distribution of the fiber through the mortar matrix. Five random distributions of the 950Y fiber for each fiber content (F=1.5%, 2.0% and 2.5%) are considered.	221
3.77	Comparison between experimental and numerical responses in terms of flexural stress $\sigma_f$ Vs. vertical displacement $\delta$ under 3PBT by assuming the HP24 fiber type with different fiber content (F=1.5%, 2.0% and 2.5%). . . . .	223
3.78	Comparison between experimental and numerical responses in terms of flexural stress $\sigma_f$ Vs. vertical displacement $\delta$ under 3PBT by assuming the HP24 fiber type with different fiber content (F=1.5%, 2.0% and 2.5%). . . . .	223
3.79	Comparison between experimental and numerical responses in terms of flexural stress $\sigma_f$ Vs. vertical displacement $\delta$ under 3PBT by assuming the HP24 fiber type with different fiber content (F=1.5%, 2.0% and 2.5%). . . . .	224
3.80	Trend of $\tau_b$ (a) and $\beta$ (b) as function of F for the two different fiber type (HP24 and 950Y). . . . .	225
3.81	Mesoscale crack patterns at different values of the deflection $\delta$ (0.75 mm, 1.5 mm and 4.5 mm) for the mortar specimens reinforced by the HP24 fiber with different fiber content F (1.5%, 2.0% and 2.5%).	226
3.82	Mesoscale crack patterns at different values of the deflection $\delta$ (0.75 mm, 1.5 mm and 4.5 mm) for the mortar specimens reinforced by the 950Y fiber with different fiber content F (1.5%, 2.0% and 2.5%).	227
3.83	Simulation of the diagonal compression test performed on mortar specimen of 250x250 mm for several cases: a) the URP; b) the RP-FRCM; c) the RF-SF1.5; d) the RF-SF2.0; e) the RF-SF2.5. . . . .	229
3.84	Mechanical responses obtained for the unreinforced panel (URP) and panel reinforced by both the FRCM system (RP-FRCM) and short fibers randomly oriented in the matrix with different fiber content (RP-SF1.5, RP-SF2.0, RP-SF2.5). . . . .	230
3.85	Shear stress-shear strain curves obtained for the unreinforced panel (URP), panel reinforced by mesh fiber (RP-grid25) and panel reinforced by combined system (short fibers with F=2.5% coupled with mesh fiber of 25 mm or 100 mm.) . . . . .	231

3.86	Crack opening at the failure obtained at the same imposed displacement for different cases: a) the URP; b) the RP-FRCM; c) the RF-SF1.5; d) the RF-SF2.0; e) the RF-SF2.5. . . . .	232
3.87	. . . . .	233
3.88	a) Reinforced stone masonry specimen tested under diagonal compression; b) detail of the fiber strands embedded in the mortar matrix (the RM-FRCM case); c) detail of the short fibers embedded in the mortar matrix (the RM-SFRM case). . . . .	234
3.89	Crack opening at the failure for the only coating mortar layer (F=2.0%) occurred at the applied vertical displacements $d_z$ of 20 mm (a) and 60 mm (b) . . . . .	235
3.90	Crack opening at the failure for stone masonry reinforced by: a) the new fibrous lime-mortar; b) the FRCM. Plots correspond to a shear strain $\gamma$ equal to 0.025. . . . .	236
4.1	Relation between the real shear strength (in both experiments and simulations) the estimated shear strength (by eq.4.2) for the estimation of the shear strength of the coupled system ( $\tau_{0,FRCM}$ ). The $\tau_{0,FRCM}^*$ parameter is the real shear strength. . . . .	249
4.2	Trend of the corrective coefficient $\alpha_s$ as a function of the wall size.	249

# List of Tables

2.1	Geometrical properties of the unreinforced (URM) and reinforced masonry (RM) specimens. Legend: $D_m$ and $t$ are the average size and the thickness of the samples. . . . .	75
2.2	Geometrical and mechanical properties of the fibers employed in the FRCM system. Legend: $\rho$ is the density; $m_{UA}$ is the mass per unit area [6]; $E$ is the Young Module; $f_t$ is the tensile strength; $\varepsilon_u$ is the ultimate strain [7]. . . . .	77
2.3	Mechanical properties of different mortar types employed for the application of the FRCM system. Legend: $\rho_{solid}$ is the density of the solid mortar; $E$ is the Young Module [8]; $f_c$ and $\sigma_f$ are the compressive and the flexural stress [9], respectively. . . . .	77
2.4	Geometrical properties of the unreinforced (URM) and reinforced masonry (RM) specimens. Legend: $D_m$ and $t$ are the average size and the thickness of the samples, $\ell$ are the gauge lengths of the LVDTs mounted along the diagonal of the specimens. . . . .	79
2.5	Mechanical properties of the unreinforced masonry URM and the reinforced RM specimens. . . . .	86
2.6	Geometrical and mechanical properties of the glass fiber used in the FRCM system. . . . .	95
2.7	Specimen configurations with indication about the reinforcement type and the location of the measuring instrument (internal strain gauges). . . . .	99
2.8	Position of the gauges. . . . .	99
2.9	Experimental results for 6 masonry specimens tested in diagonal compression . . . . .	101
2.10	Material, name and geometry of the short-fibers used in the experiments. . . . .	111
2.11	Mechanical properties of mortar specimens tested in 3PBT and reinforced by two type of short-fibers (950Y and HP24) with different fiber content. . . . .	126
2.12	Tensile strength of the specimens tested in Brazilian Test (BT) and reinforced by two type of short-fibers (950Y and HP24) with different fiber content. . . . .	131
2.13	Compressive strength of the specimens tested in Compression Test (CT) and reinforced by two type of short-fibers (950Y and HP24) with different fiber content. . . . .	135

---

3.1	Values of different stone distribution sets used in the numerical simulations and characterized by minimum and maximum stone dimension ( $d_0$ and $d_a$ ) and Fuller coefficient $n_F$ . Results are presented by using labels in which: the first part indicates the thickness value of the masonry samples (e.g. $t500$ means $t = 500$ mm), whereas the second part indicates the stone size range (e.g. $D50 \div 150$ corresponds to a stone size ranging from 50 mm to 150 mm). . . . .	164
3.2	LDPM mechanical parameter values employed for the stone masonry material. . . . .	165
3.3	Mean $m$ , standard deviation $\sigma$ , and coefficient of variation $CV$ values computed for the shear strength $\tau_0$ obtained for the eighth stone distribution sets employed in the LDPM simulations. . . . .	168
3.4	Mean $m$ , standard deviation $\sigma$ , and coefficient of variation $CV$ values computed for the shear modulus $G$ . . . . .	168
3.5	Mean $m$ , standard deviation $\sigma$ , and coefficient of variation $CV$ values computed for the ductility $\mu_{80\%}$ . . . . .	169
3.6	Specimen size employed for the investigation of the size effect of stone masonry panels. Value of reference dimension $D_0$ is equal to 1.2m and it corresponds to the masonry wall size according to the ASTM. . . . .	174
3.7	LDPM mechanical parameter values employed for the stone masonry material. . . . .	175
3.8	The LDPM mix design parameter values adopted for the simulation of the stone masonry material. . . . .	187
3.9	LDPM mechanical parameter values employed for the stone masonry material. . . . .	188
3.10	LDPM mix design parameter values adopted for the mortar material.	188
3.11	LDPM mechanical parameter values employed for the mortar material. . . . .	189
3.12	Geometrical and mechanical properties of the glass fiber used in the FRCM system ( $SG$ is the space gap, $\rho_{fib}$ is the density, $t_{fib}$ is the thickness of a fiber strand, $E_{fib}$ is the fiber Young's Module, $f_{t,fib}$ is the tensile strength, $\varepsilon_{u,fib}$ is the ultimate strain). . . . .	190
3.13	LDPM-F mechanical parameter values employed for the fiber material.	222
3.14	Comparison between the mean mechanical properties computed for the mortar specimens under 3PBT by the experiments and the simulations. . . . .	224
4.1	Geometrical and mechanical properties of the unreinforced masonry and the reinforcement mortar (N=Numerical test, S=experimental on-site test, L=experimental lab-test). . . . .	250

# Foreword

*“... any engineer or architect with some formation in structural theory feels more comfortable within the frame of the strength approach of Galileo and the classical theory of structures. It requires an effort, and some study, to overcome our own prejudices and to accept that, for example, the medieval master masons, knowing nothing of mathematics, elastic theory and strength of materials, had a deeper understanding of masonry architecture than we engineers and architects of the twenty-first century do [10].”*

---

*Santiago Huerta*

Historically, masonry structures have exhibited, despite the intrinsic fragility of the material, extraordinary stability withstanding the effects of aging, human settlements, and natural elements (e.g., strong winds and earthquakes) over the centuries. This has led to the thinking that such structures would be eternal. However, most architectural and artistic heritage, such as castles, churches, monuments, lighthouses, mosques, arch bridges, vaults, and domes have been destroyed. Each year, we witness the further collapse of remaining historic masonry structures.

In the last decade, there has been a growing demand for protecting heritage structures around the world. This demand reflects humanity’s deep awareness, responsibility, and necessity to maintain the existing architectural heritage and to pass it on to future generations. Furthermore, restoration initiatives have increased, in part, because of new technologies that produce new materials and strengthening systems. The disproportionate use of reinforced concrete, which was considered one of the best materials for the reinforcement of historic masonry buildings during the 1970s, has proven an inappropriate solution, as highlighted in recent earthquakes.

The development of a fiber-based strengthening system began in the 1960s, when the potential for adding steel fibers to enhance the ductility of concrete

material was recognized. However, this technology has been commonly adopted for the reinforcement of masonry structures only in the last decade as an alternative to traditional systems, such as mortar injections, reinforced drilling, and reinforced concrete plaster. Indeed, because of the strict rules for the preservation of historic structures, conservation committees usually request structurally efficient but less intrusive techniques to protect the original aesthetic and architectural functions.

Nowadays new and less invasive strengthening techniques are preferred; among them a fiber-based reinforced system with lime-based mortar, which is considered to be more compatible with the intrinsic properties of these ancient structures as compared to cement-based mortar.

The study of historic masonry structures, especially if coupled with a sophisticated strengthening system, is a challenging task because of the difficulties encountered in the description of the complex geometry, morphology, material heterogeneity, material properties characterization, and material variation. Despite its simple composition, masonry is characterized by a composite material that leads to a complex prediction of its mechanical behavior.

Usually, the failure of historic masonry is caused by an unknown alteration of its natural equilibrium, which is based on the so-called strength by shape. This is also typical of other structures carrying axial forces, such as a cord or a membrane, that are unilateral structures.

The unilateral model, which appears as the key of structural interpretation behind the design of the great Architecture masterpieces of the past, was first rationally introduced in the scientific community by Heyman in 1966, with his book “The Stone Skeleton: Structural Engineering of Masonry Architecture”. In this book, the author explains the stone behavior by using only a few equations.

The unilateral model can be useful to practitioners and applied engineers since it captures the essence of masonry mechanics. However, such a simple model presents strong limitations in many aspects of masonry behavior that need to be understood, such as damage, degradation, friction, heterogeneity, and particularly the role of the interface behavior in the overall response of masonry.

To appreciate the validity limits of the simplified approach, it is important to study and interpret the experimental results with the “eyes” of more sophisticated models.

# Research Plan

The proposed research is entitled: “Development of new materials, models and techniques for the conservation and seismic reinforcement of the historical heritage”. The theme is in line with the priorities of the Beni Culturali as defined in the (Italian) document “Accompagnamento all’Attuazione delle Politiche Nazionali e Regionali di Ricerca e Innovazione (Area di specializzazione Beni culturali)”.

This three-year research was co-financed by the Project “2014-2020 PON” (CCI 2014EN16M2OP005), which was approved by the Research Directorate of the Italian Ministry of Education (MIUR) and co-funded by the European Social Fund (ESF). The project was realized through the correspondence of interests between the University of L’Aquila (Italy), the industrial partner “Aquilaprem s.r.l.” (L’Aquila, Italy), and the research partner “Northwestern University” (Evanston, U.S.A.).

The present project aimed to characterize the existing innovative technologies as well as to identify new material for the conservation and development of the vast historical and architectural heritage, such as churches, palaces, castles entirely historical centers, and villages that nowadays are particularly vulnerable to the environmental actions. In particular, the main purpose of the present research regards the development of a new type of natural hydraulic lime mortar, reinforced by short fibers randomly arranged in the mortar matrix, that can ensure compressive and tensile strengths as well as good bond properties to the wall support. These properties are necessary to ensure proper mechanical behavior of the masonry structures, especially in case of a seismic event. This new composite material was developed by using natural hydraulic lime (NHL) -based mortar to ensure the compatibility with the original feature of the historical masonry structures (mostly in stone and clay) aiming to pursue both the effectiveness and durability of the intervention.

On the other hand, the project aimed to validate a sophisticated numerical framework, the so-so called Lattice Discrete Particle Model, for a reliable prediction of the mechanical behavior of this masonry construction, especially when it is coupled with complex strengthening system. Indeed, the heterogeneous character

of stone masonry, the chaotic distribution of stone units into the mortar matrix, and the variability of their mechanical proprieties contribute to a substantial scatter in their response. An experimental analysis of this scatter requires performing a large number of experimental tests, which is prohibitive in practice due to time and cost considerations. For this reason, a dedicated numerical approach was essential to support the experiments.

## State of the art

In the last two decades, strengthening solutions based on composite materials, such as the Fiber Reinforced Polymers (FRP) or the Fiber Reinforced Cementitious Matrix (FRCM), have been increasingly considered for strengthening and repair of both modern and historic masonry constructions (buildings, bridges, towers) and structural components (walls, arches and vaults, piers, and columns). As far as the FRP is concerned, several disadvantages can be detected mainly related to the epoxy matrix used to embed and bond the fibers, such as: (i) low fire resistance; (ii) high sensitivity to ultraviolet radiation when exposed to the open air; (iii) high toxicity; (iv) low vapor diffusion; (iv) needs of completely dry surfaces to ensure the adherence to the substratum. Moreover, the FRP installation is localized and, particularly in case of very brittle and heterogeneous material, such as the irregular stone masonry, the fracture may be caused in some areas where the wall is not strengthened. For all these reasons, the FRCM (based on the use of fibrous reinforcements embedded in a mortar matrix) represents a better solution as compared to the FRP. However, it is characterized by a long application procedure consisted in three phases: (i) application of the first layer of mortar on the panel surfaces; (ii) application of the fiber grids to fresh mortar layer; (iii) application of a second finishing layer of mortar to cover the fiber fabric while the previous mortar layer was still fresh. This procedure may represent a strong limitation for an extensive application of the technology. Besides, although the FRCM began to be widely applied to the masonry construction, its mechanical behavior is still not completely characterized due to a lack of both exhaustive experimental data and reliable mathematical models for the investigation of the mechanics behind the complex coupled resistance system of the masonry with fiber-based reinforced mortar.

A common disadvantage between the FRCMs and FRPs concerns the orientation of the fiber in specific directions: the FRCMs are characterized by fiber oriented in bi-directional (horizontal and vertical) strands; the FRPs are characterized by the prior design of the fiber direction. Since fibers are characterized by high resistance in their axial direction and negligible resistance in the other directions, uni- or bi-directional fibers cannot ensure proper performance in case of seismic loads that do not act in a single and defined direction.

Furthermore, the low compatibility of the cement-based mortar (or polymeric matrix) of both the classical and innovative strengthening systems with the lime-based mortar of the ancient masonry joints yet represents an issue. In several cases, extensive damage occurred to the ancient masonry due to the incompatibility of the cement-based mortars. This compatibility must be reflected in several aspects: (i)

chemical compatibility between the reinforcing mortar and the old material (stone or brick and its bedding mortar); (ii) physical compatibility, with special reference to processes of solubility and of water transport; (iii) structural and mechanical compatibility (strength of repair mortar needs to be similar to the old material). In the conservation perspective, an increasing sensitivity is nowadays directed to the choice of consolidation materials mechanically, physically, and chemically compatible with the nature of the old masonry materials. In such ambit, natural hydraulic lime (NHL)-based mortars are more and more considered (rather than cement or resin) to pursue both the effectiveness and durability of the intervention. The NHL-based mortar is considered a promising alternative to cement materials when high compatibility with historical substrates is strictly required.

In addition to the issue related to the features of the fiber-based reinforcing systems, modeling the fracture process in irregular stone masonry is challenging due to the heterogeneous character and quasi-brittle behavior of the material. Indeed, numerical modeling of this masonry type is one of the most complicated problems in structural engineering research.

Numerical continuum-based models, which homogenize material behavior, are inherently limited in capturing the mesoscale interactions, fracture propagation, and damage evolution of quasi-brittle materials. Indeed, the failure of quasi-brittle materials, such as stone masonry, is often caused by nonlinear phenomena, namely fracture, damage localization, and frictional shearing, occurring at weak locations in the internal material structure. These weak locations coincide, for example, with interfaces among particles, weak matrix layers, and compliant interfaces between stiff material grains. Due to this peculiarity, classical constitutive equations typically fail to provide a satisfactory representation of the mechanical behavior of these materials especially if failure mechanisms are associated with strain-softening.

Furthermore, for a reliable prediction of the mechanical response of mortar reinforced by short fibers, the numerical modeling capabilities should be characterized by realistic three-dimensional modeling of mortar mesostructure, including a discrete representation of individual fibers randomly distributed therein as well as a multiscale approach in which the effect of embedded fibers on the structural response is based directly on the micromechanics of the fiber-matrix interaction. Most of the existing numerical models for the analyses of fiber-reinforced material consist of modifying the mechanical behavior of inelastic constitutive models to represent the enhanced properties of fibrous material. The increase in the mechanical properties of fibrous material must be determined a priori from experiments resulting in loss of the capacity to predict the effect of specific fiber properties on the macroscopic behavior of composite material. The Lattice Discrete Particle Model offers the possibility to simulate all these aspects.

## Degree of innovation

Though reinforcement made of short-fibers is a topic that is being studied for several years from different researchers, the use of lime-mortar reinforced with short-fibers for the retrofitting of the historical masonry wall can be considered an innovative technology. Indeed, nowadays there is a lack of information about the mechanical behavior of this particular composite material, especially when coupled to the stone masonry. Currently, short fibers are especially used in the mix design of concrete elements, aiming to improve their mechanical properties, for the realization of industrial concrete slabs, structural or nonstructural precast elements and tunnel coatings. For the restoration of the masonry construction, short fibers are used in small content only to reduce the plastic shrinkage cracking. In this research, the “structural” function of the fibers not merely consists of reducing shrinkage cracking but allows for the enhancement of the shear and ductility capacities of the masonry walls.

Hence, the degree of innovation of the present research consists in a development of new material and technology perfectly compatible with the nature of the existing historical constructions leading, at the same time, higher structural performance as compared to the other strengthening solutions. Innovative elements also concern the simplification of the implementation of the reinforcement and the possibility of also practice eco-friendly choices using recycled materials coming from other industrial processes (glass, steel, plastic, basalt, etc.).

The use of the new composite material, which is characterized by short fiber randomly embedded in a lime-mortar matrix, to the masonry structures, aims to replace the use of the cementitious mortar material reinforced by uni- or bi-directional long fiber fabrics of the classic fiber-based strengthening systems.

In addition to the physical-chemical compatibility issue, the adoption of the discontinuous-fiber-reinforced composites overcome all the other disadvantages observed for the other fiber-based strengthening systems. Indeed, the use of diffuse reinforcement, namely the short fibers randomly oriented in the mortar matrix, ensure proper resistance in any directions. This is an important aspect to be considered especially in case of seismic events that do not act in a single and defined direction. As commented in the state of the art, the classic fiber-based reinforcing systems are instead characterized by the specific orientation of the fiber.

The new composite material presents high flexibility in its application methodologies to the historical masonry structures. Indeed, it can be used as a coating to the masonry surfaces and also in the structural repointing technique. As far as the coating technique is concerned, the use of the newly fibrous lime-mortar would lead to a unique application phase, consisting of the application of a single layer of

the product to the masonry surfaces. This represents a substantial advantage in terms of reduction in both cost and application time, as compared to the existing fiber-based reinforcing system, namely the FRCM system. As far as the repointing technique is concerned, it consists of replacing the deteriorated mortar or filling the missing mortar in the joints by employing the newly composite material, allowing both to enhance the shear capacity of walls and preserve the original aesthetic of the masonry texture. This application may be suggested to solve the important aesthetics issue related to the retrofitting method.

On the other hand, a sophisticated numerical framework, based on the Lattice Discrete Particle Model, was originally formulated and validated for concrete material and has been proposed here, for the first time, for the simulation of irregular stone masonry. That model has been proposed in this research for a reliable investigation of both the historical stone masonry and the fibrous mortar as well as their coupling. The intrinsic stochastic feature of the LDPM, which simulate units randomly placed into a considered volume as irregular particles interacting with each other, allows quantifying the variation of the mechanical properties of both the stone masonry and mortar materials due to the random particle size and distribution.

The adoption of a numerical framework developed for concrete to stone masonries was possible since one can observe a strong similarity in geometrical features, albeit at different observation scales, as well as similarity in the brittle-failure mode between such materials. The idea of using LDPM for stone masonries is coherent with the fact that the failure is often caused by fracture, damage localization, and frictional shearing occurring at the weak matrix layers around aggregates and stones in the cases of concrete and masonry, respectively.

In short, the innovative elements of the present research regard the development of the newly reinforcement composite material as well as the novel application of the sophisticated numerical framework for the mechanical characterization of the complex behavior of the coupled construction system, namely the masonry–fiber-based reinforcing mortar.

## Interdisciplinarity of the research

Given the wide range of disciplines represented in the Member of the Scientific Board for the PhD program, the present research project aims to reconcile the different views on the preservation of existing historical buildings, combining the needs of conservation of the old materials with the seismic retrofitting of the historical constructions.

This research has set itself the goal to collect, in a transversal way, the contribution of different disciplines all represented in the Member of the Scientific Board for the PhD program belonging to the sectors of restoration, conservation of architectural history, materials technology, computational mechanics and seismic structural engineering.

The objective of developing an innovative material, consisting of fibrous lime-based mortars for the recovery and strengthening of ancient masonry walls, as well as the development of a new sophisticated numerical framework for the evaluation and the prediction of both the unreinforced and fiber-reinforced masonry, represents a great interdisciplinary theme.

This research tried to capture the different key aspects of both the recovery and enhancement of cultural heritage by using the most advanced principles of structural engineering and the most advanced analytical framework for numerical modeling for the problem.

It is worth noting that the lack of an interdisciplinarity approach in the choice of a technical solution for the preservation of historical structures of the past has led to disastrous mistake, just think of the insertion of concrete curbs in ancient masonry buildings.

Preservation had mainly relied on an entirely forced (and damaging) distinction between consolidation and restoration, which must be resolved through the application of the art and science of building.

## Methodology

The idea of the present research comes from the correspondence of interests between the University of L'Aquila (Italy), the research partner "Northwestern University" (Evanston, U.S.), and the industrial partner "Aquilaprem s.r.l." (L'Aquila, Italy). Hence, the project followed a shared path, intending to reconcile the diverse needs of the partners. On the one hand, the propensity of the Universities to investigate the problem in a merely theoretical manner, through the analysis of the complex mechanics of the composite construction system. On the other hand, the propensity of the company to analyze the theoretical problem through an experimental approach with the ultimate goal to obtain a final result expendable for the world of work and an innovative product for construction.

Prof. G. Cusatis, in charge of the mechanics, materials, and structures group at Northwestern University, was strongly interested in addressing the proposed research topic by providing a sophisticated numerical model to characterize the mechanical behavior of the reinforcement mortars and wall panels. The research group of the Northwestern University has been engaged for years in extensive research with the overall objective to understand, simulate, and predict the behavior of brittle materials. For this reason, they were available to support and address the analyses of the retrofitting system of the masonry walls. This analysis also allowed the refinement of a numerical model on the basis of a constructive type, namely the stone masonry, which was never investigated before then by that research group. The project included the development and validation of a computational framework, the so-called Lattice Discrete Particle Model, originally developed and validated for concrete material, to simulate the mechanical behavior of irregular stone masonry as well as the coupled construction system (masonry-fiber reinforcement).

On the other hand, the Aquilaprem company represents a new and promising company operating in the premixed material for the building industry. Aquilaprem had a significant development in the area of L'Aquila, and is gradually expanding its market in the rest of the Italian territory in the field of conservation and enhancement of historical buildings. It has long been engaged in the development of innovative materials for the restoration of historic masonry and has shown high interest in the subject of the research by providing operational support to the experimental activity in terms of staff, materials, equipment, and know-how. The purpose of the research carried out at the company headquarter was to develop innovative technology for the conservation and restoration of the Italian cultural heritage. As mentioned above, such technology involves the use of a special reinforcement mortar (with tensile strength and ductility capacity) able to perform

their function in a most compatible, less invasive, and more effective way with respect to the materials and techniques of the past.

The first six months of the Ph.D. research focused on the state-of-the-art study based on the knowledge of traditional materials and technologies for the intervention on Cultural Heritage, investigating merits and limitations. Particular attention was also paid to the development of skills in the numerical simulations of masonry construction by commercial software. Moreover, in that period, a first experimental campaign was performed, also in collaboration with the Aquilaprem company. The experiments focused on the mechanical characterization of stone masonry panels, prepared at the laboratory LPMS of the University of L'Aquila, in both the unreinforced and reinforced condition.

Then, during the 12 months stay at Northwestern University, the Lattice Discrete Particle Model was first validated and improved for the stone masonry with experimental tests conducted in the first part of the Ph.D. research. The behavior of the Fiber Reinforced Cementitious Matrix (FRCM) strengthening system applied to masonry panels was deeply investigated. The main focus concerned the investigation of different variables affecting the mechanical behavior and damage evolution of stone masonry panels reinforced by FRCM systems, namely the thickness of the reinforcement, the bond behavior at the FRCM-masonry interface, the presence or not of fiber anchors and fiber grids in the strengthening system. This part was fundamental to understand the mechanics behind the complex coupled resistance system of the masonry reinforced by fiber-based reinforcing mortar.

During the one-year collaboration with the Aquilaprem company, the experimental characterization of the FRCM system on the irregular stone masonry was performed in situ, on masonry specimens isolated from the walls of the historical building "Palazzo Margherita" of L'Aquila. This experimental campaign validated the first experiments carried out on the masonry specimens reproduced in the laboratory and, therefore, also validated the numerical framework calibrated on them. Later, the newly fibrous lime mortar was developed at the laboratory of the company. This phase regarded the optimization of the mix design of the product as a function of the nature, geometry, and content of the fibers as well as the content of additives and the sieve curve of the mortar matrix. In particular, several mechanical characterization tests and workability tests were carried out on the fibrous mortar. During this phase, the computational framework was adopted to support the experimental data showing exceptional prediction capacity. After the optimization process, the newly mortar applied as a coating to the stone masonry was simulated by the LDPM. This simulation allowed the prediction of the mechanical behavior of the strengthening system, further highlighting the main feature of the new technique proposed for the retrofitting of the historical construction.



# Structure of the thesis

In the framework of the seismic vulnerability assessment of existing stone masonry structures, which constitute a great and valuable portion of the Italian cultural heritage, the present thesis focuses on the mechanical characterization of the shear behavior of masonry structural elements at the unreinforced and reinforced configurations as well as the development of a new strengthening system intending to increase its chemical-fiscal compatibility with the original feature of the historical masonries and also increasing the ductility of the reinforcement system.

Chapter 1 introduces the issues related to the preservation of the historical masonries, focusing on their main features. In particular, Chapter focuses particularly on the description of stone masonry structure typical of the territories of the central Apennines in Italy, where the use of limestone for the buildings is predominant. However, the considerations may not differ greatly from those for the historic stone masonry construction common throughout North and Latin America, the Himalayan region, Eastern and Western Europe, the Indian subcontinent, and Asia. Furthermore, an analysis of the feature of the retrofitting systems, from the classics to the innovative ones, is carried out.

Then, the main scope of the thesis is pursued on two different levels: experimental investigations and numerical simulations.

Chapter 2 regards the identification of the shear parameters of the masonry walls at the reinforced and unreinforced configurations. These tests concerned both the in situ and at the laboratory experimental campaign. In particular, the in situ tests were performed on four stone masonry samples, two unreinforced and two reinforced with FRCC, by isolating them from the walls of the municipal office “Margherita Palace” of L’Aquila. Instead, the tests performed at the laboratory LPMS (Laboratorio di Prove Materiali e Strutture) of the University of L’Aquila, concerned the evaluation of the fiber-based strengthening system on six stone masonry samples. The latter were prepared according to the ancient constructive technique featured in most of the historic buildings of the city of L’Aquila by using stone elements taken from the debris of buildings collapsed during 2009 earthquake and poor lime-mortar having similar features to the original one (char-

acterized by a very friable behavior and a low compressive strength). Furthermore, the experimental characterization of the mechanical properties of the newly lime-based mortar reinforced by short fibers randomly embedded therein the matrix is described in the last part of the Chapter.

Chapter 3 first introduces a general overview of the numerical models employed for the stone masonry. Then, a sophisticated numerical modeling, based on the Lattice Discrete Particle Model, is described. The results of the experimental study are numerically investigated. On the first hand, Chapter presents the simulation of diagonal compression tests performed on stone masonry specimens strengthened by the FRCM system. The fracture behavior and the damage evolution in masonry panels are investigated under different assumptions on the FRCM features (the bond behavior, mortar thickness, fiber anchors, and fiber grid). Moreover, Chapter also presents the numerical investigation on the variation of the mechanical properties of unreinforced stone masonry, namely the maximum shear stress, the shear modulus, and the ductility, due to the random particle size and distribution as well as the size effect of the stone panels. On the second hand, Chapter presents simulation of the experimental tests carried out for the mechanical characterization of the newly fibrous lime-mortar. A final numerical prediction of the shear enhancement of the new composite material applied as a coating to the stone masonry is presented intending to highlight the benefit of the new system, as compared to the classic FRCM.

Chapter 4 provides technical information for the characterization of the shear strength of the masonry walls reinforced by coating systems, such as the FRCM or any fibrous mortar layer applied to masonry surfaces. In particular, a simplified analytical formulation is proposed to predict the shear strength of reinforced masonry merely based on the geometry and tensile strength of both the unreinforced masonry and coating mortar.

Finally, the conclusions gather critical observations of the main results obtained by experiments and numerical investigation. The second part of the conclusions focuses on further research developments, articulated in different scenarios.

# Abstract in italian

La tematica principale di questo lavoro si allinea con le priorità di intervento nell'ambito dei Beni Culturali, proponendo lo sviluppo di tecnologie e l'uso di nuovi materiali che possano favorire il recupero e la valorizzazione del vasto patrimonio storico-architettonico italiano in riferimento sia ai Beni monumentali che ai numerosi borghi antichi, di inestimabile valore artistico e di grande interesse culturale e turistico.

Questa tesi è incentrata sulle strutture murarie di pietrame ed in particolare quella riscontrata nei territori dell'Appennino centrale. Nel corso dei secoli la natura prettamente calcarea di tali territori ha favorito lo sviluppo di agglomerati urbani di media e piccola entità in cui era predominante l'uso della pietra calcarea non lavorata proveniente da cave locali, diversamente della pietra squadrata in conci, tipologia utilizzata solo per gli edifici più prestigiosi. Unitamente al calcare, era spesso utilizzato materiale erratico e alluvionale sia per le murature che per la realizzazione delle malte. Nella tipologia muraria analizzata, l'utilizzo del laterizio era piuttosto raro, essendo, quasi sempre, usato come materiale di recupero all'interno del paramento murario e, comunque, in quantità modesta. Tale tipologia muraria è ampiamente diffusa, con forti similarità, anche in tutto il Nord America, America Latina, la regione Himalayana, Europa orientale e occidentale, il subcontinente indiano e l'Asia. Purtroppo, molte di queste aree sono caratterizzate da un elevato rischio sismico, che, abbinato alla natura eterogenea, alla scarsa resistenza dei materiali costituenti e al comportamento strutturale di tipo disgregativo determina una estrema vulnerabilità di tali edifici fortemente provata dagli effetti disastrosi causati dai terremoti che hanno colpito tali aree, anche negli ultimi anni.

Lo stato di degrado, in cui talvolta si trovano tali edifici, rende spesso necessari interventi strutturali volti a garantirne l'integrità. In tale senso, negli ultimi decenni sono state sviluppate nuove metodologie d'intervento, sfruttando sia materiali tradizionali che innovativi, per preservare tali strutture da ulteriori danni, in particolare quelli indotti da eventi sismici. Tuttavia, nuovi materiali e tecniche d'intervento vengono spesso commercializzati ed applicati senza l'esecuzione di un

esaustivo studio preliminare che ne verifichi l'applicabilità e l'efficacia.

Lo studio, finanziato dalla Borsa di Studi PON, nasce dalla corrispondenza di interessi tra l'Università degli Studi dell'Aquila, il partner industriale Aquilaprem srl (AQ) e il partner di ricerca estero Northwestern University (USA). Le attività di ricerca sono nate con l'obiettivo di sviluppare un innovativo prodotto commerciale per il rinforzo delle murature storiche di pietrame irregolare, una delle tipologie costruttive maggiormente impiegate nell'edilizia storica. In questa ricerca è stato infatti validato l'impiego di questa metodologia d'intervento mediante la realizzazione di un'ampia campagna di prove sperimentali combinata ad una sofisticata modellazione numerica.

L'obiettivo principale della ricerca è stato quello di creare un sistema di rinforzo capace di mantenere i vantaggi dei sistemi classici basati sull'utilizzo di materiali compositi (Fiber Reinforced Polymers - FRPs o Fiber Reinforced Cementitious Matrixs - FRCMs), migliorandone le proprietà meccaniche e semplificandone l'applicazione in situ. L'innovativo materiale composito sviluppato in questa ricerca è caratterizzato da una malta a base di calce idraulica naturale con fibre corte distribuite caoticamente all'interno della matrice della malta. Tale materiale innovativo presenta svariate possibilità di applicazione sugli edifici esistenti in muratura. Nella presente tesi, il materiale innovativo è stato studiato all'interno della tecnica dell'"intonaco armato", che consiste nell'applicazione di uno strato di materiale composito sulle superfici murarie. Si può anche pensare di applicare il materiale innovativo nella tradizionale tecnica di stilatura dei giunti, che consiste nel sostituire la malta deteriorata o di inserire all'interno di essa la malta mancante impiegando il nuovo materiale composito, consentendo il miglioramento della resistenza a taglio delle pareti e di preservare l'estetica originale della tessitura muraria. In aggiunta, l'innovativo materiale composito presenta la possibilità di essere applicato in combinazione con sistemi di rinforzo esistenti: si pensi ad esempio all'utilizzo della malta fibrosa per la realizzazione del sistema FRCM.

I vantaggi forniti dall'aggiunta di fibre, di qualsiasi natura, a materiali quasi-fragili, ad esempio le malte, consentono di migliorare il comportamento strutturale del composito, dando vita ad un nuovo materiale capace di lavorare non solo a compressione ma anche a trazione. Inoltre, le fibre incrementano la duttilità del sistema di rinforzo, aumentando l'assorbimento di energia durante un evento sismico e limitando il danneggiamento della struttura muraria.

La disposizione delle fibre lungo direttrici obbligate (FRCM) o studiate a priori (FRP) non sempre riesce a prevenire e, soprattutto, a limitare l'ampiezza delle lesioni. È ben noto, infatti, che i compositi unidirezionali a fibre lunghe, quali i classici FRCM o FRP, sono caratterizzati da una elevata resistenza nella direzione delle fibre e da una pressoché nulla resistenza in direzione trasversale. Noto quindi lo

stato tensionale nel componente in progetto, l'uso corretto di tali compositi prevede di orientare opportunamente le fibre nella direzione della massima tensione in modo da ottimizzare lo sfruttamento del materiale. Tuttavia, gli stati tensionali indotti dagli eventi sismici non sempre agiscono in una sola e ben definita direzione. Per le motivazioni sopraesposte, si è pensato di introdurre, nella matrice della malta, un rinforzo costituito da fibre corte disposte caoticamente in modo da assorbire gli sforzi di trazione agenti in qualsiasi direzione, garantendo un'azione di cucitura puntuale che impedisce alle cricche di propagarsi rapidamente e conseguentemente di raggiungere ampiezze elevate. I laminati rinforzati con fibre corte orientate in modo pressoché casuale sono caratterizzati da un comportamento meccanico, che differisce da quello a fibre lunghe, legato principalmente al rapporto geometrico tra lunghezza e diametro caratteristico delle fibre da cui dipende sia la distribuzione delle tensioni e sia il meccanismo di trasferimento del carico dalla matrice alla fibra. Il prodotto innovativo sviluppato nella presente ricerca garantisce, quindi, prestazioni meccaniche che, a parità di costo totale dell'intervento realizzato con i classici sistemi di rinforzo con materiali compositi, sono maggiori sia in termini di massima resistenza (sia di compressione che, soprattutto, di trazione) che di capacità di mantenimento del carico per grandi spostamenti (duttilità). Questo è dovuto all'effetto di confinamento conferito dalle fibre corte presenti nella matrice cementizia che, come già spiegato, forniscono eccellenti prestazioni per forzanti agenti in qualsiasi direzione sia nel piano e sia fuori dal piano dei pannelli di muratura. Gli FRCM, inoltre, presentano alcune modalità di rottura di difficile caratterizzazione come il distacco della rete rispetto alla malta e la rottura delle fibre. Queste due modalità di rottura non sono invece presenti per i sistemi di rinforzo con fibre corte disperse all'interno della matrice. Inoltre, anche la modalità di rottura caratterizzata dal distacco dello strato di malta di rinforzo dalle superfici murarie (problema di deaminazione) risulterà di entità minore con l'utilizzo di materiali compositi a fibre corte. Infatti, a seguito dell'introduzione massiva di fibre corte nella matrice di malta, è inevitabile l'utilizzo di additivi che migliorino la lavorabilità del prodotto. Tali additivi incrementano, inoltre, anche la capacità di adesione del sistema di rinforzo alle superfici murarie. Infine, un altro notevole vantaggio che il nuovo sistema di rinforzo può apportare riguarda la tempistica di applicazione in situ, che risulterà drasticamente più bassa rispetto agli FRCM. Infatti, l'applicazione del rinforzo FRCM è strutturata in tre fasi: i) applicazione di un primo strato di malta sulla superficie muraria, di norma applicato a mano, ii) applicazione di un telo in fibra e iii) applicazione fresco su fresco del secondo strato di malta strutturale. Al contrario, il nuovo materiale composito consente di rinforzare i paramenti murari attraverso l'applicazione di un unico strato di prodotto. Inoltre, il prodotto è stato studiato per garantire un'applicazione a

“spruzzo” sul paramento murario, con ulteriore riduzione della tempistica di applicazione in cantiere.

Come anzi detto, la ricerca deriva dalla corrispondenza di interessi tra l’Università degli Studi dell’Aquila, il partner di ricerca Northwestern University e il partner industriale Aquilaprem. Quindi, il progetto ha seguito un percorso comune, con l’obiettivo di conciliare le diverse esigenze dei partner. Da un lato, la propensione delle Università all’indagare il problema in modo puramente teorico, attraverso l’analisi dei complessi meccanismi del sistema costruzione composita. D’altra parte, la propensione della società ad analizzare il problema teorico attraverso un approccio sperimentale con un procedimento euristico e l’obiettivo finale di ottenere un risultato spendibile per il mondo del lavoro.

L’impresa partner del progetto rappresenta una nuova e promettente realtà operante nel settore dei premiscelati per l’edilizia che sta gradualmente espandendo il proprio mercato in tutto il territorio italiano nel campo degli interventi di conservazione e rafforzamento dei monumenti storici. Tale azienda si è mostrata molto sensibile alla tematica di studio presentata, essendo da anni impegnata nella ricerca e sviluppo di materiali innovativi per il risanamento delle murature storiche. Essa ha garantito un supporto operativo in termini di disponibilità di personale, materiali, attrezzature e know-how già a sua disposizione. Tutte queste componenti hanno costituito un supporto fondamentale per lo svolgimento delle attività di ricerca.

In parallelo, anche il partner estero di ricerca è stato fortemente interessato ad affrontare la tematica di ricerca proposta, mettendo a disposizione un sofisticato modello numerico per la caratterizzazione del comportamento meccanico delle malte di rinforzo e dei pannelli murari. Il tutor accademico presso l’istituto di ricerca estero (Prof. G. Cusatis) è da anni impegnato in approfondite ricerche aventi come obiettivo generale quello di capire, simulare e prevedere il comportamento dei materiali fragili. Per tale motivo, il tutor estero di ricerca si è reso disponibile ad analizzare il fenomeno del risanamento delle murature, cogliendo l’occasione di perfezionare alcuni modelli numerici sulla base di tipologie costruttive non ampiamente diffuse all’Estero come in Italia.

Durante i 12 mesi di svolgimento delle attività di ricerca presso l’istituto estero Northwestern University (USA), sono stati sviluppati gli aspetti di modellazione analitica attraverso i quali, sono state indagate le variabili che maggiormente influenzano l’efficacia di un rinforzo esterno applicato alle murature. Per definire i principali fattori che influenzano l’aderenza tra materiale di rinforzo e supporto murario e quindi arrivare alla loro ottimizzazione, sono state effettuate simulazioni numeriche, cercando di adattare i modelli analitici, già sviluppati con successo in riferimento ad altri materiali (calcestruzzi), al caso di studio riguardante le malte

fibro-rinforzate a base di calce idraulica naturale. In particolare, le simulazioni numeriche sono state inizialmente rivolte allo studio dei pannelli di pietrame non rinforzati. Poi, la modellazione è stata estesa ai sistemi murari accoppiati ai materiali di rinforzo a base di fibra. Inoltre, la caratterizzazione meccanica per via numerica ha interessato anche la sola malta composita, cercando di indagarne la variazione delle proprietà meccaniche, in funzione della composizione della miscela e delle diverse lunghezze, tipologie e quantitativi di fibre introdotte all'interno della malta.

Nel Capitolo 1 della tesi sono descritte le principali caratteristiche delle muraure storiche di pietrame, focalizzando soprattutto la tipologia di pietrame irregolare fortemente riscontrata nei territori dell'Appennino centrale. Inoltre, il capitolo presenta un'analisi sulle caratteristiche dei sistemi di rinforzo, sia tradizionali che innovativi, utilizzati per la conservazione delle strutture murarie storiche. Il capitolo presenta poi un'ampia discussione sulle potenzialità del nuovo materiale sviluppato.

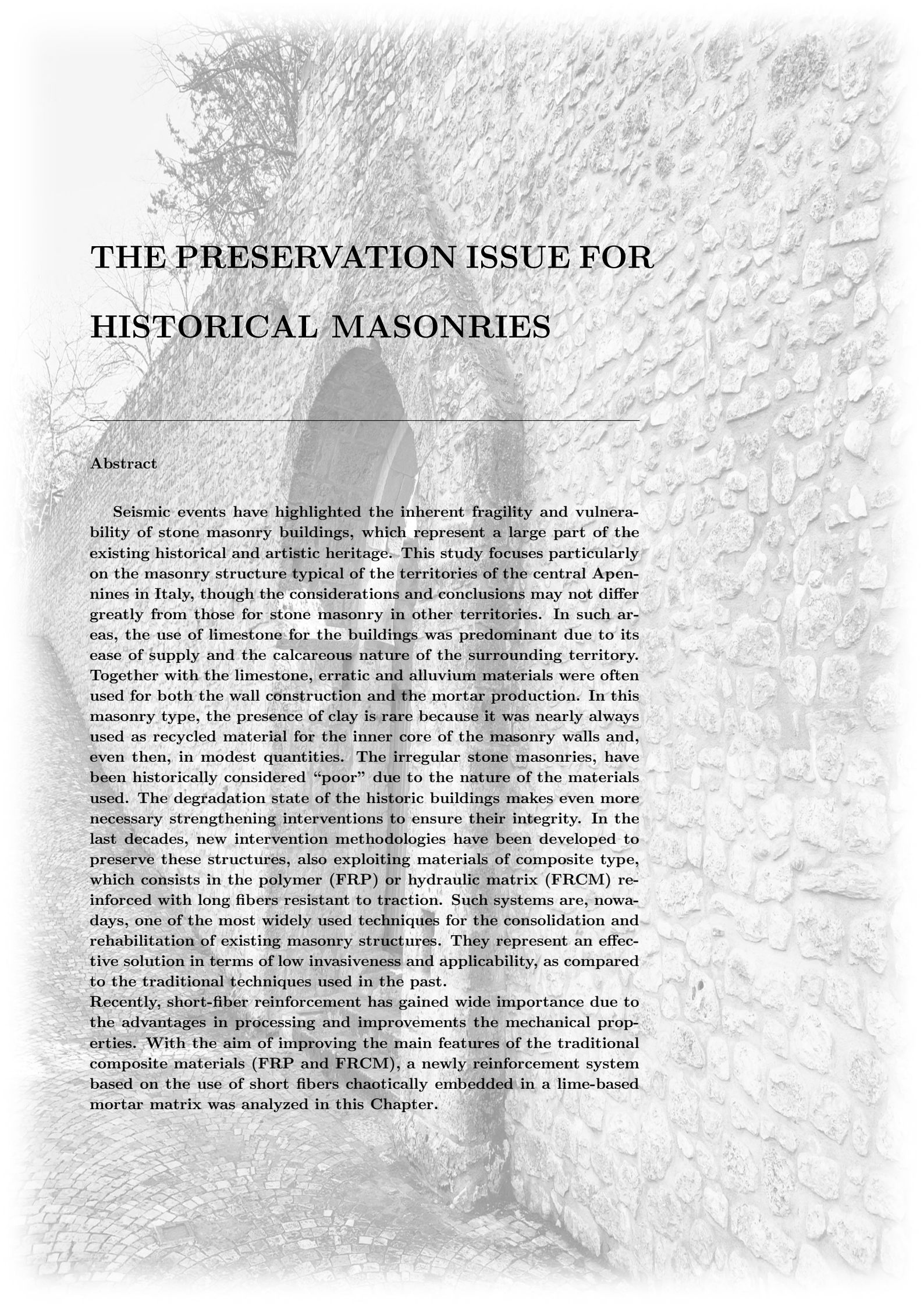
Nel Capitolo 2 della tesi è stata descritta la campagna sperimentale condotta sia sul sistema di rinforzo in fibra di tipo tradizionale, quale quello FRCM, sia su quello innovativo. La prima parte sperimentale riguarda test eseguiti in situ, su pannelli murari estratti dalle murature portanti della sede comunale "Palazzo Margherita" dell'Aquila. Tale edificio è rappresentativo degli edifici storici in muratura di pietrame irregolare presenti nel territorio aquilano, fortemente danneggiato dal sisma del 2009. La seconda parte sperimentale riguarda test eseguiti in laboratorio su pannelli murari preparati secondo la tecnica costruttiva storica, riscontrata nei numerosi palazzi monumentali della città dell'Aquila. In particolare, sono stati utilizzati elementi lapidei costituiti da pietre irregolari recuperate dai crolli parziali degli edifici e una malta riprodotta in modo che fosse simile a quella storica (caratterizzata da una resistenza a compressione inferiore a 2 MPa). Sia i test in situ e sia quelli in laboratorio sono stati eseguiti nella configurazione di compressione diagonale descritta dalla normativa ASTM E 519 2007. In particolare, tali test sono stati eseguiti sia su pannelli rinforzati con sistema FRCM e sia su quelli non rinforzati, con lo scopo di individuare l'efficacia prestazionale del sistema di rinforzo. L'ultima parte del Capitolo 2, invece, riguarda la descrizione delle prove sperimentali eseguite sull'innovativo materiale composito sviluppato. Tale materiale di rinforzo è stato investigato attraverso prove di flessione su tre punti, compressione e di trazione indiretta, eseguite su provini di malta rinforzati con differenti quantitativi di fibre disperse nella matrice di malta. Fibre di diversa geometria e materiale sono state analizzate con lo scopo di individuare la tipologia più adatta da adottare per il sistema di rinforzo.

Il Capitolo 3 introduce una panoramica generale dei modelli numerici impiegati

per le murature. Successivamente, un sofisticato modello numerico, denominato Lattice Discrete Particle Model (LDPM) è descritto in dettaglio. Esso è formulato nel framework dei modelli discreti ed è stato originariamente ideato, calibrato e validato per il materiale calcestruzzo. In questa ricerca, tale modello è stato applicato per la prima volta per la simulazione delle murature di pietrame irregolare. Con diverse scale di osservazione, infatti, è possibile individuare una forte somiglianza tra la rappresentazione particellare definita in LDPM per il materiale calcestruzzo, con quella delle murature di pietrame caotiche, in cui le dimensioni delle particelle sono maggiori (circa 50 mm – 250 mm). Inoltre, l'ipotesi alla base di LDPM, in cui si considerano le particelle come dei corpi rigidi, può essere considerata accettabile e ininfluenza sulla qualità dei risultati ottenuti, anche per le murature di pietrame. Tale considerazione trova fondamento nel fatto che le principali modalità di rottura di una muratura di pietrame avvengono per lo slittamento delle pietre sulla matrice di malta o per schiacciamento della sola malta. LDPM può rappresentare le unità di pietra come celle irregolari che interagiscono tra loro mediante opportune leggi costitutive. Nel Capitolo, i risultati sperimentali che hanno riguardato la caratterizzazione meccanica del sistema di rinforzo a base di fibre per le murature storiche di pietrame, sono stati simulati e interpretati con LDPM. Infine, la predizione del comportamento meccanico di un pannello murario rinforzato con la nuova malta fibrosa è stata proposta mettendo in luce le peculiarità del nuovo sistema di rinforzo. Lo sforzo computazionale nell'utilizzo di tale metodo è stato premiato dalla possibilità di catturare gli aspetti principali della eterogeneità del materiale, sia in termini di propagazione della frattura, sia in quelli del comportamento meccanico.

Il Capitolo 4 fornisce alcune indicazioni tecniche per la caratterizzazione meccanica dei sistemi FRCM o più in generale, sui sistemi di rinforzo caratterizzati dall'applicazione di uno strato di malta (rinforzate con fibre lunghe o corte) sulle superfici murarie. Una semplice formulazione analitica è stata proposta con lo scopo di stimare qualitativamente l'efficienza dei sistemi di rinforzo ad intonaco sulla resistenza di taglio delle murature così rinforzate. Tale formulazione considera solamente le principali informazioni della muratura non rinforzata e della malta di rinforzo applicata superficialmente ed è stata validata da un set di 60 test sperimentali provenienti anche da altri studi presenti in letteratura.

Infine, le Conclusioni si concentrano sulla discussione generale dei risultati più importanti ottenuti sia sperimentalmente che numericamente. Una dettagliata analisi sul comportamento meccanico dei sistemi FRCM è stata presentata. Inoltre, sono state esposte le principali caratteristiche osservate per l'innovativa malta a base-calce. La seconda parte delle conclusioni si concentra su ulteriori sviluppi di ricerca, articolati in diversi scenari.



# THE PRESERVATION ISSUE FOR HISTORICAL MASONRIES

---

## Abstract

Seismic events have highlighted the inherent fragility and vulnerability of stone masonry buildings, which represent a large part of the existing historical and artistic heritage. This study focuses particularly on the masonry structure typical of the territories of the central Apennines in Italy, though the considerations and conclusions may not differ greatly from those for stone masonry in other territories. In such areas, the use of limestone for the buildings was predominant due to its ease of supply and the calcareous nature of the surrounding territory. Together with the limestone, erratic and alluvium materials were often used for both the wall construction and the mortar production. In this masonry type, the presence of clay is rare because it was nearly always used as recycled material for the inner core of the masonry walls and, even then, in modest quantities. The irregular stone masonries, have been historically considered “poor” due to the nature of the materials used. The degradation state of the historic buildings makes even more necessary strengthening interventions to ensure their integrity. In the last decades, new intervention methodologies have been developed to preserve these structures, also exploiting materials of composite type, which consists in the polymer (FRP) or hydraulic matrix (FRCM) reinforced with long fibers resistant to traction. Such systems are, nowadays, one of the most widely used techniques for the consolidation and rehabilitation of existing masonry structures. They represent an effective solution in terms of low invasiveness and applicability, as compared to the traditional techniques used in the past.

Recently, short-fiber reinforcement has gained wide importance due to the advantages in processing and improvements the mechanical properties. With the aim of improving the main features of the traditional composite materials (FRP and FRCM), a newly reinforcement system based on the use of short fibers chaotically embedded in a lime-based mortar matrix was analyzed in this Chapter.



# The preservation issue for historical masonries

---

## Abstract in italiano

Il presente Capitolo descrive le strutture murarie di pietrame ed in particolare quelle riscontrate nei territori dell'Appennino centrale. In tali territori, si sono sviluppati, nei secoli, agglomerati urbani di media e piccola entità in cui era predominante l'uso della pietra calcarea non lavorata come principale elemento costruttivo. Unitamente al calcare, era spesso utilizzato materiale erratico e alluvionale, sia come elemento di riempimento dei vuoti delle murature, sia per la fattura delle malte. L'utilizzo del laterizio era piuttosto raro, essendo quasi sempre usato come materiale di recupero all'interno del paramento murario e, comunque, in quantità modesta. La tipologia muraria descritta presenta forti similarità con strutture collocate anche in altre aree geografiche. Questo capitolo mette in luce l'elevata fragilità della tipologia muraria analizzata, dovuta alla natura eterogenea, alla scarsa resistenza dei materiali costituenti e al comportamento strutturale di tipo disgregativo che, abbinato all'elevata sismicità delle aree su cui sorgono tali strutture, determina una estrema vulnerabilità del costruito ivi esistente. Tale aspetto è stato fortemente messo in luce dagli effetti disastrosi causati dai terremoti che hanno colpito queste aree, anche negli ultimi anni. Lo stato di degrado, in cui talvolta si trovano tali edifici, rende ancor più necessario interventi strutturali volti a garantirne l'integrità. In tale senso, negli ultimi decenni sono state sviluppate nuove metodologie d'intervento con lo scopo di preservare tali strutture, sfruttando anche materiali innovativi di tipo composito, a matrice polimerica (FRP) o idraulica (FRCM), rinforzate con fibre lunghe resistenti a trazione. Tali sistemi sono stati ampiamente discussi nel Capitolo, individuando e analizzando i punti critici di tali sistemi che, oggi giorno, sono maggiormente impiegati per il ripristino e il miglioramento sismico degli edifici murari in pietrame. Infine, il Capitolo presenta l'innovativo sistema di rinforzo, basato sull'utilizzo di malta a base-calce, rinforzato da fibre corte disposte caoticamente nella matrice. Nel Capitolo sono descritti i vantaggi relativi all'utilizzo di tale materiale composito nel campo dell'edilizia rivolta agli edifici storici, nonché alle sue diverse possibilità di applicazione.

## 1.1 Introduction

The use of masonry is very common in many historic constructions, both architectural monuments and whole urban centers all over the world. This masonry is generally made of various and very poor materials, characterized by different typologies.

This thesis is focused on the stone masonry, which is an old historic construction common throughout North and Latin America, the Himalayan region, Eastern and Western Europe, the Indian subcontinent, and Asia [11]. It is worth mentioning that many of those areas are characterized by medium-high seismic hazard [1] as observed in Figure 1.1.

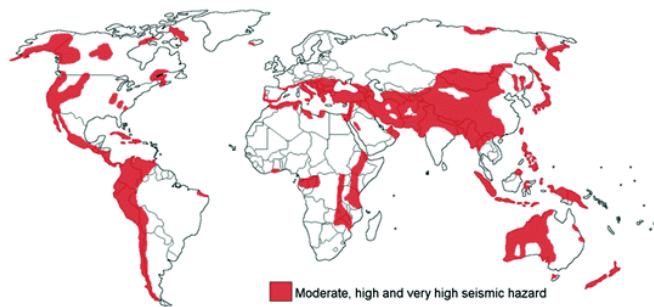


**Figure 1.1:** Medium-high seismic risk areas in the world [1].

The long-documented seismic history reports many catastrophes to these structures due to earthquakes. Indeed, the extreme vulnerability of stone masonry buildings was observed by recent seismic events, for example in Iran 2003 [12], Pakistan 2005 [13], Italy 2009-2012-2016 [14, 15, 16, 17, 18], New Zealand 2011 [19, 20], Chile 2012 [21], Nepal 2015 [22] and Albania 2019. This was mainly due to the mortar joints which represent the weak zone in masonry systems, especially in case of strong units combined to weak mortar joints, as frequently found in ancient stone masonries [23, 24]. The mechanical properties of stone masonry highly depend on the overall quality and mutual arrangement of both masonry units and mortar layers. Historical constructions, both monumental complex and vernacular architectures are often characterized by oversized structural components, mainly due to the need to effectively deal with seismic events. Despite the technical approach of stone masonry resulted in the realization of buildings having a considerable endurance, on the other hand, it is possible to notice that some constructive details negatively affected the seismic response of these constructions.

The constructive flaws, such as high percentage of voids in masonry panels and lack of effective connections among structural components, as well as low-quality stone units and mortar used in the building process, can lead to typical local mechanisms affecting historical buildings, such as the out-of-plane failure of masonry walls.

The worst defect of a masonry wall concerns its not monolithic behavior that is empathized when the wall is made of small pebbles arranged in two external layers that are not mutually connected and containing a rubble infill. This causes an increase in the brittle behavior of the masonry wall, particularly when external forces act in the horizontal direction. The same problem can happen under vertical loads if they act eccentrically [25].

The possible modes of vibration of a masonry building during an earthquake are strictly related to the quality of connections/anchoring between walls and horizontal structural elements.

The lack of transverse connection affects the vibrations mode of the walls in such a way that they become uncoupled and collapse may occur, especially caused by the out-of-plane forces. On the other hand, if walls are connected with rigid horizontal floor diaphragm and tie beams, the building vibrates as a monolithic box.

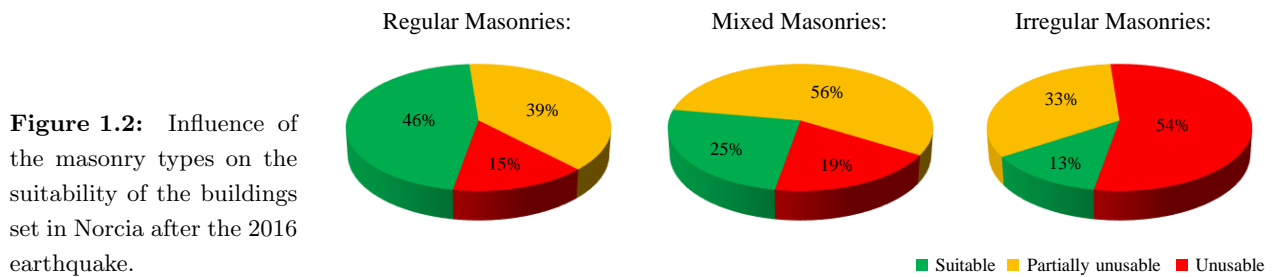
The low resistance of existing masonry buildings is often due to the lack of proper horizontal diaphragm action of floor and roof structures. Indeed, if adequately anchored to the walls, rigid floor diaphragms, and tie-beams prevent the out-of-plane vibration and possible collapses of walls.

Definitely, the fragility of this heterogeneous material, namely the stone masonry, interferes with the ductility criteria based on energy dissipation, which nowadays constitutes the safety principles of structural design for the safeguarding of human lives.

Given the great number of existing cross-sections and the great influence of the construction technique on masonry behavior, a systematic study of the mechanical behavior of stonework masonry should begin from an extensive investigation of the different geometry and building techniques, taking into account the different layers constituting the wall and the kind of constraints which may or may not be present between the layers themselves [26].

Recently, Borri [27] proposed a method for the characterization of the masonry structures based on the “quality” of their constituent elements. In particular, the quality of the masonry is quantified by an index value (the so-called Masonry Quality Index - IQM), computed for the masonry panels based on the presence of a series of construction devices which form the “rule of the art” in the building processes. The study on the building types of the central part of Italy damaged during the 2006 earthquake highlighted that the quality index of the masonries significantly affects their structural behavior. One can see in Figure 1.2 that most of the constructions made of irregular masonry suffered a total or partial collapse due to the “disaggregation” phenomenon concerning the total loss of cohesion between the stone elements. On the contrary, buildings with regular masonry

texture responded better to the repeated stresses induced by seismic sequence.



Obviously, the characterization of masonries is certainly complex and difficult to perform and it can not only depend on the quality of the masonry. In many cases, in addition to the poor quality of the masonry walls, the damage is also associated with the lack of the transverse connection, the presence of pushing elements, and other vulnerabilities. However, the damage observation of the masonry structures in the areas struck by recent earthquakes showed that the “masonry quality” factor plays a significant role in the characterization of the masonries [28] (see Figure 1.2).

Existing structures and buildings are subject to degradation with time, leading to a situation in which they become unable to fulfill the purpose for which they were built. Degradation of heritage structures can occur in a myriad of ways. Earthquakes constitute a significant cause of degradation and damage to the structure. The above-mentioned earthquakes have shown no mercy to these treasures and some of mankind’s living histories and memories have disappeared forever. Usually, there is an inexplicable and non-rational belief in some people that these monuments will survive future earthquakes, supported by the (false) argument that having survived previous earthquakes, they have passed a natural selection process and they will be able to survive future ones also [29]. This belief has been proven to be wrong on several occasions in which large parts of World Heritage were completely destroyed.

The seismic assessment and rehabilitation of heritage buildings and monuments have become issues of great importance around the world nowadays. It is due to the outcome of the need to improve existing buildings for adverse conditions, and, at the same time, to conserve humanity’s architectural heritage. Rehabilitation of heritage buildings comprises a way of sustainable development and also an act of cultural significance. The most crucial aspect of the restoration of existing buildings lies in structural rehabilitation and the improvement of the structural capacity ensuring long-term structural survival and public safety.

The assessment of the structural safety of existing buildings is a much more complex task, as compared to the design of a new building. This is because the

methods used in the past significantly differ from those adopted in the design of new structures. Furthermore, in the case of historical and monumental structures, the assessment and rehabilitation process is an even more difficult task as the eventual strengthening can conflict with cultural requirements.

Differing opinions have characterized this field throughout history aiming to attempt to establish criteria for the rehabilitation of historic and monumental structures. Nevertheless, a widely accepted framework was the “Venice Charter for the Conservation and Restoration of Monuments and Sites” [30, 31], which was formulated in May 1964, as a result of deliberations of many specialists and professionals in the restoration of historic monumental structures.

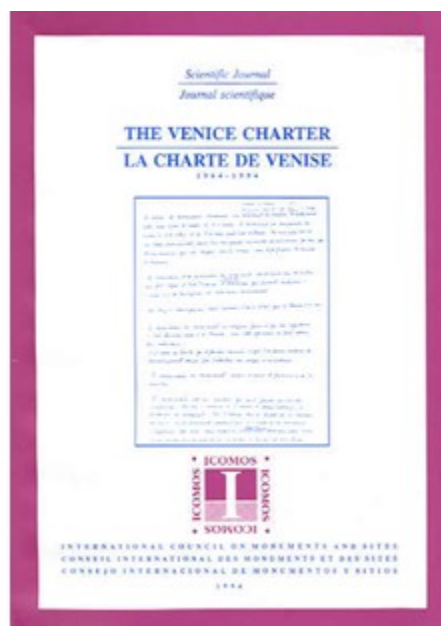


**Figure 1.3:** The “Venice Charter for the Conservation and Restoration of Monuments and Sites” is a set of guidelines, drawn up in 1964 by a group of conservation professionals in Venice, that provides an international framework for the conservation and restoration of historic buildings.

Although the document is now seen as outdated, since reconstruction is now cautiously accepted by UNESCO in exceptional circumstances, the Charter (among the many issues discussed for the preservation of historic structures) focused on achieving harmony between the existing structure and the rehabilitation work to be performed upon it. According to the Venice Charter, such interventions must follow some basic principles, such as material compatibility, conservation of overall lay-out or decoration and mass-color relationship, avoidance of the removal of any part, or additions to the building. The Charter requires detailed documentation of all rehabilitation works through critical reports (including drawings and photographs) and recommends its publication. According to ICOMOS recommendations, a thorough understanding of the structural behavior and material characteristics is essential for any project related to architectural heritage. It is also recommended that the work of analysis and evaluation should be done with the cooperation of specialists from different disciplines, such as earthquake specialists, architects, engineers, and art historians.

## 1.2 Description of the historical stone masonry of central Italy

In the light of the final aim of the present research involving the study of stone masonries, this category can be further divided as follows: 1) masonry with blocks of regular shape; 2) masonry with blocks of irregular shape (rubble masonry); 3) dry masonry. However, it is worth noting that some mixed masonries are characterized by the presence of more than one material. Different stone masonry types recognized in L'Aquila are illustrated in Figures 1.4a-f.

This thesis is mainly focused on rubble stone masonry (see Figures 1.4c-e), which consists of irregular stone elements distributed in a chaotic texture of weak mortar joints, the latter composed of poor lime or clay. That masonry type can be considered representative for the entire masonry structures in the territories of the central Apennines in Italy, though the considerations and conclusions may not differ greatly from those for stone masonry in other territories.

The morphology of the central part of Italy consists of valleys and mountains of considerable size. This favored the development of rural areas and medium-sized urban agglomerations, in which the use of limestone in buildings was predominant. Only the oldest and/or ecclesiastical buildings were built with square stone blocks, which were often recovered from older ruins. The almost exclusive use of limestone was due to the calcareous nature of the surrounding territory and its ease of supply. Together with the limestone, erratic and alluvium materials were often used for both the wall construction and the mortar production. In this masonry type, the presence of clay is rare, therefore, it was nearly always used as recycled material for the inner core of the masonry walls and, even then, in modest quantities. The almost exclusive presence of limestone led to different types of processing, finishing, and installation over the centuries. This created differences in both the structure and the shape between the ecclesiastical, or other important edifices, and the residential buildings [32].

The masonry type of historic buildings is characterized by fixed planimetric and volumetric schemes relating to a broad-ranging series of technical and formal solutions. These solutions emerged from, and were largely dependent on, the differing abilities of individual workers and the nature of available materials at the construction site.

Historical masonries are characterized, in the majority of cases, by limestone textured facades with regular or irregular mortar joints. In the case of carved stone walls, the outer elements of the facade were put in place last, after the underlying structure had settled. In those cases, the outer elements consisted



**Figure 1.4:** Different masonry types of the historical building of L'Aquila.

of blocks (or slabs) were self-supporting and were secured to the main structure by using binding stone elements and metal anchors. The internal parts of the walls were often plastered since, for the majority of cases, they were less valuable. The use of poor technologies and materials for the external facade of the walls, as compared to the internal ones, emphasized a scale of decreasing architectural values within the buildings, highlighting differences between prestigious buildings

and the more mundane. Indeed, the adoption of the non-square stones was as much due to difficulties in finding appropriate materials as to a lack of adequate capital, and to the necessity to rebuild, often in difficult conditions. Seismic events favored, especially after the seventeenth century, also a slow coverage of the external facades by plasters, except for the most representative buildings.

Irregular stone masonries spread especially between the fourteenth and eighteenth centuries and were historically considered “poor” due to the nature of the materials used. They were constructed using multiple elements across a wide range of sizes between the external and internal parts of the walls. In this type of masonry, the irregularity of the material inevitably caused a loss of horizontality that required a regularization process, which involved the use of wedges made of small stones or pieces of clay. Furthermore, due to the depth of the walls, the nature of the inner core of such structures is not easy to categorize because, in most cases, the materials are hidden from view.

The characterization of existing masonry is difficult to perform due to the large variety available all over the world. Indeed, the component materials, their combination, and the processes of manufacture are only a few, among several important aspects that should be considered. Nevertheless, an appropriate definition of existing masonry typologies would lead to identify their overall mechanical characteristics and lead to the most appropriate selection of intervention techniques.

Several classifications have been already proposed, mainly depending on the final aim to be pursued. One of the simpler classifications is based on a survey of the resisting elements or the masonry texture, and it can be found in classical restoration manuals [33, 34].

Based on the first aspect two main categories can be identified: stone masonry and brick masonry. Indeed, the features of stone masonry are characterized by stiff and strong stones connected with compliant and weak mortar layers. Its failure type is caused by damage localization, and frictional shearing occurring at interfaces among the stone units, through the weak matrix layers. On the other hand, the features of brick masonry are characterized by clay brick elements that are also involved in the failure, as well as for the weak mortar layers.

However, many cases of ancient masonry constructions are not characterized by only a specific type of masonry, as already described above (see again Figures 1.4d–e). Several mixed masonries are characterized by the presence of more than one material or by different compositions on the masonry depth. Considering a greater number of variables leads to a more complex classification. Further studies [35, 36, 37] underlined the importance of characterizing the transversal section of the masonry. This aspect became one of the discriminating elements to identify the mechanical behavior of the considered structural element. Giuffrè [25] stud-

ied the mechanical behavior of stonework masonry typologies based on a visual inspection and typology classification. The presence of some characteristic, such as the connection elements, called diatons, can be a discriminating parameter for the evaluation of mechanical behavior of walls. Other parameters can be: the size of the elements, shape of the stones, masonry texture, mortar quality, mortar content, presence of wedges, presence of horizontal courses, presence of leave connections and diatons, characteristic of the section, homogeneity of the material, the physical-chemical and mechanical characteristics of the components (brick, stone, mortar), the characteristics of masonry as a composite material.

Although the masonry types are susceptible to infinite-dimensional and formal variables, the identification is based on the survey of the leaves on the cross-section of a wall and it can be summarized in:

- Single leaf: stone elements are bound together using the mortar. This type is made up of compacted stone elements and is very common for walls with about 0.2 – 0.4 m in thickness;
- Double-leaf: two different layers can be identified in the cross-section. Nevertheless, this typology can be differentiated in two further sections: i) accosted leaves, they are completely separated by a vertical joint, that can be made by mortar or voids; ii) interlocked leaves, where stones of subsequent courses of opposite layers are slightly overlapped.
- Three-leaf: two load-bearing external leaves with high thickness value and an internal core comprised of stone fragments and waste materials, normally on incoherent form and without any bound element. This inner core has no static function not cooperating with the outer walls. In some (rare) cases, a transversal connection is provided by passing elements.

In the present thesis, both in the experiments and simulations, single leaf masonry was analyzed.

Furthermore, Giuffrè [25] proposed a classification based on a parameter which indicates the ratio of the distance between two subsequent diatons to the thickness of the masonry wall. Classification of single- and multiple-leaf masonry sections according to the number of leaves and their connections and the importance of this knowledge for the implementation of numerical models was suggested in [38]. Results obtained from an experimental campaign carried out on the transfer of shear stresses between leaves of multiple-leaf walls subject to vertical and horizontal actions were presented in [39].

### 1.3 Classic strengthening system

Recent seismic events revealed that the rehabilitation of masonry buildings was often performed without any feasibility study, with serious consequences on their structural safety.

The disasters generated by seismic actions discouraged the use of unreinforced masonry from ancient times until the more modern era. The traditional earthquake strengthening system can be considered as the result of practical expertise addressed to the mitigation of seismic disaster risk.

To improve buildings' structural performances under seismic actions, the most common construction materials, namely stone masonry and timber, were combined. Timber elements were incorporated in the masonry components to strengthen some critical/weak points of the structure such as corners and load-bearing wall intersections or, in the most advanced solutions, timber frames were realized.

Suffice it to say that the adoption of retrofitting systems began with the primordial civilization, such as traditional earthquake-resistant timber frames [40, 41]. According to the geographical area in which the technique was applied and developed, it is possible to identify several different configurations. That system is also known in the territories of the central Apennines in Italy, the so-called "baraccamenti", that is obtained by coupling wooden frames to masonry walls. Even with no specific knowledge about material structural behavior, these construction techniques proved, not always, to be effective, reducing the impact of seismic events both in terms of building damages and economic losses.

The discipline of techniques of intervention on existing buildings has developed rapidly over the past 50 years. For many centuries, up to 1900s, masonry and wood materials were predominantly used in the construction field. In the case of damage caused by earthquakes or atmospheric agents, such as the degradation of wood, the structures were repaired by using localized interventions. These interventions consisted of replacing damaged parts with new elements of the same material. Specifically, the techniques of the repair/replacement, and reinsertion technique.

The only exception concerned the addition of new material in the original structure of existing buildings was represented by steel chains for the hoops of damaged structures. The use of iron, as a reinforcing element of the buildings, has been known since the end of the fifteenth century, particularly as a tie rod, capable of efficiently fulfill the dual function of connecting the wall leaves and absorb any thrusts. Since the end of the sixteenth century the system of tie roads connected to each other, perhaps based on their massive use performed by Sinan for the magnificent dome of St. Sophia, has been widely spread up to be considered as the main and traditional reinforcement intervention system for the masonry domes

[42].

The iron hoops (and later in steel material) have demonstrated over time their undoubted effectiveness slowing down the lesions on the masonry caused by the thrust of the domed structures. Observing the beneficial effects and considerable resistance, the spread of iron in the consolidation interventions has increased rapidly, going hand in hand with an equally rapid technological development. Indeed, this material has been declined gradually in chains, structural staples, up to the latest application of reinforcing drilling.

Materials technology has had a growing development, bringing to light the use of concrete and other materials, thanks to the chemistry advances in construction.

Reinforced concrete has substantially influenced the cultural conception of the structures due to its enormous potential that allowed to build structures up hitherto unimaginable possibilities. Since then, the cognitive process and technological progress have stimulated technical and construction industries to design also suitable materials to increase the resistance of existing buildings.

The entrance of the cement in the field of restoration takes place in the second half of the 800 when it was used for the injections with the aim to consolidate the masonry walls. As often happens, the technological acceleration occurs on the push of a catastrophic event. Indeed, after the Messina earthquake of 1908, that material has been systematically spread to most of the masonry structures.

The rapidity of implementation and high mechanical performance of the concrete material determined the massively spread, with frequent replacements of the original static scheme of the ancient buildings with framed concrete structures, which was easier to design and, for this reason, considered more reliable.

The concrete on the other hand, newer than iron, is probably the material that has had the most rapid spread as reinforcement. Confidence in its infinite capacity led to replacing, in some periods, perishable original wooden structures with the concrete ones, resulting in serious damage on the buildings restored in that way, not only from the historical and formal point of view but also structural.

In the years after World War II, but also more recently, the cases of replacement of individual parts of masonry by reinforced concrete elements were numerous, influencing the overall static and dynamic behavior of the buildings.

The most interesting example concerns the frequent replacement of the old, and often destroyed, wooden trusses with similar elements in reinforced concrete. In this way, the original structure was completely unnatural and the new one was not capable of fully exploits the possibilities offered by the concrete material. Apart from this intervention type, it followed a greater involvement in the use of the reinforced concrete due to the significant increase of the vertical loads on the outside walls. Such interventions, already heavily invasive in both the historical

and aesthetic point of view, posed numerous problems of technical-structural types, such as the increase in the loads (and the consequent seismic action), stiffness, and shear strength inadequacy for some elements.

The application of reinforced cement coating (jacket) on one or both sides of the wall was massively used to improve the lateral resistance and energy dissipation capacity of the structural component. This method was very easy to apply and, at the same time, had good efficiency (based on the technical knowledge of that time). For these reasons, it was widely used to strengthen masonry walls in different countries all over the world.

Hence, the walls were covered by concrete slabs, with rigid concrete floors and a massive concrete curb on the top of the perimeter walls. In this way, it was possible to calculate the structure with the well-known POR method proposed by Tomazevic in 1978 [43].

In that frame model, the masonry walls are schematized by a set of piers connected by a rigid spandrel. This model considers the piers working in parallel with a shear-type behavior. However, this scheme is reliable only for structures with few floors and rigid spandrels because, if used in different conditions, it could overestimate the resistance.

In short, the attempt was trying to make reality look like the analytical model, thereby reversing the structural restoration priority that has to make the analytical model look like reality, even if it is not easily outlined.

For centuries, the iron and cement materials were thought to be effective for the restoration of the historical buildings. Even though they were applied to the historic architecture for a long time with scarce results and their chemical-physical characteristics are now known, even in recent times, such materials have been adopted by technicians. The lack of compatibility of these materials with the original one has produced enormous damage to the buildings in which they were applied with the aim to preserve them.

Furthermore, the polymer-based grouts, apart from the cement-based one, were one of the most commonly used techniques in repair and strengthening of both modern and old structures [44]. However, in the case of structures belonging to the architectural heritage, the use of polymer-based grouts should be as restricted as possible, both because of the incompatibility with the old materials and their possibly sensitive in-time behavior.

At the time, the debate about such materials varies with technology growth. Indeed, from the last forty-fifty years, even the reinforced concrete has observed with a mixture of caution and enthusiasm. The motivated trust in the capacity of that material has been opposed to the mistrust in both the physico-chemical and structural incompatibilities with the original construction since structural elements

in reinforced concrete elements were capable of altering the weakly equilibrium of the structure due to their rigidity.

The structural and formal damage occurs when one claims to vary, or even to replace, the original features of the historic masonries, which have anisotropic nature and are based on precise proportions and sizing rules that only rely on high compressive strength. It is clear that once entrusted to the iron/steel and concrete their higher mechanical properties, the structural behavior of historic masonry it would be completely different.

In the conservation perspective, an increasing sensitivity is nowadays directed to the choice of consolidation materials mechanically, physically, and chemically compatible with the original ones. In such ambit, lime-based mortars grouts are more and more considered (rather than cement or resins) to pursue both the effectiveness and durability of the intervention. Surprisingly, however, despite the evidence of error highlighted by the seismic events, the use of reinforced concrete curbs and the cement- or polymer-based grouts remained the most common intervention for the reinforcement of masonries until a few years ago. This attitude was due to an entirely forced (and damaging) distinction between consolidation and restoration, which must be resolved through the application of the art and science of building.

## 1.4 The classic fiber-based strengthening system

Traditional reinforcement used in practice in masonry structures is considered to be particularly invasive, as described in the previous subsection. Innovative technologies consisting of strengthening interventions performed with the use of fiber-based materials represent the most used systems in the construction field nowadays. Such systems are specially used for the retrofitting of the historical heritage. Indeed, due to the strict rules of preservation of historic structures, conservation committees usually request structurally efficient but less intrusive techniques intending to protect the historical structures.

In the last two decades, among modern and innovative solutions of intervention on existing structures, composite materials, such as the Fiber Reinforced Polymers (FRP) or the Fiber Reinforced Cementitious Matrix (FRCM), have been increasingly considered for strengthening and repair of both modern and historic masonry constructions (buildings, bridges, towers) and structural components (walls, arches and vaults, piers, and columns. These technologies consist of the use of composites material characterized by uni- or bi-directional long fibers.

These materials are proven to be effective in increasing the load-carrying capacity of masonry elements and improving their structural behavior through a reduction of critical brittle failure modes. Most importantly, the increase in strength is obtained with a lower increment of the structural weight, as compared to the traditional ones (e.g. reinforced concrete plaster).

The first applications of FRP materials for reinforcing structural elements date back to '80. As a result of the evolution of the FRP materials, in 2001 are patented the first FRCM systems. These applications can be considered as the technological evolution of the so-called "betón plaquè". The latter was largely applied in the static reinforcement of buildings by applying sheets of steel cut in various sizes and thicknesses and attached to masonry surfaces with the help of special epoxy resins and special plugs.

The composite materials have two important advantages related to both the durability and the implementation. Indeed, in the FRP and FRCM systems, the metal reinforcement exposed to corrosion is replaced with an armature consisting of non-corrodible synthetic fiber materials, such as glass, carbon, kevlar, aramid, and basalt.

As far as the FRP is concerned, its implementation is much more simple, as compared to the old systems, because it is characterized by no length limitations (due to the low weight of the fiber), and easy handling procedure. The FRP technology merely consists of the application of laminates and/or rods.

The use of laminates involves the application of fiber sheets by manual lay-up

to the surface of the masonry panels (Figure 1.5), which is previously prepared by sandblasting and puttying procedure. The fibers are impregnated by an epoxy resin, which after hardening enables the newly formed laminate to become an integral part of the strengthened member.



**Figure 1.5:** The FRP system consisting of the application of fiber laminates on the surface of stone masonry wall.

The other FRP technology concerns the use of pultruded rods, which consists in placing them into grooves cut onto the surface of the member being strengthened. The groove is filled with an epoxy-based paste, the rod is then placed into the groove and lightly pressed to force the paste to flow around the rod. The groove is then filled with more paste and the surface is leveled [45]. When the FRP rods are placed in the mortar joints, the technique is denominated “FRP structural repointing”. As compared to the traditional repointing technique, which consists of replacing missing mortar in the joints, the “structural” one not merely consists of filling the joints but allows for restoring the enhance of the shear capacity of walls [45].

High tensile strength and stiffness-to-weight ratio, fatigue and corrosion resistance, easy in-situ feasibility and adaptability, and progressive reduction in production and distribution costs, are the main characteristics that encouraged the diffusion of the FRPs [46]. The FRP is employed to improve the global behavior in the seismic zone (tying, connections among components, strengthening), to counteract specific incipient or developed damage (high compression, shear and/or flexural conditions), and to repair very specific local weaknesses depending on the peculiar construction typology.

Investigations have shown that for walls subjected to in-plane loads, the shear capacity and the ductile behavior of the unreinforced masonry walls (URM) were notably enhanced when strengthened with FRP laminates [47, 45]. Other investigations on the out-of-plane behavior of URM walls strengthened with FRP laminates demonstrated that the flexural capacity of the strengthened walls can be greatly increased [48, 49]

The use of FRP may be attractive since the surface preparation required for the installation of the laminates is greatly reduced, as compared to the traditional

system. Besides, FRP laminates not only offer solutions for the strengthening of masonry walls potentially subject to overloading caused by natural hazards such as high wind pressures and earthquakes but also to high pressures caused by shock waves [50].

The main failure mode of that system consists of the debonding of the FRP laminates from the masonry substrate. This failure phenomenon may have a direct relationship with the nature of the masonry unit, which can be characterized by the initial rate of absorption (IRA) test. For example, an investigation showed that the absorption of the epoxy may be limited in the extruded brick units compared to molded bricks [51]. This is attributed to the glazed nature of their surface, which leads to a reduction of the bond strength between the FRP laminate and the masonry surface. To prevent the FRP debonding, a common solution consists of anchor the fiber laminates into adjacent RC members (i.e. slabs, columns, and beams).

However, despite the fact that force transfer is probably sufficiently assured if surfaces are adequately prepared [52], externally bonded FRP have some drawbacks mainly related to epoxy adhesives [53, 54, 55, 56, 57, 58, 59, 52]: (i) high potential of harm for workers if the epoxies are not worked carefully; (ii) it is not possible to apply epoxies on humid surfaces whereas freeze problems may appear from isolated water; (iii) organic matrices are not permeable, hence frescoes existing at the opposite side of the walls may be affected; (iv) different thermal coefficients with masonry substrate cause strain incompatibilities; moreover, it is difficult to apply epoxies at low temperatures; (v) polymer composites exposed to fire have no protection; (vi) polymeric resins cannot be detached masonry substrates. (vii) the cost of epoxies is relatively high; (viii) the substrate roughness and irregularity may cause premature delamination and reduce the effectiveness of the intervention. As the executive phase is concerned, it is worth noting that the laying of the FRP materials must take place on completely dry surfaces avoiding that the epoxy resin comes into contact with moist parts otherwise the adhesion may be compromised. In masonry structures is good practice to proceed to re-point the joints of mortar, which consists of the removal of the outer parts of the mortar followed by reconstruction with new hydraulic mortar. This determines the possibility of applying the FRP reinforcement only when the curing of the new mortar layer is completed and, then, after a few days by repointing operations.

Moreover, due to the nature of the FRP installation, the fracture may be caused in some areas where the masonry wall is not strengthened, particularly in case of very brittle masonries, such as the irregular stone masonry. Since this masonry type is characterized by a disaggregation phenomenon, which consists of the total loss of cohesion between the stone elements, the merely local strengthening of the

FRP system may be not adequate for it. Diffuse strengthening would be preferred.

Most of the drawbacks listed above are mainly related to the epoxy matrix used to embed and bond the fibers. That material is completely no compatible with the chemical property of the ancient mortars, leading to a severe breathable issue of the masonry walls. Thus, substituting the epoxy matrix with a mortar matrix appeared to be the most reasonable solution to improve the overall performance of externally-bonded composite systems.

The latest generation of composite systems for the strengthening of masonry structures is known as Fiber Reinforced Cementitious Matrix (FRCM). In the literature, FRCM is also known as Textile Reinforced Concrete (TRC), or Textile Reinforced Mortar (TRM) [60].

Presently, the application of the FRCM, based on the use of fibrous reinforcements embedded in a mortar matrix, may overcome the disadvantages observed for the FRPs.



**Figure 1.6:** The FRCM system applied as a coating to the stone masonry surface.

Recent researches [61, 62, 63, 64, 65, 66, 67, 68, 69, 70] revealed the mechanical efficiency of the FRCM, its resistance to high temperatures and radiation, high vapor diffusion ability, easy preparation on-site (shorter preparation process), and the possibility to perform installation even on a wet substratum.

With regards to the out of plane behavior, a research [56] showed that for masonry wall subjected to out-of-plane cyclic bending, the textile-reinforced mortar provides a substantial increase in strength and deformability that was higher as the number of layers increased. In definitive, if failure is controlled by damage in the masonry, the FRCM outperforms its counterpart (the FRP) based on maximum load and displacement at failure, whereas if the failure mechanism involves a tensile fracture of the textile reinforcement the effectiveness of FRCM versus FRP is slightly reduced. From the results obtained in that study, the authors believe that FRCM jacketing was the best solution for strengthening and seismic retrofitting of unreinforced masonry subjected to out-of-plane bending. Most of the experimental campaign present in the actual literature on the FRM system was performed on masonry characterized by regular texture. Indeed, it has been

widely investigated for the one-leaf and two-leaf bricks (e.g. [71, 72, 73]), regular tuff blocks (e.g. [74, 75, 76]), and concrete blocks (e.g.[64]).

In [77] are collected more than 400 results of diagonal compression tests on masonry reinforced by FRM coating, pointing out the scarce presence in the literature of experimental tests performed on masonry with irregular texture. For the latter case, experimental campaigns can be found in [78, 79, 65, 80, 81, 82]. In general, also for the irregular masonry, the improved behavior of UnReinforced Masonry (URM) with FRM in terms of strength and deformation capacity has been demonstrated.

The influence of the fiber grid on the shear strength of the masonry panel was experimentally investigated in [79, 81]. In particular, any appreciable differences emerged in tensile strength (and shear modulus) of specimens reinforced with different percentages of reinforcement [79]. The authors realized that the tensile strength and the stiffness of the reinforced coating are negligibly influenced by the composite before cracking. Whereas the fiber mesh has great importance in the post-peak behavior of the Reinforced Masonry (RM), providing tensile resistance after cracking through the stress redistribution and permitting the masonry to reach significant values of the deformation capacity. On the contrary, [81] showed that the presence of the fiber grid increased up to about 150% the strength of the RM panel, although the number of the tests were limited and a similar investigation carried out by the same authors on clay brick masonry [83] showed the almost null effect of the fiber on the RM strength. The effectiveness of the fiber grid was also numerically investigated in [84] by adopting a sophisticated discrete particle model to simulate experiments performed on irregular stone masonry reinforced by FRM coating. Results showed that fibers have mainly the function to carry tensile stresses (load-bearing capacity) and redistribute the stress on the masonry panel, whereas the increase in the shear strength of the RM panel is highly related to the geometrical and mechanical properties of the reinforcing mortar.

The effectiveness of fibrous connectors for multi-leaf masonry panel was investigated in [79] under both shear compression and diagonal compression tests. Authors emphasized the role of fiber connectors in the failure mechanisms of the masonry because the reinforced masonry specimens failed due to local collapse mechanisms of few fiber connectors. Similar results were highlighted in [85], showing that the presence of transversal elements can avoid premature failure allowing an increase in the shear strength and ductility.

On the contrary, the effectiveness of connectors is less significant for single-leaf masonry panel [84] since that they have no effect in the shear strength of the masonry but only slight increase in the load-bearing capacity for large displacements.

Despite the two-sided jacketing is preferable, often is not permitted or is not

practically possible (e.g. presence of side frescos or fair-face on one side of the masonry). In this context, the performance of both the single-side and double-side strengthening configurations under cyclic shear test was also investigated in [80], showing that the strength of the double-side configuration increased of about 1.3 times, as compared to the single one. However, a comparable increase in ductility was obtained for the two solutions. A similar investigation on the strengthening configurations under diagonal compression was proposed in [81], showing a higher strength of about 2.5 times for the double-side configuration. In general, results confirmed that the presence of reinforcement on both the faces of specimens can be extremely efficient, providing a stable confining effect and allowing to avoid a premature disaggregation of the stones.

When the two-sided jacketing is not possible to be applied, a practical solution may consist of the application of a hybrid system composed of FRM jacketing (on one face) and the “reticolatus” (on the other face). The latter is a reinforced grout system characterized by steel or composite cords inserted into the mortar joints on the side. This technique is known was originally proposed by Borri (e.g. [86, 87, 88]). The hybrid system (reticolatus and FRM jacketing) was investigated in [80]. Results showed that the hybrid system offered an increment in resistance and ductility almost comparable to the double FRM coating.

Recent advances in fiber reinforcement for masonry was extended to short-fibers [81, 89] aiming to substitute the long fiber strands of the FRM embedded in the mortar coating and aiming to overcome the common disadvantage of both the FRPs and FRMs related to the orientation of the fibers in specific directions. That technique can significantly improve tensile strength, ductility, toughness, and durability of the mortar matrix by preventing or controlling the initiation and propagation of cracks because of the short-fiber effect [90, 91]. However, the fiber content, as well as the aspect ratio, shape, and nature of the fibers play a fundamental role in the mechanical properties of the composites (adequate load-bearing capacity should be ensured).

At present time, the CNR-DT 200/2004 [92], CNR-DT 215/2015 [93], ICC Evaluation Service [94], ACI440/2010 [58], and ACI549/2013 [95] codes are available as a guide to the FRM design and experimental tests for the application on masonry structures.

For the reasons mentioned above, the use of FRCM systems for the reinforcement of existing masonry structures is preferable to the FRP system and they represent the most favored choices in many projects [69].

Hence, the FRCM can be considered as the natural evolution of the FRP. Differently from the FRP, the long fibers are embedded in a mortar matrix capable of ensuring the adhesion with the support. The function of the fibers is to carry

tensile stresses, whereas the function of the matrix is to encapsulate and protect the fibers and transfer stresses from the mortar or masonry substrate to the fibers.

In FRCM composite systems, the fiber sheets or fabrics that are typically used in FRP are replaced with open fabric meshes in which the strands are assembled in at least two directions. Commonly, fiber strands are spaced in both vertical and horizontal directions forming a bidirectional orthogonal fabric grid. Closed fiber fabrics are not suitable because the mortar matrix cannot penetrate and impregnate the fiber filaments. However, the open structure of the fabric meshes provides a higher matrix-reinforcement interface area which is needed to achieve the composite action between the matrix and the reinforcing system. Typically, the mesh openings do not exceed 30 mm. The strands are typically coated with resin to improve the bond to the mortar matrix, enhance the long-term durability, and improve the load transfer among the roving filaments. The fabric meshes are typically made of carbon, alkali-resistant glass, basalt, polymeric fibers (such as Polyparaphenylene benzobisoxazole, PBO), or hybrid systems.

Stress transfer is accomplished through bonding between the substrate and the matrix, and the mechanical interlock between the fabric and the matrix. The composition of the cementitious matrix is very important and crucial for the performance of the FRCM system. The mortar should be non-shrinkable, workable (to be easily applied with a trowel and to penetrate the fabric mesh openings), and viscous (to be applied on vertical surfaces).

Hydraulic and non-hydraulic cement is usually used, though the use of lime-based mortar is increasing recently.

Finely graded sands help improve the workability of the fresh mix and the impregnation of the fabric mesh. The mortar mix can include chopped fibers to reduce the plastic shrinkage cracking. Organic compounds can also be used to control the hardening rate and the workability of the fresh mix, to improve the bond to the fabric mesh, and to enhance the mechanical properties. Their content is generally limited to be less than 5% by weight of the mortar binder to obtain a fire-proof matrix and ensure the compatibility with the original materials of the structures.

The performance of FRCM systems is highly dependent on their tensile strength and bond strength. The FRCM tensile behavior can be differentiated in three phases. In the first phase, the load is carried primarily by the mortar matrix until cracking. In the second phase, the matrix undergoes a multi-cracking process resulting in the transfer of stresses from the matrix to reinforcing fabric. In the third phase, the load is carried almost exclusively by the fibers [96].

As a comparison, FRP has a single-phase linear elastic tensile behavior until failure. The ultimate tensile strain in FRP is limited by the ultimate strain of the

fibers. The tensile properties of FRCM cannot be generalized, and each system should be evaluated individually. The tensile failure generally occurs for strain value much lower than the ultimate tensile strain of the fiber filament.

The bond strength of FRCM to the substrate material is difficult to quantify as it depends on the type of fibers, fiber sizing, mesh layout, the composition of the matrix, substrate properties, and quality of the surface preparation.

FRCM systems offer better performance under elevated temperatures, humidity, and ultraviolet radiation than FRP systems. In contrast to FRP, FRCM is inherently noncombustible and can be used unprotected. Combined with their noncombustibility and nontoxic characteristics, the FRCM system is a good option for strengthening when resistance to high temperatures is required.

FRCM for structural strengthening applications is a relatively new material. The results of durability testing are still limited. However, based on available tests, FRCM is expected to overcome most of the issues observed for the FRP because the cementitious matrix performs better than the polymeric matrix in moist and chemically aggressive environments. Moreover, research studies have proven the longevity of alkali-resistant (AR) glass fiber within the mortar matrix.

Despite all advantages that these strengthening systems can provide, as compared to the traditional ones, they are characterized by a long application procedure consisted of three phases: i) application of the first layer of mortar on the panel surfaces; ii) application of the fiber grids on the panel surface lightly pressing them on the fresh mortar layer to have the fresh mortar passing through the grid openings; iii) application of a second finishing layer of mortar on the panel surfaces to cover the glass fabric while the previous mortar layer was still fresh. Even if this procedure can be considered easier than the ones concerned for the FRPs and concrete plaster, it still represents a limitation.

A common disadvantage between the FRCMs and FRPs concerns the orientation of the fibers in specific directions: the FRCMs are characterized by fiber strands oriented in the bidirectional (horizontal and vertical) way (see Figure 1.6); the FRPs are characterized by a prior defined fiber direction (usually along the diagonal and the edges of the wall, as illustrated in Figure 1.5).

When the stress state is known, the proper use of such composites expected to suitably orient the fibers in the direction of the maximum stress to optimize the efficiency of the material.

Fibers activate their characteristics along with their axial direction, whereas they have negligible properties in the other directions [46]. Hence, the composites with long fibers, such as the FRCM or FRP, are characterized by high resistance only in the direction of the fibers. However, stress may vary substantially in different load conditions. In particular, tensional states induced by seismic events

do not act in a single and defined direction. In this case, that system may be not really efficient.

Therefore, it is necessary to consider the adoption of a diffuse reinforcement consisting of short fibers randomly oriented in the mortar matrix (discontinuous-fiber-reinforced composites).

## 1.5 The newly short fiber-based strengthening system

The technique involving the dispersion of fibers in a binder matrix in order to improve its mechanical properties, can certainly not be considered innovative. Indeed, this process began with the primordial civilization, in which clay bricks were realized by adding straw, and the lime-based mortars were reinforced by horsehair to increase their resistance. However, at the time, the main scope in adopting various types of fibers was to reduce the use of clay and mortar.

More recently, towards the end of the '40s, asbestos fibers were used to improve the mechanical properties of the cement paste as well as for their properties of fire resistance, thermal and electrical insulation, etc. However, as is well known, the limitation of such material is due to its extremely dangerousness, since exposure to asbestos causes several cancers and diseases.

In recent years, considerable interest has been aroused by different nature of fibers to reinforce the cementitious materials and principally to improve the ductility. The use of the fibers is greatly increased especially in concrete material. After the use of asbestos fibers in the production of prefabricated slabs, the steel fibers, and then glass as well as organic fibers (polypropylene, polyacrylonitrile, polyolefin) appeared in the construction field.

Short-fibers reinforcement has gained wide importance due to the advantages in processing and improvements the mechanical properties, included increased modulus, increased strength for high fiber content, decreased elongation at rupture, increased hardness even with relatively low fiber content, and possible improvements in cut, tear, puncture and impact load resistance. Moreover, another advantage concerns the easier execution of structural elements, as compared to the traditional technology based on the use of reinforcing bars and / or welded mesh.

The properties of short-fiber reinforcement depend on many factors, such as geometry, fiber content, fiber dispersion, fiber orientation, and fiber-matrix adhesion. Among the several factors that influence the properties of fiber-reinforced materials, the bond behavior at the fiber-matrix interface plays a role of primary importance. Indeed, the ultimate elongation of the fibers is about 2-3 orders of magnitude higher than the ultimate strain of the mortar matrix and, therefore, the failure of the mortar matrix takes place before of fiber failure. The fibers provide the greatest benefits especially in the softening phase when the maximum resistance of the material is achieved. In that phase, fibers are arranged astride the lesion allowing the transmission of forces through a "sewing effect" that prevents the brittle collapse of the material (as one would observe in absence of fiber

reinforcement).

The performance of a fiber-reinforced material, although in part related to the elastic properties of the fibers (depending on their nature), is strictly dependent on the adherence property of the fiber to the mortar matrix. In particular, the adherence property of the mortar usually increases for high mechanical properties of the mortar, namely compressive and tensile strengths.

Besides, the geometrical parameters of the fiber play a fundamental role, such as: (i) the length of the fiber ( $\ell_f$ ), which is the distance between the ends of the fiber; (ii) the equivalent diameter ( $d_f$ ), which is the diameter of an ideal circle area of the fiber cross-section; (iii) the aspect ratio (AR), which is defined as the ratio between length and equivalent diameter.

Since the behavior of fiber-reinforced material strictly depends on the bond behavior at the fiber-matrix interface, the aspect ratio assumes considerable importance in the load-bearing capacity, when the cracks through the material occur. Obviously, the sewing effect of the fibers is also influenced by the geometric shape of the fiber. Indeed, fibers with bent ends as well as hooked and wavy fibers, etc. allow to maximize the anchoring of the fiber from the matrix and, consequently, yield more efficient the effect of the fiber on the mechanical behavior of the fiber-reinforced material.

The sewing effect also depends on the number of fibers that are arranged astride the lesion. Therefore, both the fiber content and the fiber distribution play an important role in the mechanical behavior of the composite material. Obviously, the higher the fiber content, the higher the fiber distribution. Therefore, the higher the fiber distribution, the higher the efficiency of the fiber reinforcement. However, it worth noting that high quantities of fibers also produce a reduction in the fluidity of the fresh product. This aspect should be taken into account in the mix-design phase.

Reinforcement made of short-fibers is a topic that is being studied for several years from different researchers. However, nowadays, no commercial product made of lime-mortar reinforced with short-fibers is employed for the strengthening of the existing historical structures. Currently, short fibers are used, in partial or total replacement of traditional reinforcement. Moreover, they are adopted in the mix design of concrete elements, aiming to improve their mechanical properties, for the realization of industrial concrete slabs, structural or nonstructural precast elements and tunnel coatings.

The idea, developed in the present thesis, of using short-fibers embedded in a lime-based mortar matrix for the strengthening of the walls of the historical stone masonries can be considered innovative. Indeed, no literature study describes the mechanical behavior of that composite material applied to the masonry. That

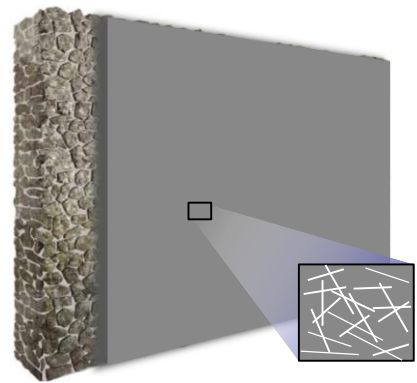
composite material can be considered as a promising newly reinforcement system that may ensure an adequate safety level for seismic forces acting in any direction. The new material, called in the follows with the acronym SFRLM (Short Fiber Reinforcing Lime Mortar), was conceived to be compatible with old constituent material of existing historical masonry. Indeed, the low compatibility of the cement-based mortar of the classic strengthening system with the lime-based mortar of the masonry joints yet represents an issue. In several recent cases, extensive damage occurred to the ancient masonry due to the incompatibility of the cement-based mortars [97, 98, 99]. Current standards [100, 101] define cement-based mortars to be inadequate for strengthening interventions of historical masonries. Natural Hydraulic Lime (NHL)-based mortars [99, 102, 103] are considered a promising alternative to cement materials when high compatibility with historical substrates is strictly required. This compatibility must be reflected in several aspects: (i) chemical compatibility between the reinforcing mortar and the old material (stone or brick and its bedding mortar); (ii) physical compatibility, with special reference to processes of solubility and of water transport; (iii) structural and mechanical compatibility (strength of repair mortar needs to be similar to the old material) [99].

Hence, the SFRLM system can solve all the issues related to the traditional reinforcing system as well as the classic fiber-based strengthening system. The aim of the thesis concerns the mechanical characterization of the SFRLM to provide effective efficiency in terms of strength and ductility.

The main application thought for this newly reinforcing system consisted of the application of a layer of the SFRLM as a coating to the surface of the masonry walls. This technique was inspired by the classic FRCM system. However, the SFRLM presents greater advantages in terms of easiness and time application in situ, as compared to the FRCM. Suffice it to say that the application of the FRCM is performed according to three phases: (a) application of the first layer of mortar on the panel surfaces; (b) application of the fiber grid on the panel surface lightly pressing the fabric on the fresh mortar layer to have the fresh mortar passing through the grid openings; (c) application of a second finishing layer of mortar on the panel surfaces to cover the glass fabric while the previous mortar layer was still fresh. On the contrary, the SFRLM can be applied to the masonry surfaces in a unique phase, consisting of the application of a single layer of the SFRLM to the surface of the masonry. This application would consistently reduce the cost.

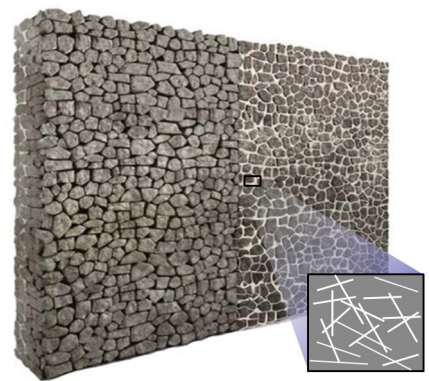
In Figure 1.7 is illustrated the newly reinforcing system based on the SFRLM investigated in the thesis.

**Figure 1.7:** The newly strengthening system, based on a lime-based mortar with short fibers chaotically embedded in the matrix, applied as coating to the masonry surface.



On the other hand, the new material presents high flexibility in its application on historical masonry structures. Indeed, it can be also used in the structural repointing technique. The latter consists of replacing the deteriorated mortar or filling the missing mortar in the joints by employing the new composite material, allowing both to enhance the shear capacity of walls and preserve the original aesthetic of the masonry texture. Indeed, when choosing a retrofit method, its impact on the aesthetics of the building being retrofitted needs to be evaluated [45]. As far as the aesthetical impact is concerned, to be completely successful, retrofit work should be carried out with the least possible irrevocable alteration to the building's appearance. Many unreinforced masonry buildings are part of the cultural heritage of a determined city or country. Thereby, the preservation of their aesthetic and architecture is of main importance. It is recognized that the use of external reinforcing, such as the FRP or the FRCM, can alter the aesthetic of a masonry wall. The use of the structural repointing by using the SFRLM material is an alternative to strengthen masonry walls where aesthetics is an important issue. Aesthetic considerations are fundamental for historic structures. Traditional repair techniques, including steel plates or external tendons, resulted as unsatisfactory to retrofit churches and historical building after the last earthquakes in Europe. The new material proposed in the thesis can solve this problematic aspect.

**Figure 1.8:** The newly strengthening system applied for the structural repointing of the old and damaged mortar joints.



# EXPERIMENTS

---

## Abstract

The first phase of the experimental campaign focused on the mechanical characterization of the traditional FRCM system. This system was first tested on irregular stone masonry specimens isolated from the walls of the historical building “Palazzo Margherita” of L’Aquila. This masonry type is representative of historical buildings, widespread in the territory of L’Aquila, that were strongly damaged in 2009 earthquake. The FRCM system was also tested on masonry specimens prepared at the laboratory LPMS of L’Aquila, using the original limestone units and the ancient constructive technique adopted in most of the monumental buildings of L’Aquila. In particular, the difference between experimental results (laboratory and in-situ tests) was relatively small, encouraging the possibility to obtain reliable results when investigating irregular stone masonry prepared in the laboratory, at the condition that the latter are strictly built in line with features of the existing buildings. Furthermore, in the last part of the Chapter it is described the experimental campaign carried out at the laboratory of the “Aquilaprem” company for the mechanical characterization of the the newly fibrous lime-based mortar. Results regards the optimization of the mix design of the product as a function of the nature, geometry and content of the fibers. The innovative composite material was tested in several destructive test, namely the three-point bending test, indirect tensile test, and compressive test as well as test for the estimation of the workability of the product.



# Experiments

---

## Abstract in italiano

Il capitolo descrive le attività svolte durante l'ampia campagna sperimentale riguardante la caratterizzazione meccanica dei sistemi di rinforzo in fibra tradizionali (FRCM) e innovativi (fibre corte disperse caoticamente nella matrice). In particolare, nella prima parte del capitolo, sono state descritte le prove di compressione diagonale eseguite su pannelli di muratura di pietrame irregolare, sia nella condizione originale e sia nella condizione rinforzata con FRCM. Tali prove sono state dapprima eseguite su provini murari di pietrame irregolare isolati dai paramenti portanti dell'edificio storico "Palazzo Margherita" dell'Aquila. La tipologia muraria di tale edificio è rappresentativa delle strutture storiche ampiamente diffuse nel territorio aquilano che sono state fortemente danneggiate dal sisma del 2009. Il sistema FRCM è stato poi sperimentato anche su provini murari preparati presso il laboratorio LPMS dell'Aquila, utilizzando la tecnica costruttiva degli edifici storici. In particolare, per la realizzazione dei provini, sono stati utilizzati elementi lapidei irregolari recuperati dai crolli parziali di Palazzo Margherita e una malta a base-calce riprodotta con le stesse peculiarità di quella storica. I risultati ottenuti hanno evidenziato che le proprietà meccaniche e le modalità di rottura dei pannelli riprodotti in laboratorio sono state in linea con quelle ottenute per i campioni murari storici di Palazzo Margherita. Questo permetterà, in future sperimentazioni, di utilizzare campioni murari riprodotti in laboratorio anche per testare il nuovo sistema di rinforzo, basato sull'applicazione di un intonaco di malta a base-calce fibrosa sulle superfici murarie. Nell'ultima parte del capitolo, sono state descritte le prove di caratterizzazione meccanica del materiale innovativo, sviluppato presso il laboratorio del partner industriale "Aquilaprem". In particolare, prove di flessione su tre punti, di trazione indiretta e di compressione, insieme a prove di lavorabilità del prodotto, hanno permesso di ottimizzare il mix design del prodotto in funzione della natura, geometria e contenuto delle fibre nonché della tipologia e del quantitativo degli additivi atti a migliorarne la lavorabilità. I risultati mostrano il confronto delle prestazioni meccaniche ottenute per il materiale fibroso rispetto alla semplice malta non rinforzata.

## 2.1 Investigation on the FRCM system

### 2.1.1 Diagonal tests carried out in situ

The experimental campaign on the FRCM system was performed in situ by diagonal compression tests. In particular, tests consisted of the application of cyclic monotonic quasi-static load to the masonry specimens until their failure. The tests were carried out in situ by isolating four masonry samples from the walls of the municipal office “Margherita Palace” of L’Aquila (Figure 2.1). Two of the four tested panels were strengthened by the FRCM system, consisting of NHL3.5 natural hydraulic lime-based layer of mortar (M15 strength class) reinforced with glass-fiber grids. These mortar layers were applied on both the external surfaces of the masonry panels. The natural lime-based mortar was used to ensure the chemical-physical compatibility with the nature of historic walls. Furthermore, the strengthening system consisted also in the application of four carbon-fiber anchors and one steel bar anchor covered with a carbon-fiber fabric. Results allowed to analyze the variation of the mechanical properties of the panels during the cyclic tests.

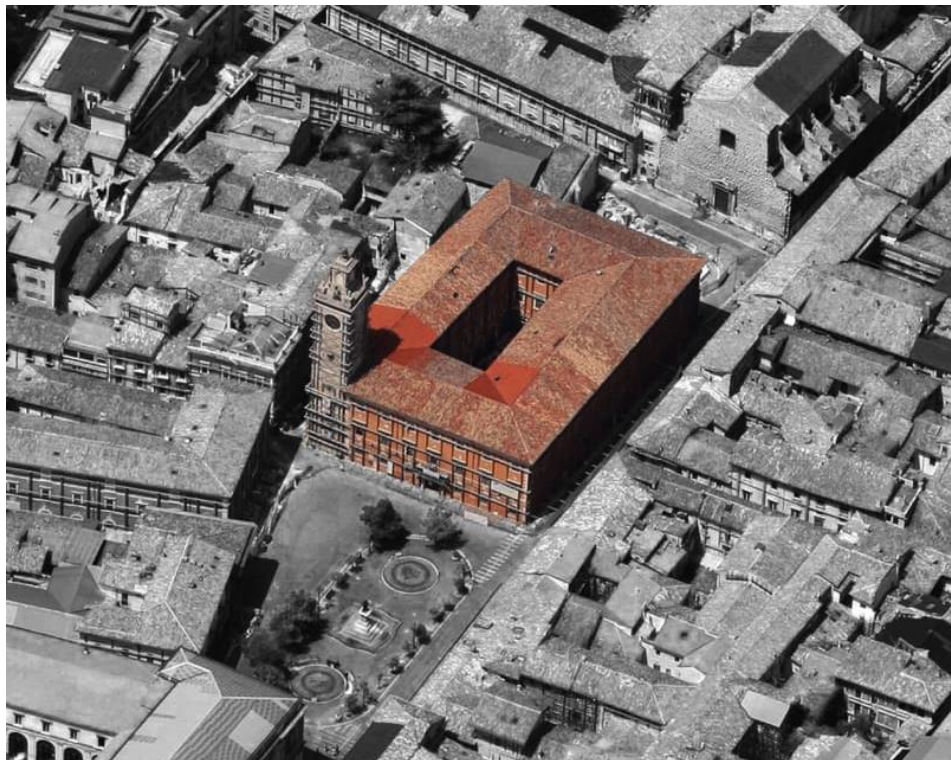


**Figure 2.1:** The monumental masonry building “Margherita Palace” standing in the city of L’Aquila, almost at the center of the old fortified town. (photo taken from [2]).

### 2.1.1.1 Brief description of the Margherita Palace

The construction of the Margherita palace started in 1294 in L'Aquila (Italy) and struck during the 2009 earthquake. It is almost placed at the center of the old fortified town. The main front of the building faces Palazzo Square. On the back side, the building faces S. Margherita Square. Next to Palazzo Margherita there are several other historical buildings including Palazzo Camponeschi (XVI century), the old Jesuits' Church (XVII), Palazzetto dei Nobili (XVII century).

Original site plan probably dates XIII century, although profound intervention were made on the building during XVI century. In [104] is well described the restorations processing performed on the building during the years. In particular, the construction of the palace started in 1294 and originally was used as a civic building for the Captain of Justice. Jerome Pico Fonticulano, architect, mathematician and writer was the designer of the renovation of the Renaissance town hall in 1541, as indicated by a plaque on the facade. In 1573 the building was almost completely rebuilt by Battista Marchiolo of Naples (decorated with stucco and interior design by Bedeschini and frescoes by Fantilli). Unfortunately, it seems that the building does not retain much of the original design and the reconstruction of the second half of the 16th-century structures in the current reconstructed version of the 19th century [104]. Only the plan settings and the monumental proportions, and the pleasant courtyard compound, are elements of the late 16th century that recall the importance of the place.

Building geometry is currently characterized by a rectangular shaped plan measuring about 40 m × 60 m with the longer sides aligned in SE-NW direction. The four sides of the building surround an internal courtyard. The palace consists of three stories, each of them measuring about 5 m in height. The first level is partially set below the sloping ground level, with the highest fronts of the building at the North corner of the building. The building's facades present a regular vertical and horizontal distribution of three orders of rectangular windows. At the south corner of the building stands a 41 m high civic tower, one of the town's iconic symbol, characterized by an almost square plan, and consisting of stone made walls measuring about 1.70 m in thickness at the base.

The structure is made primarily of irregular stone and a small content of clay brick bound together by lime mortar of poor quality. The floors are made of masonry vaults (with and without tie rods) at the ground floor and of steel and brick at the first and second floors. Tie rods are in the north façade and at the two angles in the east façade (Piazza Palazzo) and west façade (Piazza Santa Margherita). There are no tie rods in the south façade. There are tie rods in the internal courtyard in the east-west façade, but they are not present in the north-

south façade. The building is located on a slope and has a height differential of 1.5 m between the north wall in Via Baffle and the south wall in Via delle Aquile. It also has a height differential of 2.40 m in the east-west direction because Piazza Palazzo is elevated compared to Piazza Margherita.

The main damage mechanisms detected during field observations [104] can be divided into two groups: (1) wall overturned caused by seismic forces applied perpendicularly to the walls, and (2) shear mechanism caused by seismic forces applied parallel to the walls which develop the typical diagonal cracks. The first mechanism regards the south external facade of the palace, where 5 cm displacement at the top external lateral wall was observed and is also present on the north internal wall of the courtyard. The second mechanism occurred below the external windows of the first floor on the east side and some internal walls of the palace.

Additionally, there is another localized damage that does not fit in the two previous categories, like damage to the roof cover, shear cracks in the cross vaults of the stairs, and the collapse of some vaults and of a floor slab on the second floor. Furthermore, the tower partially collapsed to the ground during the earthquake. Its tall and slender shape as well as the cantilever-type boundary condition of the basement generated a concentration of stresses at the basement that was also amplified by the brittleness of deteriorated masonry. However, the vulnerability of the tower may be due the 20th-century renovations, which replaced a wooden deck with one made of reinforced concrete, thus making the tower top-heavy [105].

The detailed crack survey showed the presence of diffused and severe crack patterns on the outer surface that also appear in the inner walls. Cracks were observed at the base of the tower and on the south and east sides. Some of those cracks already existed from the 1703 earthquake, and they reopened; and new cracks occurred with the 2009 earthquake [106].

### 2.1.1.2 Materials and method

Four masonry samples measured 1.2 m in length and 1.2 m in height, in accordance with the ASTM E 519 [107], were tested. The thickness of the analyzed walls was ranging from 0.5 m to 0.75 m. The masonry type consisted of irregular stones and small inclusions of clay bricks chaotically distributed within poor mortar joints that is a typical configuration of the historical buildings of the central part of Italy. Stone elements were of a calcareous nature and their size was ranging from about 100 mm to 250 mm. Mortar was characterized by a very friable behavior and a low compressive strength of about 2 MPa. Figures 2.1a,b illustrate the masonry texture of the historical building.

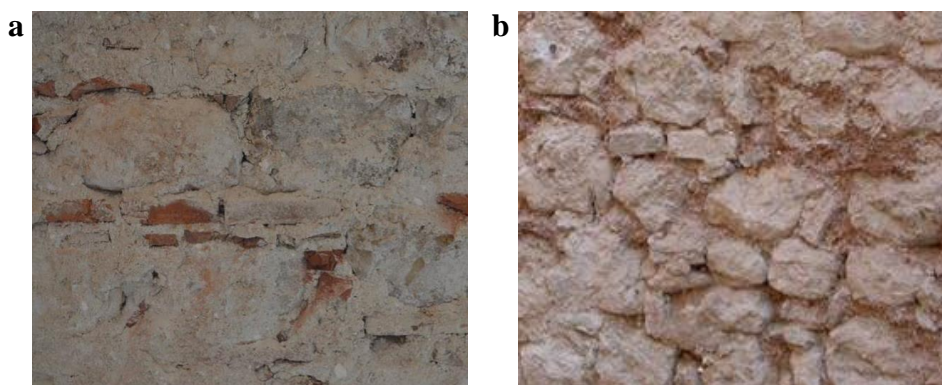


**Figure 2.2:** a,b) Chaotic masonry texture made of irregular stone units, poor lime-clay mortar and inclusions of bricks.

To isolate each sample from the historical walls, a preliminary operation consisting of the execution of four cuts made with a circular saw was performed according to the following procedure: i) a horizontal cut was performed in correspondence of the upper part of the sample; ii) vertical cuts were performed in correspondence of the edges of the sample; iii) a final horizontal cut was performed only for about 0.4 m in length in correspondence of the bottom part of the sample.

The main geometrical properties of the masonry samples are listed in Table 2.1.

**Table 2.1:** Geometrical properties of the unreinforced (URM) and reinforced masonry (RM) specimens. Legend:  $D_m$  and  $t$  are the average size and the thickness of the samples.

Name	$D_m$ [m]	$t$ [m]
1URM	1.205	0.580
2RM	1.195	0.750
3RM	1.210	0.565
4URM	1.215	0.510

Two diagonal compression tests were carried out on reinforced masonry (RM) by the FRCM system and two tests were conducted on unreinforced masonry (URM). The strengthening system was consisting of a glass-fiber grid embedded in the NHL-based mortar layers applied on the masonry surfaces. In particular, glass fiber strands were spaced with a gap of 25 mm in both vertical and horizontal directions forming a balanced bidirectional fabric (Figure 2.3).

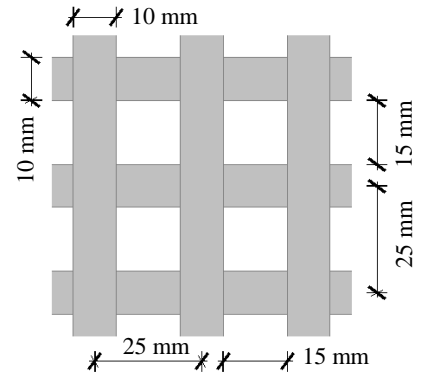


**Figure 2.3:** Geometrical characterization of the glass fiber grid.

Since grids were manufactured with standard dimension of 1.0 m in width, with the goal to recover the square masonry samples with size of 1.2 m, a square piece of glass fiber grid of 1.0 m was first applied at the center of the masonry samples. Then, four pieces of the fiber grids of  $0.2 \text{ m} \times 1.2 \text{ m}$  were placed at the edges of the specimen (see Figure 2.4a). In this case, the overlapping length between the central grid and the lateral pieces of the grid was equal to 0.1 m.

Furthermore, both the reinforced panels were equipped with five embedded anchors, which were designed to connect the two external FRCM layers to each other. Four anchors consisted of glass fiber bundles and characterized by a nominal diameter of 10 mm were placed at a distance of about 225 mm from the lateral edges of the panels. Their bundle ends were characterized by a circular configuration with 300 mm in diameter. Furthermore, one steel corrugated bar (B450C) covered with a carbon-fiber fabric was placed in the center of the face of a panel. That anchor was characterized by a nominal diameter of 12 mm. Figure 2.4b shows the detail of the anchor positions.

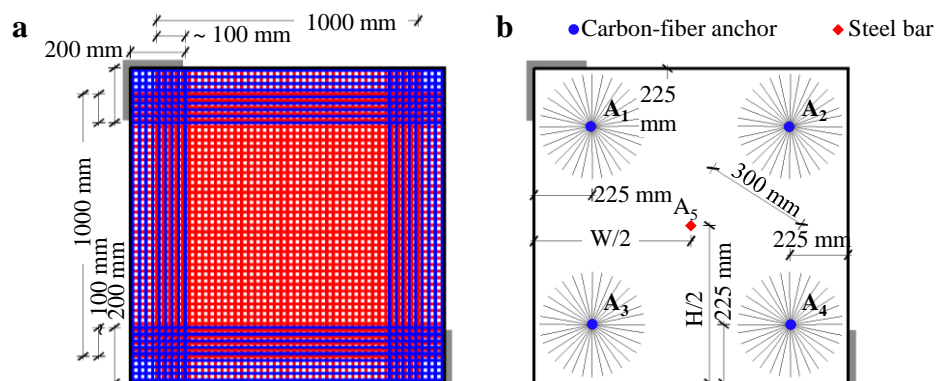


**Figure 2.4:** a) Particular of the disposition of the fiber grids: a square glass fabric grid of 1 m is placed on fabric stripes placed at the edges of the specimen; b) Details of the anchors.

Mechanical properties of the fiber and the mortar types employed for the FRCM system are listed in Table 2.2 and Table 2.3, respectively.

**Table 2.2:** Geometrical and mechanical properties of the fibers employed in the FRCM system. Legend:  $\rho$  is the density;  $m_{UA}$  is the mass per unit area [6];  $E$  is the Young Module;  $f_t$  is the tensile strength;  $\varepsilon_u$  is the ultimate strain [7].

Material	$\rho$ [kg/m <sup>3</sup> ]	$m_{UA}$ [kg/m <sup>2</sup> ]	$E$ [GPa]	$f_t$ [MPa]	$\varepsilon_u$ [%]
Glass (grid)	2680	-	72	1700	3.7
Carbon (anchor)	1820	4.55	250	4700	1.9
Carbon (tape)	1800	0.383	230	4900	2.1

**Table 2.3:** Mechanical properties of different mortar types employed for the application of the FRCM system. Legend:  $\rho_{solid}$  is the density of the solid mortar;  $E$  is the Young Module [8];  $f_c$  and  $\sigma_f$  are the compressive and the flexural stress [9], respectively.

Material	$\rho_{solid}$ [kg/m <sup>3</sup> ]	$E$ [MPa]	$f_c$ [MPa]	$\sigma_f$ [MPa]
mortar(BridgeSystem)	1110	-	12.0	1.15
mortar(CH15)	1835	9100	15.0	4.0
mortar(CI15)	1500	6200	15.0	3.9

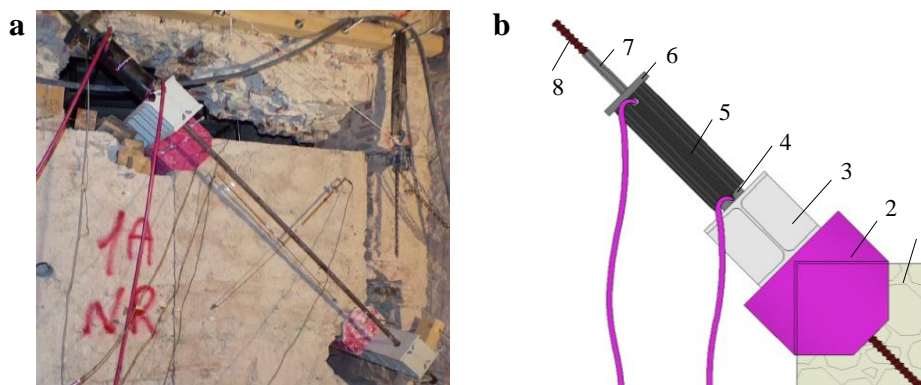
The application of the FRCM system to the reinforced stone masonry samples was performed according to the following procedure: (a) the panel surfaces were first cleaned to remove any loose material and were wet; (b) five holes, characterized by a diameter equal to 30 mm, were performed by means of a rotating drill in correspondence of the anchor allocations (see Figure 2.4b); (c) the anchors were inserted in the holes; (d) an injection of a lime-based mortar (the *CI15*) was made into the holes to fill the voids and to guarantee for a good adherence between the connectors and the masonry; (e) a rendering coat (rinzafo) of about 1-2 mm in thickness was applied on the wet panel surfaces to ensure proper bond condition between the masonry specimen and the mortar layer; (f) a first layer of NHL-based mortar (*CH15*) was applied on the rendering coat layer with a thickness of about 15 mm; (g) a fiber grid was applied on the panel surface slightly pressing the fabric on the fresh mortar layer to have the fresh mortar passing through the grid openings; (h) the ends of the  $A_1$ ,  $A_2$ ,  $A_3$  and  $A_4$  anchors were refolded on the panel surfaces and were spread in a circular configuration of 30 mm in diameter (Figure 2.4b) and recovered by the *BridgeSystem* mortar; (i) a second finishing layer of mortar was applied on the panel surfaces to cover the glass fabric while the previous mortar layer was still fresh for a total final reinforcement thickness of about 30 mm; (j) the same operation was repeated on the other side of the wall.

### 2.1.1.3 Test setup

Performing the diagonal compression test allows the evaluation of the shear strength, the shear elastic modulus, and the ductility of the masonry [108]. Although no specific standard exists on mechanical tests to be performed on chaotic stone masonry, testing apparatus and loading protocol adopted in this study were designed to be in accordance with ASTM standard [107]. Differently from the ASTM code, the specimens were kept in a horizontal configuration while the load was applied along an inclined direction of  $45^\circ$ , as illustrated in Figure 2.5a.

Figure 2.5b shows a detail of the testing apparatus used to perform the diagonal compression tests. In particular, it consisted of a couple of “L-shape” steel elements, measuring about 152 mm in length and 152 mm in height placed at two corners of the panel (see detail 2 in Figure 2.5b). These elements were connected by two steel threaded bars (one for each side of the specimens, see detail 8 in Figure 2.5b) to have a self-constrained system in which the upper L-shape elements is designed to move along the diagonal direction of the sample.

**Figure 2.5:** a) Masonry specimen isolated from a wall of “Margherita Palace” (L’Aquila); b) Detail of the upper apparatus: 1) Masonry specimen; 2) Steel confinement corner plate closed on the lateral surfaces; 3) HEA180 steel beam; 4) Load cell; 5) Hydraulic jack compresses; 6) Apparatus of contrast; 7) Steel nut; 8) Threaded bar.



Loading was transferred to the specimens by a hydraulic jack (COF30N250 - Euro Press Pack Spa, see detail 5 in Figure 2.5b) with the aid of a hydraulic pump (VPM4 12/03547 - Euro Press Pack Spa). The load recording was performed by a load cell (H.B.M. Italia S.r.l., see detail 4 in Figure 2.5b) mounted in line with the hydraulic jack. A steel beam is inserted between the upper steel plate and the load cell (see detail 3 in Figure 2.5b).

Particular attention was given to ensure a uniform load distribution across the thickness of the samples by minimizing the eccentricity of the steel plates and by applying a plaster layer at the plates - specimen interfaces.

As far as data acquisition is concerned the displacements were recorded by four Linear Variable Displacement Transducers - LVDTs (H.B.M. Italia S.r.l.) with based length of almost 900 mm. The LVDTs were mounted on each side of

the specimens to record both the shortening of the compressed diagonal and the elongation of the other diagonal. In particular,  $\ell_{v1}$  and  $\ell_{v2}$  are the gauge lengths of the LVDTs mounted on the compressed diagonal, whereas  $\ell_{h1}$  and  $\ell_{h2}$  are those of the LVDTs mounted on the other diagonal. (see Figures 2.6a – c).

Figure 2.6 shows the geometry of the masonry walls and the placement of the LVDTs mounted on the diagonals of the specimen. In particular,  $D_m$  and  $t$  are the average size and the thickness of the samples, respectively. The main geometrical properties of the masonry samples are described in Table 2.4.

**Table 2.4:** Geometrical properties of the unreinforced (URM) and reinforced masonry (RM) specimens. Legend:  $D_m$  and  $t$  are the average size and the thickness of the samples,  $\ell$  are the gauge lengths of the LVDTs mounted along the diagonal of the specimens.

Name	$D_m$ [m]	$t$ [m]	$\ell_{v1}$ [m]	$\ell_{h1}$ [m]	$\ell_{v2}$ [m]	$\ell_{h2}$ [m]
1URM	1.205	0.580	1.020	1.090	0.990	1.030
2RM	1.195	0.750	1.005	0.995	0.995	0.998
3RM	1.210	0.565	0.905	0.900	0.900	0.902
4URM	1.215	0.510	0.885	0.935	0.900	0.916

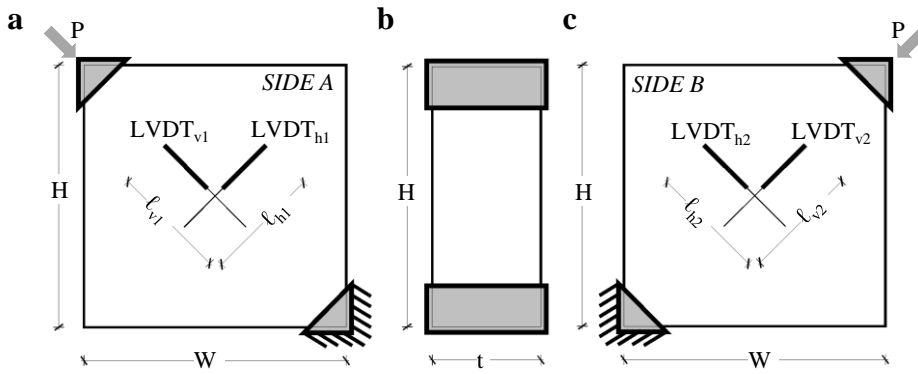


**Figure 2.6:** Configuration of the diagonal compression test. The LVDT $_{v1}$  and the LVDT $_{v2}$  transducers measured the compressive shortening whereas the LVDT $_{h1}$  and the LVDT $_{h2}$  ones measured the tensile elongation.

The tests were performed using a “force-control” procedure by applying a uniform increase of  $P$  of about  $20 \pm 5$  kN for each cycle up to the failure of the samples. Moreover, a preliminary load cycle, of about 5 kN, was applied in order to verify the correct positioning of the test apparatus and the data acquisition system. Data of loads and displacements were recorded at a frequency of 5 Hz for the entire test duration.

According to ASTM E519-02 [107], the shear stress  $\tau$  of the masonry can be calculated as follows:

$$\tau = \frac{0.707 P}{A_n} \quad (2.1)$$

where  $P$  is the load applied by the jack and  $A_n$  is the net area of the panel given by  $A_n = (W + h)/2 t$ , being  $W$ ,  $h$  and  $t$  the width, height, and thickness of the specimen, respectively. For  $P = P_{max}$ , (Eq. 2.1) allows computing the maximum shear stress  $\tau_0$ .

Besides the characterization in terms of strength, the mechanical behavior of the masonry requires to be discussed also in terms of deformation capacity. This is possible by computing the shear strain  $\gamma$  as follows (Eq. 2.2):

$$\gamma = \varepsilon_h + |\varepsilon_v| \quad (2.2)$$

where  $\varepsilon_h$  and  $\varepsilon_v$  are the tensile and compressive strains of the two diagonals of the specimen. In particular,  $\varepsilon_v$  is computed as the average of the deformation values  $d_{v1}$  and  $d_{v2}$ , measured by the  $LVDT_{C1}$  and the  $LVDT_{C2}$  transducers, divided by the gage lengths  $\ell_{C1}$  and  $\ell_{C2}$ , respectively. Furthermore, one can estimate  $\varepsilon_v$  by computing the average of the ratios of the deformation values  $d_{h1}$  and  $d_{h2}$  and the gage lengths  $\ell_{LVDT_{e1}}$  and  $\ell_{LVDT_{e2}}$ , respectively.

The initial portion of the experimental curve  $\tau - \gamma$  allows calculating the shear modulus  $G$  of the masonry. In the literature, one can find different indications for the values of  $\tau$  and  $\gamma$  to be considered for the computation of  $G$  [64, 75, 78]. In the present study, the shear modulus was computed in two different ways, as follows:

- the secant shear modulus  $G_{30\%}$  measuring the slope of the backbone curves in correspondence of the 30% of the maximum shear stress  $\tau_0$  (see Figure 2.7) and computed as (Eq. 2.3):

$$G_{30\%} = \frac{0.3 \tau_0}{\gamma_{30\%}} \quad (2.3)$$

where  $\gamma_{30\%}$  is the shear strain measured at 0.3  $\tau_0$ ;

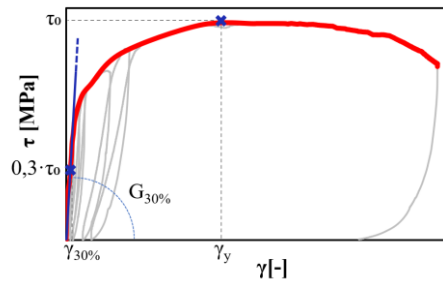


**Figure 2.7:** Graphical procedure for the computation of: a) the secant shear modulus  $G_{30\%}$ .

- the cyclic shear modulus  $G_i$  measuring the slope of the  $\tau - \gamma$  curves for each  $i$ -th cycling loads (see Figure 2.8) and computed as (Eq. 2.4):

$$G_i = \frac{\tau_{0,i}}{\gamma_i} \quad (2.4)$$

where  $\tau_i$  and  $\gamma_i$  are the shear stress and the shear strain measured at the  $i$ -th cycling load, respectively.

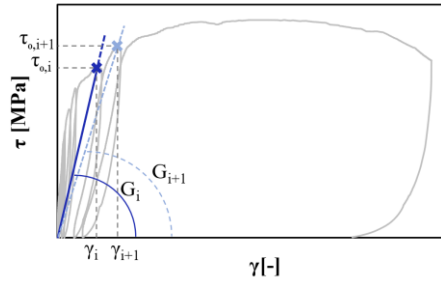


**Figure 2.8:** Graphical procedure for the computation of the cyclic shear modulus  $G_i$ .

### 2.1.1.4 Experimental results

Results of the diagonal compression tests carried out on four masonry specimens are presented in this Section. In particular, results are presented by using the following labels: the number of the specimens (from 1 to 4) followed by “RM” or “URM” for reinforced or unreinforced masonry specimen cases, respectively.

Figures 2.9 present the measurement of the load  $P$  applied to the masonry specimens during the experimental tests. One can observe an almost constant increase in  $P$  for each load cycle and equal to  $15 \text{ kN} \pm 5 \text{ kN}$  and  $25 \text{ kN} \pm 5 \text{ kN}$  for the unreinforced cases (the 1URM and the 4URM) and reinforced cases (the 2RM and the 3RM), respectively. In particular, for the 1URM test, a maximum value of the applied load  $P_{max} = 120.4 \text{ kN}$  was reached at the 7th load cycle. For the 2RM test one can observe that  $P_{max} = 371.6 \text{ kN}$  was reached at the 13th load cycle. For the 3RM test,  $P_{max} = 356.1 \text{ kN}$  was achieved at the 15th load cycle. Finally, for the 4URM test one can see that  $P_{max} = 99.9 \text{ kN}$  was reached at the 10th load cycle. Hence, the mean values of the maximum load were equal to  $110.1 \text{ kN}$  and  $363.8 \text{ kN}$  for the URM and the RM cases, respectively.

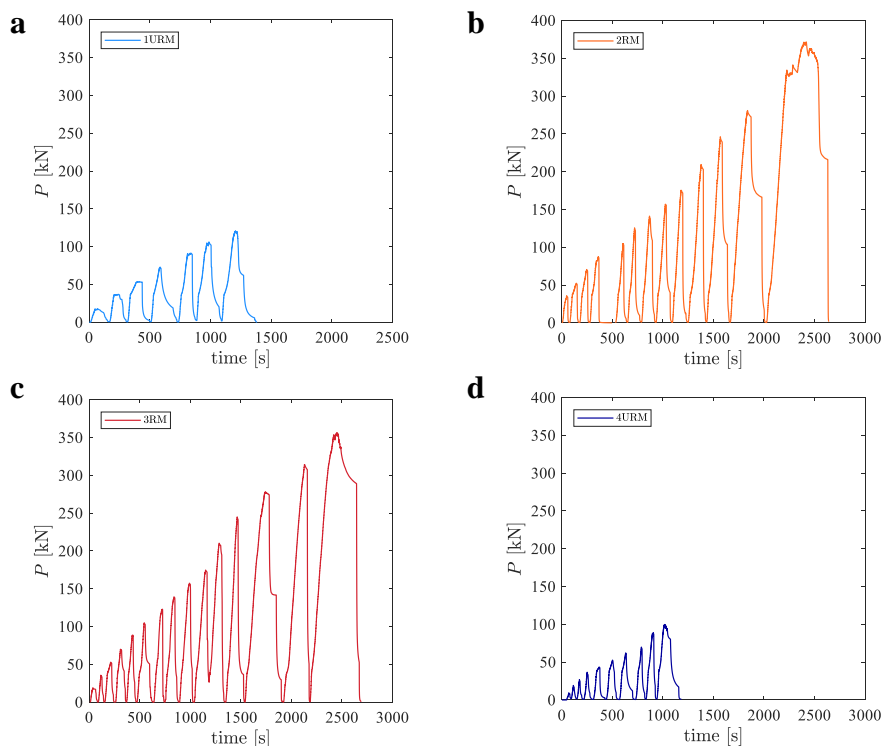


**Figure 2.9:** Measurement of the compressive load  $P$  during the time  $t$  of the experimental tests.

Since experiments were carried out in load-control, once the specimens achieved the maximum load (i.e.  $\tau_0$ ) it was not possible to carry out further load cycles. Indeed, the load-control procedure led to a catastrophic failure of the specimens when the maximum shear stress was reached. Hence, the load  $P$  measured after the achievement of the maximum load  $P_{max}$  could not be considered for discussing

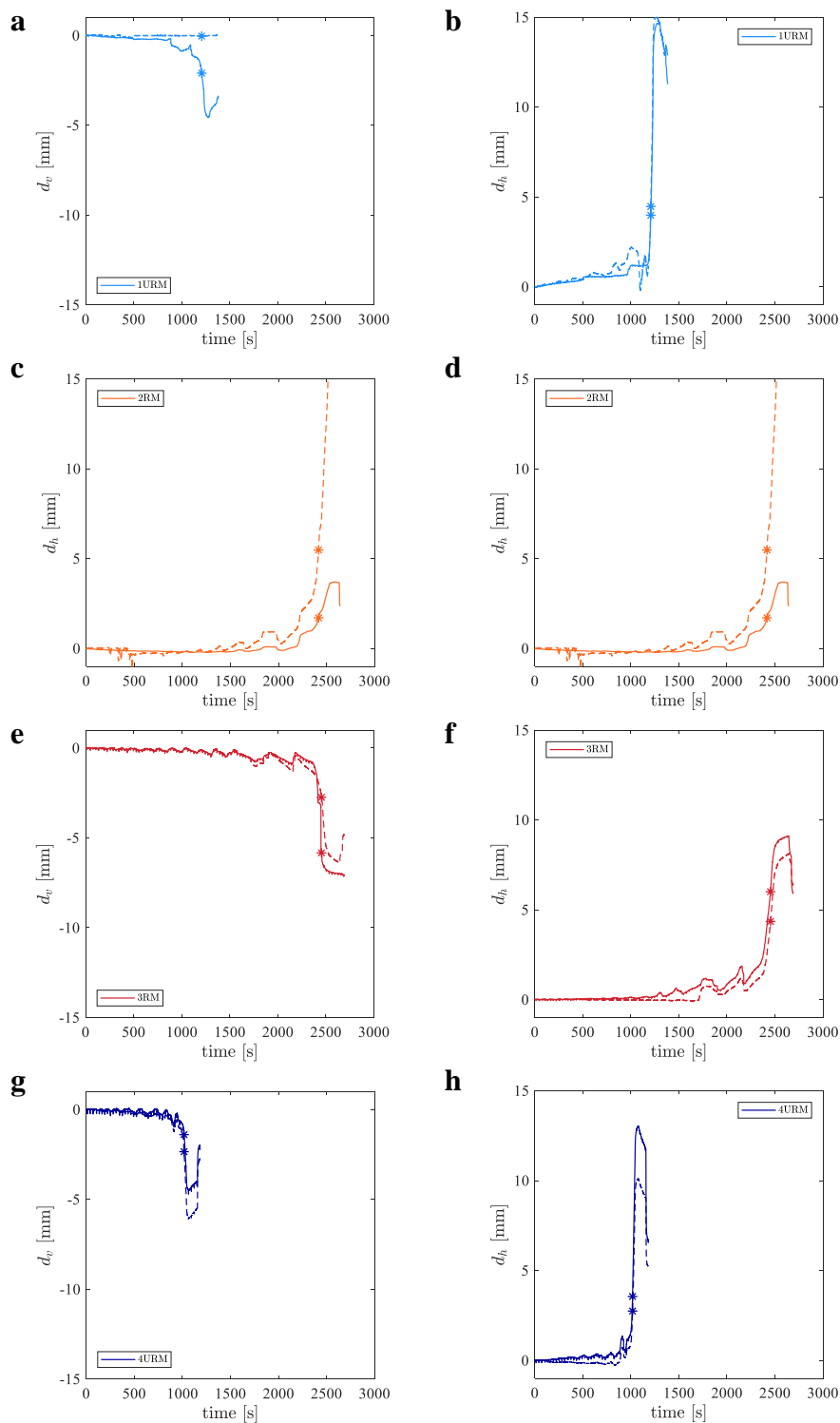
the softening behavior of the masonry walls. Hence, the discussion of the following results only focuses on the mechanical behavior of the specimens up to their maximum load (i.e.  $\tau_0$ ).

Figure 2.10 illustrate both the vertical (negative) and horizontal displacements (positive),  $d_v$  and  $d_h$ , recorded during the tests by the transducers mounted on both the surfaces of the masonry specimens. Especially for the URM cases, one can observe that the  $d_h$  values were higher than the  $d_v$  ones. Furthermore, for all the cases, one can see that  $d_v$  and  $d_h$  strongly increase a bit before the achievement of the maximum shear stress (i.e.  $\tau_0$ ), which is represented in the figures by asterisk markers. It should be pointed out that, the two values of both  $d_v$  and  $d_h$  of the 1URM and 2RM cases were clearly different from each other near the end of the tests, meaning that the panels were subjected to a overturning phenomenon for high load level.

Figure 2.11 shows the correlation between the shear stress  $\tau$  and both the compressive (negative) strain  $\varepsilon_v$  and tensile (positive) strain  $\varepsilon_h$ . In particular, for the unreinforced panels, values of the shear strength  $\tau_0$  equal to 0.122 MPa and 0.114 MPa were computed for the 1URM and the 4URM cases, respectively. For the reinforced panel, the  $\tau_0$  values were equal to 0.293 MPa and 0.368 MPa for the 2RM and the 3RM cases, respectively. Hence, the strength of the two URM specimens were very similar. On the contrary, the two RM specimens were characterized by a higher scattering of the results. Indeed, the shear strength of the 3RM case was 1.25 times the one of the 2RM case. This difference can be attributed to the different thickness  $t$  of the two RM specimens, as the ratio between the masonry thicknesses of the 2RM and 3RM cases was equal to 1.3 (0.750 m/0.565 m). Hence, one can observe an almost linear proportionality between the shear strength and the original thickness of the reinforced masonry specimen.

Definitely, the efficiency of the FRCM can be strongly affected by the thickness of the original (unreinforced) masonry wall. The higher the thickness of the original walls, the lower the efficiency of the FRCM in terms of shear strength of the reinforced panel, end vice-versa.

Figures 2.12 shows the shear stress - shear strain ( $\tau - \gamma$ ) plots. One can see that the values of  $\gamma$  occurred in correspondence of the shear strengths ( $\gamma_{\tau_0}$ ) is almost equal to 0.005 for both the URM cases. For the RM cases, one can see that  $\gamma_{\tau_0}$  is ranging from 0.005 to 0.01. This result highlights that  $\gamma_{\tau_0}$  is almost the same for the unreinforced and reinforced cases.



**Figure 2.10:** Measurement of the displacements  $d_v$  and  $d_h$  recorded during the time  $t$  of the tests. The achievement of maximum shear stress is represented by asterisk markers.

Therefore, the mean strength value for the URM cases was equal to 0.118 MPa, which is almost four times higher than the maximum value proposed by the NTC2018 code. Indeed, that code suggests a strength value ranging from 0.02 MPa to 0.032 MPa for the design of the unreinforced masonry structures. Furthermore, the ratio between the mean strength value of the RM ( $\tau_{0,RM}=0.331$  MPa) and URM cases ( $\tau_{0,URM}=0.118$  MPa) is equal to 2.8, which is higher than the

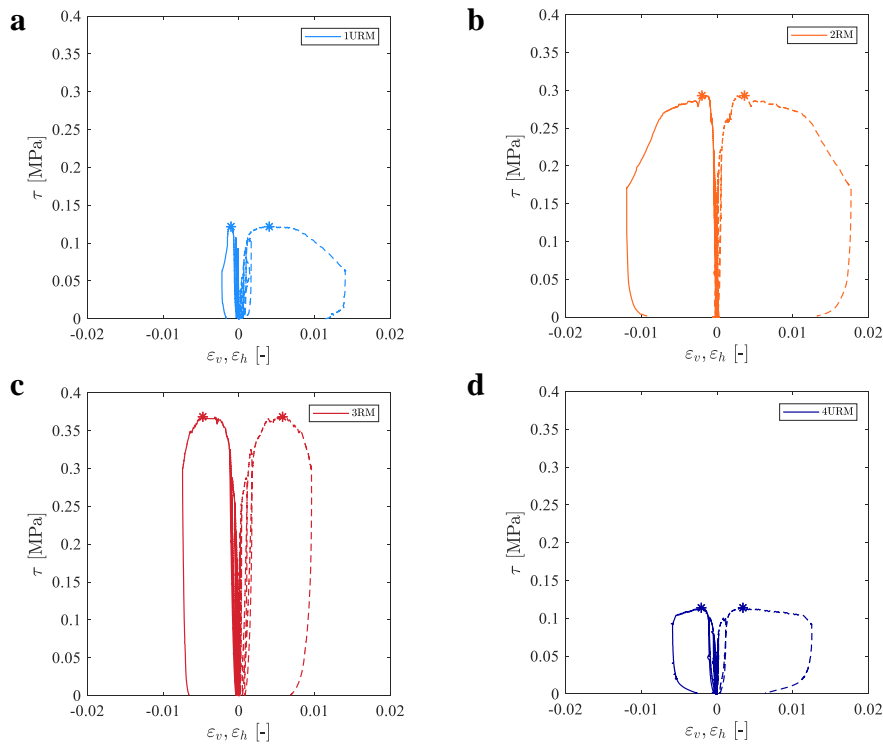


**Figure 2.11:** Shear stress  $\tau$  computed for the four specimens and related to the compressive and tensile strains,  $\varepsilon_v$  and  $\varepsilon_h$ , respectively

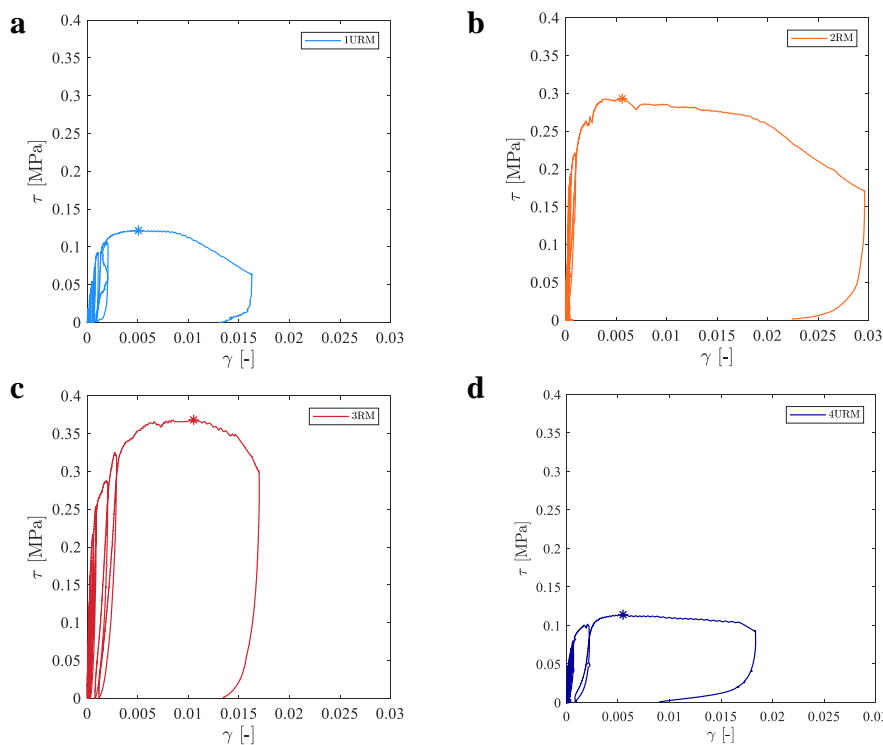


**Figure 2.12:** Shear stress  $\tau$  computed for the four specimens and related to the the shear strain  $\gamma$ .

coefficient proposed by standards for the design of stone masonry strengthened by FRCM in absence of experimental investigation. In particular, standard CNR-DT 215/2018 and NTC2018 propose, as a simplification, an amplification coefficient of 1.5 and 2.5, respectively, for the mechanical properties of irregular stone masonry walls reinforced by FRCM.

Results of the mechanical properties obtained for the URM and RM specimens are listed in Table 2.5.

**Table 2.5:** Mechanical properties of the unreinforced masonry URM and the reinforced RM specimens.

Name test	$\tau_0$ [MPa]	$G_{30\%}$ [MPa]
1URM	0.122	61.4
2RM	0.293	203.6
3RM	0.368	134.0
4URM	0.114	72.1

In Fig. 2.13 are illustrated the backbone curves obtained for both the unreinforced (URM) and the reinforced (RM) panels. Such curves were obtained by connecting  $\tau$  and  $\gamma$  obtained for the  $i$ -th cycles. From the backbone curves, it is possible to observe the benefit of the FRCM on the mechanical properties of the masonry panel in terms of shear stress, stiffness, and ductility.

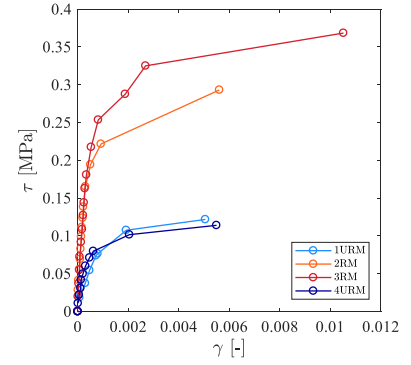


**Figure 2.13:** Backbone curves obtained for the unreinforced (URM) and the reinforced (RM) panels.

Figure 2.14 shows the relation between  $G_i$  and  $\gamma$  for both the URM and RM cases. In particular, one can see that the shear modulus of the masonry panels strongly decreases by increasing the deformation of the panels by following an exponential law. This trend can be observed for both the URM and the RM cases. In particular, one can see that  $G_i$  of the RM cases ( $G_{i,URM}$ ) is constantly higher than the values computed for the URM case ( $G_{i,RM}$ ), highlighting that the FRCM enhances the shear modulus of the masonry wall even for high shear strain value. A relation of the variation of  $G_i$  as a function of  $\gamma$  was also found, showing a good correlation with the experimental data (R-squared equal to 0.975 and 0.964 for the URM and RM cases, respectively), as follows:

$$G_{i,URM} = 2.06\gamma^{-0.539}; G_{i,RM} = 8.11\gamma^{-0.496} \quad (2.5)$$

Curves of Eq. 2.5 are represented by the dotted lines (URM fit and RM fit) of Fig.2.14.

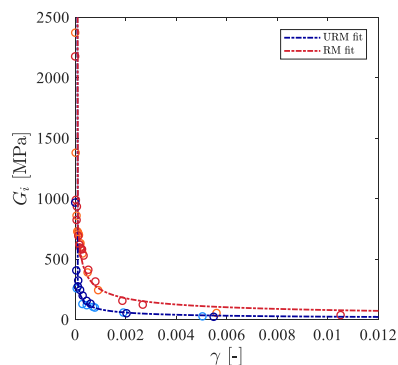


**Figure 2.14:** Cyclic shear modulus  $G_i$  as a function of  $\gamma$ .

To investigate the variation of the mechanical properties of the masonry specimens during the cyclic tests and to better compare the results obtained for the URM and the RM cases, Figure 2.15 show the dimensionless mechanical properties  $G_{i,ND}$  and  $\gamma_{ND}$ , respectively, as a function of the number of the load cycles. In particular,  $G_{i,ND}$  and  $\gamma_{ND}$  were computed by dividing  $G_i$  and  $\gamma$  of the  $i$ -th cycle by the  $\gamma_{\tau_0}$  and  $G_{i=1}$  values obtained for each tests, respectively. Figure 2.15a shows that the shear modulus of the masonry panels strongly decreases by increasing the number of the load cycles. In particular, one can see a sudden drop of the  $G_{i,ND}$  value (about 50% compared to the initial value) already after the first load cycle. This trend can be observed for both the URM and RM cases. This may suggest that even for low compressive load values (almost equal to  $0.2P_{max}$ ) micro-cracks occurred on the masonry leading to a decrease in the stiffness of the panels, emphasizing the propensity of the stone walls being subjected to the disintegration phenomena [109], which strongly vary the mechanical properties as a function of load cycles.

Figure 2.15b shows that the shear strain of the masonry panels  $\gamma_{ND}$  increases almost linearly during the initial load cycles. Then, the shear strain strongly increases only in the last 2-3 cycles.

Since the tests were performed by assuming a different number of load cycles, a proper comparison between URM and RM cases is not possible to be carried out only by observing Fig.6e,f. Hence, Fig.2.15c,d show the variation of the mechanical properties  $G_{i,ND}$  and  $\gamma_{ND}$  as a function of the dimensionless load cycles. When the latter is equal to 1, the shear strength occurred. Furthermore, since  $P$  was almost kept constant during the loading steps, the dimensionless load cycles can be also associated with the load level. In particular, Fig.2.15c,d show the scatter between the lower and the upper curves obtained for the two URM and RM experimental tests.

Figure 2.15c shows that the trend of  $G_{i,ND}$  is similar for both the URM and RM cases. In particular,  $G_{i,ND}$  decrease of about 50% for about 20% of the maximum load. Then,  $G_{i,ND}$  decreases linearly up to 70% of the maximum load.

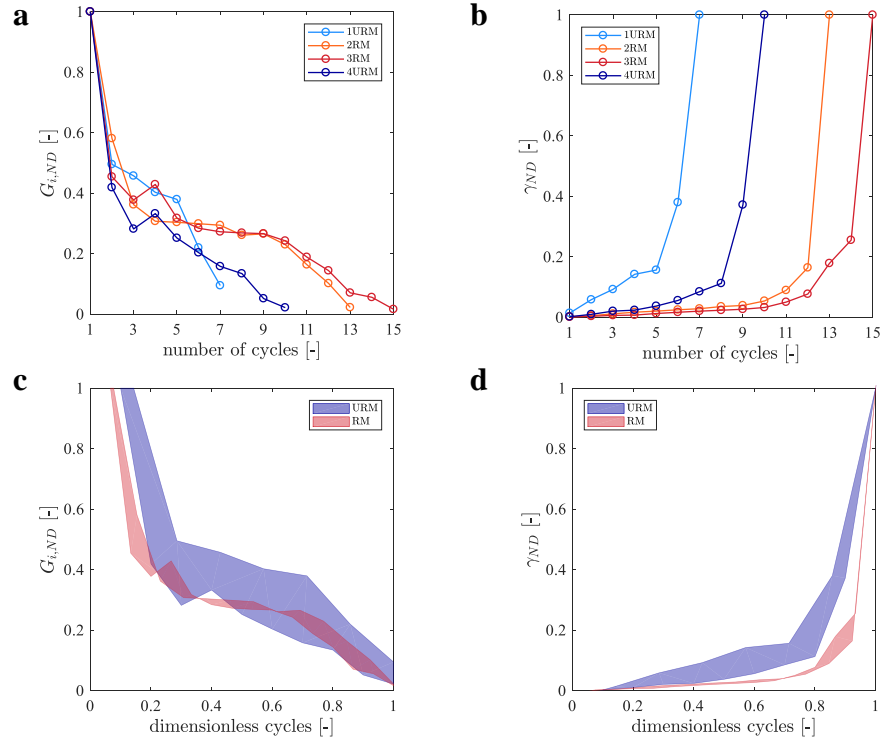


**Figure 2.15:** a,b) Dimensionless shear modulus and shear strain ( $G_{i,ND}$  and  $\gamma_{ND}$ ) as a function of the load cycles; c,d)  $G_{i,ND}$  and  $\gamma_{ND}$  related to the dimensionless load cycles.

Finally,  $G_{i,ND}$  is about 10% of the initial value when the dimensionless cycles are equal to 1.

On the contrary, by observing the curves of Fig.2.15d, one can see four distinct steps as follows: i) small initial value of  $\gamma_{ND}$  (about 0.08 and 0.015 for the URM and RM cases, respectively) can be noted up to 20% of the load level; ii) an increase in  $\gamma_{ND}$  up to 70% of the load level ( $\gamma_{ND}$  equal to about 0.07 and 0.12 for the URM and RM cases, respectively); iii) an increase in  $\gamma_{ND}$  up to 90% of the load level ( $\gamma_{ND}$  equal to about 0.3 and 0.4 for the URM and RM cases, respectively); iv) after the 90% of the load level,  $\gamma_{ND}$  strongly increase until the shear strength occur.

Definitely, these results highlighted that the constitutive law of the stone masonry panels can be characterized by four phases and is far to be assumed as linear elastic up to the achievement of the shear strength (simplified hypothesis generally assumed for masonries). Based on the results observed in Fig.2.15, one can define a multi-linear constitutive law for stone masonry panels for both the URM and RM cases, as illustrated in Fig.2.16. That figure shows the best fitting of the dimensionless  $\tau - \gamma$  experimental curves. In particular, the variation of the mechanical properties of the masonry occurs at 20%, 70% and 90% of the shear strength. The differences between the URM and the RM cases concern the slope (i.e. shear modulus) of the segments of the multi-linear law.

The results of the experimental tests may also permit to draw some important information about the ductility of the masonry specimen. In particular, the total

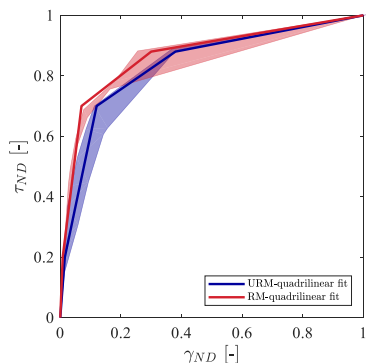


**Figure 2.16:** Multilinear fit of the  $\tau_{0,ND}$ - $\gamma_{0,ND}$  backbone curves of the URM and RM cases.

strain energy  $U$  of the URM and RM specimens was evaluated as the area delimited by the force-displacement curve ( $P - d$ ) [65], where  $d$  is the sum of  $|d_v|$  and  $d_h$ . It should be pointed out that also the evaluation of  $U$  was performed until the shear strength of the walls occurred (i.e.  $P = P_{max}$ ). Fig. 2.17 illustrates the  $U - \gamma_{ND}$  plot for both the URM and RM cases. In that figure, one can see that  $U$  of the RM case (mean value of 2335 J) is about 5 times higher than the value computed for the URM case (mean value equal to 467 J). Obviously, the ratio between  $U_{RM}$  and  $U_{URM}$  would be much higher by considering also the softening behavior of the panels, as the unreinforced stone masonry is characterized by a quasi-brittle behavior whereas the FRCM strongly increases the load-bearing capacity even for large shear strain value.

Results of Fig. 2.17 highlighted that the masonry reinforced by FRCM can dissipate energy also before the achievement of the shear strength. Furthermore, the figure shows that  $U$  increases only when the deformation  $\gamma_{ND}$  is higher than about 0.15 and 0.06 for the URM and the RM cases, respectively, corresponding to about 70% of the load level of Fig. 2.16. Hence, it can be concluded that the first two linear branches of the idealized constitutive law of Fig. 2.16 can be characterized by an elastic behavior (negligible values of  $U$ ) highlighting that the initial micro-cracks occurred on the masonry only led to a reduction of the wall stiffness without the occurrence of significant permanent deformations. On the contrary, the third and the fourth linear branches of the idealized constitutive law should be considered with a hysteretic behavior.

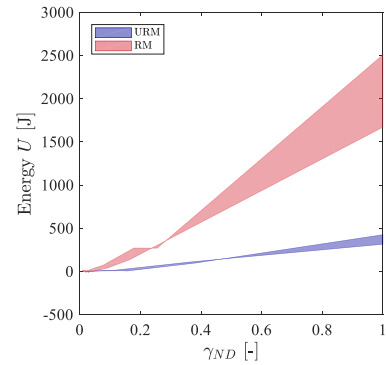


**Figure 2.17:** Total strain energy  $U$  as a function of  $\gamma_{ND}$  for the unreinforced (URM) and the reinforced (RM) panels.

As far as the fracture propagation on the masonry panels is concerned, Fig. 2.18–2.21 show the crack opening observed at the end of the experimental tests for the four masonry samples. For all the tests, typical crack propagation along the compressed diagonal of the specimens was observed. In particular, one can see that the panels reinforced by the FRCM system were characterized by a more distributed cracking along the compressed diagonal of the specimens, as compared to the unreinforced masonry for which a damage concentration was clearly observed. It is worth noting that by analyzing the damage of the unreinforced masonry panels (the 1URM and the 4URM cases of Fig. 2.18 and Fig. 2.21, respectively), the failure on the walls took place only at the stone-masonry interface and through the mortar matrix. The stones were found undamaged. This highlights that the lime-based mortar of ancient masonry building is much more compliant than stones.

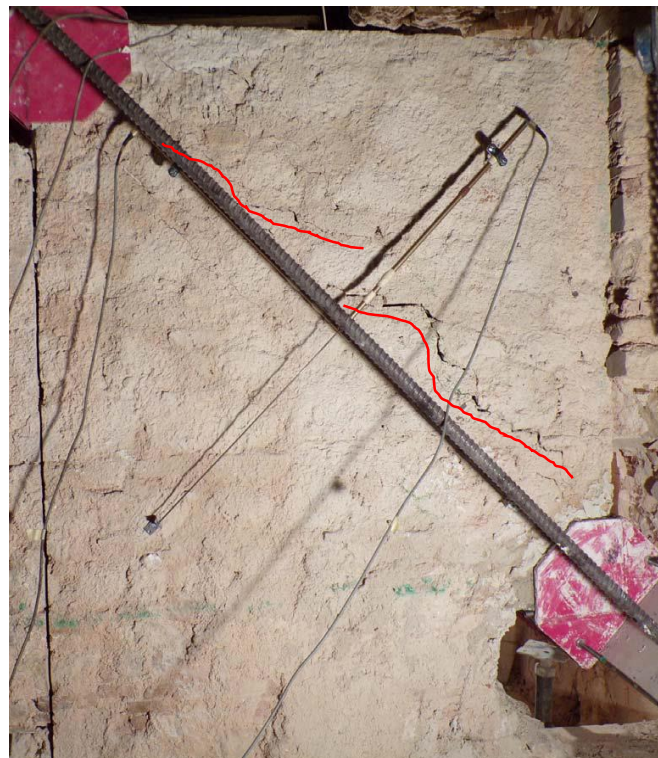


**Figure 2.18:** Cracking opening on the unreinforced masonry specimen during the 1URM test.



**Figure 2.19:** Cracking opening on the reinforced masonry specimen during the 2RM test.

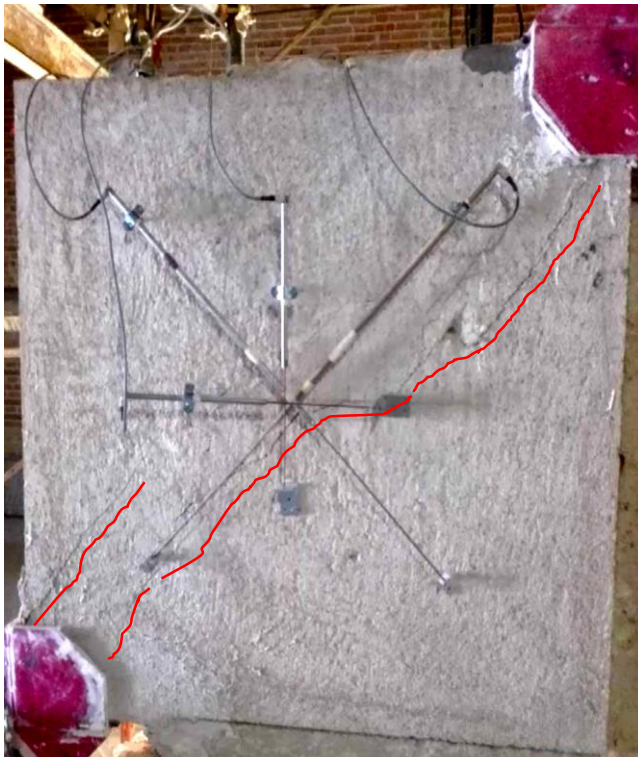


**Figure 2.20:** Cracking opening on the reinforced masonry specimen during the 3RM test.

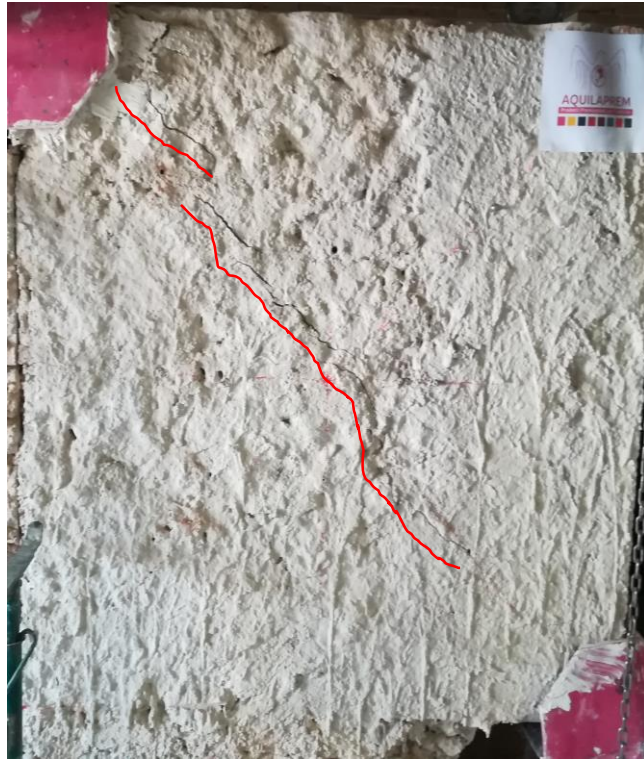


**Figure 2.21:** Cracking opening on the unreinforced masonry specimen during the 4URM test.

In Figure 2.22 one can observe the cracking propagation through the thickness of the reinforced specimen (3RM). Indeed, that panel was subjected to an overturning phenomenon at the end of the test. That phenomena was limited by the anchors that kept together the external leafs of the masonry.



**Figure 2.22:** Cracking propagation through the thickness of the 3RM specimen;

In Figure 2.23 one can observe the undamaged level of the glass fiber grid by removing the external layer of the mortar at the end of the 3M test . Indeed, the cracking is concerning only on the underlying mortar level, as well as the overlying one previously removed.

Furthermore, to investigate the possible damage of the anchors, they were extracted from the masonry specimens at the end of the tests. Both the carbon fiber anchor (Figure 2.24a) and the steel bar anchor (Figure 2.24b) were in undamaged condition, still presenting the infilled mortar in adhesion with them, highlighting excellent bond behavior at their interface.



**Figure 2.23:** Particular of the undamaged fiber grid at the end of the test. The external layer of the reinforcement mortar was previously removed.



**Figure 2.24:** Carbon fiber anchor (a) and steel bar anchor (b) extracted from the specimen at the end of the test 3RM to investigate their damage.

## 2.1.2 Diagonal tests carried out in laboratory

### 2.1.2.1 Materials and method

Six masonry samples measuring 1.2 m in length, 1.2 m in height and 0.34 m in thickness were prepared according to the ancient constructive technique featured in most of the historic buildings of the city of L'Aquila. The stone elements, with a characteristic size of about 150 mm, were taken from the debris of buildings collapsed during L'Aquila 2009 earthquake. The original mortar features of the historical masonry (characterized by a very friable behavior and a low compressive strength of about 2 MPa) were reproduced by mixing commercial natural hydraulic lime mortars, local crushed limestone sand and local natural clay with a respective ratio of 1:2:1. Water was added to the mortar mixture until a plastic consistency was reached. The addition of natural clay to the mortar mixture produced a hydraulic lime similar to the ancient lime [110]. All the wall specimens were cured for about 15 months, allowing the lime-based mortar to harden at room conditions.

After the curing period, two of the six specimens were kept unreinforced while the remaining four were reinforced using a FRCM system applied as described in the following section.

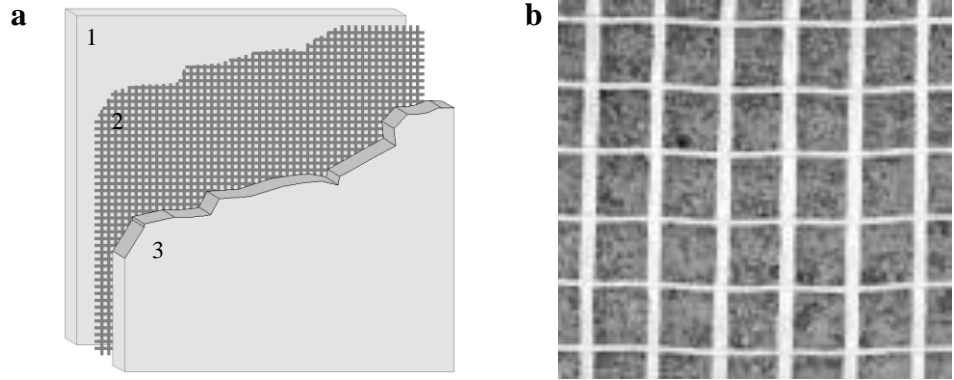
The applied FRCM system (Figure 2.25a) consisted of a grid of glass fibers strands (AQMesh240V-Aquilaprem [111]) embedded in a Natural Hydraulic Lime mortars (Ch15-Aquilaprem [112]). The glass fiber strands were spaced with a gap of 25 mm in both vertical and horizontal directions forming a balanced bidirectional fabric (Figures 2.25b). Two of the four reinforced panels were equipped with four embedded anchors, which were designed to connect the two external FRCM layers to each other and consisted of glass fiber bundles characterized by a nominal diameter of 10 mm. They were placed at a distance of about 200 mm from the lateral edges of the panels. Their bundle ends were characterized by a circular configuration with 300 mm in diameter.

The geometrical and mechanical proprieties of the glass fibers are listed in Table 3.12 in which the  $SG$  is the space gap,  $\rho_{fib}$  is the density,  $t_{fib}$  is the thickness of a fiber strand,  $E_{fib}$  is the fiber Young's Module,  $f_{t,fib}$  is the tensile strength,  $\varepsilon_{u,fib}$  is the ultimate strain.

**Table 2.6:** Geometrical and mechanical properties of the glass fiber used in the FRCM system.

$SG$ [mm]	$\rho_{fib}$ [kg/m <sup>3</sup> ]	$t_{fib}$ [mm]	$E_{fib}$ [MPa]	$f_{t,fib}$ [MPa]	$\varepsilon_{u,fib}$ [%]
25	2680.0	0.1	72000.0	1700.0	3.7

**Figure 2.25:** Schematic of the layers constituting the FRCM system applied on the masonry wall specimens: 1 and 3 are NHL mortar layers with a thickness of about 10 mm each; 2 is the glass fiber grid embedded in the mortar; b) Picture of the glass fiber grid used in the experiments.



The application of the FRCM system to the reinforced stone masonry specimens was performed according to the following procedure: (a) the panel surfaces were cleaned to remove any loose material and were soaked with water; (b) a first layer of mortar was applied on the panel surfaces (Figure 2.26a) with a thickness of about 10 mm; (c) a square piece of glass fiber grid of size 1.0 m by 1.0 m was applied on the panel surface slightly pressing the fabric on the fresh mortar layer to have the fresh mortar passing through the grid openings (Figure 2.26b); (e) a second finishing layer of mortar was applied on the panel surfaces to cover the glass fabric while the previous mortar layer was still fresh for a total final reinforcement thickness of about 20 mm; (f) the same operation was repeated on the other side of the wall.

As described for the tests performed in situ, fiber grids were composed by a square fabric with size of 1.0 m placed at the middle of the masonry panel and four pieces of the fiber grids of 0.2 m  $\times$  1.2 m placed at the edges of the specimen (see also Section 2.1.1.2).

**Figure 2.26:** a) First layer of mortar applied on the panel surface using a metal trowel; b) and application of the fiber grid slightly pressing it into the mortar layer.

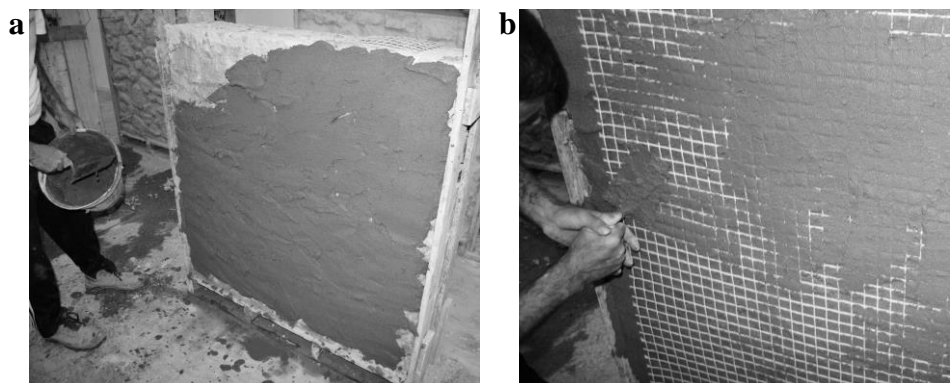
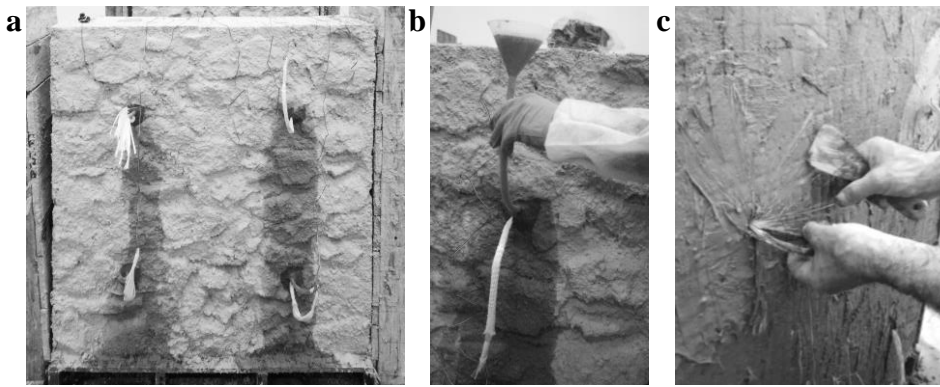


Figure 2.27a show the anchors inserted in four holes previously prepared during the specimen casting phase. Figure 2.27b shows the mortar injection performed into the holes to fill the voids and to ensure proper bond resistance between the anchors and the masonry. Figure 2.27c shows the refolding of the bundle fibers in a circular configuration on the first layer of the mortar.



**Figure 2.27:** a) Insertion the fiber anchors into the holes positioned in correspondence of the corners; b) filling the vacuum between the connectors and the masonry with lime-based mortar; c) refolding of the fiber anchors on the fiber grid with an angle splay of  $360^\circ$ .

The masonry specimens reinforced by the GFRCM were kept moist for 48 hours by applying a waterproof film around them. After that, they were left in laboratory condition for 26 days, for a total age of the specimen of 28 days, before testing them in diagonal compression.

### 2.1.2.2 Test setup

Performing the diagonal compression test allows the evaluation of the shear strength, the shear elastic modulus, and the ductility of the masonry [108]. Although no specific standard exists on mechanical tests to be performed on chaotic stone masonry, testing apparatus and loading protocol adopted in this study were designed to be in accordance with ASTM standard [107].

In the diagonal compression test, a square masonry panel was subjected to a compressive force applied along one of the panel diagonals (Figures 2.28). Due to their brittleness and to reduce the risk of damaging the panels, the specimens were kept in a horizontal configuration while the load was applied along an inclined direction of  $45^\circ$ .

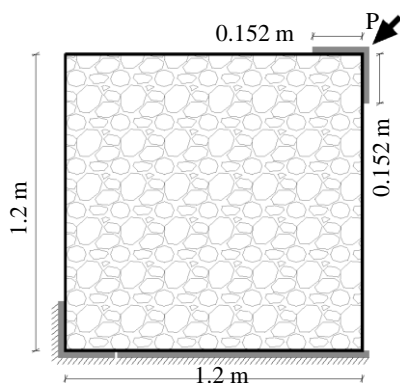


**Figure 2.28:** Picture of stone masonry specimen of dimension 1.2 m x 1.2 m x 0.34 m.

Figure 2.29a, b shows the testing apparatus used to perform the diagonal compression tests. The apparatus consisted of a couple of “L-shape” steel elements (triangular bearing platens), measuring about 152 mm in length, 152 mm in height and 30 mm in thickness (see item (3) in Figure 2.29b) and were placed at two cor-

ners of the panel in a diagonal direction. These elements were connected by two steel rigid bars (one for each side of the specimens, see item (7) in Figure 2.29b) in order to have a self-constrained system in which the upper L-shape block is designed to move along the diagonal direction of the sample.

A hydraulic jack, manually activated and placed at the top corner of the specimens (see item (5) in Figure 2.29b) was used to apply the compressive load.

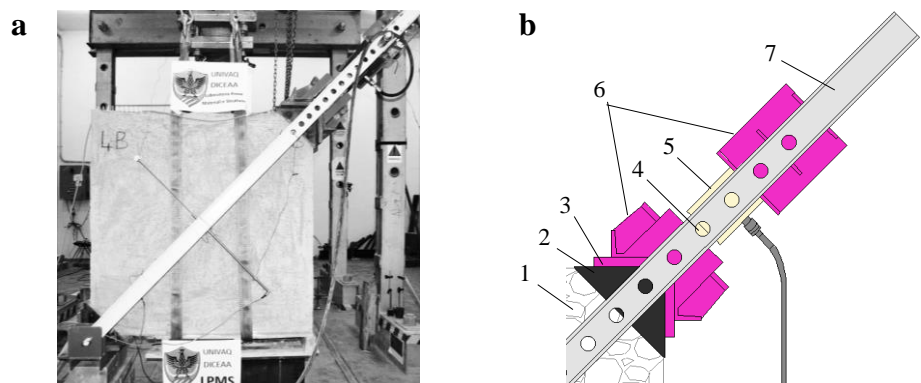
Particular attention was given to ensure a uniform load distribution across the thickness of the samples at its upper corners in order to avoid stress concentration and premature failure. Indeed, experience has shown that a premature splitting failure might occur due to compression at the loading points [107] if stress concentration is not prevented. In particular, to ensure proper contact between the loading steel plates and the corners of the specimen, a fluid cement mortar was previously distributed on the contact interfaces using a thin steel cap as a mould (see item (2) in Figure 2.29c).

As far as data acquisition is concerned, the applied load was recorded by a load cell mounted in line with the hydraulic jack as illustrated by the item (4) of Figure 2.29c.

Moreover, two Linear Variable Differential Transformer (LVDT) transducers (H.B.M. Italia S.r.l.) with based length of almost 900 mm were mounted on each side of the specimen to record the shortening of the compressed diagonal during the test. Additional transducers were mounted one on each side of the specimen to record the elongation of the second diagonal (Figure 2.29a). Additional LVDT transducers with same characteristic were mounted one on each side of the specimen to record the elongation of the second diagonal.

The list of the experimental tests carried out in this study is provided in Table 2.7 together with the details of reinforcement and instrumentation. The results are presented by using the following labels: RM= Reinforced Masonry; URM= Un-Reinforced Masonry; G= with fiber Grid;  $\bar{G}$  reinforcing grid instrumented with

**Figure 2.29:** a) Configuration of the diagonal compression test; c) details of the upper apparatus: (1) masonry sample; (2) steel confinement corner plate closed on the lateral surfaces; (3) “L-shape” steel element ; (4) load cell; (5) hydraulic jack compresses; (6) apparatus of contrast; (7) UPN180 beam connection.



strain gauges; C= with fiber Connectors;  $\bar{C}$  reinforcing anchors instrumented with strain gauges.

**Table 2.7:** Specimen configurations with indication about the reinforcement type and the location of the measuring instrument (internal strain gauges).

Test name	Reinforcement		Strain gauges	
	Fiber grid	Fiber anchor	Fiber grid	Fiber anchor
1RM- $\bar{C}$	Yes	Yes	Yes	No
2RM- $\bar{C}$	Yes	No	Yes	No
3RM- $\bar{C}$	Yes	Yes	No	Yes
4RM-G	Yes	No	No	No
5URM	No	No	-	-
6URM	No	No	-	-

In particular, for the 1RM- $\bar{C}$  and 2RM- $\bar{C}$  tests, the reinforcing grids were instrumented with 8 strain gauges on each side of the specimen. These strain gauges recorded the deformation of the vertical strands of the grid close to the compressed diagonal of the specimen where the cracking of the panel was expected to take place. The position of the gauges are listed in Table 2.8. In particular, the 1–8 gauges were placed on a side of the wall and 9–16 on the other side. The application of the gauges on the strands was performed according to the following procedure: (a) the fiber strands were cleaned; (b) a film of cyanoacrylate adhesive was applied; (c) gauge was fixed to the adhesive; (d) a film of air-drying solvent-thinned polyurethane was applied on the gauges aiming to protect the gauges.

**Table 2.8:** Position of the gauges.

ID gauges	X coord. [mm]	Z coord. [mm]
1;9	825	825
2;10	675	675
3;11	525	525
4;12	375	375
5;13	400	600
6;14	600	400
7;15	800	600
8;16	600	800

Data of loads, displacements and deformations were recorded at a frequency of 5 Hz for the entire test duration. The tests were performed using a “force-control” procedure with loading rate of about 10 kN/min  $\pm$  5 kN/min up to the failure of the panel.

As already described in Section 2.1.1.3, the shear stress ( $\tau$ ) of the masonry was calculated according to ASTM E519-02 [107] by the equation  $\tau = 0.707 P/A_n$ , where  $P$  is the load applied by the jack and  $A_n$  is the net area of the panel  $A_n = (W + h)/2 t$ , where  $W$ ,  $h$  and  $t$  are the width, height, and thickness of the specimen, respectively. In that equation, for  $P = P_{max}$ , one can compute the maximum shear stress  $\tau_0$ .

Moreover, the shear strain  $\gamma$  is computed by the equation  $\gamma = \varepsilon_h + |\varepsilon_v|$ , where  $\varepsilon_h$  and  $\varepsilon_v$  are the tensile (positive) and compressive strain (negative) measured along the two diagonals.

The shear modulus  $G$  of the masonry was computed by the equation  $G = \tau_{30\%}/\gamma_{30\%}$ , in which  $\tau_{30\%}$  represents 30% of the maximum shear stress of the specimen  $\tau_0$  and  $\gamma_{30\%}$  is the shear strain value corresponding to  $\tau_{30\%}$ .

Finally, the reinforcement coefficients  $k_G$ ,  $k_{\tau_0}$  and  $k_\mu$  was computed to characterize the increase of the mechanical properties (shear modulus, strength, and load-bearing capacity for large deformation) of the specimens reinforced with the FRCM system as compared with the unreinforced ones. One can define these coefficients, as indicated by the NTC18 standard code, by the following equations:  $k_G = G_{RM}/G_{URM}$ ,  $k_{\tau_0} = \tau_{0,RM}/\tau_{0,URM}$ , and  $k_\mu = \tau_{(\gamma=0.01),RM}/\tau_{(\gamma=0.01),URM}$ , in which  $G_{RM}$ ,  $\tau_{0,RM}$ , and  $\tau_{(\gamma=0.01),RM}$  are the mechanical properties (shear strain, maximum stress, and stress at  $\gamma = 0.01$ ) of the reinforced panels and  $G_{URM}$ ,  $\tau_{0,URM}$ , and  $\tau_{(\gamma=0.01),URM}$  are the corresponding mechanical properties of the unreinforced panels.

### 2.1.2.3 Experimental results

Results of diagonal compression tests carried out at the Laboratory of Material and Structural Testing LMPS of the University of L'Aquila (Italy) are here described.

Figures 2.30*a, b* show the compressive strain  $\varepsilon_v$  and the tensile strain  $\varepsilon_h$  measured on the specimens during the time of the tests. One can see that at a specific time of the tests there is a sudden increase in the strain values (for both  $\varepsilon_v$  and  $\varepsilon_h$ ). This is due to the instability phenomenon occurred as soon as the maximum shear stress  $\tau_0$  was achieved for the specimens because of the load-control procedure, which leads to an immediate collapse of the specimens at  $\tau_0$ . The instability phenomenon occurred at the  $\tau_0$  values can be also observed in Figure 2.31*a*. In that figure is illustrated the shear stress values measured on the specimens during the time of the tests. Figure 2.31*b* shows the  $\tau$ - $\gamma$  curves obtained from the data recorded during the tests. An initial, almost elastic branch is first recognized, then the mechanical response of the masonry is characterized by a gradual reduction in stiffness up to the maximum stress ( $\tau_0$ ), and after which softening behavior is observed. The values of the mechanical properties obtained from the experimental tests are reported in Table 2.9.

**Table 2.9:** Experimental results for 6 masonry specimens tested in diagonal compression

Test name	$\tau_0$ [MPa]	$\tau_{30\%}$ [MPa]	$\gamma_{30\%}$ [-]	$G$ [MPa]
1R- $\overline{\text{GC}}$	0.749	0.225	0.000264	849
2R- $\overline{\text{G}}$	0.513	0.154	0.000808	192
3R-GC	0.503	0.151	0.000157	962
4R-G	0.569	0.171	0.000117	1220
5NR	0.143	0.043	0.000352	123
6NR	0.132	0.040	0.000285	139

The highest value of the stress  $\tau_0$  was recorded for 1R- $\overline{\text{GC}}$ , which is about 40% higher than the strength measured for the other three reinforced specimens. On the other hand, the lowest value of  $\tau_0$  was observed for the 3R-GC case. It is worth noting that both cases were characterized by the presence of fiber anchors. Hence, it is difficult to establish the effectiveness of the fiber anchors in terms of the maximum shear stress. Result obtained for the 3R-GC case is similar to the cases 2R- $\overline{\text{G}}$  and 4R- $\overline{\text{GC}}$ .

Between these three tests, one can compute a standard deviation of about 0.03 MPa, which is small also considering the heterogeneous character of this material. Therefore, it appears more reasonable that the shear strength computed for 1R- $\overline{\text{GC}}$  was overestimated. This may be related to many factors, such as to the irregularity of the cross-section, presence of micro-cracks, different and non-constant thickness of both the mortar and specimen, and stone arrangement along the compressed diagonal. Finally, similar values for the unreinforced cases (5NR and 6NR) were

**Figure 2.30:** Compressive strain  $\varepsilon_v$  (a) and tensile strain  $\varepsilon_h$  (b) measured on the specimens during the time of the tests.

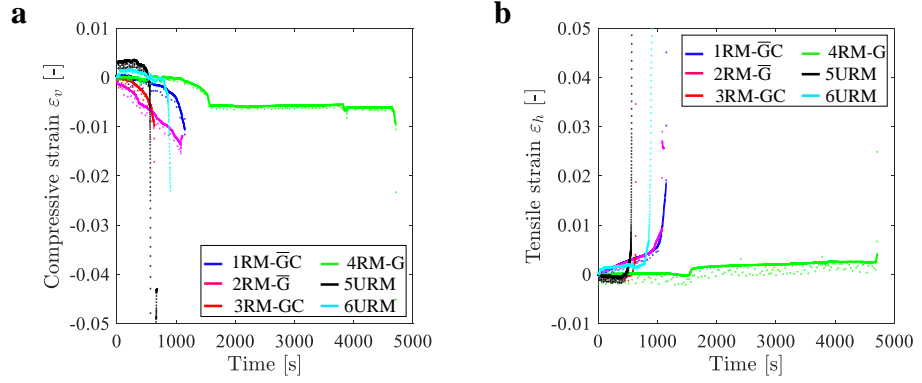
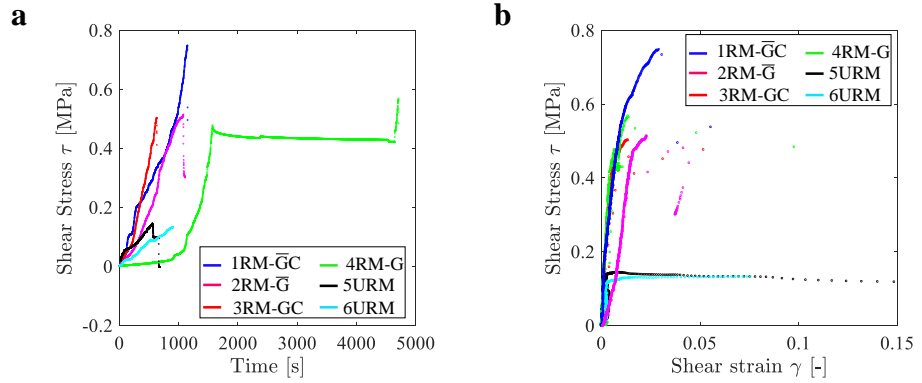


**Figure 2.31:** Shear stress  $\tau$  computed for the specimens related to the duration of the tests (a) and the shear strain  $\gamma$  of the panels (b).



also computed.

In particular, the average values of the shear modulus and maximum shear stress are 806 MPa and 0.583 MPa, respectively, for the reinforced specimens and 131 MPa and 0.138 MPa, respectively, for the unreinforced specimens. On the other hand, for mechanical property assessment of existing unreinforced irregular stone masonry, the Standard [113] suggests values of  $\tau_0$  and  $G$  ranging from 0.018 MPa to 0.32 MPa and 230 MPa to 350 MPa, respectively. Hence, one can observe that the experimental values of  $\tau_0$  slightly overestimate the one proposed in the standard code. On the contrary, the experimental values of  $G$  underestimate the one proposed in the standard code.

Actually, that code tends to underestimate the mechanical parameters applying safety factor so that that values could be taken without further analysis on the masonry from technician. Hence, the experimental value obtained for  $\tau_0$  is in line with the expectations, differently from  $G$  value. This may be also caused from the sensitivity of acquisition data sensitivity of the instruments used for the data acquisition.

From results, one can calculate the reinforcement coefficients as  $k_G = 806 / 131 = 6.2$  and  $k_\tau = 0.583 / 0.138 = 4.2$ . Since the experiments were conducted in load-control, a proper computation of the reinforcement coefficient  $k_\mu$  is impossible to perform.

Figures 2.32a, b show the values of the compressive and tensile strain  $\varepsilon_s$  of the

vertical fiber strands measured during the 1RM- $\overline{GC}$  and the 2RM- $\overline{G}$  tests. In particular, one can observe compressive strains up to about - 0.5 mm/m for both tests. It is worth noting that the compressive strains concerned the initial phase of the tests and their maximum values occurred when the shear stress is maximum, i.e.  $\tau_0$ . This highlights that the fiber strands began to be strained only after the achievement of  $\tau_0$ . This result is also due to the fact that the ideal condition of pure shear is not possible to achieve with the designed diagonal compression test. Indeed, a pure shear condition would require an additional tensile force  $P$  applied to the other diagonal [114]. This problem has been studied by several authors who also suggested alternative formulations to evaluate the tensile and compressive principal stresses at the center of the panel [115].

In correspondence of the maximum compressive strain value, the maximum stress  $\tau_0$  was reached with appearance of cracks along the diagonal of the masonry specimens, which led to a sudden inversion of the sign of the axial strains up to their maximum tensile values equal to about 7 mm/m for the 1R- $\overline{GC}$  (Figure 2.32a) and 5 mm/m for the 2R- $\overline{G}$  (Figure 2.32b). This highlights that the fiber strands began to be strained only after the achievement of  $\tau_0$ . Moreover, no uniform distribution of the fiber strains can be observed in the results. This may be due to the heterogeneity of the material as well as the irregularity of the cross-section, which led to a varying thickness of the reinforcing mortar, and in consequence an eccentricity of the load.

The maximum values of the tensile strain measured by the 16 strain gauges applied on the vertical strands of the fiber grid are illustrated in Figure 2.33a, b.

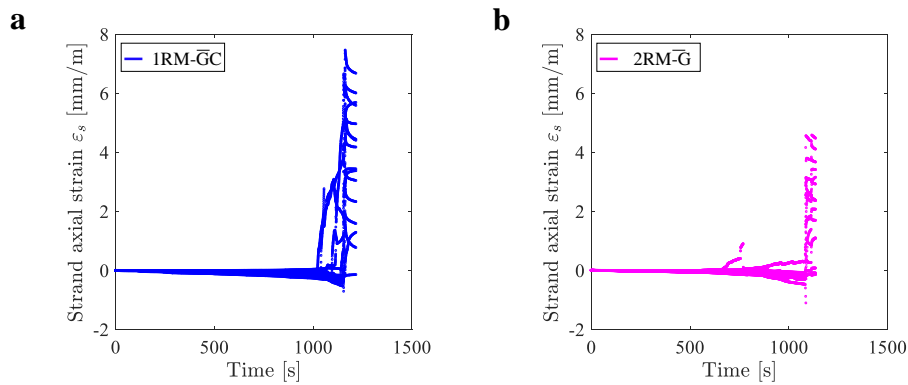


**Figure 2.32:** Axial strain  $\varepsilon_s$  measured for the vertical stands of the fiber grids during the 1RM- $\overline{GC}$  (a) and the 2RM- $\overline{G}$  tests (b).

**Figure 2.33:** Maximum values of the axial strain measured from the 16 gauges applied on the vertical stands of the fiber grids during the 1RM- $\overline{GC}$  and the 2RM- $\overline{G}$  tests

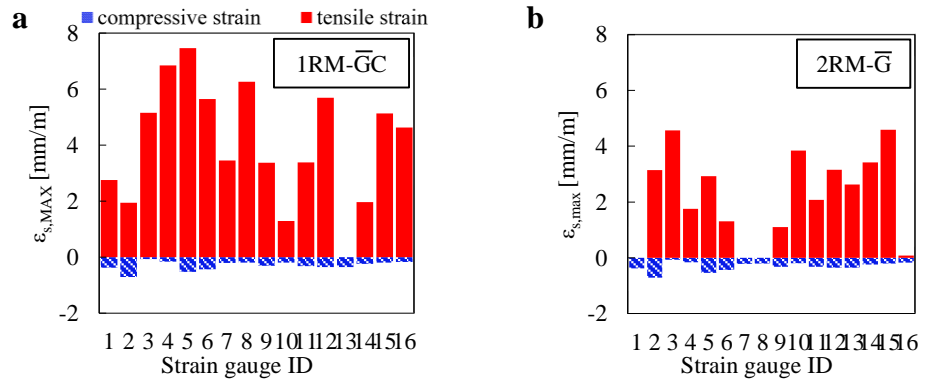
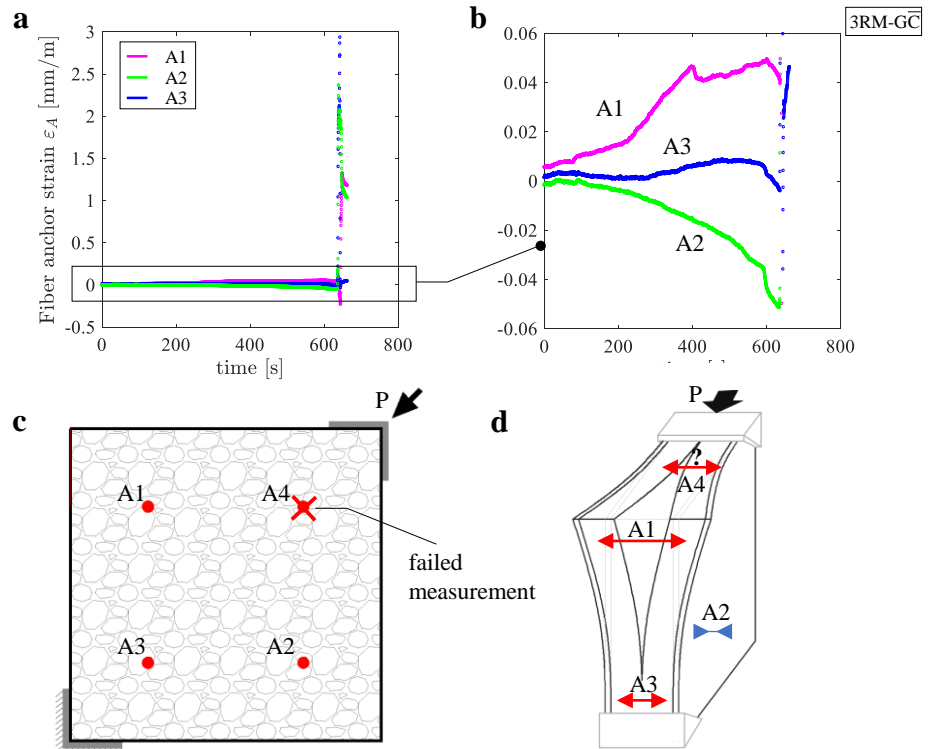


Figure 2.34 shows the axial strain measured along the fiber connectors of the 3R- $\overline{GC}$  test. In particular, one can see that the maximum measured values were equal to about 3 mm/m, 2.2 mm/m and 1.2 mm/m for the A3, the A2 and the A1 anchors, respectively (see Figure 2.34a). These maximum values occurred when the shear stress was maximum, i.e.  $\tau_0$ . It is worth noting that for the A2 anchor was measured an initial compressive axial strain of about -0.05 mm/m. After that, the specimen fails and a sudden tensile axial strain was measured also for that fiber connector. Unfortunately, no signal was recorded for the A4 connector because the gauge was damaged in the previous operation (see Figure 2.34c). The scheme of the specimen deformation is shown in Figure 2.34d. It may be considered reasonable by observing both the axial strain trends measured on the fiber anchors and the damage occurred on the specimen.



**Figure 2.34:** a) Axial strain measured along the connectors  $\varepsilon_a$  during the tests; b) zoom-in of the  $\varepsilon_a-t$  plot; c) position of the four fiber anchors; d) scheme of the deformation of the specimen at the failure.

Finally, Figures 2.35–2.39 show the crack opening observed at the end of the

experimental tests for both the unreinforced and reinforced masonry panels. In particular, Figure 2.35 shows the crack propagation on the unreinforced masonry specimen along the compressed diagonal. One can observe that damage evolution on unreinforced panels only occurred at the unit–mortar interfaces.

It is worth noting that the failure on the masonry specimens took place only at the stone-masonry interface and through the mortar matrix. The stones were found undamaged. This highlights the fact that lime-based mortar of ancient masonry building is much more compliant than stones. As far as the crack evolution is concerned, it is difficult to describe the crack evolution during the experimental tests as the test was performed under load control, which led to a catastrophic failure when the maximum shear stress was reached. However the failure in reinforced specimens initiated along the compressed diagonal of the specimen. Then crushing at the corners occurred. In particular, Figure 2.36 shows the damage that occurred on the mortar layer of the FRCM along the compressed diagonal. Moreover, one can see that the crack opening on the mortar layer is smaller than the one observed on the masonry

Figure 2.37 shows the crushing of the top corner of the reinforced specimen, where the upper steel L-shape plate was placed. In particular, one can observe a crushing and a local debonding of the mortar due to the concentration of the load. Since the debonding of the mortar was only localized in that position, one can conclude that a good bond behavior at the mortar-masonry interface was ensured by the FRCM system. For the reinforced case, the effective cracks occurred on the masonry substrate was not feasible to investigate because the repair mortar layer was not possible to remove from the masonry substrate without further damaging the specimen.

Finally, in Figure 2.38 one can observe the out of plane failure of the specimen that occurred the reinforcement specimen. This damage type observed for the masonry specimen was due to the failure of the glass fiber anchor placed on the upper corner opposite to the side of the specimen where the load was applied (Figure 2.39). The failure of the connector, was due to the shear generated on it from the irregular stones.



**Figure 2.35:** crack propagation along the compressed diagonal of the unreinforced masonry specimen.



**Figure 2.36:** Damage along the compressed diagonal observed for the reinforced panel.



**Figure 2.37:** Concentration of the damage in the top corner of the reinforced specimen.



**Figure 2.38:** Out of plane failure observed for the reinforced masonry specimens.



**Figure 2.39:** Failure of the glass fiber anchor.

## 2.2 Investigation on the fibrous lime-mortar material

Here, a description of the experimental investigation performed on the novel composite material for the retrofitting of masonry structures is presented. That material consisted of a lime-based mortar reinforced with short-fiber randomly oriented in the mortar matrix.

In the first phase of the experimental campaign, the effect of the fiber material, the aspect ratio of the fibers (i.e. the ratio between the length and the average diameter of the fibers), and the fiber content on both the compressive and tensile strengths were investigated. Concurrently, it was also designed the perfect content of additives, such as the fluidizer, air-entraining agent, resin, and accelerator. The experiments regarding the optimization of the mix design of the product were performed at the laboratory of the Aquilaprem company.

Once the mix design of the fibrous mortar material was decided, the final part of the experiments was conducted at the laboratory LPMS of the University of L'Aquila. In that phase, two different products, characterized by two fiber types, were tested in several configurations, such as three-point bending test, compression test, and splitting test. It is worth noting that in this phase, differently from the phase regarded the optimization of the mix design of the product conducted at the laboratory of the Aquilaprem company, the execution of the tests was performed in a displacement controlled hydraulic testing machine.

### 2.2.1 Optimization of the mix design

A brief description of the first part of the experimental campaign is presented. The experiments of this initial phase regarded the optimization of the mix design of the new composite material and were performed at the laboratory of the Aquilaprem company.

In this phase of the experimental campaign, the effect of the fiber material, the aspect ratio of the fibers (i.e. the ratio between the length and the average diameter of the fibers), and the fiber content on both the compressive and tensile strengths as well as the workability of the product were investigated. Concurrently, it was also designed the perfect content of additives, such as the fluidizer, air-entraining agent, resin, and accelerator. Unfortunately, that part was not possible to discuss here as the mix design of the composite material represents the company's know-how and cannot be revealed to their competitors.

In particular, the product was obtained by assuming both polyacrylonitrile and glass fibers came from different manufacturers. The first ones were characterized by a very low length of the fiber (2.5 mm - 4 mm), the second ones were characterized by a length  $l_f$  ranging from 6 mm to 24 mm. In particular, the polyacrylonitrile fibers were the same already used by the company for other commercial products, aiming to reduce their plastic shrinkage cracking. The glass fibers were instead provided by the company for the specific aim of the present research. The diameters  $d_f$  of the single yarn of both the fiber type were similar (ranging from 14 to 20  $\mu m$ ). However, the glass fibers were originally treated with dressing by manufacturers. This has resulted in greater effective diameters of the glass fibers (about from 0.3 mm to 0.5 mm), whose values were not provided by manufacturers. Hence, a measurement of the effective diameters  $d_f^*$  of the glass fiber was performed by measuring their diameters by an electronic micrometer. Actually, the cross-section of the fibers was not perfectly circular and therefore  $d_f^*$  represents the diameter of the fiber with an ideal circle cross-section of the fiber.

Table 2.10 summarizes the material type, the name, and the geometry (i.e. fiber length  $l_f$  and diameters of the single yarn  $d_f$  and the diameters of the strand  $d_f^*$ ) of the short-fibers used in the first part of the experimental campaign.

For each batch of the product, three mortar samples measuring 160 mm in length, 40 mm in height, and 40 mm in thickness were cast according to the standard code UNI EN 1015-11 [116]. Fibers were added during the mixing phase.

The specimens were cast in the molds and then were kept moist for 48 hours in the climatic chambers. After that, they were demoulded and left in laboratory condition for other 12 days, for a total age of the specimen of 14 days, prior to testing. The decision to test the specimens before of the standard age of 28 days

**Table 2.10:** Material, name and geometry of the short-fibers used in the experiments.

Material	Name	$l_f$ [mm]	$d_f$ [ $\mu m$ ]	$d_f^*$ [ $\mu m$ ]
Polyacrylonitrile	PAC2.5-4	4	18	18
Polyacrylonitrile	PAC2.5-2T	2.5	18	18
Glass	6H103	6	13.5	13.5
Glass	530X	13	18	320
Glass	950Y	13	13.5	316
Glass	H018	18	20	350
Glass	HP24	24	14	476

[116] was related to the use of accelerator in the product to speed up the first phase of the experimental campaign essentially focused on the identification of the best type of fiber for the composite mortar as well as the consistency of the fresh fibrous-mortar. Almost 100 different mixes were tested, but they were not all discussed in the thesis, as explained later.

Hence, several unnotched hardened mortar samples were tested for the determination of flexural and compressive strength of the fibrous material. It is worth noting that, in this first part of the experimental campaign, tests were performed in a load controlled hydraulic testing machine with a capacity of 15 kN by applying a constant force rate of 0.01 MPa/s and 0.3 MPa/s for the three-point bending test (3PBT) and compression test (CT), respectively. The aspect related to the test procedure (load-control) is important to stress out since only the maximum strength of the fibrous-mortar was possible to measure, leaving aside the investigation of the softening behavior of the material and therefore the most important mechanical parameter of the fibrous material, namely the fracture energy. Hence, even for this cause, the results of this first part were only briefly discussed.

Figure 2.40 shows the test machine adopted in the first part of the experimental campaign carried out at the laboratory of the Aquilaprem company.



**Figure 2.40:** Test machine of the Aquilaprem company used in the first part of the experimental campaign.

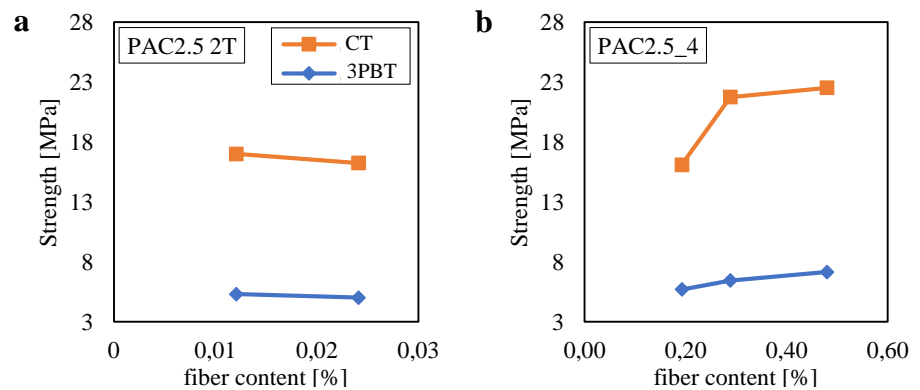
Hence, a discussion on the mechanical properties measured for the mortar specimen reinforced by several types of short fibers as well as fiber content is discussed. In particular, the graph of Figures 2.41–2.44 show the flexural and compressive strengths represented by the blue and the orange lines, respectively.

These properties were obtained by performing the 3-Point Bending Test (3PBT) and Compression Tests (CT), respectively. In particular, Figures 2.41–2.44 shows the relation between the mechanical properties and the fiber content. The latter is referred to the total mass of the product. It is worth noting that the results of Figures 2.41–2.44 were obtained without using fluidizers and resins for the mix-design of the products. The relatively small percentage of the fiber content adopted for the mortar was almost the maximum possible to ensure the workability of the product.

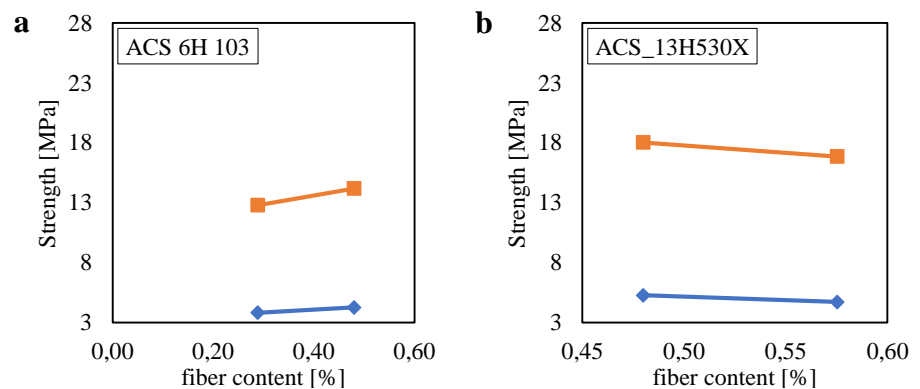
Each strength value (represented by marks) of Figures 2.41–2.44 represents the mean value of three and six tests obtained for the 3PBTs and the CTs.

Apart from the PAC2.52T case, a common fiber content equal to 0.48% was assumed for all the fiber types. This ensured a proper comparison between mechanical efficiency due to the different fiber features. Hence, for each fiber type, it was assumed fiber content higher or lower than 0.48% based on the workability of the product.

**Figure 2.41:** Compressive strength and tensile strength obtained for the Compression Test (CT) and the 3 Point Bending Test (3PBT) for two different type of fiber by varying the fiber content.



**Figure 2.42:** Compressive and tensile strengths obtained for two different type of fiber by varying the fiber content.



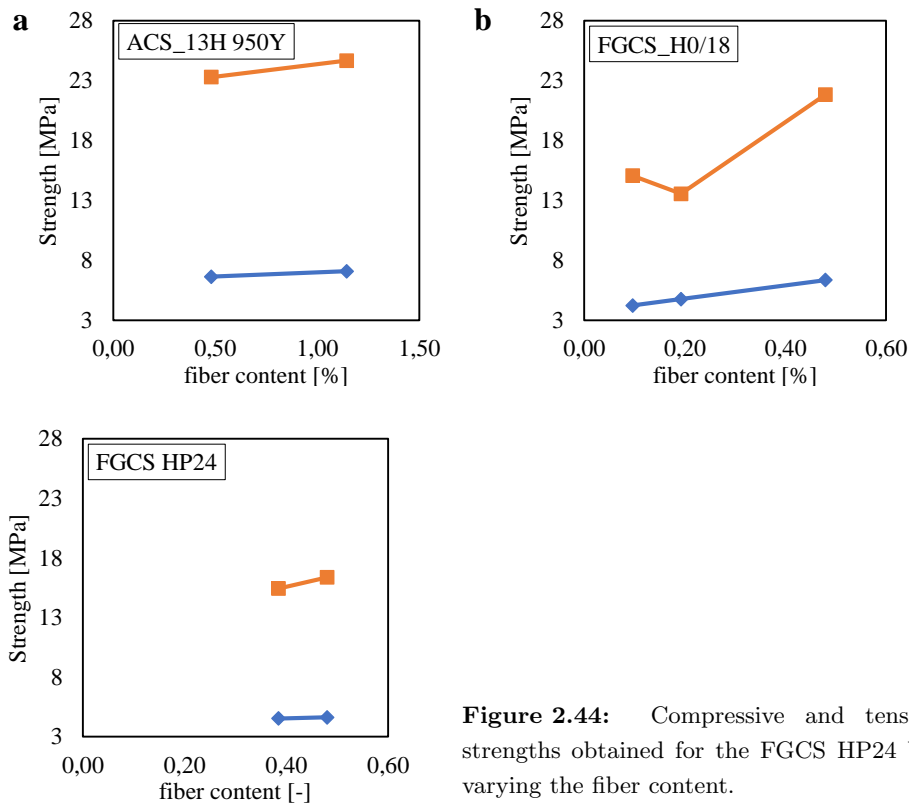


**Figure 2.43:** Compressive and tensile strengths obtained for two different type of fiber by varying the fiber content.

**Figure 2.44:** Compressive and tensile strengths obtained for the FGCS HP24 by varying the fiber content.

In general, results show that the higher the fiber content, the higher the compressive and flexural strengths. This trend was not observed for the ACS 13H 530X and the PAC2.5 2T cases (Figure 2.41–2.41a and Figure 2.41–2.42b, respectively). However, this abnormal trend may be due to the incorrect casting phase of the product also related to the inexperience of the operator (me, ed.). Moreover, the variability of the results in terms of both the maximum stress, stiffness as well as the crack propagation may be caused by many factors: specimens properties irregularity of the cross-section, presence of micro-cracks, misalignment of the samples with respect to their mid-thickness, different thickness of the specimens, the randomness of the fibers and in the end but not the least the spatial randomness of material properties.

It is worth noting that the mean strength values of the product without fiber (the NF case) was equal to 4.8 MPa and 14.8 MPa for  $\sigma_f$  and  $f_c$ , respectively.

The best performances were obtained for the ACS-13H-950Y and the PAC2.5-4 fibers. In particular, for the ACS-13H-950Y one can observe an increase in the flexural and compressive strengths of about 38% and 58%, respectively, as compared to the NF case. Instead, for the PAC2.5-4 one can observe an increase in the flexural and compressive strengths of about 48% and 52%, respectively, as compared to the NF case.

By analyzing these results, it is clear that fiber characterized by the shorter length of fiber (the PAC2.5-4 case) leads to the higher compressive strengths, as

compared to the fiber with the longer length (the 950Y case). On the contrary, the longer fiber length (the 950Y case) lead to the higher flexural strengths, as compared to the fiber with the shorter length (the PAC2.5-4 case).

The choice of the best fiber type to use for the novel composite material was not easy to perform in light of the results of the first experimental campaign. However, in the first part of the experimental campaign, the 950Y fiber was considered the best solution. Indeed, though the 950Y and the PAC2.5-4 ensured similar enhancement of the mechanical properties of the fibrous-mortar, the 950Y fiber ensured to use the higher fiber content (equal to 1.14%) because of its aspect ratio AR.

As mentioned before, the results discussed so far concerned the mechanical properties of the product without using any additives. However, to ensure higher efficiency of the fiber on the mechanical properties of the fibrous mortar, it was necessary to assume a higher fiber content and, therefore, the use of certain content of additives.

Hence, a second part of the experimental campaign focused on the identification of the best additives (i.e. fluidizers) derived from different companies. However, that part was not discussed in the thesis since the brand, type, and content of the additives represent the company's know-how and cannot be revealed to their competitors.

The following section shows the final part of the experimental campaign in which the mix-design of the fibrous mortar was already formulated. In particular, two fiber type was chosen for the most accurate evaluation of the mechanical properties carried out at the laboratory LPMS of L'Aquila, having the possibility of employing a displacement controlled hydraulic testing machine, which was unfortunately not available in the first part of the experimental campaign. That machine ensured to investigate the softening behavior of the fibrous-materials.

## 2.2.2 Mechanical characterization of the product

After the first part of the experimental campaign, two type of fiber were chosen for the final investigation of the post-peak behavior of the composite material: the 950Y (Figure 2.45a) and the HP24 (Figure 2.45b). In particular, the 950Y was the best solution in terms of both the flexural and compressive strengths, as compared to the other fiber type. Instead, although results of the initial experimental campaign in terms of compressive strength and flexural strength were not encouraging for the HP24 fiber, it was employed in this phase of the experimental campaign because it was characterized by the best aspect ratio (AR), as compared to the other available fiber types. Indeed, from the literature, it is known that the higher the AR, the higher the fiber performance in terms of ductility of the fibrous mortar. Unfortunately, this important mechanical property was not possible to measure in the previous experiments, as tests were performed in force-control not allowing the characterization of the softening behavior of the composite material. Results of the mechanical characterization of the fibrous mortars presented in the follows were instead obtained by employing a displacement controlled hydraulic testing machine.

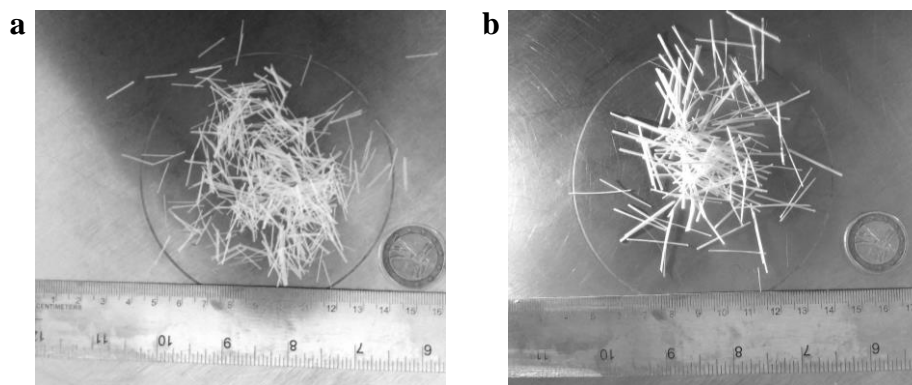


**Figure 2.45:** Two fiber types used in the experimental campaign: the 950Y (a) and the HP24 (b).

The following results were obtained by assuming the same values of lime content (almost 30% of the total weight of the binder; the remain 70% was a cementitious binder), water content (almost 80% of the binder weight), sieve curve, and content of additives. More detailed information on the mix-design of the product was not possible to reveal. The choice to employ the same mix-design for the reinforced and unreinforced mortar specimens was due to the intention to only investigate the effect of the fiber type (the 950Y and the HP24, whose geometrical properties are listed in Table 2.10) and the fiber content  $F$  on the mechanical properties of the composite material. Therefore, fresh products were characterized by different consistency. In particular,  $F$  was assumed equal to 1.5%, 2.0% and 2.5% of the total weight of the product (corresponding almost to 1%, 1.3% and 1.6% of the total volume of the product, respectively)

Hence, a comparison between results carried out for both the fibrous mortar samples and the unreinforced ones allowed to quantify the enhancement of the mechanical properties due to the fiber type and fiber content. It is worth noting that, even for the unreinforced samples, the mix design of the product ( $w/c$ , sieve curve, and content of additives) was the same as the fiber-reinforced ones.

For each batch of the product, immediately after the slump test (described in Section 2.2.2.1), three mortar samples measuring 160 mm in length, 40 mm in height and 40 mm in thickness were cast according to the standard code UNI EN 1015-11 [116]. The specimens were cast in molds and were kept moist for 48 hours in the environmental chambers. Next, the samples were demolded and left in laboratory condition (room temperature and ambient humidity of about 20° and 60%, respectively) for 26 days, for a total age of 28 days, before testing in three points bending test (Section 2.2.2.2). After the 3PBTs, the end pieces of the broken beams were used to determine the tensile strength (Section 2.2.2.3) and the compressive strength (Section 2.2.2.4) of the mortar.

In particular, a total of 21 mortar specimens were prepared, namely 3 unreinforced samples and 18 fibrous mortar samples (three samples for each of the three fiber content adopted for both the two fiber types).

### 2.2.2.1 Characterization of the consistency

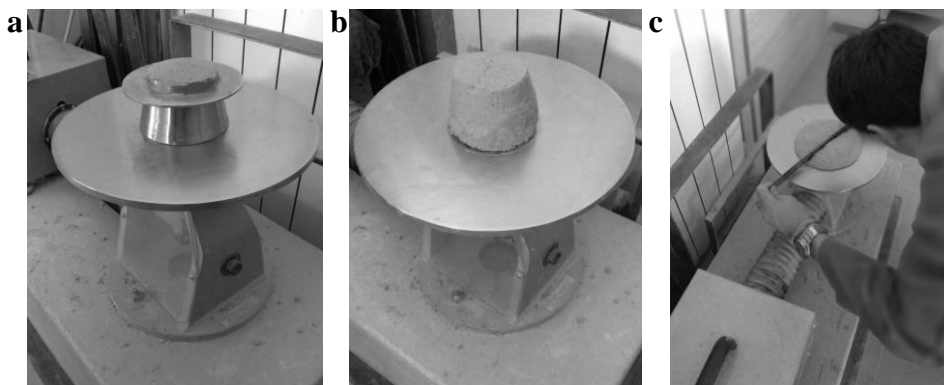
The slump test is an empirical test that measures the workability of fresh mortar (or concrete). More specifically, it measures the consistency of freshly made mortar in a specific batch of the product that can be subsequently used for the mechanical characterization tests, namely three points bending test, compressive test, and direct-indirect tensile test. It is a term that describes the state of fresh mortar. In particular, it is the relative mobility or ability of freshly mixed mortar to flow. It includes the entire range of fluidity from the driest to the wettest possible mixtures [117]. Consistency is a term very closely related to workability.

Workability of mortar (or concrete) is mainly affected by consistency, i.e. wetter mixes will be more workable than drier mixes, but mortar of the same consistency may vary in workability. In particular, workability is the property of freshly mixed mortar that determines the ease with which it can be mixed, placed, consolidated, and finished to a homogeneous condition. It is synonymous with placeability. It involves not only the concept of the consistency of mortar, but also the condition under which it is to be placed - size and shape of the member, the spacing of reinforcing, or other details interfering with the ready filling of the forms [117].

A stronger difference between workability and consistency can be noted for concrete rather than mortar. Indeed, for concrete, it is not always true that increasing water or degree of wetness increases workability of the material. If water content increases there is a greater chance of segregation, in which coarse aggregates tend to be separated from fines. In this case, it is difficult to move and place the concrete as coarse aggregates settle down. In other words, the workability of concrete decreases due to segregation. However, mortar material is less and less affected by the segregation phenomena since the absence of coarse aggregates in the paste. Hence, though consistency cannot exactly measure the workability, it can give an indication of the workability of mortar.

Practical evaluation of the consistency of the paste can be performed according to the procedure reported in the Italian Norm UNI 7044-72 (Determination of consistency of cement mortars using a flow table). In particular, the so-called slump test consists in measuring the diameter of the freshly mortar, previously cast in a specific steel mold, after 20 strokes of the flow table (see Figures 2.46a-c). The measure of the diameter value of the freshly mortar at the end of the test represents the “slump” of the product. The higher the slump value, the higher the workability of the mortar.

**Figure 2.46:** Slump test procedure: a) casting of the mortar therein the mould; b) raising of the mould from the mortar; c) Slump measurement in terms of the mean of two diameter values of the mortar after 20 strokes.



In Figure 2.47 one can observe the results of the slump tests carried out for the mortar specimens strengthened by the 950Y and the HP24 fibers. In that figure the slump value is related to the fiber content  $F$  adopted for the mortar. It is worth noting that it was assumed a linear variation of the slump (indicated by the dotted lines of Figure 2.47) from the case of the unreinforced mortar ( $F=0\%$ ) to the reinforced mortar with the content fiber of 1.5% as no tests were carried out by using fiber content in that range (0%–1.5%).

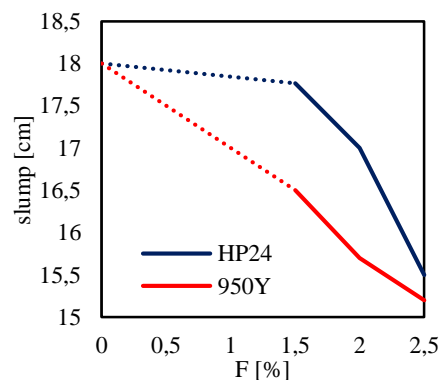


**Figure 2.47:** Slump measured for the HP24 and the 950Y cases by varying the fiber content  $F$ .

As expected, in Figure 2.47 one can observe a decrease in the slump value by increasing the fiber content. This trend can be observed for both the fiber type. For the HP24 case, one can see that no strong differences in terms of slump can be noted by comparing the unreinforced samples ( $F=0\%$ ) and the  $F=1.5\%$  case. This means that a significant compaction effect of the HP24 fiber on mortar past can be achieved only with fiber content higher than 1.5%. This is obviously related to the content of additives introduced in the product to increase its workability. Indeed, for lower additive content one would observed a higher reduction of the slump value even for fiber content lower than 1.5%. Moreover, in Figure 2.47 one can instead observe an almost linear decrease in the slump value for the 950Y case by increasing the fiber content.

Results plotted in Figure 2.47 indicate that the HP24 fiber leads to higher workability of the product (higher slump value), as compared to the 950Y one. This trend can be observed for all the fiber content  $F$ .

The large difference in the results plotted in Figure 2.47 between the two fiber types may be mainly due to their different aspect ratio AR. Indeed, for the same F, a higher value of the AR leads to a lower number of fibers per unit volume of the product, and vice-versa. Hence, the lower the number of fibers, the higher the workability of the product. Since the HP24 fiber is characterized by the higher AR, as compared to the 950Y one, one can observe higher workability of the fibrous mortar with that fiber (see Figure 2.47). Furthermore, the trend of Figure 2.47 may be influenced by the absorption level of the two types of fibers. Indeed, these fibers were produced by different manufacturers and different types of primers may have been employed for them.

### 2.2.2.2 Characterization of the flexural strength

To evaluate the enhancement of the innovative fibrous lime mortar material in terms of its flexural strength as well as its fracture energy, three points bending test (3PBT) was carried out on several specimens measuring 160 mm in length, 40 mm in height and 40 mm in thickness. The preparation of these samples is described in Section 2.2.2.

Differently from the other 3PBTs discussed in Section 2.2.1, here a 2 mm thick mechanical notch ( $t_n$ ) was fabricated on the mortar samples with a depth  $a$  of 6 mm, resulting with a notch to beam depth ratio  $a/d$  of 0.15. The beams were notched using wet sawing. Each beam was turned  $90^\circ$  from the casting surface and the notch was then sawn through the width of the beam at midspan.

The notches were fabricated on the mortar samples to minimize irreversible deformations outside the fracture zone, avoiding large parts with high stresses outside this zone. For that issue, Hillerborg [118] suggested a depth notch of 0.3 – 0.4 times the beam depth. However, in the present research, the  $a/d$  ratio was chosen equal to 0.15, since that the higher values of that ratio would have led to a larger dispersion of the results because of the presence of the short-fiber. Indeed, the lower  $a/d$  ratio leads to an increase in the number of fibers passing through the unnotched ligament ( $d - a$ ). Hence, one can easily understand that by increasing the number of fibers passing through the unnotched ligament a less scattering of the results can be obtained. Furthermore, the  $a/d$  suggested by Hillerborg referred to concrete material, in which the ratio between the size of the fracture plane and the size of the maximum aggregate is different from the mortar case. The final important reason in the choice of a  $a/d$  ratio equal to 0.15 was due to the nature of the material: lime-based mortar beams would have easily broken during handling in case of deeper notches.

The scheme of the notched beam used for the 3PBT is illustrated in Figure 2.48. In particular, the nominal distance between the supports  $L$  was 100 mm, whereas both the width  $d$  and the thickness  $b$  were equal to 40 mm. The loading  $P$  was introduced at the midspan of the beam. The two rollers at the bottom allowed for free horizontal movement.

The three-point bending test was performed on notched beams to determine the maximal tensile stress  $\sigma_f$  as well as the fracture energy  $G_f$ . Indeed, the fracture energy of quasi-brittle material (i.e. mortar and concrete) is the most useful parameter to describe the cracking mechanism in the fracture behavior of such material. As described by a Bazant's work [119], the fracture energy of quasi-brittle material is a basic material characteristic needed for a rational prediction of brittle failures of such structures.

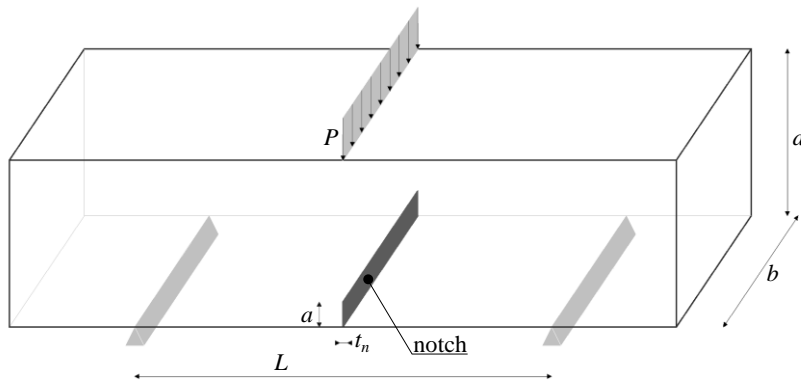


**Figure 2.48:** Notched beam adopted for the 3PBT.

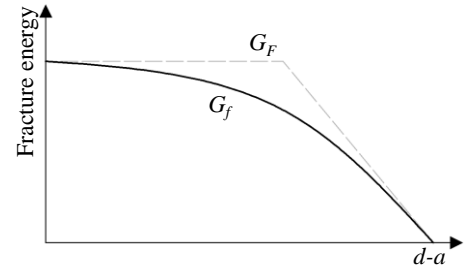
Failure of quasi-brittle structures generally consists of numerous micro-cracks that might result in fracture of the structures under service loads, accidental load and/or exposure to regular environmental conditions. Thus a micro-crack in quasi-brittle material may become a potential source of crack propagation leading to probable catastrophic failure. Definitely, the failure mechanism can be studied by quantifying the energy consumed in crack propagation and the formation of new crack surfaces.

In principle, the fracture energy as a material property should be a constant, and its value should be independent of the method of measurement, various test methods, specimen shapes, and sizes. However, these variables lead to very different results. The size effects on fracture energy and strength of concrete have been studied extensively and various size effect models have been proposed (e.g. [119, 120, 121]). Much of these efforts are directed at the explanations of why these fracture parameters vary with the specimen size or from small specimens to large concrete structures.

In a quasi-brittle structure, the crack growth requires a certain amount of energy that can only be studied through an energy-based propagation criterion, which provides a fundamental basis for understanding the phenomenon of the fracture mechanism. Quasi-brittle material exhibits a stable non-linear fracture response in tension loading when tested under displacement control. This is related to the development of a fracture process zone (FPZ) ahead of the crack tip. In a quasi-brittle material, the energy dissipated for the formation of FPZ ahead of the crack tip is termed as fracture energy. The fracture energy characterizing the failure process of quasi-brittle material is still under extensive research.

It was argued [122, 123] that the free boundary affects the fracture process zone (FPZ) so that the energy required to create a new crack decreases as the crack grows. In Figure 2.49 is illustrated the relation between the fracture energy and the un-notched ligament ( $d - a$ , where  $d$  is the width and  $a$  is the notch depth, see Figure 2.48). This trend can be approximated by a bi-linear curve (as illustrated in Figure 2.49).

**Figure 2.49:** Variation of the fracture energy of notched specimens in terms of the un-notched ligament  $d - a$ , where  $d$  is the depth and  $a$  is the notch depth.



Despite the scientific interest in chaotic stone constructions, the test method for the determination of  $G_f$  and even its precise definition has been a subject of intense debate among researchers because it has been found to vary with the size and shape of the test specimen and with the test method used. The commonly used method for measuring the fracture energy is the work-of-fracture method recommended by RILEM. Fracture energy is the averaged fracture energy over the entire projected ligament area. Although  $G_f$  is defined as a material constant, this averaged fracture energy is specimen size-dependent in most cases, particularly in the case of coarse aggregates [123].

According to RILEM codes [124, 125], In this research the total energy  $G_f$  was evaluated by dividing the total applied energy with the projected ligament area, as follows:

$$G_f = \frac{W_0 + m g \delta_0}{(d - a) b} \quad (2.6)$$

where  $W_0$  is the area of the complete load-deflection curve,  $m$  is the weight of the beam between the supports, calculated as the beam weight multiplied by  $1/L$ ,  $g$  is the acceleration due to gravity,  $\delta_0$  is the deformation at the final failure of the beam,  $d$  is the beam height,  $b$  is the beam width,  $a$  is the notch depth. For stable test performance and to obtain reliable test data, the self-weight compensation [126] was used.

The flexural stress  $\sigma_f$  was calculated by using the following equation:

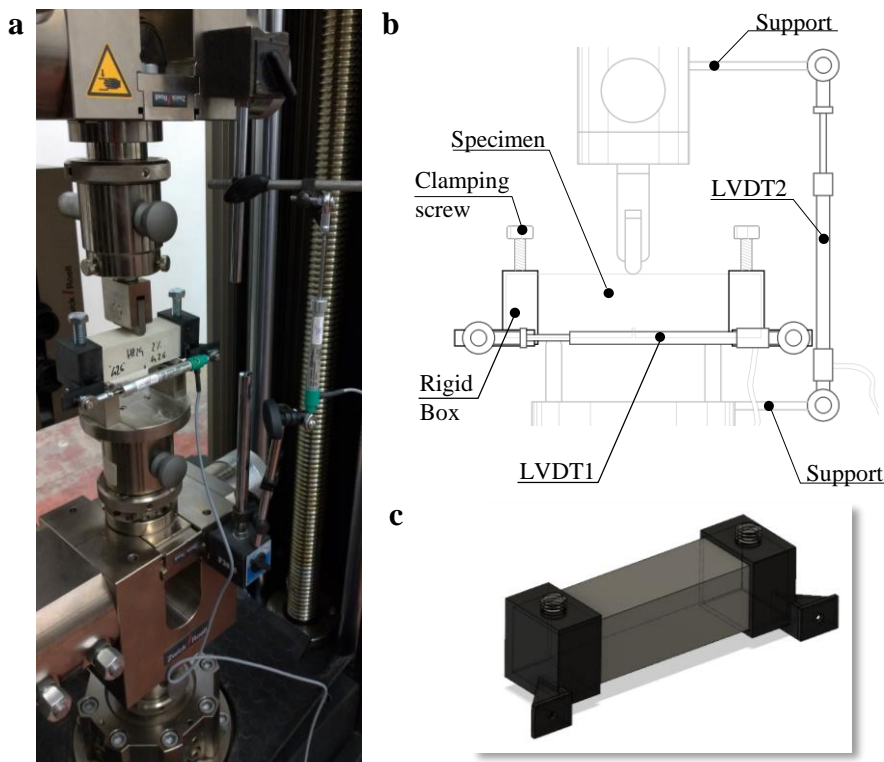
$$\sigma_f = \frac{3 P L}{2 b (d - a)^2} \quad (2.7)$$

where  $P$  is the load and  $L$  is the span of the beam, equal to 100mm. For  $P = P_{MAX}$  that equation gives the flexural strength.

As far as the execution of the three points bending test (3PBT) is concerned, tests were performed in a displacement controlled hydraulic testing machine, by using the Zwick Roell test machine of the LPMS of L'Aquila (Figure 2.50a). The

specimens were loaded at constant displacement rate of 0.5 mm/min. Apart from measuring the loading and mid-span displacement ( $\delta$ ), a crack mouth opening displacement (CMOD) was also monitored. To measure the CMOD a Linear Variable Displacement Transducer - LVDT was placed across the notch and supported by two rigid boxes mounted at the two sides of the beam and fixed thereto by two clamping screws. That boxes were specifically created for this issue by a 3D printer and using nylon material (tensile strength of 76 MPa, flexural strength of 110 MPa, and Young's modulus of 2.7 GPa). However, the CMOD measure was not considered in the present thesis. Indeed, that property assumes a notable value when test is carried out by controlling the opening of the notch. Here, tests were performed by controlling the deflection of the mortar making the CMOD less important to be investigated.

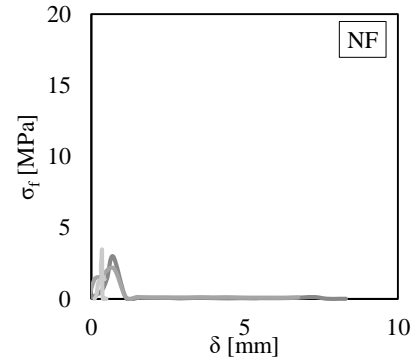
Both the force  $P$  and vertical displacement  $\delta$  were directly recorded through the test machine. However, also another LVDT was used for the measurement of  $\delta$  to ensure the synchronization with the CMOD record. In this case, the LVDT was fixed to the test machine by using two rigid supports. In Figures 2.50b, c are illustrated the details of the test apparatus and the rigid boxes, respectively.



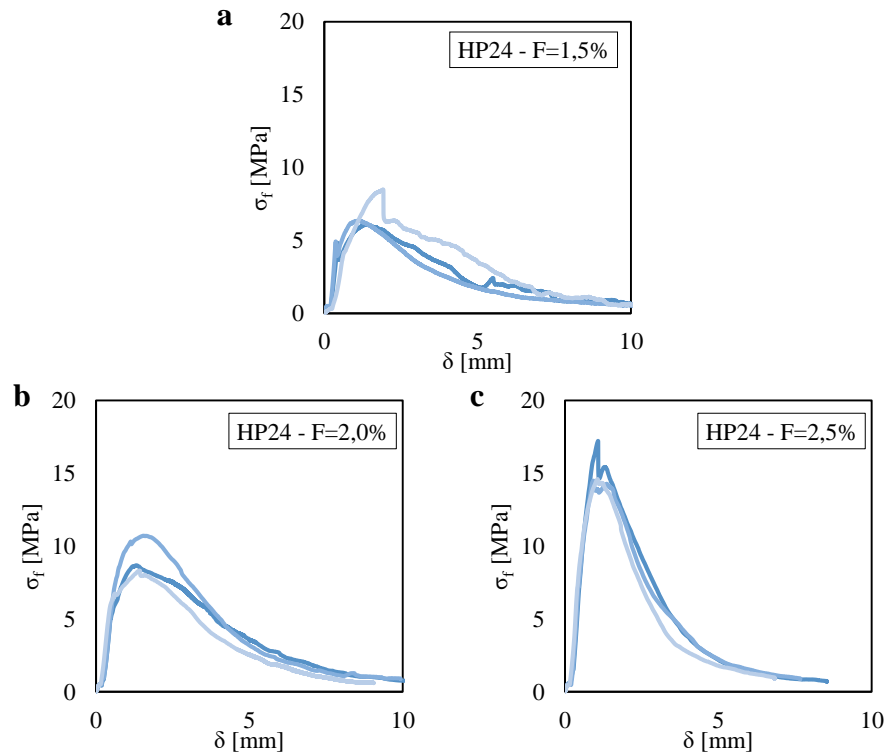
**Figure 2.50:** a) Displacement controlled hydraulic testing machine of the LPMS of L'Aquila; b) details of the test apparatus; c) detail of the rigid box, obtained by a 3D printer, for the allocation of the LVDT across the notch of the beam.

Figure 2.51 shows the relation measured between the flexural stress  $\sigma_f$  and the deflection  $\delta$  obtained for the unreinforced mortar specimens under three-point bending tests (3PBT). Plots are referred to three tests. The mean value of the maximum flexural stress is equal to 2.9 MPa. Moreover, one can observe an almost perfect brittle behavior after the achievement of the maximum flexural stress. Indeed, the  $\sigma_f$  suddenly drops after that point.

**Figure 2.51:** Flexural stress  $\sigma_f$  related to the vertical displacement  $\delta$  measured in the 3PBT for the unreinforced case (NF).



Figures 2.52 and 2.53 show the  $\sigma_f$ - $\delta$  plots obtained for the fiber-reinforced mortar specimens tested under 3PBT for different fiber F content adopted for the mortar specimens (1.5%, 2.0%, and 2.5%). Plots are referred to a number of three tests for each fiber content. In particular, Figure 2.52 shows the  $\sigma_f$ - $\delta$  curves for the HP24 fiber, whereas Figure 2.53 shows that relation for the 950Y fiber.



**Figure 2.52:** Flexural stress  $\sigma_f$  related to the vertical displacement  $\delta$  measured in the 3PBT for the HP24 with different fiber content.

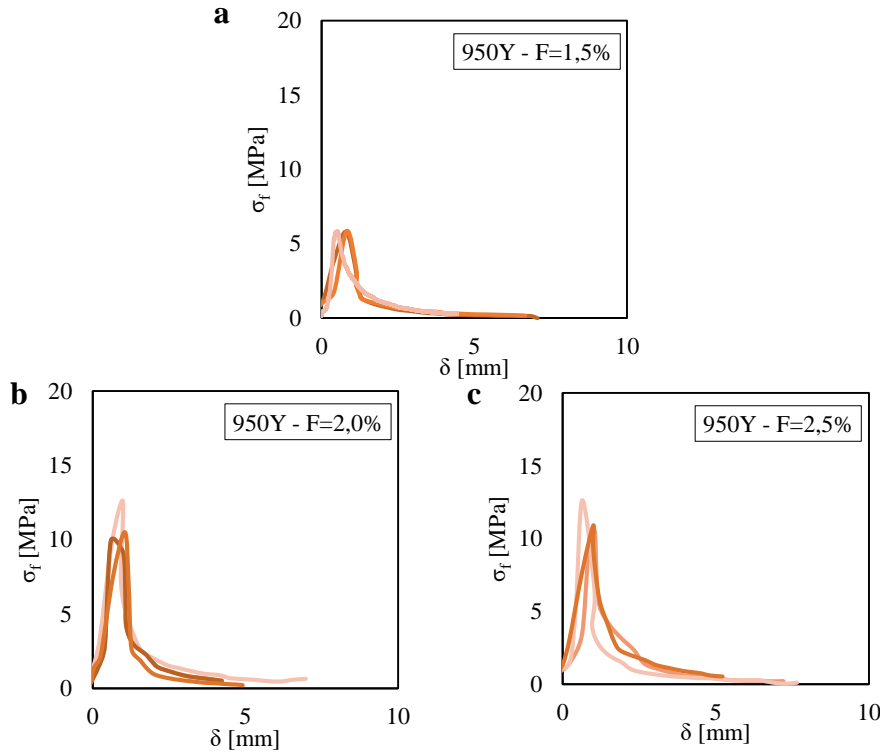


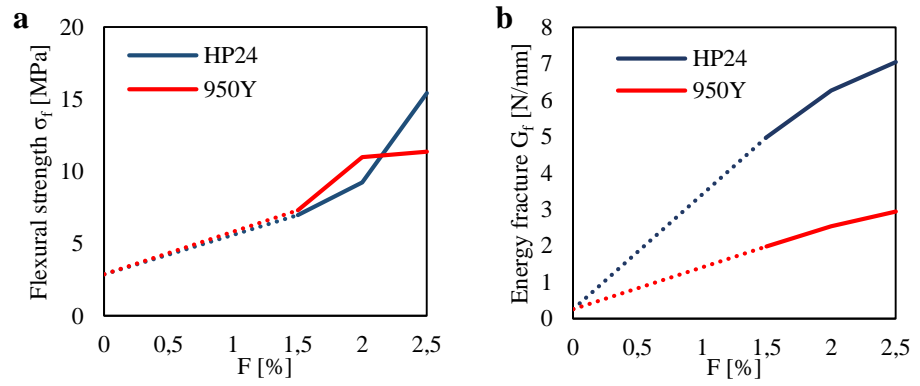
**Figure 2.53:** Flexural stress  $\sigma_f$  related to the vertical displacement  $\delta$  measured in the 3PBT for the 950Y with different fiber content.

For a better interpretation of the effect of both the fiber content and fiber type on the mechanical properties of the composite material, one can see Figure 2.54a, b. In particular, Figure 2.54a shows the variation of the flexural strength  $\sigma_f$ , computed by using the equations Eq.(2.7), as a function of the fiber content F. One can see that for lower fiber content (F=1.5%) no differences can be noted between the two different fibers (the 950Y and the HP24). Then, for higher values of fiber content (F=2.0% and F=2.5%) one can see different results by comparing the two fiber types. In particular, for the HP24 case, one can observe a gradual increase in the flexural strength up to achieve almost 15 MPa (when F=2.5%). Instead, for the 950Y case, a high increase in the flexural strength is observed from F=1.5% to F=2.0%, whereas one can observe a slight difference by comparing the case of F=2.0% and F=2.5%.

In general, from Figure 2.54a one can see the benefit of the fiber content on the flexural strength though the variability of the results may be affected by many factors (i.e. specimens properties and failure mode).

Figure 2.54b shows the variation of the fracture energy  $G_f$ , computed by using the equations Eq.(2.6), as function of the fiber content. Respect to the results commented in terms of  $\sigma_f$  one can observe a clearer trend in terms of  $G_f$ . For all the fiber content, one can see that the fracture energy computed for the HP24 is more than two times the one computed for the 950Y. This is due to the higher fiber length as well as the AR of the HP24, which allows higher bond behavior at the fiber-mortar interface.

**Figure 2.54:** Flexural strength  $\sigma_f$  (a) and fracture energy  $G_f$  (b) measured in the 3PBT for two fiber type (HP24 and 950Y) with different fiber content.



In Table 2.11 are summarized the mean values of both the flexural strength and fracture energy of the results commented for Figures 2.54a, b. Moreover, also the standard deviations of such values are listed in that Table.

**Table 2.11:** Mechanical properties of mortar specimens tested in 3PBT and reinforced by two type of short-fibers (950Y and HP24) with different fiber content.

Name	Fiber content	$\sigma_f$ [MPa]	$G_f$ [N/mm]
NF	0%	$2.9 \pm 0.71$	$0.32 \pm 0.3$
950Y	1.5%	$7.3 \pm 1.5$	$1.9 \pm 0.6$
950Y	2.0%	$11.0 \pm 1.1$	$2.7 \pm 0.4$
950Y	2.5%	$11.4 \pm 0.8$	$2.9 \pm 0.3$
HP24	1.5 %	$7.0 \pm 0.9$	$5.0 \pm 1.0$
HP24	2.0 %	$9.2 \pm 0.9$	$6.3 \pm 1.0$
HP24	2.5 %	$15.4 \pm 0.9$	$7.1 \pm 0.8$

### 2.2.2.3 Characterization of the tensile strength

Failure in quasi-brittle material, such as mortar or concrete, can be attributed to some form of tensile stress. The tensile strength of such materials can be determined from different types of tests, namely direct or indirect tensile tests. The direct test concerns the execution of direct pull tests, whereas the indirect tensile test concerns the execution of splitting tensile tests. The splitting tensile test is also called the diametrical compression test, split-tension test, and Brazilian test (BT) among other names.

There are many technical difficulties in executing a true tensile strength test. A uniform stress distribution which makes it possible to calculate the true tensile strength is difficult to obtain. The method commonly used to determine tensile properties of quasi-brittle material is the flexural beam test by three-point loading on a beam over a span (the 3PBT described in Section 2.2.2.2). The flexural strength is computed from the bending moment at failure, assuming an ideal straight line stress distribution according to Hooke's law. However, the calculated flexural strength may be higher than the true tensile strength [127].

Many attempts have been made to find a substitute for the 3PBT and the splitting tensile test of a cylindrical specimen may be the solution to the problem [128].

The splitting tensile strength test method has many merits compared with the direct tensile test method; for example, it can be conducted much more easily and the scatterings of the test results are very narrow. This method, therefore, has been prescribed in many standards as the standard test method for tensile strength of concrete. The BT is straightforward and economic and can be used on cylindrical specimens (fabricated in molds or extracted concrete cores) or on flat disk-shaped specimens as well as cubes or prisms [129]. Also, the test can be performed with the same machine that is used to perform direct compression tests, and samples identical in shape and geometry as those used in direct compression can be employed. The BT is useful to experiment brittle or quasi-brittle materials that have a much greater compression strength than their tensile strength and that are susceptible to brittle ruptures. Researchers have indicated that, among the three testing methods (direct tensile, splitting tensile, and flexural tests), the splitting tensile test gives the most accurate measurement of the true tensile strength of mortar or concrete materials in a wide strain rate [129]. Difficulties are encountered in the direct tensile tests when it requires a pure tensile without eccentricity.

In the BT, a flat, circular, or solid disk is compressed with load concentrated on a pair of antipodal points. In this way, a tensile stress is induced in the direction perpendicular to the applied load, and it is proportional to the magnitude of the

applied load. When the disk is a homogeneous, isotropic, elastic material, the induced tensile stress is greatest in magnitude at the geometric center of the disk.

When the induced stress exceeds the tensile strength, fracture initiates at the geometric center of the disk. In agreement with the Griffith criterion [130], the exact center of the disk is the only point at which the conditions for failure under tension are satisfied because, in this site, the tensile stress equals the uniaxial strength of the tested material. Indeed, the BT result is accepted if fracture initiates at the center of the disk, and in this case, the measured value is representative of the tensile strength of the tested material. In the BT, the specimen must fail along the vertical line between compression points; otherwise, the observed failure mode is considered invalid. In the case of unreinforced specimens, the test typically ends with a sudden, violent failure of the specimen when it reaches the maximum load due to the propagation of an unstable crack. Since its invention, the BT has motivated a wide variety of studies. One can gain an idea of its impact if one considers that the use of concrete test specimens has been standardized into norms in various countries, such as UNEEN 12390-6, ASTM C-496. However, the BT is far from a universal test, and it is unknown whether a geometric configuration exists that favors effective, robust testing that is less sensitive to other experimental parameters [131].

In the present research, to obtain the tensile strength of the mortar specimens, instead of performing a direct tension test, which is of needless difficulty, Brazilian Tests (BT) (ASTM C496) were conducted using 40 mm × 40 mm × 80 mm prismatic mortar specimens obtained from the two-half specimens tested in 3PBT.

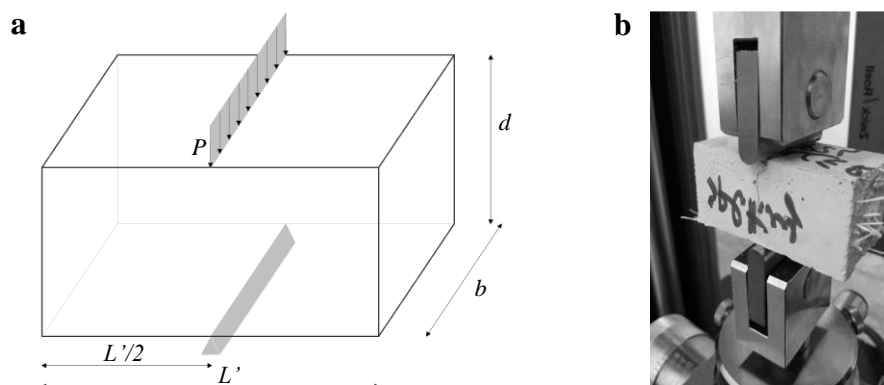


**Figure 2.55:** a) Scheme employed for the Brazilian test (BT); b) Picture of the test carried out at the LPMS of L'Aquila.

The tensile stress  $f_t$  was calculated by using the following equation:

$$f_t = \frac{2 P}{\pi b d} \quad (2.8)$$

By Eq.(2.8) one can compute the tensile strength when  $P = P_{max}$ .

Figure 2.56 shows the relation measured between the tensile stress  $f_t$  and the deflection  $\delta$  obtained for the unreinforced mortar specimens under Brazilian Tests (BT). Plots are referred to two tests. The mean value of the tensile strength is equal to 2.0 MPa. It is worth noting that the flexural strength computed in the 3PBT was equal to 2.9 MPa, which is 1.45 times higher than the tensile strength.

As already observed for the unreinforced specimens tested in 3PBT, one can observe an almost perfect brittle behavior after the achievement of the maximum tensile strength. Indeed,  $f_t$  suddenly drops after that point.

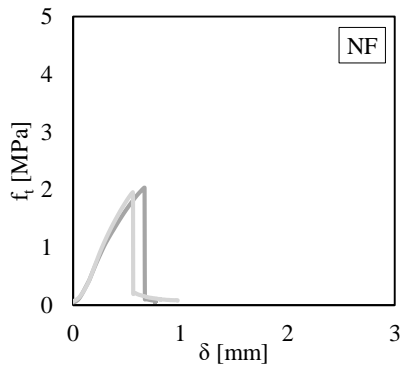
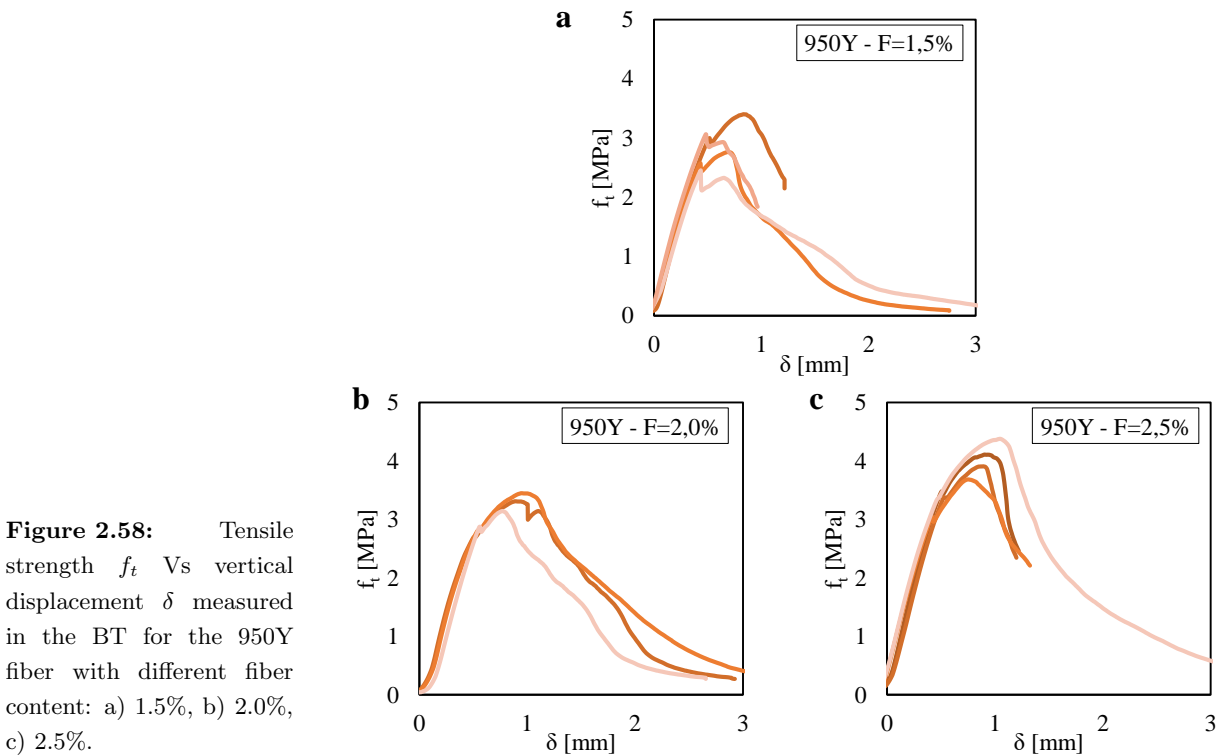
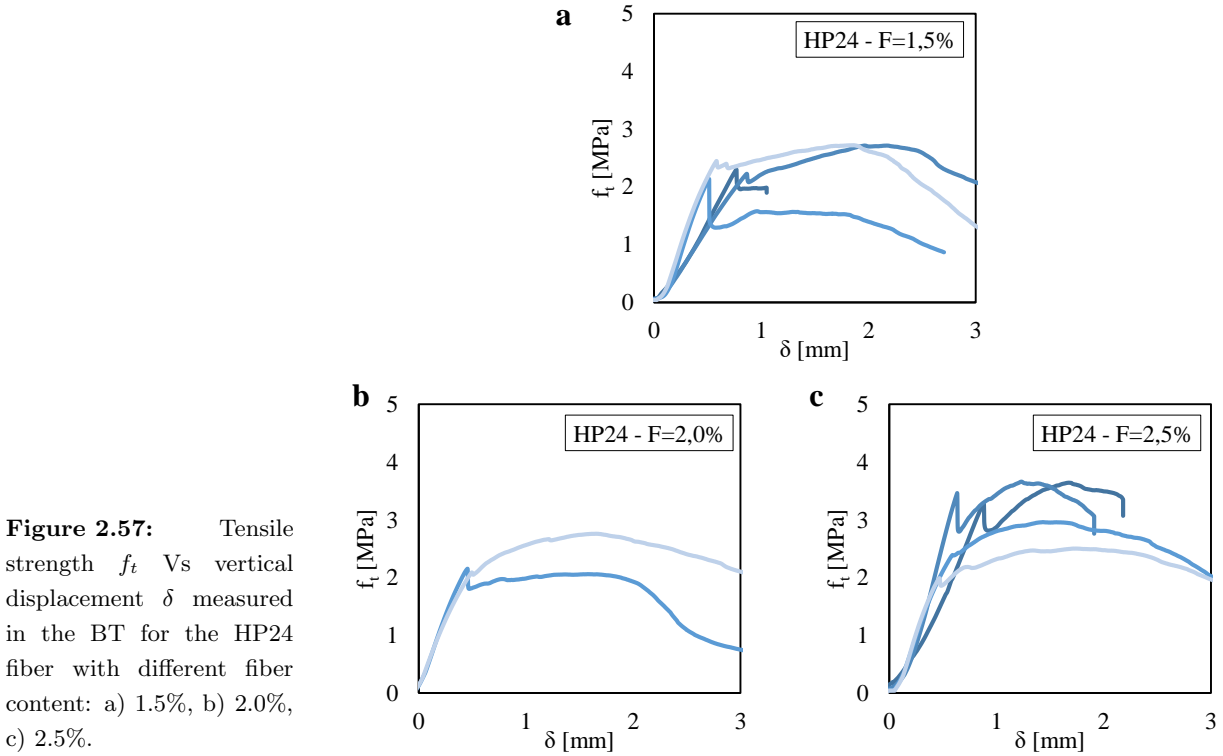


**Figure 2.56:** Tensile strength  $f_t$  Vs vertical displacement  $\delta$  measured in the BT for the unreinforced case (NF).

Figures 2.57 and 2.58 show the  $f_t$ - $\delta$  plots obtained for the fiber-reinforced mortar specimens tested under Brazilian Test (BT) by varying the fiber content therein the mortar matrix. Plots are referred to four tests for the case of fiber content  $F$  equal to 1.5% and 2.5%. Two tests are instead referred to the case of  $F = 2.0\%$ . In particular, Figure 2.57 shows the  $f_t$ - $\delta$  curves for the HP24 fiber, whereas Figure 2.58 shows that relation for the 950Y fiber.



For a better interpretation of the effect of both the fiber content and fiber type on the tensile behavior of the composite material, one can see Figure 2.59. In particular, that figure shows the variation of the tensile strength  $f_t$ , computed by using the equations Eq.(2.8) for  $P = P_{max}$ , as function of the fiber content.

One can see that higher values of tensile strength can be noted for the 950Y, as

compared to the HP24, for all the fiber content  $F$ . In particular, for the 950Y case, one can observe a gradual increase in the tensile strength up to achieve almost 4 MPa for  $F=2.5\%$ . It is worth noting that for the same fiber content, a flexural strength equal to 11.4 MPa (2.85 times the  $f_t$  value) was computed for the 3PBT. Instead, for the HP24 case, one can observe any differences in the tensile strength between the  $F=1.5\%$  and the  $F=2.0\%$  cases, in which  $f_t$  is equal to 2.5 MPa. Then, an increase in  $f_t$  is observed for  $F=2.5\%$ , in which  $f_t$  is equal to 3.2 MPa. By comparing that value with the flexural strength computed for the same fiber content ( $F=2.5\%$ ) one can see a high difference. Indeed,  $\sigma_f$  is 4.8 times the  $f_t$  value.

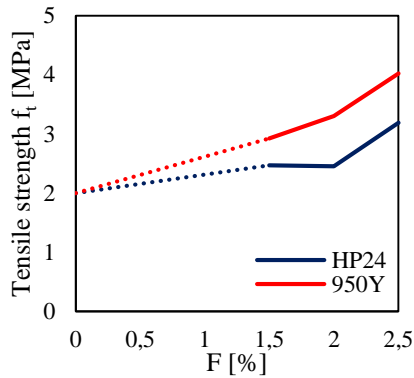


**Figure 2.59:** Tensile strength  $f_t$  measured in the BT for two fiber type (HP24 and 950Y) with different fiber content.

In general, from Figure 2.59 one can see the benefit of the fiber content on the tensile strength. It is worth noting that, the 950Y fiber type leads to the higher tensile strength though it was characterized by the lower fiber length and lower AR, as compared to the HP24 fiber. This may be due to the number of fibers that the 950Y fiber type ensured respect to the HP24 one, at the same fiber content. Indeed, a higher number of fibers lead to a higher compaction of the mortar matrix as well as a higher distribution of the fiber over the entire projected ligament area, where cracks develop.

In Table 2.12 are summarized the mean and standard deviation values of the tensile strength obtained for the Brazilian test (BT).

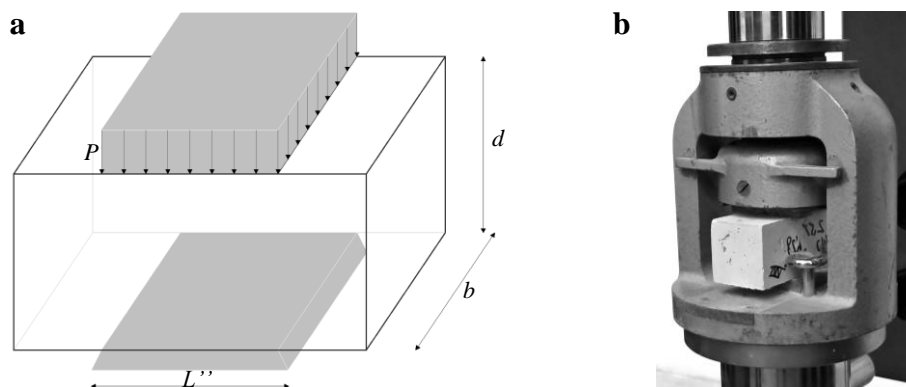
**Table 2.12:** Tensile strength of the specimens tested in Brazilian Test (BT) and reinforced by two type of short-fibers (950Y and HP24) with different fiber content.

Name	Fiber content	$f_t$ [MPa]
NF	0%	$2.0 \pm 0.1$
950Y	1.5%	$2.9 \pm 0.5$
950Y	2.0%	$3.3 \pm 0.2$
950Y	2.5%	$4.0 \pm 0.3$
HP24	1.5 %	$2.5 \pm 0.3$
HP24	2.0 %	$2.5 \pm 0.3$
HP24	2.5 %	$3.2 \pm 0.7$

### 2.2.2.4 Characterization of the compressive strength

To have a complete overview of the mechanical behavior of the fibrous lime mortar material, also the Compression Tests (CT) were carried out to obtain the compressive strength of the specimens. In particular, the tests were performed on 40 mm × 40 mm × 80 mm prismatic mortar specimens obtained from the two-half specimens tested in 3PBT. The distributed load  $P$  was applied on a squared area of 40 mm, while the specimens were placed on a squared area of 40 mm.

**Figure 2.60:** Scheme employed for the Compression Test (CT); b) Picture of the test carried out at the LPMS of L'Aquila.



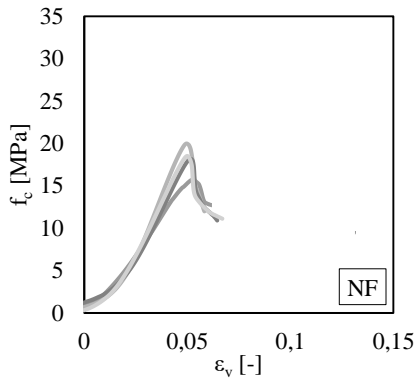
One can compute the compressive stress by using the following equation:

$$f_c = \frac{P}{b L''} \quad (2.9)$$

By Eq.(2.9) one can compute the compressive strength when  $P = P_{max}$ . Moreover, the vertical strain  $\varepsilon_v$  is computed by the following equation:

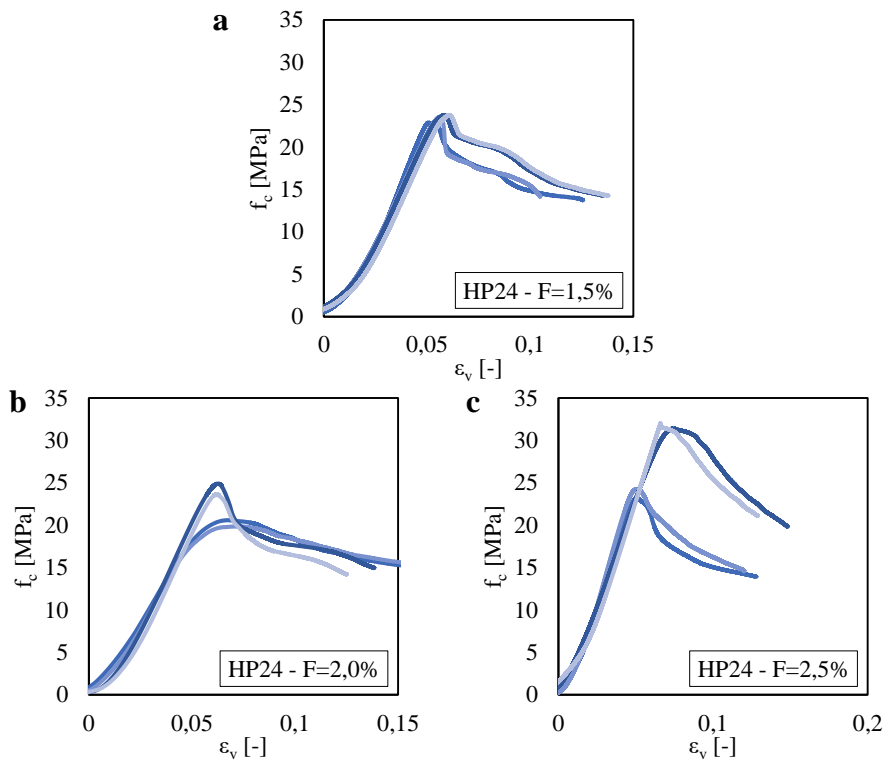
$$\varepsilon_v = \frac{\delta}{d} \quad (2.10)$$

Figure 2.61 shows the relation measured between the compressive stress  $f_c$  and the vertical strain  $\varepsilon_v$  obtained for the unreinforced mortar specimens under Compression Test (CT). Plots are referred to four tests. Each test was interrupted after the decay of 40% of the maximum load. One can compute a mean value of the compressive strength equal to 18.1 MPa. Moreover, one can observe a typical softening curve of quasi-brittle materials. Indeed, for all the curves one can see that the compressive stress suddenly drops after the achievement of the maximum stress.

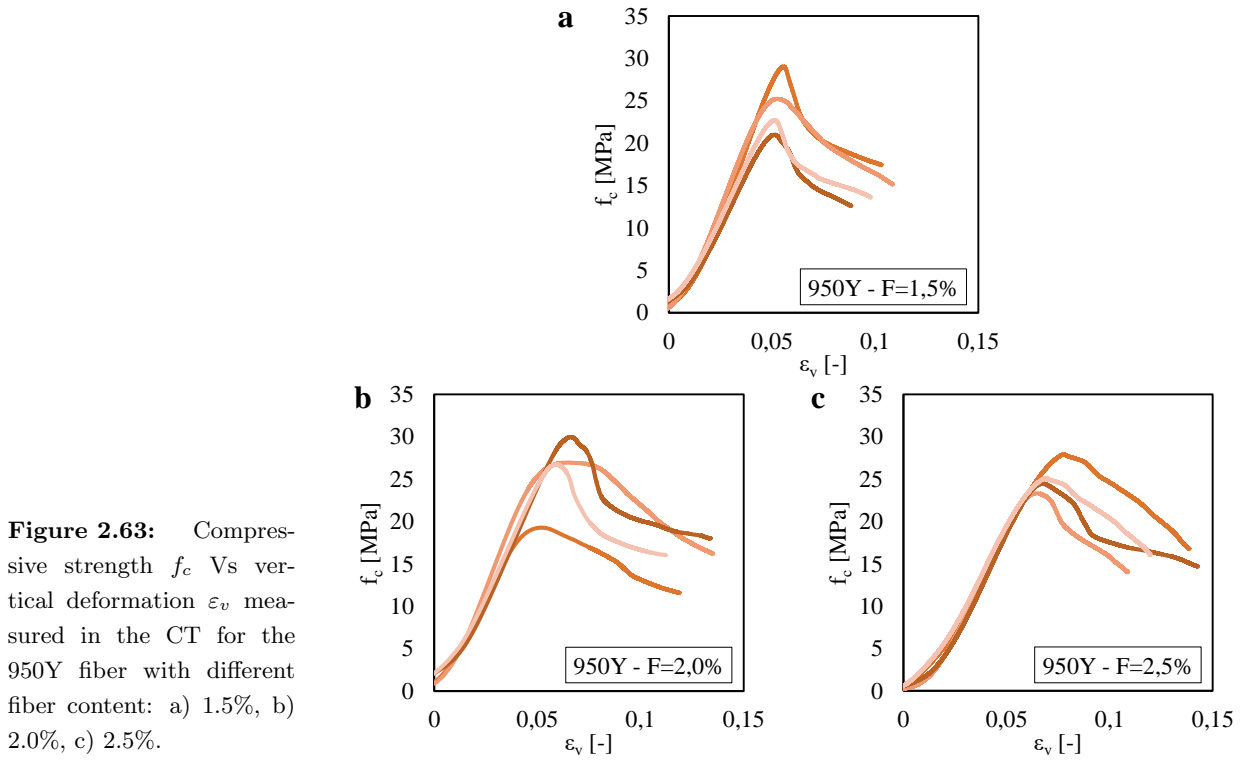


**Figure 2.61:** Compressive strength  $f_c$  Vs vertical deformation  $\varepsilon_v$  measured in the CT for the HP24 fiber with different fiber content: a) 1.5%, b) 2.0%, c) 2.5%.

Figures 2.62 and 2.63 show the  $f_c$ - $\varepsilon_v$  plots obtained for the fiber-reinforced mortar specimens tested under Compression Test (CT) by varying the fiber content therein the mortar matrix. All the plots are referred to four tests. In particular, Figure 2.62 shows the  $f_c$ - $\varepsilon_v$  curves for the HP24 fiber, whereas Figure 2.63 shows that relation for the 950Y fiber. In general, one can see from these results that the enhancement of the compressive strength due to both the fiber type and fiber content is more and more limited, as compared to the contribute offered by the fibers in the other mechanical properties. Furthermore, one can observe a large scattering of the results. In particular, except for the 950Y with  $F=2.0\%$ , an increase in the scattering of the results can be observed by increasing the fiber content. This trend was not in line with what was expected. Indeed, the higher fiber content would lead to a higher homogeneity of the product with a consequent decrease of the scatter of the results.



**Figure 2.62:** Compressive strength  $f_c$  Vs vertical deformation  $\varepsilon_v$  measured in the CT for the HP24 fiber with different fiber content: a) 1.5%, b) 2.0%, c) 2.5%.



For a better interpretation of the effect of both the fiber content and fiber type on the compressive behavior of the composite material, one can see Figure 2.64. In particular, that figure shows the variation of the compressive strength  $f_c$ , computed by using the equations Eq.(2.9) for  $P = P_{max}$ , as function of the fiber content.

As compared to the other results obtained for the 3PBT and the BT, the trends of the results obtained for the CT are less clear. Indeed, for the HP24 case one can see that, by increasing the fiber content from  $F = 1.5\%$  to  $F = 2.0\%$ , a reduction of the mean compressive strength is observed. The same unusual trend was also observed for the 950Y case by increasing the fiber content from  $F = 2.0\%$  to  $F = 2.5\%$ . However, from a general point of view, one can see a clear increase in the compressive strength of the fiber-reinforced mortar as compared to the unreinforced case.

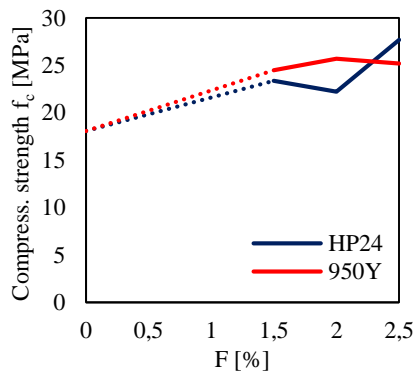


**Figure 2.64:** Compressive strength  $f_c$  measured in the CT for two fiber type (HP24 and 950Y) with different fiber content.

In Table 2.13 are summarized the mean and standard deviation values of the compressive strength obtained for the Compression test (CT).

**Table 2.13:** Compressive strength of the specimens tested in Compression Test (CT) and reinforced by two type of short-fibers (950Y and HP24) with different fiber content.

Name	Fiber content	$f_c$ [MPa]
NF	0%	$18.1 \pm 2.4$
950Y	1.5%	$24.5 \pm 3.5$
950Y	2.0%	$25.7 \pm 6.4$
950Y	2.5%	$25.2 \pm 1.9$
HP24	1.5 %	$23.4 \pm 0.5$
HP24	2.0 %	$22.2 \pm 2.4$
HP24	2.5 %	$27.7 \pm 4.5$

### 2.2.2.5 Comparison of the mechanical properties

A final comparison of the results obtained by the three-point bending test (3PBT), Brazilian test (BT), and compression test (CT) is proposed in Figure 2.65a – d. In particular, that figure shows the increase (in percentage) in the flexural strength  $\sigma_f$ , fracture energy  $G_f$ , tensile strength  $f_t$  and compressive strength  $f_c$ , as compared to the unreinforced case. One can see that the best benefit in introducing fiber therein the mortar matrix is observed in terms of the fracture energy (up to almost 2500% for the HP24 case and 1000% for the 950Y case). Excellent increase in the flexural strength can be also noted (up to almost 450% for the HP24 case and 300% for the 950Y case). As compared to the other mechanical properties, a lower increase in the tensile strength and especially in the compressive strength can be observed (less than 100% for all the cases).

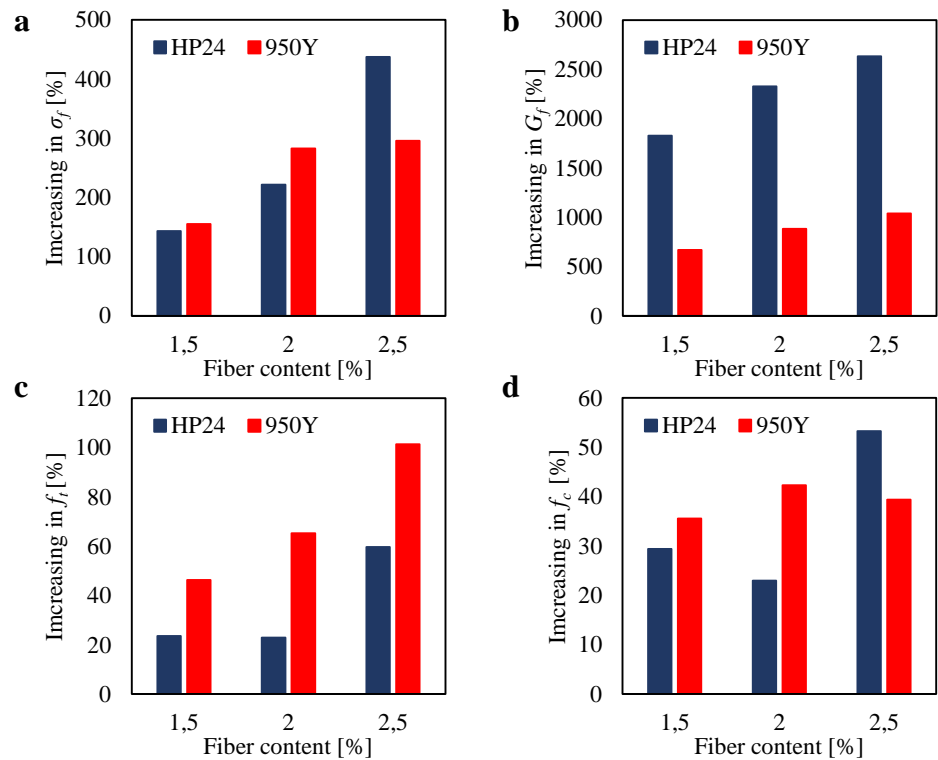


**Figure 2.65:** Increasing of the mechanical properties (flexural strength  $\sigma_f$ , fracture energy  $G_f$ , tensile strength  $f_t$  and compressive strength  $f_c$ ) respect to the unreinforced case by varying the fiber content. Figure also shows the comparison between the two fiber type (the HP24 and the 950Y).

Details of the damage that occurred at the end of the experimental tests are illustrated in Figures 2.66a–d. In particular, in Figure 2.65a one can see the fiber-reinforced mortar specimen after at the end of the 3PBT. From that picture is clear the distribution of the fibers through the mortar matrix. Figure 2.65b shows the cracking on three different specimens at the end of the 3PBT. In particular one can see that the geometry of the fiber influences the cracks propagation. Indeed, the fracture is more and more localized for the 950Y fiber, which is characterized by lower length and aspect ratio values, as compared to the HP24 one. Finally, Figures 2.65c, d show the damaged specimen at the end of the CT.

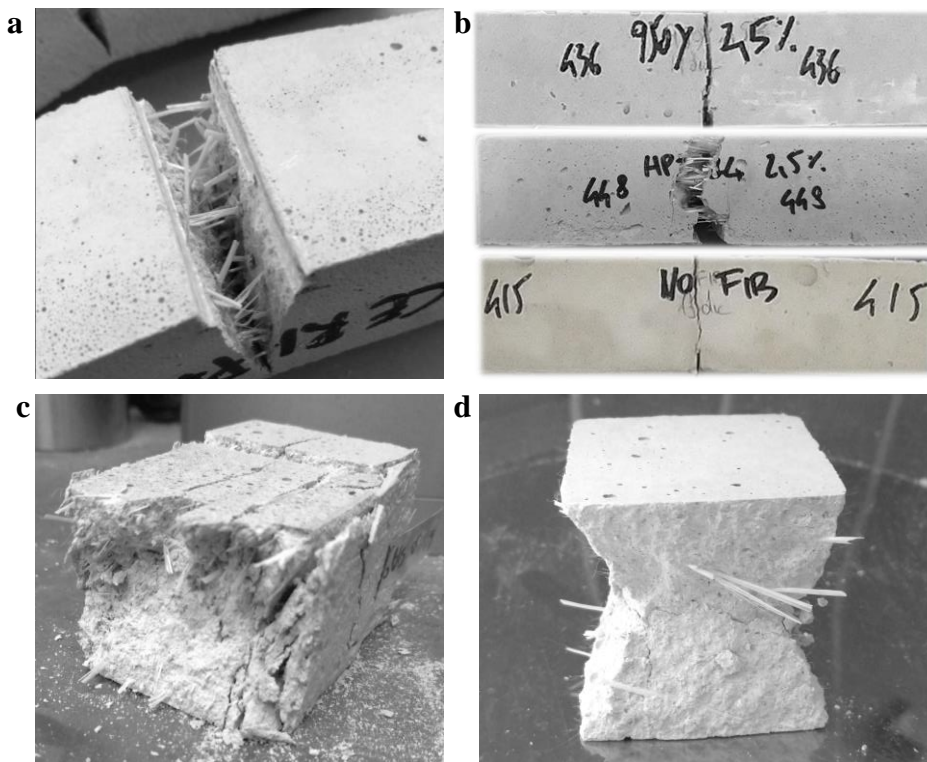


**Figure 2.66:** a) Fiber-reinforced mortar specimen after the 3PBT; b) Cracking propagation on some specimens at the end of the 3PBT; c,d) failure of the fiber-reinforced specimen after the execution of the CT.

### 2.3 Chapter conclusions

The FRCM system for the enhancement of the shear strength of the masonry wall was first investigated in this Chapter. The FRCM system consisted of the application of a layer of lime-based mortar as a coating to the masonry surface. That mortar was reinforced by a glass fiber grid embedded into the mortar matrix.

In particular, the experimental campaign consisted of diagonal compression tests carried out on both the unreinforced stone masonry specimens and the reinforced ones. Results were discussed in terms of the mechanical properties and fracture propagation. The experimental tests were conducted both in situ and at the laboratory LPMS of L'Aquila. In the first case, the stone masonry samples were isolated from the walls of the historical municipal office "Margherita Palace" of L'Aquila, whereas, in the second case, the masonry samples were prepared according to the ancient constructive technique featured in most of the historic buildings of the city of L'Aquila; the stone elements were taken from the debris of buildings collapsed during L'Aquila 2009 earthquake and the mortar were characterized by a very friable behavior and a low compressive strength of about 2 MPa, as observed in the existing cases.

As far as the unreinforced masonry panels are concerned, the average shear strength  $\tau_0$  was equal to 0.118 MPa (standard deviation  $\delta = 0.015$  MPa) and 0.137 MPa ( $\delta = 0.005$  MPa), for the specimens isolated from an existing building and the one built in the laboratory, respectively. On the other hand, the average shear modulus  $G$  was equal to 67 MPa ( $\delta = 5$  MPa) and 131 MPa ( $\delta = 8$  MPa) for the existing walls and the lab ones, respectively. Hence, one can observe that results obtained for the specimens built in the laboratory were characterized by slightly higher mechanical properties as well as a lower scattering of the data, especially in terms of  $G$ . The value of the dispersion of the results can be considered a small amount bearing in mind the heterogeneous character and the quasi-brittle behavior of this material.

As far as the reinforced masonry panels are concerned, the average shear strength  $\tau_0$  was equal to 0.331 MPa ( $\delta = 0.05$  MPa) and 0.583 MPa ( $\delta = 0.10$  MPa) for the existing walls and the lab ones, respectively. On the other hand, the average shear modulus  $G$  was equal to 168 MPa ( $\delta = 35$  MPa) and 806 MPa ( $\delta = 328$  MPa) for the existing walls and the lab ones, respectively. Hence, the FRCM system leads to an increase of the shear strength of about 180% and 320% of the original walls of Palazzo Margherita and the lab specimens, respectively.

Results highlighted that the higher mechanical properties were obtained for the specimens prepared at the laboratory rather than the ones isolated from the existing building. This is negligible for the unreinforced case but significant for

the reinforced case.

The difference between the in-situ and lab results mainly depends on the different masonry sample thicknesses of these cases. Indeed, the panels built at the laboratory measured about 340 mm in thickness, whereas the existing ones measured from 500 mm to 750 mm in thickness. By assuming the same thickness of the reinforcing mortar layer, the higher the specimen thickness, the higher the efficiency on the mechanical property of the reinforcing system. Furthermore, the other difference between in-situ and laboratory tests concerned the loading protocol. Indeed, the in situ tests were conducted by cyclic loads, whereas the lab tests were conducted by monotonic loads. This would affect the accuracy of the results.

A key aspect of the experimental campaign conducted in situ highlighted the propensity of the historical walls of stones to modify their mechanical behavior during the loading history applied. In particular, it was shown that the shear modulus and the shear strain of the unreinforced panels are strongly reduced even for a low value of the load. This reduction (especially for the shear modulus) is less evident for the masonry reinforced by FRCM.

The damage mode observed during the experiments showed that the FRCM jacket ensured excellent levels of adhesion with the masonry substrate. This result was mainly due to the interlocking between materials. Indeed, for stone masonry structures, one can observe the high roughness level of the masonry surface that enhances the bond behavior at the masonry – reinforcing mortar interface. Moreover, at the end of the tests, it was observed that the glass fiber strands, embedded into the reinforced mortar layer, were undamaged along the direction of the cracks occurred on the reinforcing mortar layer as well as perfectly embedded within the mortar matrix.

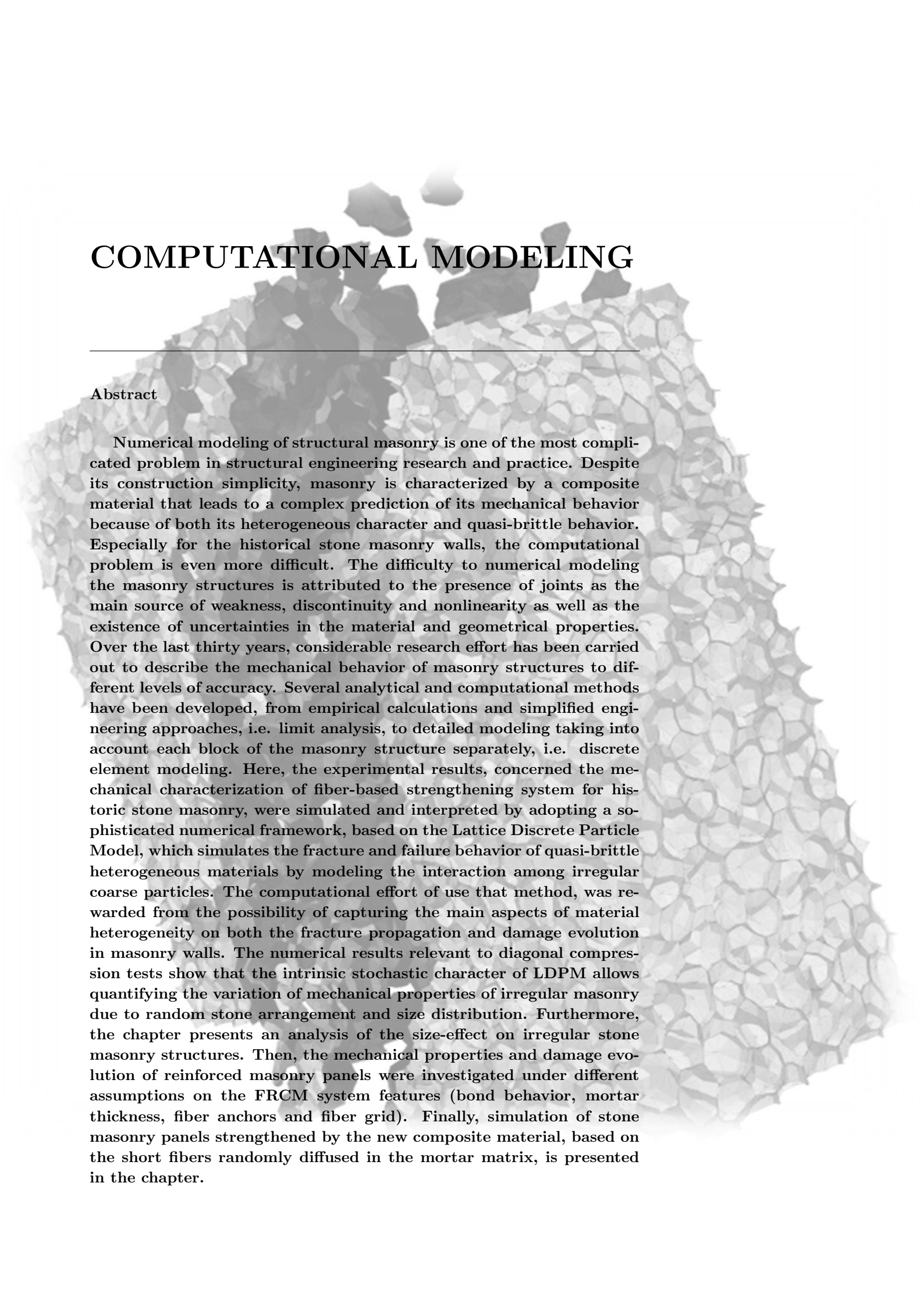
In general, the results of the experimental campaign conducted on the FRCM showed that that reinforcement system is effective in improving the in-plane mechanical behavior of the stone masonries in terms of: tensile strength, stiffness, and ductility. Moreover, it was highlighted that the panels prepared at the laboratory lead to proper identification of both the mechanical properties and damage propagation. This result can encourage the experimental campaign carried out on lab specimens, at the condition that they are strictly built in line with features of the existing buildings.

As far as the lime-based mortar samples reinforced by short fibers are concerned, experimental results showed that the contribution of diffuse short fibers greatly increased the mechanical properties of the lime-mortar. In particular, the fracture energy was the mechanical property that most benefited from the use of short fibers up to about 2500%, as compared to the unreinforced case. Then, the maximum increase in the flexural strength was about 450%. The maximum

increment of the tensile strength values was about 100%. Finally, the mechanical property less affected by the fiber contribution was the compressive strength. In this case, the maximum increase was about 50%.

Since that the fiber strands used in the FRCM system have only the function to carry tensile stresses and not to improve the tensile strength of the masonry specimens, the results obtained for the new composite material are important. Indeed, that material can significantly increase both the strength and ductility of the masonry specimens. Moreover, the enhancement in the mechanical properties due to the FRCM system is strongly related to the direction of the applied force, in contrast to the reinforcing composite material developed in this thesis.

# COMPUTATIONAL MODELING



---

## Abstract

Numerical modeling of structural masonry is one of the most complicated problem in structural engineering research and practice. Despite its construction simplicity, masonry is characterized by a composite material that leads to a complex prediction of its mechanical behavior because of both its heterogeneous character and quasi-brittle behavior. Especially for the historical stone masonry walls, the computational problem is even more difficult. The difficulty to numerical modeling the masonry structures is attributed to the presence of joints as the main source of weakness, discontinuity and nonlinearity as well as the existence of uncertainties in the material and geometrical properties. Over the last thirty years, considerable research effort has been carried out to describe the mechanical behavior of masonry structures to different levels of accuracy. Several analytical and computational methods have been developed, from empirical calculations and simplified engineering approaches, i.e. limit analysis, to detailed modeling taking into account each block of the masonry structure separately, i.e. discrete element modeling. Here, the experimental results, concerned the mechanical characterization of fiber-based strengthening system for historic stone masonry, were simulated and interpreted by adopting a sophisticated numerical framework, based on the Lattice Discrete Particle Model, which simulates the fracture and failure behavior of quasi-brittle heterogeneous materials by modeling the interaction among irregular coarse particles. The computational effort of use that method, was rewarded from the possibility of capturing the main aspects of material heterogeneity on both the fracture propagation and damage evolution in masonry walls. The numerical results relevant to diagonal compression tests show that the intrinsic stochastic character of LDPM allows quantifying the variation of mechanical properties of irregular masonry due to random stone arrangement and size distribution. Furthermore, the chapter presents an analysis of the size-effect on irregular stone masonry structures. Then, the mechanical properties and damage evolution of reinforced masonry panels were investigated under different assumptions on the FRCC system features (bond behavior, mortar thickness, fiber anchors and fiber grid). Finally, simulation of stone masonry panels strengthened by the new composite material, based on the short fibers randomly diffused in the mortar matrix, is presented in the chapter.



# Computational modeling

---

## Abstract in italiano

La modellazione numerica delle strutture murarie è uno dei problemi più complicati nel campo della ricerca e della pratica ingegneristica. Questa complessità è attribuita ad un grande numero di fattori quali la distribuzione e posizione delle unità murarie (pietre e/o mattoni), l'irregolarità dei giunti di malta e la variabilità delle proprietà dei materiali costituenti. Tali fattori sono tutti più o meno dipendenti anche dalla modalità e/o qualità di lavorazione del manufatto. Nonostante la sua semplicità costruttiva, la struttura muraria è caratterizzata, quindi, da un materiale composito che porta ad una previsione complessa del suo comportamento meccanico. Soprattutto per le murature storiche di pietrame, in cui il livello di irregolarità degli elementi amplifica notevolmente la variabilità del suo comportamento meccanico, la modellazione è una problematica ancora più ardua da affrontare. In questo capitolo, i risultati sperimentali riguardanti la caratterizzazione meccanica delle murature aquilane sono utilizzati per la calibrazione e la validazione di un sofisticato modello computazionale, il Lattice Discrete Particle Model. LDPM può rappresentare le unità di pietra come celle irregolari che interagiscono tra loro mediante opportune leggi costitutive. LDPM è stato originariamente formulato e validato per il calcestruzzo, ed è proposto in questa ricerca, per la prima volta, nella simulazione delle murature di pietrame irregolare. Lo sforzo computazionale nell'utilizzo di tale metodo è stato premiato dalla possibilità di catturare gli aspetti principali della eterogeneità del materiale sia in termini di proprietà meccaniche e sia di propagazione della frattura. Nel capitolo, i test sperimentali eseguiti sui pannelli rinforzati con sistema FRCM sono stati simulati in LDPM e ampiamente discussi, offrendo una migliore comprensione del comportamento meccanico del sistema strutturale composito. Infine, LDPM è stato utilizzato anche per la riproduzione dei test sperimentali eseguiti sull'innovativa malta fibrosa, permettendo così una predizione del comportamento meccanico di maschi murari rinforzati con tale sistema. I risultati hanno messo in luce le principali caratteristiche del nuovo sistema di rinforzo.

### 3.1 Overview of the modeling technique employed for stone masonries

Nowadays, there is an increased interest in developing reliable computational models and techniques for the assessment and rehabilitation of masonry structures. This is primarily due to the growing demand to protect heritage structures around the world, the majority of which are made mostly of masonry materials. This growing demand for heritage protection reflects humanity's deepening awareness and realization of the necessity and the responsibility to maintain the existing architectural heritage and to pass it on to future generations [132].

The study of historic masonry structures is a challenging task due to the difficulties encountered in the description of the complex geometry, morphology, material heterogeneity, material properties characterization, material variation due to weathering and deterioration effects, and complex loading conditions. Historic masonry structures such as castles, churches, lighthouses, mosques, arch bridges, etc. are composed of masonry units, such as bricks or stones, with or without mortar. Despite its construction simplicity, masonry is characterized by an anisotropic and composite material that leads to a complex prediction of its mechanical behavior. Indeed, for low-stress levels, masonry behaves can be assumed as a linear elastic material, whereas its behavior becomes more and more non-linear as the load applied on it increases.

Modeling old and deteriorated masonry structures involves special considerations and a design philosophy different from that followed for other materials. Analysis and design of old and deteriorated masonry structures must be achieved with little specific data and the awareness that deformability and strength properties of both units and mortar may vary considerably. For example, it is practically impossible to obtain complete data of boundary stresses for each individual element of an old masonry structure or it is impossible to measure accurately the strength of each mortar joint. Hence, it would be appropriate to validate these models by laboratory or in situ tests. Once the behavior of the system is understood and the results are validated, then it is possible to develop simple idealizations for the predictive response of more complicated structures.

The use of sophisticated methods of analysis and computational models may require material parameters that are difficult to be obtained from experimental tests: some of these material parameters may have only a mathematical significance and the modeler's experience it is necessary in such cases.

Numerical models must take into account (a) the behavior of masonry units (i.e. stones and bricks), and (b) the behavior of the joint material (i.e. mortar).

In the case of ancient masonry structures, the numerical model should be able to take into account large deformations as well as the complicated rocking and sliding of the individual blocks, which may arise, over the centuries, as the aftermath of dynamic loadings, such as earthquake excitations.

In the literature, there are extensive researches on the numerical modeling and analysis of masonry structures with their particular advantages and limitations in terms of their representativeness, computer efficiency, and applicability [133, 132]. The different analytical procedures could be summarized into two distinct categories based on the level of details adopted to represent material heterogeneity: (i) the macro-modeling and (ii) the micro-modeling.

Here, a new approach based on the meso-scale is presented for the mechanical characterization of the stone masonry. In particular, meso-scale is relevant to the characterization of heterogeneous material as two-phase material: mortar and irregular coarse particles (i.e. the stones).

### 3.1.1 The macro-modeling

In the macro-modeling strategy [134, 135, 136, 137], the masonry element can be represented by using a continuum homogenized model, usually, therein the finite element method, whereas the effects of mortar joints are implicitly considered. Hence, by the macro-modeling the masonry is considered as one-phase material. Units, mortar, and the unit–mortar interface are smeared out in a homogeneous continuum. In other words, with the macro-modeling approach, there is no distinction between individual masonry units and the mortar joints. Masonry is considered as a homogeneous isotropic or anisotropic composite such that the joints and any cracks are smeared out in the continuum. Although this approach is very attractive for large-scale masonry structures, because of the reduced time and memory requirements as well as user-friendly mesh generation, it is not suitable for the detailed stress analysis of small masonry panels, due to the difficulty of capturing all its expected failure mechanisms. The influence of existing mortar joints as the major source of weakness and nonlinearity cannot be addressed using this strategy. Moreover, it is shown that the modeling methods and the parameters must be carefully chosen [132].

Among the possible modeling strategies proposed in literature and codes, the frame modeling strategy considers the wall as an idealized frame, in which each resistant masonry wall is subdivided into a set of deformable and rigid portions of the masonry panels. In particular, the deformation and the nonlinear behavior are concentrated in the deformable portions, whereas the rigid portions have the function to connect the deformable ones. Focusing on the in-plane response of the masonry walls with openings, usually two main structural components may be identified: piers and spandrels. The damage observation during seismic events showed that cracks and failure modes are mainly concentrated in such elements. Piers are the main vertical resistant elements carrying both vertical and lateral loads, whereas spandrel elements are the horizontal elements which couple the response of adjacent piers in the case of lateral loads. Though spandrel can be defined as secondary elements, they significantly affect the boundary conditions of piers with significant influence on the wall lateral capacity. This approach requires a limited number of degrees of freedom, with a reasonable the computational effort, allowing the analysis of complex models of masonry structures. Several applications on the frame modeling may be found in the literature, such as [138, 139, 140].

Among the Macro-Modeling approach, it is worth noting the discrete-element model developed by Calì [141, 3, 142] for the simulation of the nonlinear seismic behavior of masonry buildings (see Figure 3.1). The basic idea of that approach is

to approximate the in-plane nonlinear response of masonry walls by an equivalent discrete element using the concept of macro-element discretization. The equivalent macro-element is modeled by using an articulated quadrilateral with surrounding rigid edges. In particular, two internal diagonal springs are utilized to simulate the shear behavior of masonry. The flexural and sliding shear behavior is also simulated by discrete distributions of springs in the sides of the quadrilateral that preside over the interaction with the adjacent macro-elements. Figure 3.1 shows a portion of the masonry wall modeled as a mesh of panel elements in the deformed configuration with the representation of: the orthogonal springs for the simulation of the flexural behavior; the transversal and diagonal springs for the simulation of shear and torsional behavior. The reliability of the approach was evaluated by means of nonlinear incremental static analyses performed on unreinforced masonry structures. The load-displacement curves and failure patterns obtained from the analyses showed a fairly good agreement with the experimental results in terms of the cyclic response, stiffness, strength and dissipative behavior, as well as damage distribution.

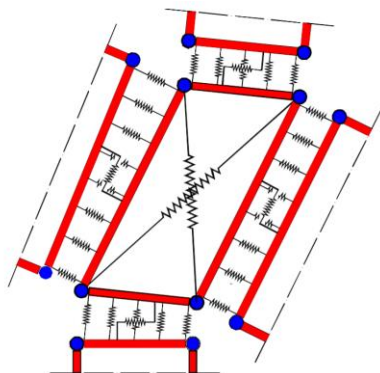


**Figure 3.1:** The discrete-element model therein the Macro-Modeling approach developed by Caliò [3].

Another discrete-element model therein the Macro-Modeling approach was developed by Casolo [4] (see Figure 3.2). In that model, the heterogeneous solid material is modeled by rigid masses connected by elastic-plastic springs. The unit cells are defined by four mass elements connected to each other by two normal springs plus one shear spring at each side. This unit cell is a discrete mechanism that approximates the macroscopic behavior of the heterogeneous masonry material. This model can account for some micro-structure features of the composite material, while it was designed to work at the macro-scale. The discrete element size should be equal or larger than the representative volume element of the masonry. The elastic characteristics of the springs are defined by a specific procedure of identification with the objective to transfer some characteristics of the internal texture to the macro-scale model. Figure 3.1 shows a couple of rigid elements subjected to horizontal (Figure 3.1a) and vertical axial loading (Figure 3.1b), and assemblage of four rigid elements subjected to shear loading (Figure 3.1c).

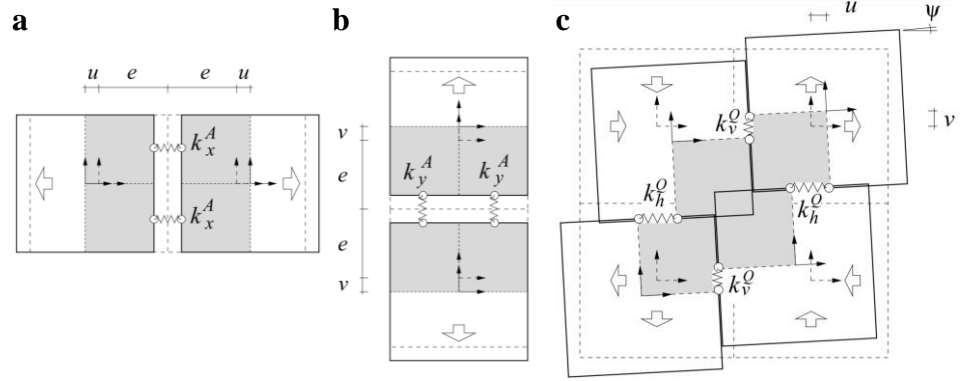


**Figure 3.2:** The discrete-element model therein the Macro-Modeling approach developed by Casolo [4].

Previous researches also showed that the response of masonry structures up to failure can be successfully modeled using techniques applied to concrete because both are characterized by brittle behavior [143, 144, 145]. In particular, the heterogeneous masonry material can be substituted with an equivalent homogeneous material [135, 136, 137] by employing a smeared crack approach, in which the process of cracking is obtained by “smearing” the damage on the adjacent finite element, introducing a degradation of the relevant mechanical properties [146]. Since smeared crack modeling approaches do not require remeshing of the FE model after the occurrence of cracks or the a priori definition of possible locations of cracks, they have been widely used in FE modeling [147]. The smeared crack models are practice-oriented due to the limited data required in the input and, for example, are successfully adopted for brick masonry and adobe walls [148, 149] and debonding problems [147, 150, 151]. An example of a Finite Element (FE) macro-model with a smearing approach of an existing historical stone building, the municipal seat called “Palazzo Margherita” [5] (the features of the building are described in Section 2.1.1), can be observed in Figure 3.3. In that figure is also possible to observe the cracking pattern on the masonry walls obtained in the pushover analysis. In particular, the cracking pattern is expressed in terms of Gauss point-occurrence, indicating whether a tension cut-off limit is exceeded at an integration point. When the stress limit is exceeded at a given integration point, this point is marked with a color in the model view, with the indication of the actual stress reached in that position. After the occurrence of the crack, the stress of the integration point tends to decrease, more or less quickly based on the softening behavior used for the material to characterize the tensile behavior, up to arrive to 0 MPa, when that Gauss point does not contribute anymore for the material resistance.

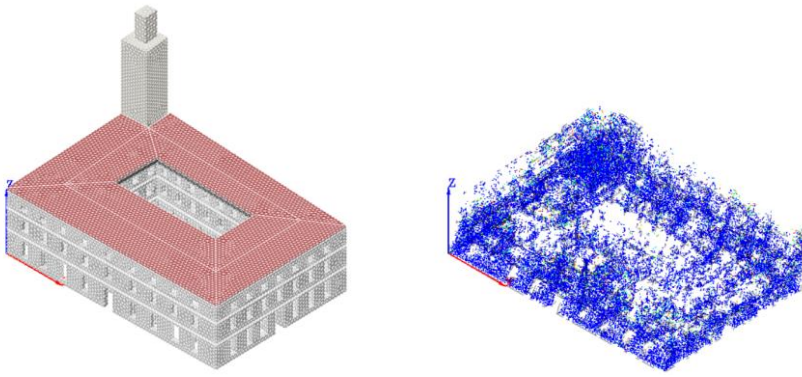
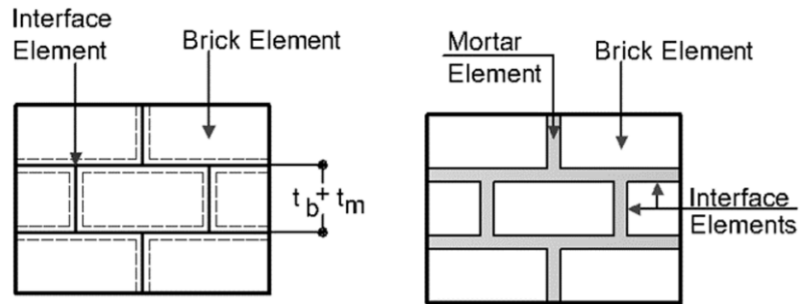


**Figure 3.3:** The FEM macro-model model of an existing historical stone building, the municipal seat called “Palazzo Margherita” [5]. On the left, the cracking pattern on the masonry walls obtained in the pushover analysis.

### 3.1.2 The micro-modeling

The micro-modeling approach [152, 153, 154, 155], can be divided into two distinct subcategories based on the level of details adopted to represent material heterogeneity: the simplified micro-modeling and the detailed micro-modeling. Figure 3.4 shows both the modeling criteria.

**Figure 3.4:** Simplified micro-modeling (two-phase material) and detailed micro-modeling (three-phase material).



#### 3.1.2.1 The simplified micro-modeling

In the simplified micro-modeling, the masonry is modeled as two-phase material. In this approach, the discontinuous masonry is represented as an assemblage of discrete units. The discontinuities are treated as boundary conditions between masonry units (e.g. bricks or stone blocks). In other words, the joints are modeled as interfaces between distinct units, while the units are slightly expanded in size in order to keep the masonry geometry unchanged. Hence, the mortar joint can be modeled as an interface with zero thickness. The stiffness of the interface is deduced from the stiffness of the real joints. According to this procedure, the properties of the mortar and the unit/mortar interface are lumped into a common element, while expanded elements are used to represent the brick units (see Figure 3.4a). Definitely, in this approach, it is possible to simulate masonry as a set of elastic and inelastic blocks bonded together by potential fracture slip lines at the joints. This approach leads to a reduction of the computational effort and yields a model that is applicable to a wider range of structures. The limitation of the simplified micro-modeling approach is that the numerical problem is anyhow complex for huge structures. Furthermore, the drawback of the simplified micro-modeling approach is that the accuracy is lost to some extent, since the real joints are lumped into zero-thickness interfaces. Hence, Poisson's effect on the mortar joints is ignored. In order to overcome the drawback, the brick model should incorporate the compressive failure of masonry, which actually involves the interactive effects of both bricks and mortar, simultaneously.

Several researches can be found in literature on the limit analysis for the assessment of masonry structures [156, 157, 158].

### 3.1.2.2 The detailed micro-modeling

Finally, in the detailed micro-modeling the masonry is modeled as three-phase material (see Figure 3.4b). This strategy is the most accurate approach to simulate the real behavior of structural masonry because both the masonry units and mortar joints are represented by continuum elements whereas the unit–mortar interface is represented by discontinuous elements accounting for potential crack or slip planes. While this modeling leads to more accurate results, the level of refinement means that the corresponding analysis is computationally intensive, limiting its application to small scale laboratory specimens, structural details, and research purposes. It is worth noting that researchers proposed simplified micro-modeling procedures to overcome this problem [159, 160].

### 3.1.2.3 General discussion

The technical literature features various approaches for the numerical simulation of masonry structures, each of which has advantages and limitations in terms of their accuracy, computational efficiency, and applicability [133]. Among these, the Finite Element (FE) method is one of the most used approaches to model masonry structures, and can be used at the macroscale [134, 135, 137, 161] or at the microscale [152, 153, 154, 155] depending upon the level of details adopted to represent material heterogeneity. However, the FE approach, strictly based on continuum mechanics, presents significant limitations to simulate strong discontinuities between different blocks in irregular stone masonry. Moreover, continuum-based models, which homogenize material behavior [162], are inherently limited in capturing fracture propagation and damage evolution of quasi-brittle materials.

In most of the case, the FE model appears to be inadequate to accurately predict the complex mechanical behavior of stone masonries. This is true especially in the simulation of small masonry panels with sophisticated boundary conditions.

Additionally, the simulated structure is highly dependent on the mesh [163] which is hardly captured through smeared crack approaches. The problem consists of simulating the real morphology of stone masonries and even though sophisticated methods exist to model accurately the facade texture of such structures [164], they still present strong limitations in representing the stone texture of the inner core.

As an alternative to FE approaches, some authors [165, 166, 167] adopted the Discrete Element Method (DEM) to model heterogeneity through the interaction of distinct blocks. For the case of masonry characterized by strong stone units and weak mortar, such as the historical stone masonry investigated in this work, a recent study [168] demonstrated the applicability of the DEM. Nevertheless,

DEM would be less effective in cases where the weaker component is the units (constructions made of tuff blocks). However, existing DEM formulations (1) do not link the particle size to the actual size of the masonry units; (2) often suffer from issues associated with excessive rotations; and (3) have unsophisticated particle interaction laws. Nevertheless, DEM would be less effective in cases where the weaker component is the units (constructions made of tuff blocks) [168].

Recent studies (e.g. [169]) have widely recognized that many macroscopic phenomena originate from the mechanics of the underlying micro-structure due to the size, shape, spatial distribution, and properties of the constituents.

The modeling fracture process in quasi-brittle materials is challenging due to the heterogeneity of the material [170]. Both the failure mechanism and the mechanical response of masonry structures may change significantly depending on its internal particle distribution.

For quasi-brittle materials, such as the masonry (especially the historical one), failure is often caused by nonlinear phenomena, such as fracture, damage localization, and frictional shearing, occurring at weak locations in the internal material structure. These weak locations coincide, for example, with interfaces among particles, weak matrix layers in composites with hard inclusions and compliant interfaces between stiff material grains, and they are typically characterized by a specific geometry and well determined orientations. Due to this peculiarity, classical tensorial constitutive equations typically fail to provide a satisfactory representation of the mechanical behavior of these materials especially if failure mechanisms are associated with strain-softening [171].

The heterogeneous character of stone masonry, the chaotic distribution of stone units into the mortar matrix, and the variability of their mechanical properties contribute to a substantial scatter in the mechanical response of masonry leading to a complicated reliable prediction, especially when masonry is coupled with a complex strengthening system. A purely experimental analysis requires performing a large number of experimental tests because of this scatter, which is prohibitive in practice due to time and cost considerations. For this reason, a dedicated numerical approach is essential to support the experiments.

Hence, a novel meso-scale model that is formulated within the framework of discrete models, the so-called Lattice Discrete Particle Model (LDPM), was proposed in this research for a reliable investigation of both the historical stone masonry and the fibrous mortar as well as their coupling. The intrinsic stochastic feature of the LDPM, which simulate units randomly placed into a considered volume as irregular particles interacting with each other, allows quantifying the variation of the mechanical properties of both the stone masonry and mortar materials due to the random particle size and distribution.

## 3.2 The Lattice Discrete Particle Model

The heterogeneous character of composite materials, such as stone masonries, has a fundamental relevance for the description of strain localization, crack initiation, and crack propagation, which in turn strongly influence the ultimate failure mode of a structural system. For this reason, a dedicated numerical approach was essential.

Here, a meso-scale model [172, 173, 174], the so-called Lattice Discrete Particle Model (LDPM) [175, 176], is described.

The Lattice Discrete Particle Model is a novel analytical approach formulated within the framework of discrete models, which enable capturing the main aspects of material heterogeneity on both the fracture propagation and damage evolution.

It was originally developed for the simulation of concrete and, in general, showed an excellent capacity to characterize all granular materials, such as composite laminates, ceramics, gravels, and soils (e.g. [177, 178, 179, 180]). Other researches highlighted the capabilities of the LDPM also in the investigation of fibers [181, 182, 183, 184], and multi-physics phenomena such as aging, the Alkali-Silica Reaction (ASR) [185, 186, 187, 188] or hygro-thermal and chemical processes [189, 190, 191, 192, 193, 194]. The constitutive equations of these studies were incorporated in the LDPM code.

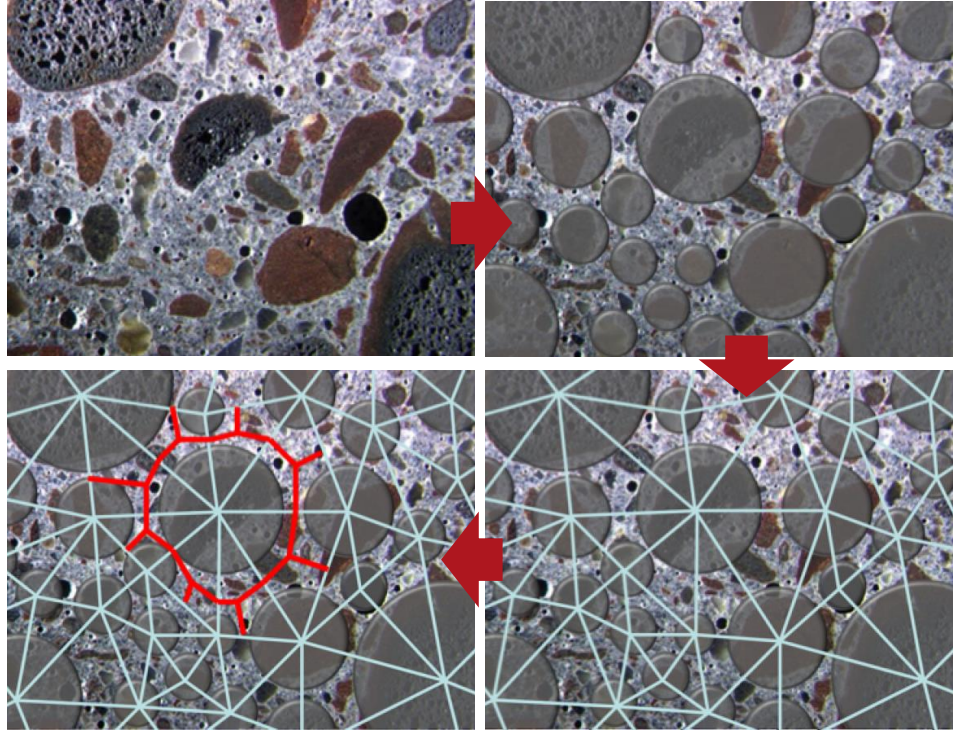
The premise of the LDPM formulation is that most materials are not homogeneous when considered at a sufficiently small dimensional scale (micro- and meso-scale).

The LDPM has been extensively calibrated and validated with a comparison to a large variety to experimental data under both quasi-static and dynamic loading conditions: its unique capability of predicting stress-strain curve and failure modes for concrete and other quasi-brittle material is due to the simulation of compressive failure through tensile and shearing softening at the meso-scale, without postulating the existence of softening in compression.

The LDPM simulates quasi-brittle materials at the length scale of coarse material heterogeneity. In particular, for concrete material, the LDPM can represent the coarse aggregates by irregular cells interacting with each other through appropriate constitutive equations. These cells are randomly placed into a given volume according to a specific granulometric distribution. This feature allows to statistically reproduce the mechanical property variations of stone masonry panels due to the particle size distribution.

In Figure 3.5 one can see the LDPM procedure for the simulation of the concrete at the length scale of coarse material heterogeneity, as better described in the follows (Section 3.2.1).

**Figure 3.5:** The LDPM geometry in 2D. In particular, one can have a first simplification in the geometry passing from the coarse irregular aggregates to the spherical particles. Then, a Delaunay tetrahedralization on the centre of the spheres is carried out to obtain the Domain Tesselation.



LDPM is based on the description of the internal structures at the length scale of coarse aggregate pieces. Hence the mesh size is not user-defined and it comes automatically from the concrete composition. The LDPM mesh directly depends on the minimum aggregate size and the aggregate gradation (both fixed by the real mix design). The only user-defined parameter is the size of the simulated minimum aggregate size which defines the resolution of the model. However, mesh sensitivity with respect to the minimum aggregate size does not have meaning from a physical point of view because the LDPM constitutive equations (and the associated parameters) represent the behavior of the material at a scale smaller than the minimum aggregate size. This implies that for different values of the minimum aggregate size the model parameters must be necessarily different. Hence, simulations for different values of the minimum aggregate size and constant parameters do not have any physical meaning. Of course, it is important to handle correctly fracture and localization at the mesoscale and that is handled with the classical crack-band theory as described in the original LDPM papers [175].

Compatibility equations are formulated by describing the deformation of an assemblage of particles through rigid-body kinematics. Equilibrium equations are obtained through the force and moment equilibrium of each cell. The material behavior is assumed to be governed by a vectorial constitutive law imposed at the interfaces among cells. Moreover, the mechanical interaction between the cells is characterized by both normal and shear stresses.

The adoption of a numerical framework developed for concrete to stone masonries was possible since one can observe a strong similarity in geometrical features, albeit at different observation scales, as well as similarity in the brittle-failure mode between such materials.

The idea of using LDPM for stone masonries is coherent with the fact that the failure is often caused by fracture, damage localization, and frictional shearing occurring at the weak matrix layers around aggregates and stones in the cases of concrete and masonry, respectively. Indeed, as largely demonstrated in the literature (e.g. [195]) as well as in the experiments described in Sections 2.1.1 and 2.1.2, the failure of unreinforced stone masonry only takes place at the unit–mortar interfaces. Hence, the hypothesis of considering stone cells as rigid bodies can be accepted also for the simulation stone masonries.

LDPM simulates concrete material at the coarse aggregate level, which is typically up to 20 mm, whereas it can simulate stone masonry at the stone level, from about 50 mm to 250 mm.

The similarity in geometrical features, albeit at different observation scales, between concrete and stone masonry is illustrated in Figure 3.6.

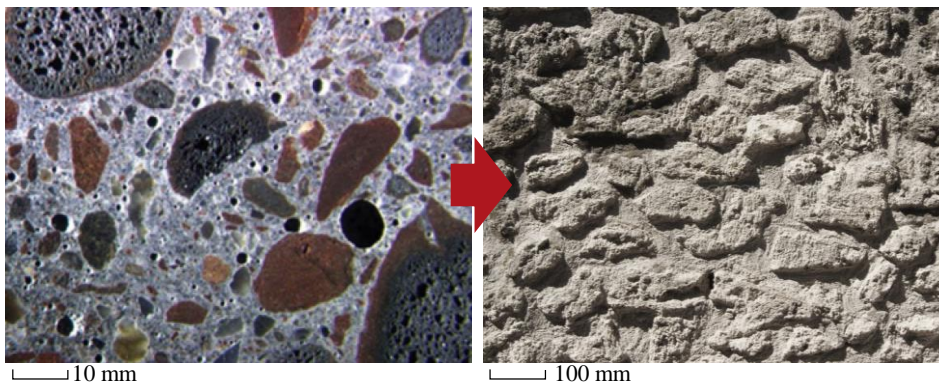


**Figure 3.6:** Similarity between concrete and stone masonry materials at different observation scales.

### 3.2.1 Geometrical characterization

Mix design parameters are necessary to construct the meso-scale numerical granular skeleton, including minimum and maximum stone sizes,  $d_0$  and  $d_a$ , respectively; mortar content  $c$ ; water-to-mortar ratio  $w/c$ . After assuming these parameters and following an assigned grain distribution law, particles are randomly introduced into the volume by considering their initial spherical shape (Figure 3.7a).

In the past, workmanship randomly placed the stones in the mold to build masonry walls. Hence, the assemblage methodology of stones did not follow a specific sieve distribution.

Figure 3.5b shows the sieve curve envelope as opposed to a well-defined distribution, for typical masonry panels [196, 197]. In particular, the experimental sieve curve is represented by the scattering area between the lower and the upper curves for three stone masonry panels. Such panels were prepared at the Laboratory LPMS of the University of L'Aquila Samples using the original limestone units and the ancient constructive technique recognized in most of the monumental buildings of the central Italy. Each particle length is considered as mean values between the maximum stone length and the corresponding length measured in the orthogonal direction.

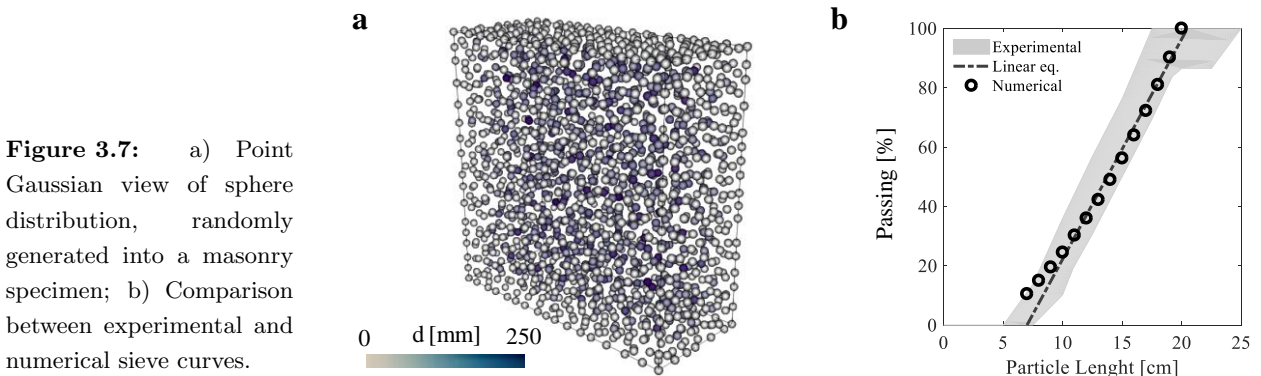


**Figure 3.7:** a) Point Gaussian view of sphere distribution, randomly generated into a masonry specimen; b) Comparison between experimental and numerical sieve curves.

One can observe that the experimental sieve curve in Figure 3.5b can be approximated by an ideal curve having both the hypotheses of infinity particles generated into a volume and random particle distribution. This ideal curve corresponds to a straight line intersecting the abscissa axis in the value of the minimum diameter by the equation:

$$P = \frac{d - d_0}{d_a - d_0} \quad (3.1)$$

where  $P$  is the percentage of aggregate by weight retained by a sieve of characteristic size  $d$ .

For the sake of simplicity, one can assume the distribution to follow a Fuller

curve, computed as:

$$P = \left( \frac{d}{d_a} \right)^{n_F} \quad (3.2)$$

By equating the equations (3.1) and (3.2) it is possible to identify the Fuller coefficient  $n_F$ , as a function of  $d_0$  and  $d_a$  from the real masonry texture.

Once the particles are generated and inserted in the given volume, a lattice system is then defined to describe the interaction between particles by means of a Delaunay tetrahedralization [198, 199] performed with the centers of the spherical particles. The potential failure locations are defined after performing a domain tessellation (Figure 3.8a), which in turn produces a system of polyhedral cells, each of them enclosing a spherical particle. The triangular facets of the polyhedral cells (Figure 3.8b) and the generated lattice linking the centers of the particles are used to compute the interaction between adjacent cells. Figures 3.8e, f show the cell outline and the possible failure layers generated around the spherical particles.

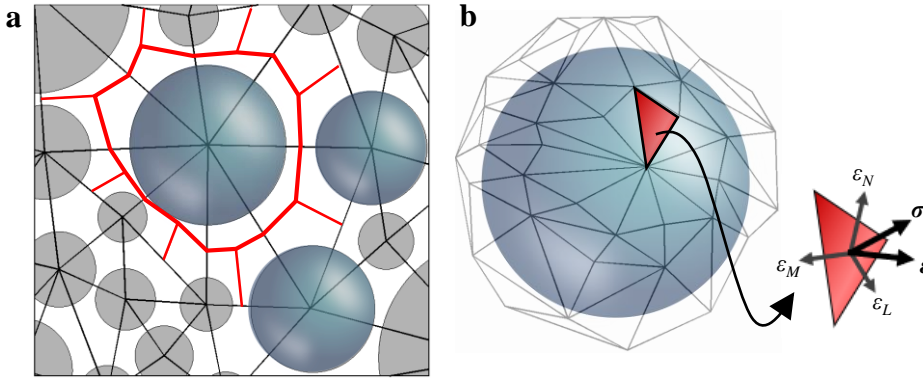


**Figure 3.8:** a) Delaunay tetrahedralization and domain tessellation; b) single stone unit represented by a polyhedral cell and its triangular facets, enclosing a spherical particle.

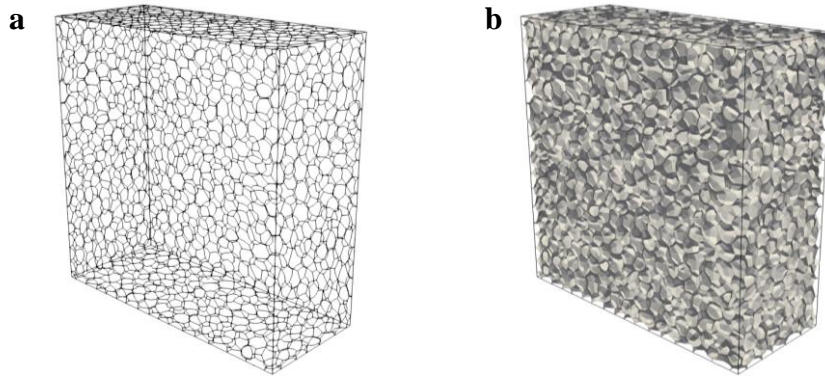


**Figure 3.9:** a) Cell outline generated around the spheres; b) possible failure layers generated around the spherical particles.

A detailed description of the LDPM meso-structure generation can be found in the work of Cusatis and coworkers [173, 175].

However, the classic particle generation procedure described above was created for the simulation of concrete materials. It does not provide a realistic representation of most existing masonry buildings, in which the size of external stones is much larger than the internal ones.

In the standard procedure, nodes are first placed over the surfaces with an

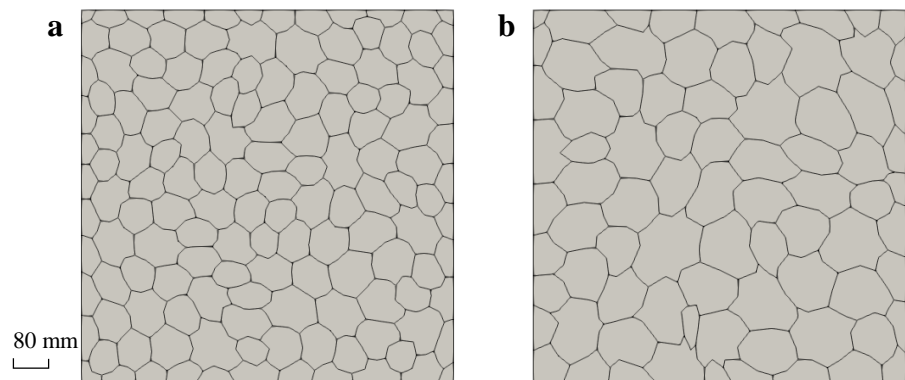
average distance of  $\delta_s d_0$  ( $\delta_s \approx 1.5$ ), where  $d_0$  is the minimum particle size. In this way, the mesh on the external surfaces is characterized only by the minimum diameter  $d_0$  (Figure 3.10) and not employing the assumed particle distribution in the range from  $d_0$  to  $d_a$ . Besides, in the case of particles characterized by diameter lengths similar to the thickness of the specimen to be filled (as in the studied case), one obtains an internal mesh size larger than the external one by using the standard procedure. This is because particles are placed throughout the specimen volume one by one from the largest to the smallest size, filling the internal volume with only large particles leaving no space for the small ones.

This assumption is acceptable for the simulation of concrete materials since all large aggregate pieces are forced to be inside the volume during casting by the presence of the formwork. Moreover, this simplification can be acceptable for concrete material since particle lengths are much smaller than the specimen size and, therefore, the distribution of few particles placed on the external surface does not influence the mechanical behavior of the specimen.

However, that assumption is not acceptable for the simulation of stone masonries which are characterized by a different manufacturing procedure that leads to the larger stones to be mainly on the surface. Indeed, in common practice, the internal stone elements were used only to fill the voids in the inner core of the masonry walls. Moreover, the mechanical properties of stone masonry materials can be largely affected by the particle distribution on the external faces.

In summary, assuming a particle distribution in the range of  $[d_0, d_a]$ , the standard procedure generates a discretization characterized by small size particle on the specimen surface and large size particle into the specimen volume. This is the opposite condition of real cases of disordered masonry.

**Figure 3.10:** Visualization of the masonry panel surface. The LDPM cells generated by the standard procedure and the newly developed procedure (using for both the cases  $d_0=80$  mm,  $d_a=220$  mm, and  $n_F=0.5$ ).



The problem has been solved by uncoupling the generation of particles in two distinct procedures. Two sets of granulometric distributions were introduced: one for the internal particles and one for the surface ones.

The newly developed procedure is described in details as follows:

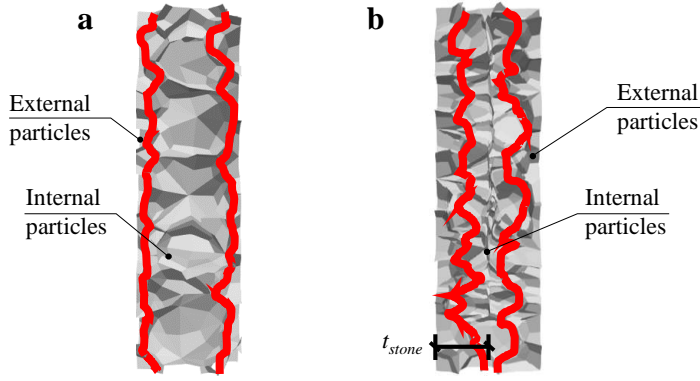


**Figure 3.11:** Sectional views of the masonry specimen. Stone particles generated by employing: a) the standard procedure; b) the newly procedure developed for disordered masonries.

- a 2D unstructured mesh of the specimen surfaces is generated by the GMSH [200] adopting an average mesh spacing of  $d_m^e = (d_a^e + d_0^e)/2$ , where  $d_0^e$  and  $d_a^e$  are the minimum and the maximum external stone sizes;
- the node coordinates of the surface mesh generated through the first step are randomly perturbed by an amount  $\xi = R\Delta$  to obtain new node coordinates, where  $R$  is a random number generated in the range  $[-1, 1]$ , and  $\Delta = (d_m^e - d_0^e)/2$  is the maximum perturbation which ensures no overlap;
- the new node coordinates are imported in the LDPM as coordinates of the surface particle centers around which irregular cells are created for the specimen surface (Figure 3.11b);
- an internal particle size distribution consistent with a Fuller sieve curve and characterized by  $d_0^i$  and  $d_a^i$  is defined (where  $d_0^i$  and  $d_a^i$  are the minima and the maximum internal stone sizes). In particular, the particle size adopted for the internal particles to represent the internal aggregate distribution was chosen within the range  $d_0^i = 32$  mm to  $d_a^i = 64$  mm in order to model only the *very coarse gravel* (pebbles) subclasses [201].
- the generation of the particles throughout the volume is made by defining a minimum distance between the internal particles and the surfaces to obtain the desired thickness of the external stones  $t_{stone}$  (see Figure 3.11b).

With the first three steps described above, the LDPM surface mesh is characterized by a random distribution of spheres that have diameters from  $d_0^e$  to  $d_a^e$ , which represent the sizes of the stones observed in the real texture of the facade walls. Through the last two steps, the LDPM volume mesh is characterized by internal particles ranging from  $d_0^i$  to  $d_a^i$ . In Figures 3.10, one can clearly observe the difference in the generated LDPM cells between standard particle generation procedure (Figure 3.10a) and the newest one described above (Figure 3.10b).

### 3.2.2 Governing equations

LDPM describes the meso-structure deformation through the adoption of rigid-body kinematics [175] for each individual particle. Based on this assumption and for given displacements and rotations of the particles associated with a given facet, the relative displacement  $\llbracket \mathbf{u}_c \rrbracket$  at the centroid of the facet can be used to define the following strain measures:

$$\varepsilon_N = \frac{\mathbf{n}^T \llbracket \mathbf{u}_c \rrbracket}{\ell}; \quad \varepsilon_M = \frac{\mathbf{m}^T \llbracket \mathbf{u}_c \rrbracket}{\ell}; \quad \varepsilon_L = \frac{\mathbf{l}^T \llbracket \mathbf{u}_c \rrbracket}{\ell} \quad (3.3)$$

where  $\ell$  is the length of the straight line connecting two adjacent particle centers, and  $\mathbf{n}$ ,  $\mathbf{m}$ ,  $\mathbf{l}$  are unit vectors defining a local system of reference such that  $\mathbf{n}$  is orthogonal to the facet, and  $\mathbf{m}$ ,  $\mathbf{l}$  are mutually orthogonal as well as tangential to the facet. Cusatis and coworkers [202, 203, 204, 205] showed that the strain definitions in equations are consistent with the definition of strains in classical continuum mechanics.

The corresponding normal and shear stresses are calculated through meso-scale constitutive laws. The equilibrium is finally imposed through the Principle of Virtual Work (PVW) or equivalently by the force and moment equilibrium of each cell:

$$\sum_{k \in \mathcal{F}_I} A_k \boldsymbol{\sigma}_k + V_I \mathbf{b} = \mathbf{0}, \quad \sum_{k \in \mathcal{F}_I} A_k \mathbf{c}_k \times \boldsymbol{\sigma}_k = \mathbf{0} \quad (3.4)$$

where  $\mathcal{F}_I$  is the set containing all the facets of a generic polyhedral cell  $I$ ,  $A_k$  is the projected area of facet  $k$ ,  $\mathbf{c}_k$  is the vector representing the distance between the center of the cell and the center of facet  $k$ ,  $V_I$  is the cell volume,  $\mathbf{b}$  is the external body force applied to the cell, and  $\boldsymbol{\sigma}_k$  is the traction vector containing the normal and the two shear stress components.

The elastic behavior is formulated by assuming that normal and shear stresses are proportional to the corresponding strains:  $\sigma_N = E_N \varepsilon_N$ ,  $\sigma_M = E_T \varepsilon_M$  and  $\sigma_L = E_T \varepsilon_L$ , with  $E_N = E_0$ ,  $E_T = \alpha E_0$ , where  $E_0$  and  $\alpha$  are the effective normal modulus and the shear-normal coupling parameter, respectively. In LDPM,  $E_0$  and  $\alpha$  are different from but related to Young's modulus  $E$  and Poisson's ratio  $\nu$ . Indeed, an approximated relation between macro and LDPM elastic parameters exists:  $E_0 = E/[(1 - 2\nu)]$  and  $\alpha = (1 - 4\nu)/(1 + \nu)$ .

For the nonlinear and inelastic behavior, the LDPM formulation simulates different physical mechanisms characterizing meso-scale failure behavior. In particular, for masonry, it simulates the fracturing and cohesive behavior under tension/shear, the compressive behavior, and the frictional behavior under compression/shear for two adjacent masonry stones.

### 3.2.2.1 Fracturing and cohesive behavior under tension/shear

With tensile loading ( $\varepsilon_N > 0$ ), the fracturing behavior is formulated through an effective strain  $\varepsilon$  and an effective stress  $\sigma$ :

$$\varepsilon = \sqrt{\varepsilon_N^2 + \alpha(\varepsilon_M^2 + \varepsilon_L^2)}; \quad \sigma = \sqrt{\sigma_N^2 + (\sigma_M^2 + \sigma_L^2)/\alpha} \quad (3.5)$$

allowing the computation of the normal stress as  $\sigma_N = \varepsilon_N(\sigma/\varepsilon)$  and shear stresses as  $\sigma_M = \varepsilon_M\alpha(\sigma/\varepsilon)$  and  $\sigma_L = \varepsilon_L\alpha(\sigma/\varepsilon)$ . The effective stress  $\sigma$  is assumed to be incrementally elastic, and it is formulated such that it satisfies the inequality  $0 \leq \sigma \leq \sigma_{bt}$ , where  $\sigma_{bt}$  is the upper tensile limit that can be expressed as:

$$\sigma_{bt} = \sigma_0 \exp \left[ -H_0 \frac{\langle \varepsilon - \varepsilon_0 \rangle}{\sigma_0} \right] \quad (3.6)$$

in which  $\varepsilon_0 = \sigma_0/E_0$ . The post peak softening modulus  $H_0$  and the strength limit function for the effective stress  $\sigma_0$  depend on the coupling variable  $\omega$ . In particular,  $H_0 = H_t (2\omega/\pi)^{n_t}$ , where  $n_t$  is the softening exponent governing the interaction between shear and tensile behavior, and  $\sigma_0$  is defined as:

$$\sigma_0 = \frac{-\sin(\omega) + \sqrt{\sin^2(\omega) + 4\alpha \cos^2(\omega) / r_{st}^2}}{2\alpha \cos^2(\omega) / r_{st}^2} \quad (3.7)$$

where  $H_t = 2E_0/(\ell_t/r - 1)$ ,  $\ell_t = 2E_0G_t/\sigma_t^2$  is the tensile characteristic length,  $G_t$  is the meso-scale fracture energy,  $r_{st} = \sigma_s/\sigma_t$ ,  $\sigma_t$  is the tensile strength and  $\sigma_s$  is the shear strength.

The variable  $\omega$ , represents the degree of interaction between shear and normal deformation:  $\tan \omega = \varepsilon_N/(\sqrt{\alpha}\varepsilon_T)$ ; where  $\varepsilon_T = \sqrt{\varepsilon_M^2 + \varepsilon_L^2}$  is the total shear strain.

### 3.2.2.2 Compressive behavior

The second failure type considered in LDPM is relevant to the compressive behavior ( $\varepsilon_N < 0$ ) and it simulates material compaction. The LDPM constitutive law in compression is based on a strain-hardening normal boundary  $\sigma_{bc}$  limiting the compressive normal stress component at the facet level and it is assumed to be a function of both the volumetric strain computed at the LDPM tetrahedral level  $\varepsilon_V = (V - V_0)/V_0$  and the  $\varepsilon_D = \varepsilon_N - \varepsilon_V$ , where  $V$  and  $V_0$  are the current and initial volume of the generic LDPM tetrahedron. The compressive boundary can be formulated as:

$$\sigma_{bc} = \begin{cases} \sigma_{c0} + H_c \langle -\varepsilon_V - \varepsilon_{c0} \rangle & -\varepsilon_V \leq \varepsilon_{c1} \\ \sigma_{c1} \exp[(-\varepsilon_V - \varepsilon_{C1})H_c/\sigma_{c1}] & \text{otherwise} \end{cases} \quad (3.8)$$

where  $\sigma_{c1} = \sigma_{c0} + H_c(\varepsilon_{c1} - \varepsilon_{c0})$ ,  $\varepsilon_{c1} = k_{c0}\varepsilon_{c0}$ ,  $\varepsilon_{c0} = \sigma_{c0}/E_0$ ,  $\sigma_{c0}$  is the meso-scale yielding compressive stress,  $k_{c0}$ ,  $k_{c1}$ ,  $k_{c2}$  are parameters governing the triaxial behavior at very high confinement, and  $H_{c0}$  is a material parameter:

$$H_c = [H_{c1} + (H_{c0} - H_{c1})]/[1 + \kappa_{c2}(r_{DV} - \kappa_{c1})] \quad (3.9)$$

where  $H_{c0}$  is a material parameter:  $r_{DV} = |\varepsilon_D|/(\varepsilon_{V0} - \varepsilon_V)$  for  $\varepsilon_D \leq 0$  or  $r_{DV} = |\varepsilon_D|/\varepsilon_{V0}$  for  $\varepsilon_D > 0$ ,  $H_{c0}$  is a material parameter,  $\varepsilon_{V0} = 0.1\varepsilon_0$ , and  $H_{c1} = 0.1E_0$ .

### 3.2.2.3 Frictional behavior

Finally, the third failure type considered in LDPM is relevant to the frictional behavior. In the presence of compressive stresses, the shear strength increases due to frictional effects. The frictional behavior is simulated by means of a nonlinear Mohr-Coulomb model in which the internal friction coefficient varies from an initial value  $\mu_0$  to zero by the following formulation:

$$\sigma_{bs} = \sigma_s + \mu_0\sigma_{N0} - \mu_0\sigma_{N0} \exp(\sigma_N/\sigma_{N0}) \quad (3.10)$$

where  $\sigma_s$  is the cohesion and  $\sigma_{N0}$  is the transitional stress.

### 3.3 Simulation of unreinforced stone masonry walls

#### 3.3.1 Investigation of the stone and size distribution

Prediction of the strength of masonry subjected to in-plane forces plays a crucial role in the seismic design and assessment of ordinary masonry buildings [206]. In the experimental campaign, as well described in Chapter 2, a direct approach to estimate the mechanical proprieties of masonry panels consists of performing the diagonal-compression test. This test allows for evaluating the main mechanical properties of the masonry [108]. However, the experimental tests are usually characterized by a substantial scatter in data results, mainly due to the irregular shape of stones and the random distribution of them into the mortar matrix as well as and the variability of the mechanical proprieties of the constituent materials. This phenomenon determines a strong heterogeneity level of the masonry panels.

Here, in order to numerically investigate this phenomenon, only the heterogeneity effect on the mechanical response of stone masonry panels under the diagonal compression test, is analyzed, neglecting the high variability of the mechanical proprieties of the constituent materials (which obviously influence the dispersion of the results). In particular, In the test, a square masonry panel of dimension equal to 1.2 m and thickness  $t$  is subjected to a compressive force applied along one of the diagonal of the panels.

Following the international standards ASTM [107], one can compute the shear stress of the masonry  $\tau = 0.707P/(A_n)$ , where  $P$  is the applied load and  $A_n$  is the net area of the panel given by  $A_n = (W + h)/2 t$ , where  $W$ ,  $h$  and  $t$  are the width, height, and thickness of specimen, respectively. For  $P = P_{max}$ , that equation provides the maximum shear stress  $\tau_0$ . Moreover, one can compute the shear strain  $\gamma = \varepsilon_h + |\varepsilon_v|$ , where  $\varepsilon_h$  and  $\varepsilon_v$  are the tensile (positive) and compressive strain (negative) measured along the two diagonals.

Furthermore, the initial portion of the  $\tau - \gamma$  curve allows calculating the shear modulus of the masonry  $G = \tau_{30\%}/\gamma_{30\%}$ , in which  $\tau_{30\%}$  represents the 30% of the maximum stress of the specimen  $\tau_0$  and  $\gamma_{30\%}$  is the shear strain value corresponding to  $\tau_{30\%}$ . Finally, the evaluation of the ductility parameter  $\mu = \gamma_{\tau_{80\%}}/\gamma_{\tau_0}$ , where  $\gamma_{\tau_0}$  and  $\gamma_{\tau_{80\%}}$  represent the values of the shear strain  $\gamma$  read in correspondence of  $\tau_0$  and  $0.8 \tau_0$ , respectively.

In order to numerically investigate this phenomenon, the heterogeneity effect on the mechanical response of stone masonry panels under diagonal compression test is analyzed by varying size and distribution of the stones but neglecting the variability of the mechanical proprieties of the constituent materials.

To this end, eight different sets of samples were employed for the LDPM simu-

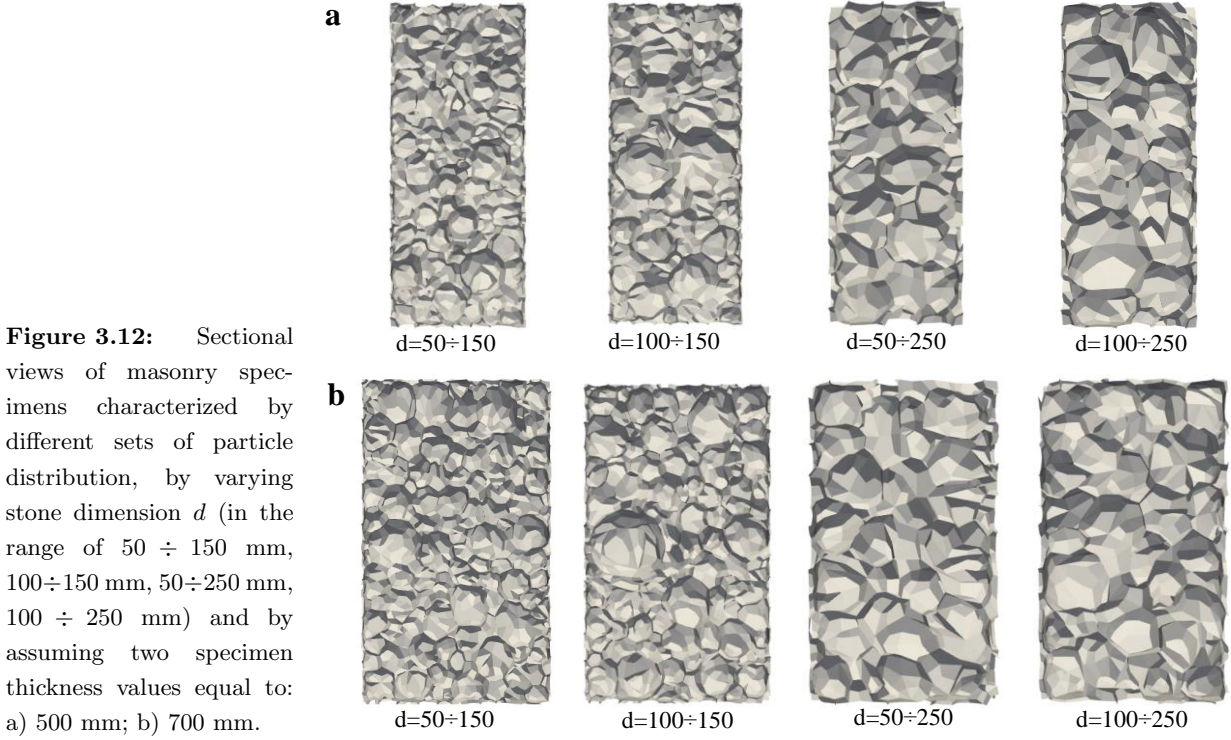


**Figure 3.12:** Sectional views of masonry specimens characterized by different sets of particle distribution, by varying stone dimension  $d$  (in the range of  $50 \div 150$  mm,  $100 \div 150$  mm,  $50 \div 250$  mm,  $100 \div 250$  mm) and by assuming two specimen thickness values equal to: a) 500 mm; b) 700 mm.

lations (Figures 3.12a, b and Table 3.1). The results are presented by using labels in which the first part indicates the thickness value of the masonry samples (e.g.  $t500$  means  $t = 500$  mm), whereas the second part indicates the stone size range (e.g.  $D50 - 150$  corresponds to a stone size ranging from 50 mm to 150 mm).

Table 3.1 summarizes the geometrical parameters used for the definition of the eight sieve curves. In particular, one can see that values of stone dimension  $d$  are ranging from  $d_0 = 50$  mm to  $d_a = 250$  mm, as usually observed for historical masonry structures [196, 207]. Moreover, calibration of the Fuller coefficients  $n_F$  listed in Table 3.1 was carried out following the procedure described above, by the equations Eq.(3.1) and Eq.(3.2).

**Table 3.1:** Values of different stone distribution sets used in the numerical simulations and characterized by minimum and maximum stone dimension ( $d_0$  and  $d_a$ ) and Fuller coefficient  $n_F$ . Results are presented by using labels in which: the first part indicates the thickness value of the masonry samples (e.g.  $t500$  means  $t = 500$  mm), whereas the second part indicates the stone size range (e.g.  $D50 \div 150$  corresponds to a stone size ranging from 50 mm to 150 mm).

Test name	Thickness [mm]	$d_0$ [mm]	$d_a$ [mm]	$n_F$ [-]
t500-D50÷150	500	50	150	1.7
t500-D100÷150	500	100	150	1.7
t500-D50÷250	500	50	250	1.6
t500-D100÷250	500	100	250	5
t700-D50÷150	700	50	150	1.7
t700-D100÷150	700	100	150	1.7
t700-D50÷250	700	50	250	1.6
t700-D100÷250	700	100	250	5

For the mix design definition, the stone-mortar ratio  $a/c$  was assumed equal to 3.4, which corresponds to the ratio between the volume of the stones (equal to 77.5% of the total volume of the specimen) and the lime mortar volume (equal to 22.5%) used to prepare the masonry specimens in the lab. The water-mortar ratio  $w/c = 0.6$  was assumed based on the mix design adopted to build the laboratory specimens. Mortar content parameter  $c$  was computed with the goal to obtain a total mass density  $\rho_{masonry}$  equal to 1,800.0 kg/m<sup>3</sup> (according to [113]) by the following formula:  $\rho_{masonry} = c [1 + w/c + a/c]$ .

In order to calibrate the LDPM parameters, an extensive literature investigation was conducted on the mechanical parameters of masonries, only considering unreinforced panels constituted by coarse stones and poor mortar. In particular, the calibration procedure was performed through the best fitting of the load-displacement curves relevant to experimental tests of both the vertical compression tests [208, 209, 210, 211] and diagonal compression tests [208, 108, 87, 78, 207] present in literature as well as the experimental tests carried out in this research (Chapter 2). From these experimental data, the target values for compression stress, elastic module, and shear strength were assumed ranging from 0.8 MPa to 1.2 MPa, from 500 MPa to 800 MPa, and from 0.1 MPa to 0.15 MPa, respectively. Thereby, by the calibration procedure, it was possible to determine the LDPM parameter values.

In Table 3.9 are listed the parameters obtained by previous sensitivity analyses not reported in the thesis.

**Table 3.2:** LDPM mechanical parameter values employed for the stone masonry material.

$E_0$	$\alpha$	$\sigma_t$	$G_t$	$n_t$	$\sigma_s/\sigma_t$	$\sigma_{c0}$	$\sigma_{N0}$	$H_{c0}$	$\mu_0$
[MPa]	[-]	[MPa]	[N/m]	[-]	[-]	[MPa]	[MPa]	[-]	[-]
1120.0	0.065	0.3	13	0.1	1.35	125	42	0.4	0.2

In particular, both the normal elastic modulus  $E_0$  and shear-normal coupling parameter  $\alpha$  govern LDPM response in the elastic regime; both the tensile strength  $\sigma_t$  and the tensile fracture energy  $G_t$ , which is equal to  $\ell\sigma_t^2/(2E_0)$  (where  $\ell$  is the characteristic length), govern the softening tensile fracturing behavior of LDPM facets and, consequently, govern all macroscopic behaviors featuring softening; the softening exponent  $n_t$  governs the interaction between shear and tensile behavior during softening at the facet level; the shear strength  $\sigma_s$  is the facet strength for pure shear and facets mostly the macroscopic behavior in compression; the yielding compressive stress  $\sigma_{c0}$ , the initial hardening modulus  $H_{c0}$  and the transitional strain ratio  $k_{c0}$  define the behavior of the facet normal component under compression and affect the macroscopic behavior in compression; the initial internal friction

coefficient  $\mu_0$ , the internal asymptotic friction coefficient  $\mu_\infty$  (assumed equal to 0) and the transitional stress  $\sigma_{N0}$  contribute to LDPM response in compression while they have basically no effect on tensile behavior.

In the LDPM simulation, the two steel plates (L-shape), placed at the specimen corners, were modeled as triangular shell elements and were assumed to be rigid bodies. Furthermore, a sliding with ‘stick-slip’ friction constraint [212] between the corner plate faces and the masonry particle nodes were used. This constraint is designed to force a set of nodes to move over a frictional surface while the constraint perpendicular to the surface is treated using a master-slave formulation. The simulations used a dynamic friction coefficient  $f_k = 0.5$  and a static friction coefficient  $f_s = 0.5$  to simulate the high friction conditions. Assuming  $f_s = f_k$  allows preventing the reduction of the friction once sliding between surfaces appeared.

Finally, the rotations perpendicular to the normal plate directions were fixed for all particle nodes in contact with the corner plates (L-shape).

In Figures 3.13 – 3.16, one can observe the mechanical response of stone masonry panels under diagonal compression tests, expressed by the shear stress and shear strain ( $\tau$ - $\gamma$ ) curves. In particular, mechanical responses for the eighth granulometric distribution sets were computed by varying the range of stone size and thickness of the masonry specimens (see Figure 3.5 and Table 3.1). For each of the eighth granulometric distributions, 50 simulations for each case were carried out by assuming 50 random stone arrangements. The circle markers represent the achievement of the maximum shear stress.

The response curves illustrated in Figures 3.13*a, b* are characterized by the same thickness value of the samples (equal to 500 mm) and the same minimum stone size (equal to 50 mm). On the contrary, the maximum stone sizes are equal to 50 mm and 150 mm for the responses of Figure 3.13*a* and Figure 3.13*b*, respectively. Results show that the scattering of the response curves is slightly more pronounced in case of a larger variation of the stone dimension  $d$ . Indeed, Figure 3.13*b*, where the stone dimension is ranging from 50 mm to 150 mm, is characterized by a larger dispersion of the results as compared to 3.13*a*, where the stone dimension is ranging from 50 mm to 250 mm. Furthermore, the response curves illustrated in Figure 3.13*a* are much dispersed as compared to the ones illustrated in Figure 3.14*a*. In these two cases, both the minimum and maximum stone sizes are the same (50 mm and 150 mm, respectively) and the only difference regards the thickness  $t$  of the samples. Indeed,  $t$  are equal to 500 mm and 700 mm in Figure 3.13*a* and Figure 3.14*a*, respectively. Hence, results highlight that for a higher level of homogeneity of the material one can have a smaller dispersion of the mechanical responses.

Again, by observing the results of Figures 3.16a, b one can confirm the same trends of the other results discussed above.

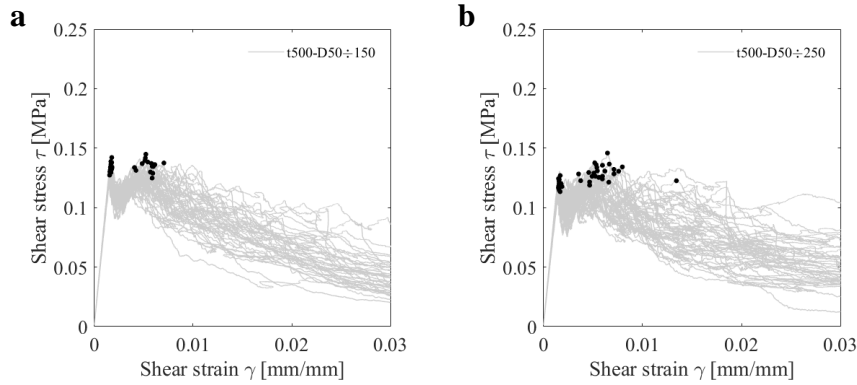


**Figure 3.13:** Diagonal compression tests carried out by LDPM using two of the eight different granulometric distribution assumed: t500-D50÷150 and t500-D50÷250. Each graph represents 50 simulations by varying the stone arrangements.

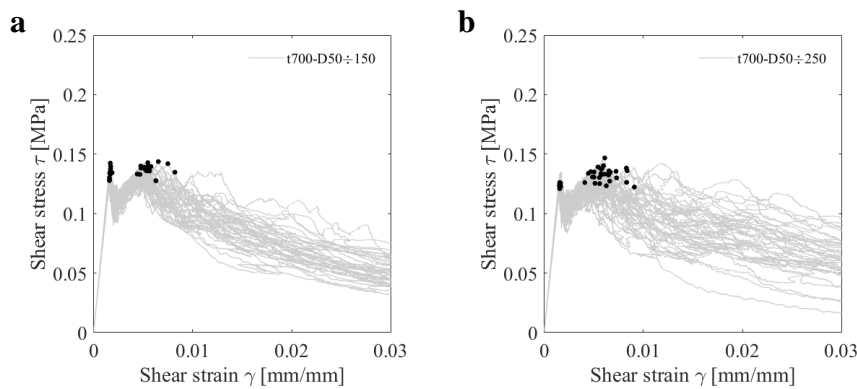


**Figure 3.14:** Diagonal compression tests carried out by LDPM for the t700-D50÷150 and t700-D50÷250 cases.

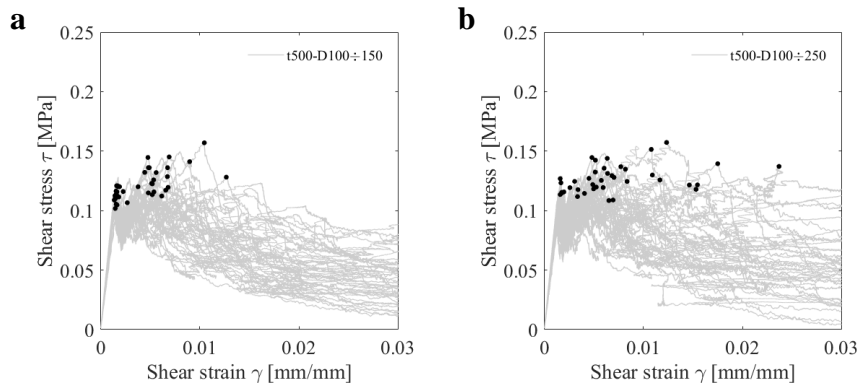


**Figure 3.15:** Diagonal compression tests carried out by LDPM for the t500-D100÷150 and t500-D100÷250 cases.

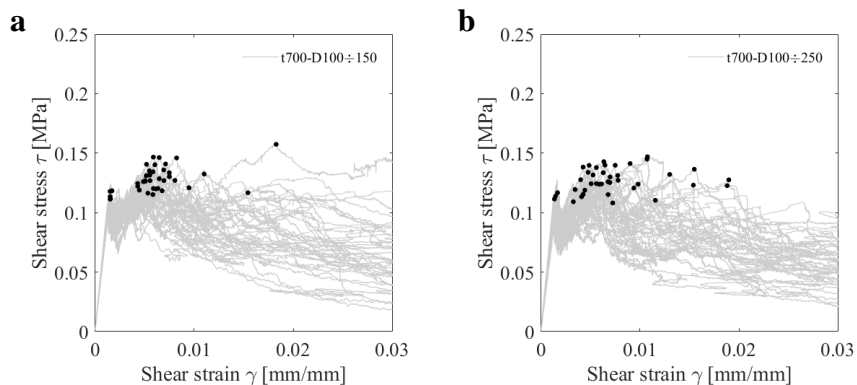


**Figure 3.16:** Diagonal compression tests carried out by LDPM for the t700-D100÷150 and t700-D100÷250 cases.

From the results of Figures 3.13–3.16 it is possible to evaluate the mechanical properties of stone masonries in terms of  $\tau_0$ ,  $G$ , and  $\mu_{80\%}$  (following the procedure described above). Thereby, one can compute the Probability Density Function - PDF and the Cumulative Density Function - CDF for those mechanical properties assuming a log-normal distribution function. The CDF is a very useful tool for the assessment of mechanical property variations. Indeed, the slope of each curve indicates the reliability of a mechanical property: higher the slope, higher the dispersion of the results and vice versa. Comments of the CDF curves are obviously the same as the PDF ones. Tables 3.3–3.5 list the values of mean  $m$ , standard deviation  $\sigma$  and the coefficient of variation  $CV$  computed for  $\tau_0$ ,  $G$ , and  $\mu_{80\%}$ , respectively. In particular,  $CV$  is the standardized measure of the dispersion of a probability distribution and is defined as the ratio of the standard deviation  $\sigma$  to the mean  $m$ . The higher  $CV$ , the higher the dispersion of the results, and vice versa.

**Table 3.3:** Mean  $m$ , standard deviation  $\sigma$ , and coefficient of variation  $CV$  values computed for the shear strength  $\tau_0$  obtained for the eighth stone distribution sets employed in the LDPM simulations.

Test name	$m_{\tau_0}$	$\sigma_{\tau_0}$	$CV_{\tau_0}$
t500-D50÷150	0.134	0.004	0.031
t500-D50÷250	0.126	0.007	0.057
t700-D50÷150	0.136	0.004	0.028
t700-D50÷250	0.130	0.006	0.047
t500-D50÷150	0.121	0.012	0.101
t500-D100÷250	0.127	0.012	0.091
t700-D100÷150	0.128	0.010	0.082
t700-D100÷250	0.127	0.010	0.082
average	0.129		

**Table 3.4:** Mean  $m$ , standard deviation  $\sigma$ , and coefficient of variation  $CV$  values computed for the shear modulus  $G$ .

Test name	$m_G$	$\sigma_G$	$CV_G$
t500-D50÷150	59.012	1.127	0.016
t500-D50÷250	57.792	1.917	0.028
t700-D50÷150	59.310	1.222	0.017
t700-D50÷250	58.502	1.683	0.024
t500-D50÷150	54.906	3.853	0.058
t500-D100÷250	54.254	4.475	0.069
t700-D100÷150	57.108	2.339	0.034
t700-D100÷250	55.956	3.890	0.058
average	57.105		

**Table 3.5:** Mean  $m$ , standard deviation  $\sigma$ , and coefficient of variation  $CV$  values computed for the ductility  $\mu_{80\%}$ .

Test name	$m_{\mu_{80\%}}$	$\sigma_{\mu_{80\%}}$	$CV_{\mu_{80\%}}$
t500-D50÷150	1.434	0.289	0.202
t500-D50÷250	1.369	0.461	0.337
t700-D50÷150	1.735	1.042	0.601
t700-D50÷250	1.555	0.629	0.405
t500-D50÷150	1.274	0.329	0.258
t500-D100÷250	1.146	0.100	0.087
t700-D100÷150	1.283	0.242	0.189
t700-D100÷250	1.274	1.188	0.932
average	1.384		

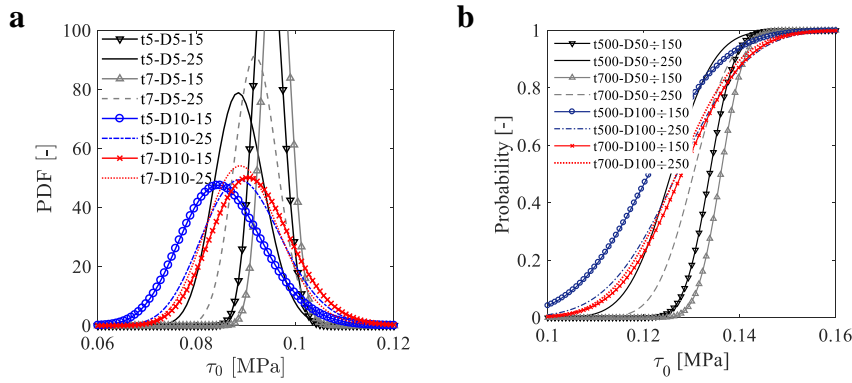


**Figure 3.17:** Probability Density Function - PDF (a) and Cumulative Density Function - CDF (b) obtained by employing 8 different grain size distribution and assuming a Gaussian distribution for the maximum stress  $\tau_0$ .

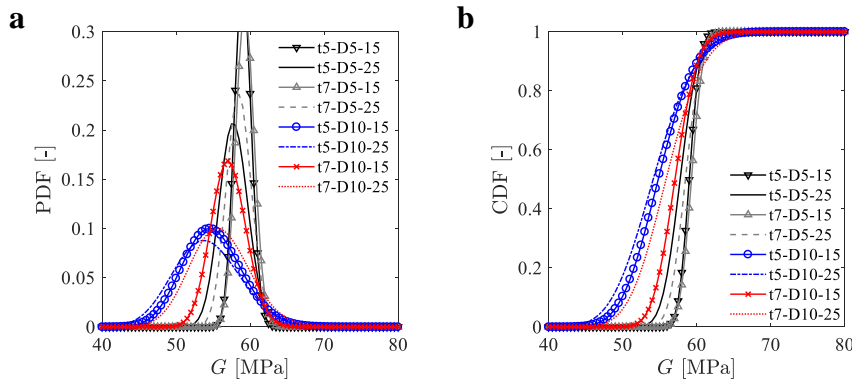


**Figure 3.18:** PDF (a) and CDF (b) obtained for the shear modulus  $G$ .

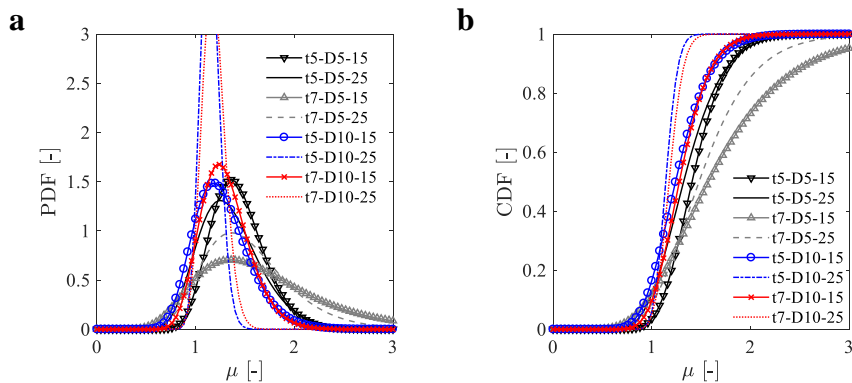


**Figure 3.19:** PDF (a) and CDF (b) obtained for the the ductility  $\mu_{80\%}$ .

In particular, Figures 3.17*a, b* show that mean values of  $\tau_0$  ( $m_{\tau_0}$ ) are ranging from 0.121 MPa to 0.136 MPa, corresponding to a variation of about 11% as compared to the average value of 0.129 MPa. This highlights that the maximum shear stress  $\tau_0$  is not strongly influenced by varying the granulometric distribution. This may suggest that a large variation of  $\tau_0$  values observed in the experimental tests is instead due to the large variability of the mechanical properties of the constituent materials (especially concerning the mortar material, which mainly govern the failure process in stone masonry structures). Comparing results obtained with same granulometric distribution (e.g. t500-D50÷150 and t700-D50÷150), one can observe a decrease of both the mean and standard deviation of  $\tau_0$  ( $m_{\tau_0}$  and  $\sigma_{\tau_0}$  respectively) for the case of greater thickness value ( $t = 700$  mm), as compared to the case of smaller ones ( $t = 500$  mm). On the other hand, comparing results obtained for same specimen thickness  $t$  (e.g. t500-D50÷150 and t500-D50÷250), one can observe an increase in the mean value  $m_{\tau_0}$  and a decrease in standard deviation value  $\sigma_{\tau_0}$  for the case of lower variation of granulometric distribution ( $d_i = 50 \div 150$  mm), as compared to the case of higher variation ones ( $d_i = 50 \div 250$  mm). Definitely, results highlight that for greater uniformity of the range of the stone size of masonry panels, which correspond to a higher level of homogeneity of the material, a bigger value of  $\tau_0$  and greater reliability of results can be noticed. Similar comment can be also write for dispersion of  $G$  (showing a variation of less than 10% (see Figure 3.18). This result highlights how the granulometric distribution can affect the variation of  $G$  by influencing the micro-cracks propagation even for low levels of load ( $G$  evaluated at the 30% of the maximum load  $P_{max}$ ). Furthermore, as in the case of  $\tau_0$ , comparing results obtained for same granulometric distribution (e.g. t500-D50÷150 and t700-D50÷150), one can observe a decrease in both the values of  $m_G$  and  $\sigma_G$  for the case of greater thickness values ( $t=700$  mm), as compared to the case of smaller ones ( $t=500$  mm). Instead, by contrast with the results expressed in terms of  $\tau_0$ , comparing results obtained for same  $t$ , one can observe a decrease in  $m_G$  and an increase in  $\sigma_G$  for the case of lower variation of granulometric distribution ( $d_i = 50 \div 150$  mm), as compared to the case of higher variation ones ( $d_i = 50 \div 250$  mm).

In Figure 3.19, one can observe that the mean values computed for  $\mu_{80\%}$  are ranging from 1.146 to 1.735, corresponding to a variation of about 43% as compared to the average value of 1.384. It is clear that the level of ductility of stone masonry panels is low. Indeed,  $m_{\mu_{80\%}}$  values are almost equal to 1, which corresponds to the case of perfect brittle behavior. In particular, the trend of results allows affirming that higher dissipation capacity of stone masonry is obtained in case of a higher homogeneity level of the stone into masonry panels (lower range of stone size and higher specimen thickness).

Furthermore, the variation observed for  $m_{\mu_{80\%}}$  is even larger if one computes ductility value in correspondence of the 70% or 60% of the maximum shear stress ( $\mu_{70\%}$  and  $\mu_{60\%}$ , respectively) as illustrated in Figure 3.20.

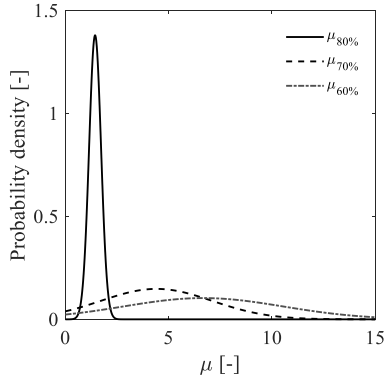
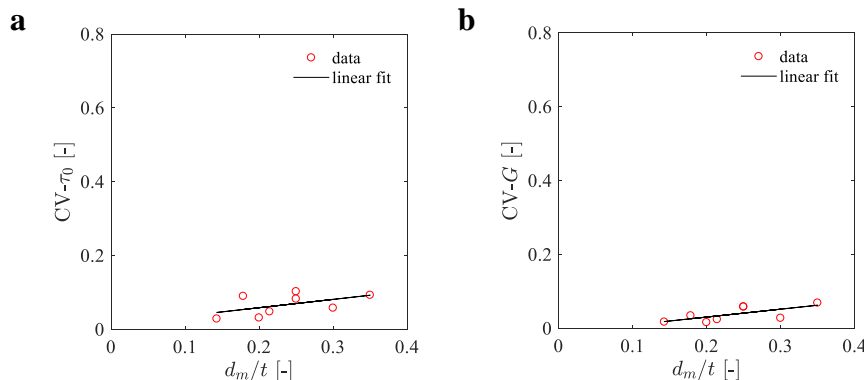


**Figure 3.20:** Probability density function obtained by assuming Gaussian distribution for the ductility capacity  $\mu_{80\%}$ ,  $\mu_{70\%}$ , and  $\mu_{60\%}$  estimated in correspondence of the 80%, 70%, and 60% of the maximum shear stress  $\tau_0$ , respectively. Results are referred to the  $t500 - D50 \div 150$  case.

Since any standard procedure defines a unique way to estimate the ductility value of stone masonry panels, this result highlight that for greater reliability of this mechanical property it is better to consider  $\mu_{80\%}$  instead of  $\mu_{70\%}$  or  $\mu_{60\%}$ .

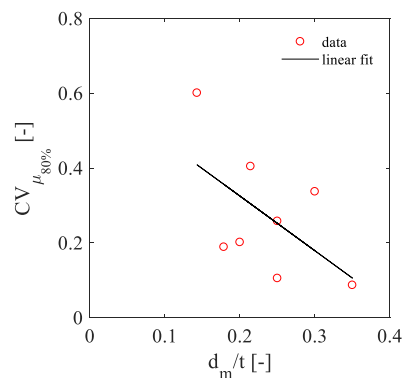
Finally, to better understand the effect of the stone distribution on the scatter of the mechanical properties, it is appropriate to plot the coefficient of variation  $CV$  of  $\tau_0$ ,  $G$  and  $\mu_{80\%}$  as a function of the geometry of the masonry walls ( $d_m/t$ ).  $CV$  is a standardized measure of a probability distribution dispersion and is defined as the ratio of the standard deviation  $\delta$  and the mean values  $\mu$  of the Gaussian curves. Since results were carried out for different specimen thickness as well as different stone sizes, here the dimensionless geometric parameter  $d_m/t$  is introduced. In particular, such parameter is the ratio between the mean stone size  $d_m$  and the thickness  $t$ , where  $d_m$  is computed as the average between  $d_0$  and  $d_a$ . The  $d_m/t$  ratio can be assumed as a measure of homogeneity of the masonry panel.

Figure 3.21a and 3.21b show the  $CV-d_m/t$  plots for the mechanical properties, namely  $\tau_0$ ,  $G$  and  $\mu_{80\%}$ . In particular, one can see that by increasing  $d_m/t$ , and therefore the homogeneity of the masonry panel, the scatter of  $\tau_0$  and  $G$  increases (see Fig. 3.21a and 3.21b, respectively).



**Figure 3.21:** Coefficient of variation  $CV$  related to the ratio  $d_m/t$ .  $CV$  is computed for: (a) the maximum stress  $\tau_0$ ; (b) the shear modulus  $G$ .

On the contrary, in Figure 3.22, one can observe a decrease in the scatter of  $\mu_{80\%}$  values by increasing  $d_m/t$ . This is because, for lower homogeneity of the masonry panel (low value of  $d_m/t$ ), the ductility of the panels corresponds to the case of perfectly brittle behavior, with  $m_{\mu_{80\%}}$  values constantly equal to almost 1 and very low values of  $\delta_{\mu_{80\%}}$ . Instead, for higher homogeneity of the masonry panel (high value of  $d_m/t$ ) the ductility of the panels tends to be higher with a consequent increase in the scattering. Hence, the scatter of  $\mu_{80\%}$  is lower for lower  $d_m/t$ , as compared to the case of higher  $d_m/t$ .



**Figure 3.22:** Coefficient of variation  $CV$  related to the ratio  $d_m/t$ .  $CV$  is computed for the ductility  $\mu_{80\%}$ .

Definitely, the LDPM-based approach allows stochastic predictions for the failure of such structures, as opposed to providing a deterministic numerical prediction that most often would be not realistic for this type of chaotic structures. Based on the obtained results, one can conclude that:

- the stone distribution does not strongly influence the maximum shear stress  $\tau_0$  and  $G$  (up to 10%), whereas it highly affects the variation of  $\mu_{80\%}$  (up to 40%);
- a large data scattering in the results depend on the level of homogeneity of the masonry samples: the larger the specimen normalized dimension ( $D/t$ ), the higher the coefficient of variation is for both  $\tau_0$  and  $G$ ;
- the reliability of the estimation of the ductility  $\mu$  is related to the level of stress for which it is computed: the higher the stress, the higher the reliability of  $\mu$ .

### 3.3.2 Size-effect of the wall

For quasi-brittle materials, the nominal strength depends on structure size [213]. Indeed, it is well known that the strength decreases with increasing structure size. The size effect is explained by fracture mechanism theory [213] which is here adopted to analyze the fracturing behavior of masonry.

Fracture mechanics have been the subject of many research studies [214, 215, 216, 217, 218, 219, 220], in which it was shown that the classical Linear Elastic Fracture Mechanism (LEFM) is inadequate for quasi-brittle materials. Such materials are characterized by the occurrence of microcracks before the peak load is reached. Crack propagation in quasi-brittle materials is characterized by a nonlinear and dissipative zone at the crack tip. These microcracks occur in the so-called Fracture Process Zone (FPZ), whose size is not negligible compared to the structural size. In the FPZ a significant amount of fracture energy is absorbed [221]

Linear Elastic Fracture Mechanics (LEFM) that assumes the size of the FPZ to be negligible is a coarse approximation. The inapplicability of LEFM for quasi-brittle materials is due to the fact that the FPZ in quasi-brittle materials is large compared to the structure size. This, in turn, is due to the large size of material heterogeneity.

Mechanics approach proposed in [119] suggests that size effect on strength is related primarily to the largeness of the FPZ in quasi-brittle materials. Indeed, the behavior of the FPZ needs to be directly simulated. For this purpose, several mathematical and numerical models can be found in the literature (i) cohesive (or fictitious) crack models [217] simulates the FPZ as a line. It is assumed that the fracture is already formed, but the two adjacent surfaces can still transmit stresses; (ii) crack band models [222] for fracture of concrete explicitly introduce in the formulation the width of the FPZ which is considered as a material property. In these models, the strain distribution is constant across the FPZ and there is a discontinuity at the FPZ boundaries; (iii) non-local models [223] involve the definition of a characteristic internal length that describes the heterogeneous nature of quasi-brittle material. The strain distribution in the FPZ is continuous and smooth. They are quite demanding in terms of computational cost and require the use of adaptive mesh procedures; (iv) meso-models simulate directly the complexity of the meso-structure of quasi-brittle materials allowing precise modeling of the phenomena undergoing in the FPZ in both 2D [224] and 3D [225]. In order to reduce the computational demand intrinsic to this approach, many authors simulated the material meso-structure by replacing the continuum by a system of discrete elements [172, 226].

For more details on the size effect of quasi-brittle materials, the reader is re-

ferred to the classical fracture mechanics textbook of Bazant and Planas [213].

Size effect has already been studied for concrete [227, 119, 228, 220] and brick masonry [229]. However, there is a significant lack of information about the size effect of stone masonries. Here, for the experimental investigation of this phenomenon, the geometrical and material similitude, and a minimum size range of 1:4 [230] are required for test samples. These requirements have discouraged the experimental study of the phenomenon over the years. Hence, a proper numerical investigation of size effect on stone masonries is carried out in this work and described below.

Here, the Lattice Discrete Particle Model (LDPM) is adopted to investigate the size effect on the sample size. LDPM is capable to overcome most of the limitations underlying the aforementioned numerical approaches and allows to model masonry fracturing behavior at the meso-scale. LDPM is able to simulate the heterogeneity and anisotropy of masonry made of stone aggregates embedded in an irregular matrix of weak lime or clay mortar. The damage evolution phenomenon of quasi-brittle materials is captured, starting from cracks localization, propagation to the overall collapse.

Five series of masonry specimens characterized by different sizes were simulated under diagonal compression. The specimen reference size of 1.2 m was scaled with a factor of 2 within the range of 0.5:8. As often done in the literature, the samples were geometrically scaled in 2D, namely the thickness was kept constant for all sizes and equal to 0.5 m. For each panel size, 50 different simulations were carried out by using 50 random stone arrangements. Furthermore, a unique granulometric distribution was adopted for the generation of the masonry specimens by using  $d_0 = 50$  mm,  $d_a = 250$  mm and  $n_F = 1.7$ .

Dimensions of the five sets assumed for the masonry specimens are listed in Table 3.6. The LDPM parameters governing the mechanical response of stone masonry are assumed as the same as those employed for the study of the particle distribution effect, and listed in Table 3.7.

**Table 3.6:** Specimen size employed for the investigation of the size effect of stone masonry panels. Value of reference dimension  $D_0$  is equal to 1.2m and it corresponds to the masonry wall size according to the ASTM.

Test name	$D/D_0$	Width [m]	Height [m]	Thickness [m]
D0.6	0.5	0.60	0.60	0.50
D1.2	1	1.20	1.20	0.50
D2.4	2	2.40	2.40	0.50
D4.8	4	4.80	4.80	0.50
D9.6	8	9.60	9.60	0.50

**Table 3.7:** LDPM mechanical parameter values employed for the stone masonry material.

$E_0$	$\alpha$	$\sigma_t$	$G_t$	$n_t$	$\sigma_s/\sigma_t$	$\sigma_{c0}$	$\sigma_{N0}$	$H_{c0}$	$\mu_0$
[MPa]	[-]	[MPa]	[N/m]	[-]	[-]	[MPa]	[MPa]	[-]	[-]
1120.0	0.065	0.3	13	0.1	1.35	125	42	0.4	0.2

Figure 3.23 shows the geometrical scheme assumed for the size effect investigation, in which the scale factor  $n$ , equal to  $D/D_0$ , is assumed equal to 0.5, 1, 2, 4, and 8. Moreover, it is worth noting that also the sizes of the two L-shape plates proportionally increased by the same factor  $n$ .

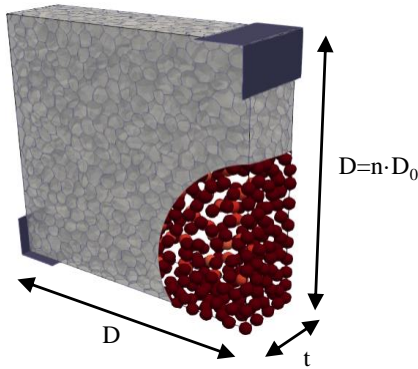
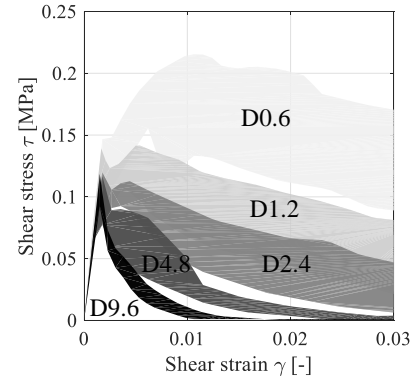
**Figure 3.23:** Size effect scheme adopted in the LDPM simulation.

Figure 3.24 shows the effect of the sample size on their mechanical response, expressed by the correlation between shear strain and shear stress ( $\gamma$ - $\tau$ ), under diagonal compression tests. One can observe that the larger the masonry specimen size, the more brittle the material behaves. Indeed, as observed for concrete materials, it is well known that quasi-brittle structures become more brittle as their size increases [230, 231]. This phenomenon is related to fracture energy dissipation, which varies with the width of the FPZ. By increasing the specimen size, the dissipated fracture energy decreases due to the decrease of the FPZ.

Moreover, Figure 3.24 shows that the larger specimen size is, the lower is the scattering of the results. That dispersion may be due to the rocking effect that is a predominant phenomenon that occurs when particle sizes are close to the specimen sizes. As already observed in the study of the stone distribution effect (Section 3.3.1), the large data scattering of the results depends on the level of homogeneity of the masonry samples: the bigger the specimen size, the higher the homogeneity level. From Figure 3.24 one can observe that the maximum shear stress  $\tau_0$  exhibits size effect.

Values of  $\tau_0$  are reported in Figure 3.25a as a function of the size of the masonry panels  $D$ . In this figure, one can observe a clear decrease in  $\tau_0$  value by increasing  $D$ . In particular, this trend is quite evident from the  $D0.6$  test to the  $D2.4$  one, whereas  $\tau_0$  is kept almost constant for  $D$  bigger than 2.4 m. For a better



**Figure 3.24:** Mechanical response computed by varying the size specimens.

interpretation of the results, Figure 3.25b shows a correlation between  $\tau_0$  and the sample dimension  $D$  in a log-log scale representation. In particular, it is possible to notice that the linear regression of results provides a slope equal to  $-1/2$  until the specimens are smaller than  $D = D_0 = 1.2$  m. This trend is consistent with the LEFM, which gives nominal strength inversely proportional to the square root of size. In contrast, by increasing the specimen sizes, for  $D > 1.2$  m, one can observe that the correlation tends to a horizontal asymptote.

Figure 3.25a plots the shear strength  $\tau_0$  versus the sample size  $D$  and one can see that the average  $\tau_0$  decreases from about 0.18 MPa for  $D = 0.6$  m to 0.12 MPa for  $D = 9.6$  m – a 50% difference. However, most of the reduction occurs for  $D < 3$  m, and the shear strength remains fairly constant for larger sizes. This behavior is consistent with the so-called Type 1 size-effect [126, 232] typical of samples without sharp notches. The log-log plot of  $\tau_0$  vs.  $D$  shown in Figure 3.25b highlights with additional clarity the size effect transition. Indeed, one can see that the slope of the log-log plot is close to  $-1/2$  for sizes between 0.6 and 1.2: this is the fracture mechanics controlled regime. For large size, the behavior transitions to a purely brittle behavior. For smaller sizes, the behavior is supposed to be purely plastic and the size effect curve should feature another horizontal asymptote coinciding with the plastic limit. This regime is not visible in neither Figure 3.25b. This shows that in disordered masonry structures the plastic limit is only relevant to very small sizes of negligible practical relevance. This is a very important observation since all existing design guidelines are based on the assumption of plastic behavior and limit analysis. As far as the scatter of the predicted response as a function of size is concerned, the results show that the scatter decreases for increasing size. This is consistent with the results presented earlier in this paper and it is due to the fact that the particle size does not scale with the specimen size and so larger sizes are less heterogeneous than smaller ones. The same phenomenon was previously observed for concrete by Cusatis and his collaborators [233].

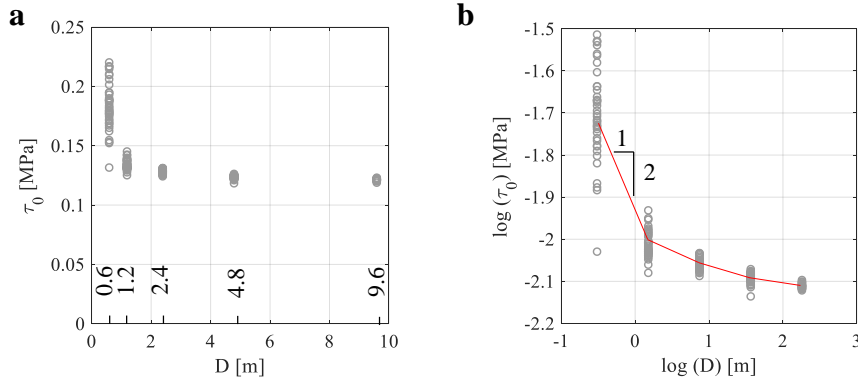


**Figure 3.25:** a) Representation of the maximum shear stress  $\tau_0$  as function of specimen size  $D$ ; b) log-log scale representation for  $\tau_0$  as function of  $D$ .

The ductility of the masonry samples is also strongly affected by the sample size. This is first and foremost demonstrated by the stress vs. strain curves whose post-peak becomes steeper for increasing size. This phenomenon can be characterized quantitatively by the plot of  $\mu_{80\%}$  vs.  $D$  shown in Figure 3.26. One can see that  $\mu_{80\%}$  drops from about 1.6 for  $D = 0.6$ m to 1.1 for  $D = 2.4$ m and it approaches asymptotically the purely-brittle value of 1 for larger sizes.

The results demonstrate that relying on typical experiments on laboratory samples leads to almost 30% overestimation of the ductility of actual masonry walls for which  $D > 5$ m. The reason for this behavior can be traced back to the issue of damage localization.

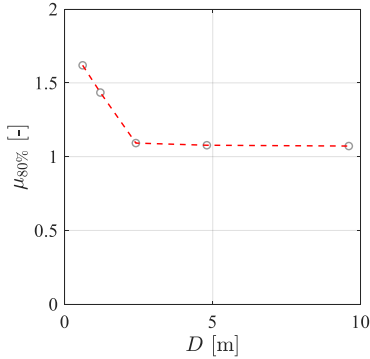


**Figure 3.26:** Size effect on ductility parameter,  $\mu_{80\%}$ .

To investigate this aspect, Figure 3.27 reports the contours of the LDPM effective crack opening defined as:  $w = [w_N^2 + w_M^2 + w_L^2]^{1/2}$ , where  $w_N = \ell(\varepsilon_N - \sigma_N/E_N)$  and  $w_i = \ell(\varepsilon_i - \sigma_N/E_T)$  ( $i = M, L$ ).

In Figures 3.27, the samples are shown consistently with their size. On the contrary, in Figures 3.28– 3.32, zoomed-in portions of the samples are depicted as having the same size to provide a better view of the cracks in the smaller samples. These figures show the crack opening at failure on the masonry specimen for the shear strain  $\gamma$  equal to 0.02. As one can see, the width of the damaged zone, which corresponds to the width of the fracture process zone (FPZ) and is visualized by the dark areas, does not scale with the size. Indeed for the smallest sample size (Figure 3.28) the damaged zone is almost as large as the sample itself. On the

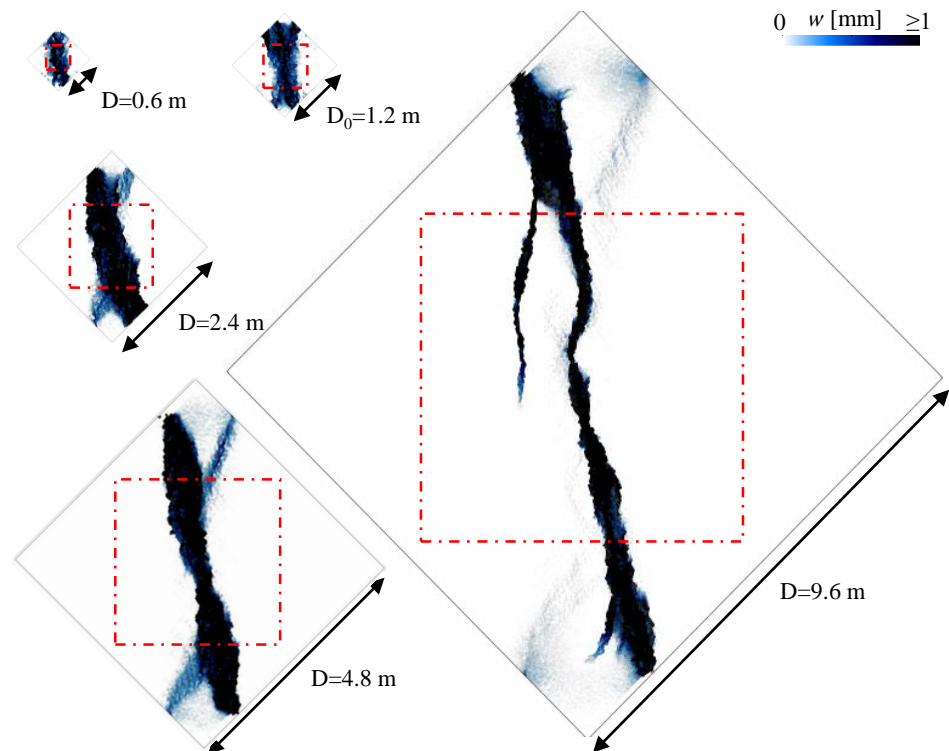


**Figure 3.27:** Contours of crack opening at failure  $w$  of the D0.6, D1.2, D2.4, D4.8, and D9.6 specimens.

other extreme, for the largest sample size (Fig. 3.32), the damaged zone is very localized along the diagonal of the panel.

Definitely, for large sizes, the size of the FPZ can be negligible compared to the size of the specimen, which allows using and characterizing the material based on LEFM as it behaves in a brittle way. For the same material, as the specimen size becomes smaller, the aforementioned assumption is not valid anymore and one needs to employ theories for quasi-brittle materials.

This result is remarkable as it seems to deviate from the widely accepted energetical size effect or Size Effect Law (SEL). Indeed, Bazant derived this size effect law that now bears his name from equivalent LEFM [213]. However, one primordial assumption in LEFM is the presence of a sharp notch, that is not the case in the performed numerical simulations. For unnotched geometries, Bazant proposed an empirical-based formulation as an extension of the classical SEL, by matching the plastic asymptote to the elastic limit [234]. In a recent work [232], the crack initiation and propagation from a smooth surface were numerically studied using a cohesive model and it was demonstrated that as the size increases, the strength tends to the elastic limit. Such a trend is here confirmed using the LDPM, which is equipped with more complex constitutive equations.

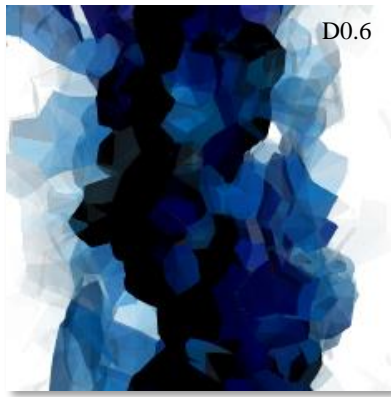


**Figure 3.28:** Zoom in of the crack opening at failure on the central part of the specimen (Figure 3.27) concerned the D0.6 case.

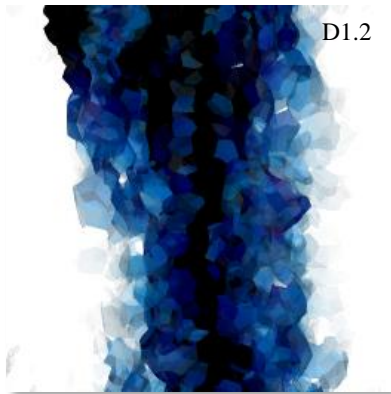


**Figure 3.29:** Zoom in of the crack opening at failure on the central part of the specimen (Figure 3.27) concerned the D1.2 case.

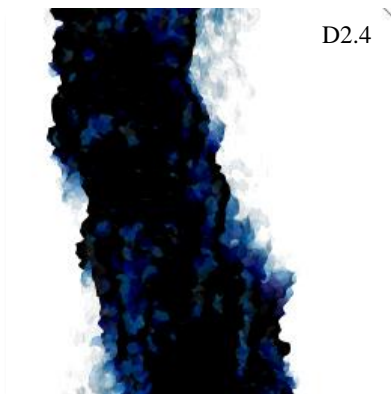


**Figure 3.30:** Zoom in of the crack opening at failure on the central part of the specimen (Figure 3.27) concerned the D2.4 case.

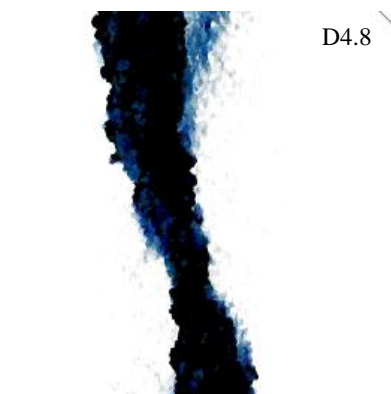


**Figure 3.31:** Zoom in of the crack opening at failure on the central part of the specimen (Figure 3.27) concerned the D4.8 case.

By assuming that the fracture process zone FPZ is related to the average breadth of the crack opening occurred on the samples, one can correlate the FPZ as a function of the dimension  $D$  of the masonry specimens. In the graph of Figure

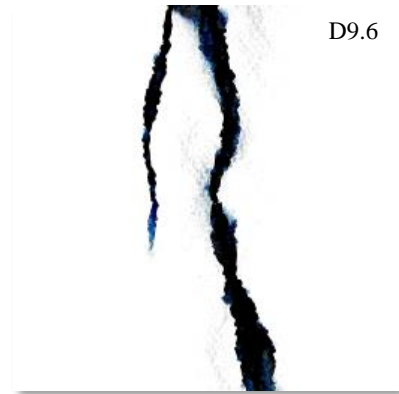
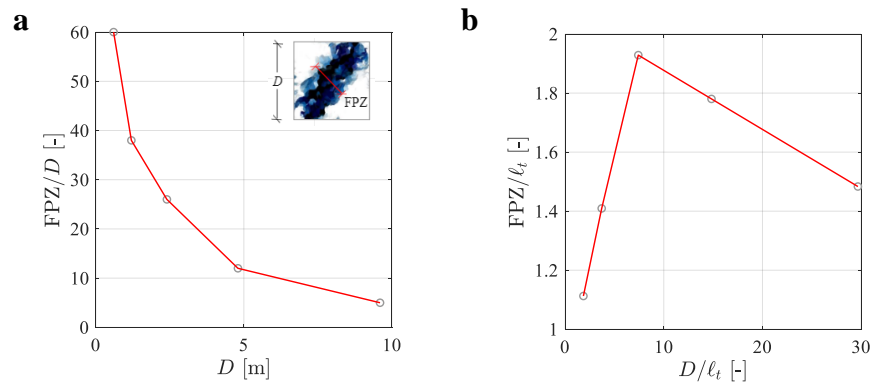


**Figure 3.32:** Zoom in of the crack opening at failure on the central part of the specimen (Figure 3.27) concerned the D9.6 case.

3.33a, one can observe on the abscissa the value of  $D$ ; on the ordinate the value of the FPZ normalized respect of the specimen dimension  $D$ . The  $FPZ/D$  value may represent the amount of the damage on the masonry specimen.

For  $D=0.6$  m, one can see that almost 60 % of the specimen is damaged. The damage amount decreases up to arrive to  $D=9.8$  m where only about 5 % of the specimen is damaged. This demonstrates again the occurrence of damage localization, which, ultimately leads to a significant reduction of the ductility. Figure 3.33b shows the correlation between the measure of the Fracture Process Zone FPZ and  $D$ , which are both normalized respect of the tensile characteristic length  $\ell_t$ . In particular, one can see that the FPZ size first increases and then slightly decreases for increasing size but its value is always between one to two times the characteristic length of the material.

**Figure 3.33:** Correlation between the measure of the Fracture Process Zone FPZ (normalized respect of the specimen dimension  $D$ ) as function of  $D/D_0$ .



Definitively, this paragraph has presented a numerical study of the size effect on the maximum shear stress  $\tau_0$  of masonry panels. In particular, five size sets of square masonry specimens were tested under the diagonal compression test by assuming dimension  $D$  of 0.6 m, 1.2 m, 2.4 m, 4.8 m, and 9.6 m. Each mechanical response computed for the five specimen size were characterized by envelope curves  $\tau - \gamma$  obtained assuming 50 random stone arrangements. Results highlighted that:

- the mechanical response is consistent with the theory of linear elastic fracture mechanics for specimen sizes smaller than  $D = 1.2$  m (slope of the linear regression between  $\tau_0$  and the normalized sample dimension  $D/D_0$  in a log-log scale representation provides an angular coefficient equal to  $-1/2$ );
- the maximum shear stress  $\tau_0$  tended to be almost constant for specimen larger than 1.2 m. This asymptote corresponds to the elastic limit;
- the mechanical behavior becomes brittle as the specimen size increases due to the decrease of the Fracture Process Zone (FPZ);
- the larger the specimen size, the lower the data scattering of the results in the post-peak behavior.

It is worth noting that only randomness solely due to the variable stone distribution has been introduced. Spatial randomness of material properties and consequently the resulting statistical size effect are not taken into account. Results show that the LDPM is able to successfully capture fracture and failure mechanisms depending on the size effect.

### 3.3.3 Effect of the configuration test

Here, the study is focused on a particular aspect that is usually not considered as relevant in the diagonal compression tests. In particular, both the standard codes (ASTM and RILEM) for the evaluation of the shear properties through diagonal compression test are referred to a specific configuration test, in which the panel is kept in a vertical configuration while the compressive load is applied along the direction of  $90^\circ$  (see Figure 3.34). However, most of the time, especially for the URM case, the masonry specimens are usually kept in a horizontal configuration while the load is applied along an inclined direction of  $45^\circ$ , due to brittleness of the masonry panels and to reduce the risk of damaging the panels. However, the correct evaluation of the shear strength of the masonry walls can also be influenced by boundary conditions that, even if they may be considered as detail aspects, can affect the propagation of the fracture in the wall panels and, therefore, their mechanical response.

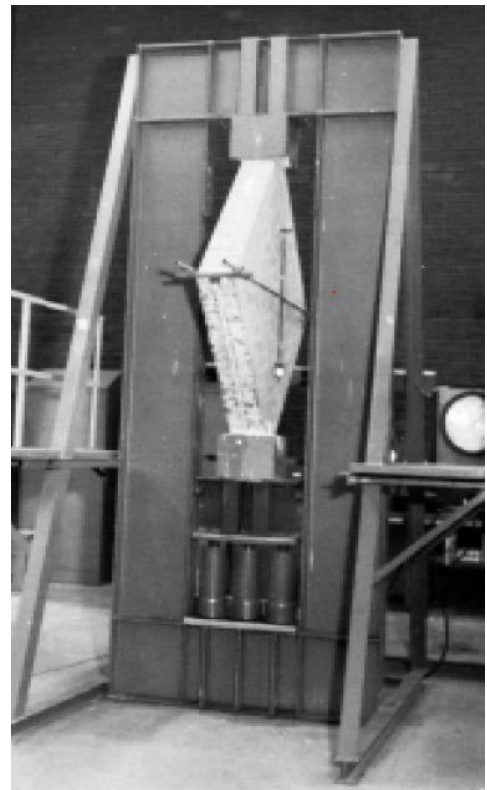


**Figure 3.34:** Apparatus for determination of the shear strength of masonry specimen, according to ASTM code.

Here, a LDPM investigation of the effect of the two different configurations on the evaluation of the mechanical properties of stone masonry is carried out. Indeed, LDPM is able to successfully capture fracture and failure mechanisms that would otherwise be difficult to investigate through an experimental campaign or by numerical modeling based on the FEM. Figure 3.35 shows the two different configurations, S1 and S2, that are usually adopted for the diagonal compression

test. These configurations were assumed for the LDPM simulations aiming to evaluate the mechanical parameters of the masonry wall, namely the shear strength  $\tau_0$ , the shear modulus  $G$ , and the ductility parameter  $\mu$ .

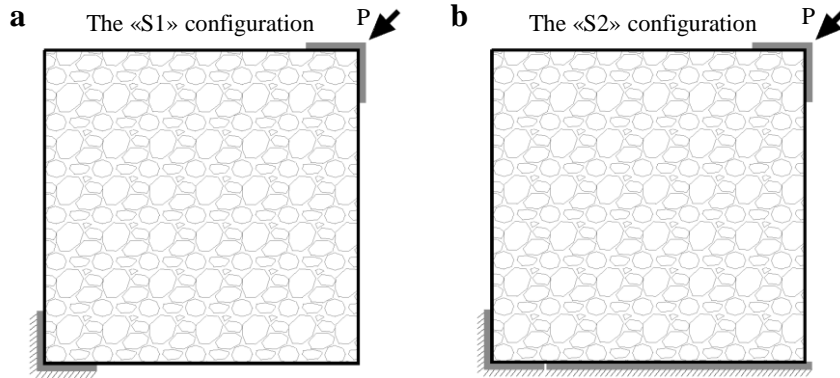


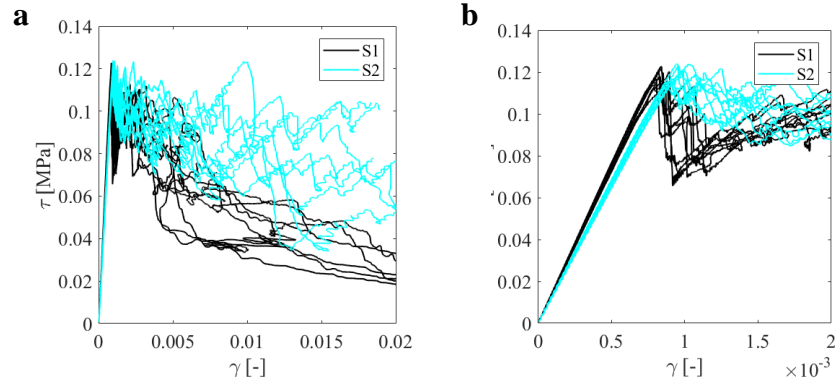
**Figure 3.35:** Two different test configurations (S1 and S2) adopted for the characterization of shear parameters of the masonry wall.

For the LDPM simulations, the two steel L-shaped plates (placed at the specimen corners) and the horizontal steel plate (placed at the specimen basement) were modeled as rigid triangular shell elements. A sliding with ‘stick-slip’ friction constraint [212] between the corner plates and the masonry particle nodes was used. and simulating high friction conditions at the L-shape plates-specimen interfaces by assuming static and dynamic friction coefficient  $f_s = f_k = 0.5$ . Moreover, a contact bond with friction constraint was assigned between the base plate and the masonry particle to sustain the specimen after the failure occurred. A static friction coefficient  $f_s = 0.1$  and a dynamic friction coefficient  $f_k = 0.0084$  were assumed to simulate the low friction conditions at the basement-specimen interface. The rotations perpendicular to the normal plate directions were fixed for all particle nodes in contact with the corner plates (L-shape).

Since mechanical responses are highly affected by the arrangement of the stone in the masonry specimen (see in Section 3.3.1), simulations were carried out for both the configurations (S1 and S2) by using 10 random stone configurations.

In Figure 3.36a, one can observe the mechanical response of stone masonry panels under diagonal compression tests. The numerical responses are expressed by the correlation between the shear strain and shear stress ( $\gamma$ - $\tau$ ). From that graph, it is possible to observe the effect of the two different configurations on the mechanical response of the panels, especially in the post-peak behavior. To better appreciate the difference in terms of strength and stiffness of the masonry panels Figure 3.36b shows the zoom-in of the first branch of Figure 3.36a. In particular, no substantial differences can be observed in terms of the shear strength  $\tau_0$ . Instead, one can observe a decrease in the shear modulus  $G$  of the masonry panels for the S2 configuration, as compared to the S1 configuration. In particular, a difference of about 23% is observed by comparing the mean shear modulus computed for the S1 case (68 MPa) and the mean shear modulus for the S2 case (52 MPa).

**Figure 3.36:** a) Numerical responses carried out for the configurations S1 and S2; b) zoom in of the results to better observe the difference in terms of stiffness between S1 and S2.



Then, after the achievement of the maximum shear stresses, that occurred for  $\gamma$  almost equal to 0.001 for both the configurations, one can see a higher load-bearing capacity for large deformations for the S2 case, as compared to the S1 case. In particular, after the achievement of that stress, an almost sudden drop in the shear stress is observed for the S1 case due to the brittleness of the specimens. Then, a slight re-hardening can be observed. This may be related to the rocking phenomenon that occurs between the stones. Hence, for the S1 configuration, 80% of the shear strengths in the post-peak behavior is observed almost in correspondence of the same  $\gamma$  of the maximum shear stress ( $\gamma = 0.001$ ). Instead, 80% of the shear strengths of the S2 case is observed for almost  $\gamma = 0.003$ .

The difference between the mechanical responses obtained for the two configurations can be explained as follows: (i) for the S1 configuration, the fracture propagation and the damage evolution on the walls occurred exclusively along the compressed diagonal of the panel leading to an almost sudden failure of the specimens; (ii) for the S2 configuration, one can have higher confinement of the specimens due to the bottom basement that supports the walls. Hence, once the cracks on the specimens occur along the compressed diagonal, the upper portion of the panels tends to slip along that diagonal increasing the load-bearing capacity of the panel due to the rocking phenomenon between stones.

Definitely, the results of Figure 3.36 highlighted that the different boundary conditions regarded the two configurations may affect the evaluation of the ductility of the stone masonry panel.

In addition, one can also observe an increase in the scattering of the results in the post-peak behavior of the  $\tau - \gamma$  plots for the S2 configuration, as compared to the S1 one.

Figure 3.37 and Figure 3.38 show the crack opening at failure for three unreinforced specimens characterized by different stone arrangement by using the S1 and the S2 configurations, respectively. The failure plots correspond to a value of the macroscopic shear strain  $\gamma$  equal to 0.01.

In particular, in Figure 3.37 (S1 configuration) one can observe that fracture mainly propagated along the compressed diagonal of masonry panels. This is due to the fact that almost pure tension occurs.

On the contrary, in Figure 3.38 (S2 configuration) one can see, apart from the fracture propagation along the compressed diagonal, also a typical flexural failure on the side of the specimens. The triggering of additional cracks on the side of the wall is due to the boundary condition at the basement of the specimens.

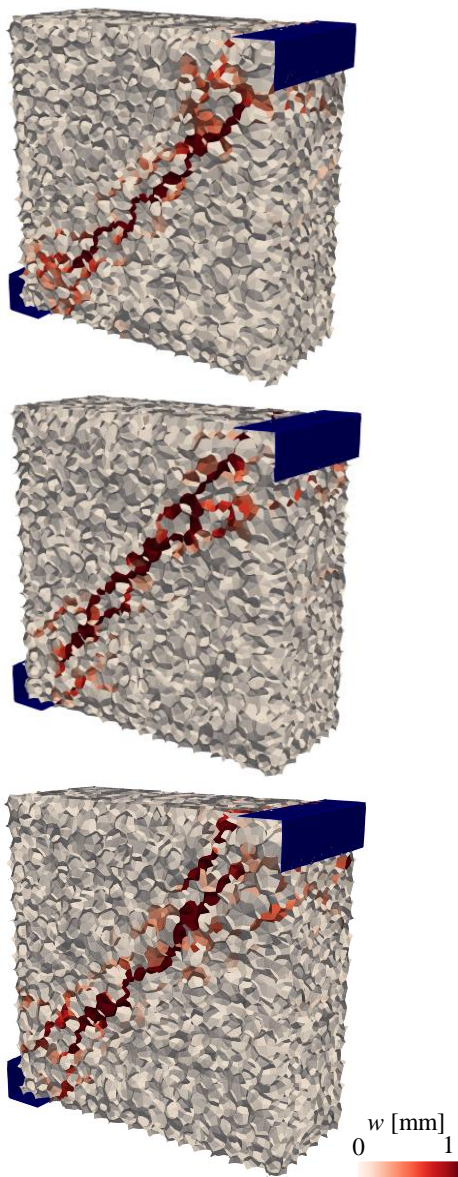


**Figure 3.37:** Contours of meso-scale crack opening at failure for three unreinforced masonry specimens at  $\gamma=0.01$ , by adopting the S1 configuration ( $w$  is the crack opening).

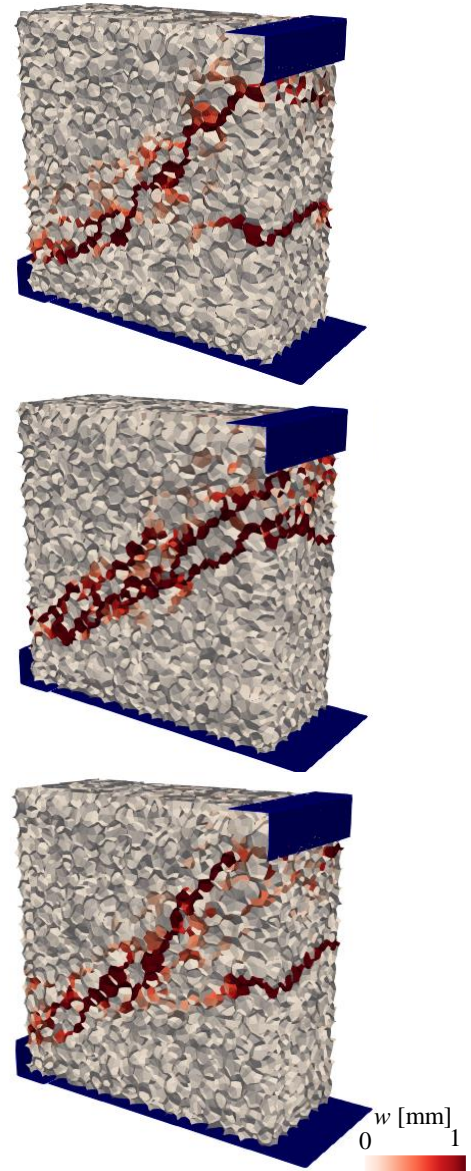


**Figure 3.38:** Contours of meso-scale crack opening at failure for three unreinforced masonry specimens at  $\gamma=0.01$ , by adopting the S2 configuration ( $w$  is the crack opening).

### 3.4 Simulation of stone masonry walls reinforced by FRCM system

Despite the scientific interest in chaotic stone constructions, which has significantly increased in recent years [235, 108, 236, 27, 237], available experimental data is scattered and a large number of tests would be required to obtain consistent results. The experimental results, provided in Chapter 2, relevant to stone masonry walls strengthened by Glass-FRCM (FRCM) with a lime-based mortar and tested under diagonal compression were simulated by using the computational framework based on the so-called Lattice Discrete Particle Model (LDPM) [175, 176].

In particular, the experimental and numerical investigations presented here offer a better understanding of the variables affecting the mechanical behavior and damage evolution of stone masonry panels reinforced by the FRCM systems, namely the thickness of the reinforcement, the bond behavior at the FRCM-masonry interface, the presence or not of fiber anchors and fiber grids in the strengthening system.

The geometrical characterization of the meso-structure is defined by a set of parameters reported in Table 3.8. In particular, the stone-mortar ratio  $a/c = 3.4$  which corresponds to the ratio between the volume of the stones (equal to 77.5% of the total volume of the specimen) and the lime mortar volume (equal to 22.5%) used to prepare the masonry specimens in the lab. The water-mortar ratio  $w/c = 0.5$  was assumed based on the mix design adopted to build the laboratory specimens. Mortar content parameter  $c$  is computed with the goal to obtain a total mass density  $\rho_{masonry}$  equal to  $1800.0 \text{ kg/m}^3$  (according to [113]) by the following formula:  $\rho_{masonry} = c [1 + w/c + a/c]$ .

**Table 3.8:** The LDPM mix design parameter values adopted for the simulation of the stone masonry material.

$c$ [kg/m <sup>3</sup> ]	$w/c$ [-]	$a/c$ [-]	$n_F$ [-]	$d_0^i$ [mm]	$d_a^i$ [mm]	$d_0^e$ [mm]	$d_a^e$ [mm]
367.35	0.5	3.4	0.5	32	64	80	220

For the surface particles, the dimension of the aggregate pieces adopted to represent the real dimension of the stones are chosen between  $d_0^e = 80 \text{ mm}$  and  $d_a^e = 220 \text{ mm}$  by using the particle generation procedure described in Section 3.2.1.

For the internal particles, the particle size adopted to represent the internal aggregate distribution is chosen within the range  $d_0^i = 32 \text{ mm}$  to  $d_a^i = 64 \text{ mm}$  in order to model only the *very coarse gravel* (pebbles) subclasses [201]. The Fuller coefficient  $n_F$  was assumed to 0.6.

The composite nature of the masonry makes it difficult to assign material properties, which depend on many factors as described above. For this reason,

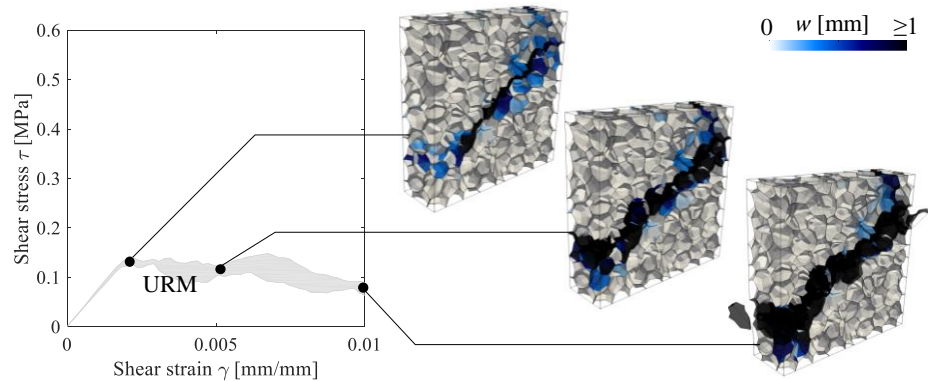
the first important part of the project consisted of calibrating the LDPM parameters in order to reproduce the mechanical behavior observed during experimental tests. In particular, the calibration process consisted of the best fitting of the  $\tau$ - $\gamma$  experimental curves recorded during the diagonal compression tests as well as the compressive strength of unreinforced samples in the range from 0.8 MPa to 1.2 MPa chosen on the basis of Standards [113, 238, 239] and experimental tests [211, 210, 240]. Table 3.9 shows the parameters obtained by the calibration procedure.

**Table 3.9:** LDPM mechanical parameter values employed for the stone masonry material.

$E_0$ [MPa]	$\alpha$ [-]	$\sigma_t$ [MPa]	$G_t$ [N/m]	$n_t$ [-]	$\sigma_s/\sigma_t$ [-]	$\sigma_{c0}$ [MPa]	$\sigma_{N0}$ [MPa]	$H_{c0}$ [-]	$\mu_0$ [-]
1120.0	0.065	0.3	13	0.1	1.35	125	42	0.4	0.2

Figure 3.39 shows the mechanical response, represented by the scattering area between the lower and the upper responses obtained by using three different stone arrangements, of the URM specimens under diagonal compression test. One can see that different stone arrangement leads to higher scattering in terms of softening response as compared to the strength of the walls. This phenomenon has been better discussed in the Section 3.3.1. The response of Figure 3.39 have been obtained by using the geometrical and mechanical parameters listed in Tables 3.8–3.9, respectively. Moreover, that figure also shows the damage evolution of a URM specimen for different values of the shear strain  $\gamma$ . One can see that cracks mainly occur along the compressed diagonal of the panel.

**Figure 3.39:** Numerical response of the UnReinforced Masonry (URM) specimens under diagonal compression test (on the left). Cracking evolution on the specimen for different values of the shear strain  $\gamma$  (on the right).



As far as the reinforcement mortar employed in the FRCM system is concerned, the LDPM geometric parameters (Table 3.10) are selected based on the actual mixture design of the mortar used in the experiments.

**Table 3.10:** LDPM mix design parameter values adopted for the mortar material.

$c$ [kg/m <sup>3</sup> ]	$w/c$ [-]	$a/c$ [-]	$n_F$ [-]	$d_0$ [mm]	$d_a$ [mm]
480	0.5	2.25	0.5	4	4.75

The calibration of the material parameters in LDPM for mortar was obtained through the best fitting of the experimental curves relevant to 21 three-point flexural tests and to 42 compressive tests carried out at the laboratory of L'Aquila (Italy) on prismatic mortar specimens in accordance to UNI EN 1015-11 [116]. In particular, the calibration procedure was carried out to achieve a flexural strength and compressive strength equal to 4.5 MPa and 17.3 MPa, respectively, which were the average values experimentally measured (Figure 3.40). The other mechanical parameters were assumed based on the characteristics provided by the vendor Aquilaprem [112]. Figures 3.41a,b show the crack opening at failure for mortar specimens that occurred in the LDPM simulations for the compression and three-point bending tests, respectively. Other LDPM parameter values were assumed according to Pathirage et al. [185] in the absence of specific experimental data. Table 3.11 shows the mechanical parameters of the reinforcement mortar employed in the simulations.

**Table 3.11:** LDPM mechanical parameter values employed for the mortar material.

$E_0$	$\alpha$	$\sigma_t$	$G_t$	$n_t$	$\sigma_s/\sigma_t$	$\sigma_{c0}$	$\sigma_{N0}$	$H_{c0}$	$\mu_0$
[MPa]	[-]	[MPa]	[N/m]	[-]	[-]	[MPa]	[MPa]	[-]	[-]
19,750.0	0.25	3.3	23.4	0.1	1.38	150	600	0.4	0.2

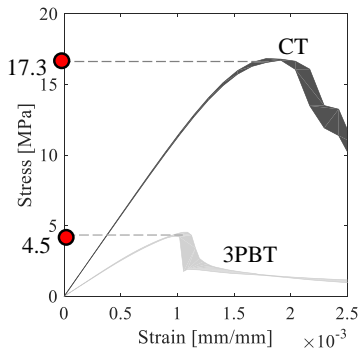


**Figure 3.40:** Numerical responses computed for the mortar samples under the three-point bending test (3PBT) and the compression test (CT)

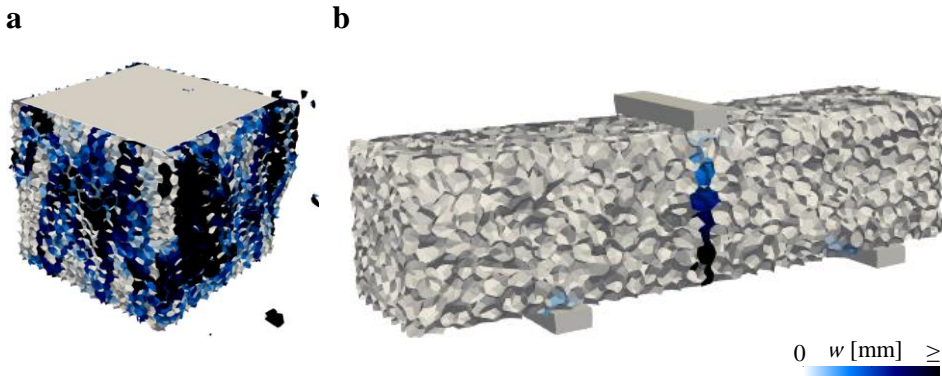
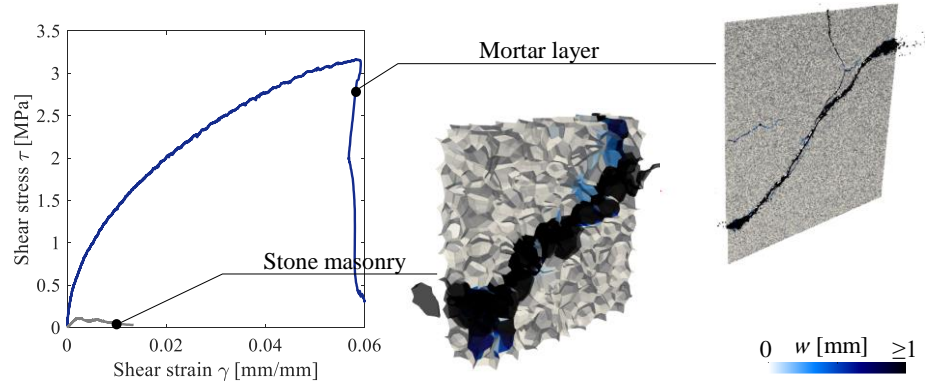


**Figure 3.41:** contours of meso-scale crack opening at failure for mortar samples at strain value equal to 0.0025 in the compression test (a) and the three-point bending test (b).

Hence, the geometry and the mechanical parameters were separately calibrated for both the masonry specimen and the mortar layer this far. In Figure 3.43 are

illustrated the responses of the two materials under the diagonal compression test. The coupling of the stone specimen and the reinforcement mortar layer will lead to a mechanical response, in terms of the shear strength, comprised between such responses.

**Figure 3.42:** Numerical responses and crack opening at failure computed for both the masonry and mortar material under diagonal test.



As far as the fiber grids are concerned, the same mechanical and geometrical properties of the experimental test were used for them. In particular, they are summarized in Table 3.12. Moreover, both the vertical and horizontal fiber strands, not constrained to each other, were modeled with elastic beam elements with equivalent rectangular sections of  $0.1 \text{ mm} \times 10 \text{ mm}$ . The fiber strands and the mortar particles were connected via a node-node penalty constraint.

**Table 3.12:** Geometrical and mechanical properties of the glass fiber used in the FRCM system ( $SG$  is the space gap,  $\rho_{fib}$  is the density,  $t_{fib}$  is the thickness of a fiber strand,  $E_{fib}$  is the fiber Young's Module,  $f_{t,fib}$  is the tensile strength,  $\varepsilon_{u,fib}$  is the ultimate strain).

$SG$ [mm]	$\rho_{fib}$ [kg/m <sup>3</sup> ]	$t_{fib}$ [mm]	$E_{fib}$ [MPa]	$f_{t,fib}$ [MPa]	$\varepsilon_{u,fib}$ [%]
25	2680.0	0.1	72000.0	1700.0	3.7

Finally, as far as the fiber anchors are concerned, they were modeled with hexahedral solid elements and assuming elastic mechanical properties (Table 3.12). The central part of the the anchors was assumed as cylindrical, whereas the ends of the anchors were modeled as 16 hexahedral elements measuring 14.7 mm in width, 0.2 mm in thickness, and 150 mm in length. These measures are equivalent to an ideal circular configuration measuring 0.1 mm in thickness and 150 mm in radius. The fiber anchors were connected to both the mortar particles and the stones via a node-node penalty constraint.

Figure 3.43 shows the modeling of the FRCM system applied on the stone masonry panel for the simulation of the diagonal compression test by LDPM.

In the following are described the other modeling criteria assumed for the LDPM simulations. Some choices are a consequence of the sensitivity analyses previously carried out and not reported in the thesis. In particular, the two steel plates (L-shape), placed at the specimen corners, and the horizontal steel plate,

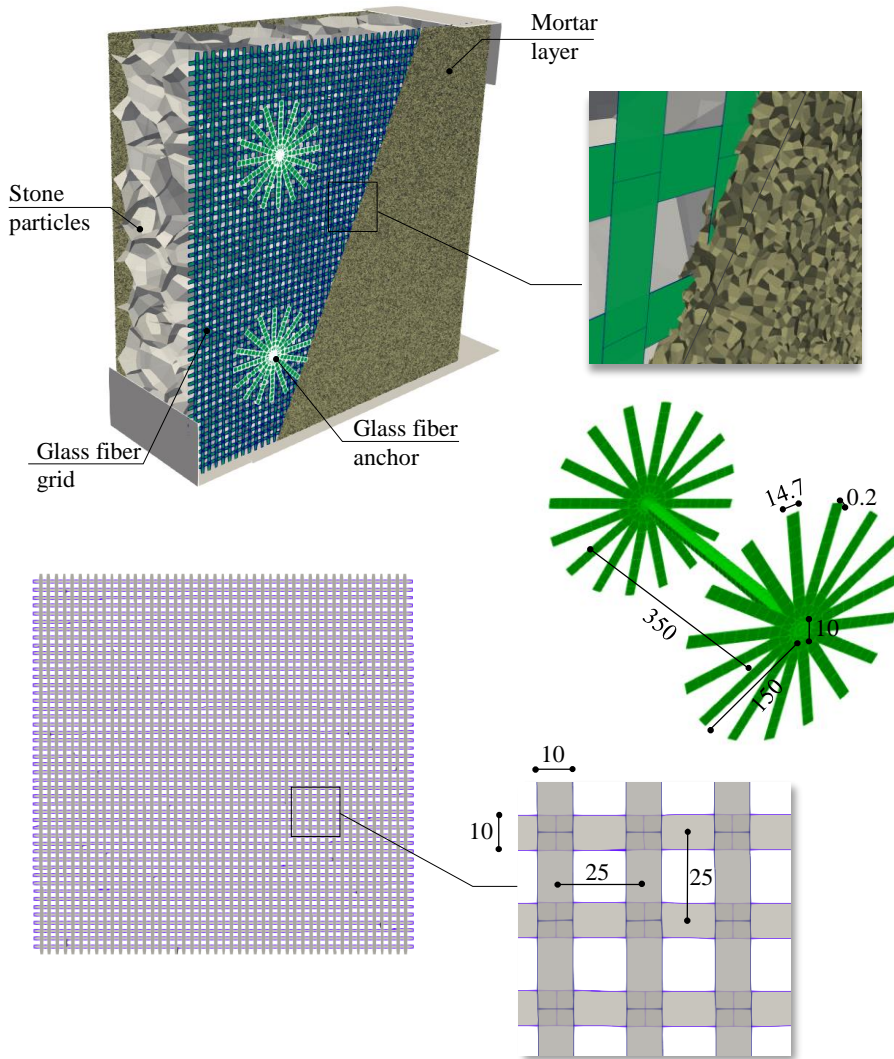


**Figure 3.43:** Stone masonry specimen reinforced with fiber grids and fiber anchors (both embedded in external mortar layers). On the right is illustrated in detail the fiber anchor modeled with hexahedral solid elements; the geometrical properties of the 16 anchor ends (14.7 mm in width, 0.2 mm in thickness and 150 mm in length) are equivalent to an ideal circular configuration (0.1 mm in thickness and 150 mm in radius).

placed at the specimen basement, were modeled as rigid triangular shell elements. A sliding with ‘stick-slip’ friction constraint [212] between the corner plates and the masonry particle nodes was used. This constraint is designed to force a set of nodes to move over a frictional surface while the constraint perpendicular to the surface is treated using a master-slave formulation. The simulations used a static friction coefficient  $f_s = 0.5$  and a dynamic friction coefficient  $f_k = 0.5$  to simulate the high friction conditions. A contact bond with friction constraint ( $f_s = 0.1$ ,  $f_k = 0.0084$ ) was assigned between the base plate and the masonry particle to sustain the specimen after the failure occurred. The rotations perpendicular to the normal plate directions were fixed for all particle nodes in contact with the corner plates (L-shape). The mortar particles were connected to the masonry sample via a frictional penalty constraint;  $f_k = f_s = 0.5$  were assumed to simulate the almost perfect bond (PB) conditions at the masonry-mortar interfaces.

Before reproducing the experimental results, a numerical investigation is pre-

sented. It offers a better understanding of the variables affecting the mechanical behavior and damage evolution of stone masonry panels reinforced by the FRM systems, namely the thickness of the reinforcement, the bond behavior at the FRM-masonry interface, the presence or not of fiber anchors and fiber grids in the strengthening system.

To investigate the benefit of the reinforcement system on the mechanical properties of the masonry panel, the reinforcement coefficients  $k_G$ ,  $k_{\tau_0}$  and  $k_{\mu}$  are introduced. They are computed by Equation 3.11 to characterize the increase of the mechanical properties (shear modulus, strength, and load-bearing capacity for large deformation) of the specimens reinforced with the FRM system as compared with the unreinforced ones. One can define these coefficients as follows:

$$k_G = \frac{G_R}{G_{NR}} ; k_{\tau_0} = \frac{\tau_{0,R}}{\tau_{0,NR}} ; k_{\mu} = \frac{\tau_{(\gamma=0.01),R}}{\tau_{(\gamma=0.01),NR}} \quad (3.11)$$

in which  $G_R$ ,  $\tau_{0,R}$ , and  $\tau_{(\gamma=0.01),R}$  are the mechanical proprieties (shear strain, maximum stress, and stress at  $\gamma = 0.01$ ) of the reinforced panels and  $G_{NR}$ ,  $\tau_{0,NR}$ , and  $\tau_{(\gamma=0.01),NR}$  are the corresponding mechanical properties of the unreinforced panels.

### 3.4.1 Mortar thickness effect

As far as the strengthening obtained only by mortar layers (without both fiber grids and fiber anchors) is concerned, numerical investigations were performed to determine the effect of the thickness  $t$  of the mortar layers on the mechanical behavior of the specimens. Values of  $t$  equal to 10 mm, 15 mm, 20 mm, 25 mm, and 30 mm were considered in the LDPM simulations.

Figure 3.44a shows the mechanical responses in terms of  $\tau - \gamma$  curves. For each value of the mortar  $t$ , three different stone arrangements were assumed. The colored areas in the graphs represent the scattering areas between the lower and the upper response curves measured in the simulations by varying the stone arrangements.

In particular, Figure 3.44a shows an increase of both the stiffness and the strength by increasing the value of  $t$ . At the same time, one can observe a more brittle behavior by increasing  $t$ .

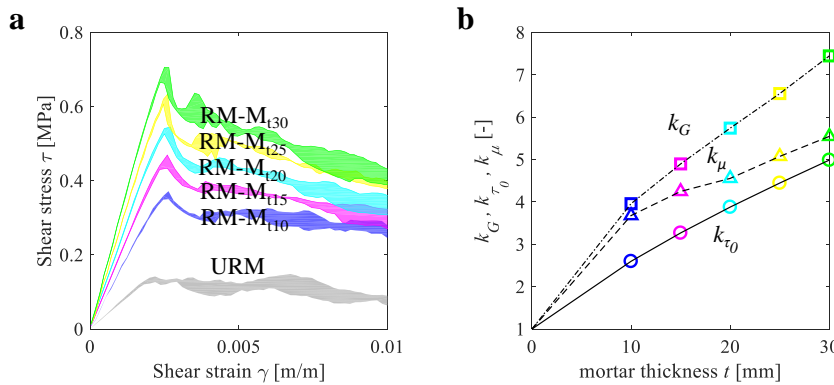


**Figure 3.44:** a) Comparison between unreinforced panels (URM) and panels reinforced by only mortar layer (without both fiber grid and anchors) having different values of thickness  $t$ : 10 mm, 15 mm, 20 mm, 25 mm and 30 mm; b) reinforcement coefficients  $k_G$ ,  $k_{\tau_0}$ , and  $k_{\mu}$  function of  $t$ .

Figures 3.44b shows reinforcement coefficient values  $k_G$ ,  $k_{\tau_0}$  and  $k_{\mu}$  (equation 3.11) as function of  $t$ . In particular, the increase in both  $k_G$  and  $k_{\tau_0}$  is almost linearly proportional to the increase of  $t$ . On the contrary, by observing the slope of the  $k_{\mu}$  curve one can notice a non-linear trend by increasing the value of  $t$ . This result suggests that the behavior of the reinforcing mortar can be approximately considered linear up to the achievement of the maximum shear stress  $\tau_0$ .

On the contrary, by observing the slope of both the  $k_{\mu}$  curve one can notice a non-linear trend by increasing the value of  $t$ . This is because, as already observed in Figure 3.44a, the higher the  $t$  value, the higher the brittle behavior is. Hence, the benefits of the mortar layer in terms of ductility decrease by increasing the value of  $t$ .

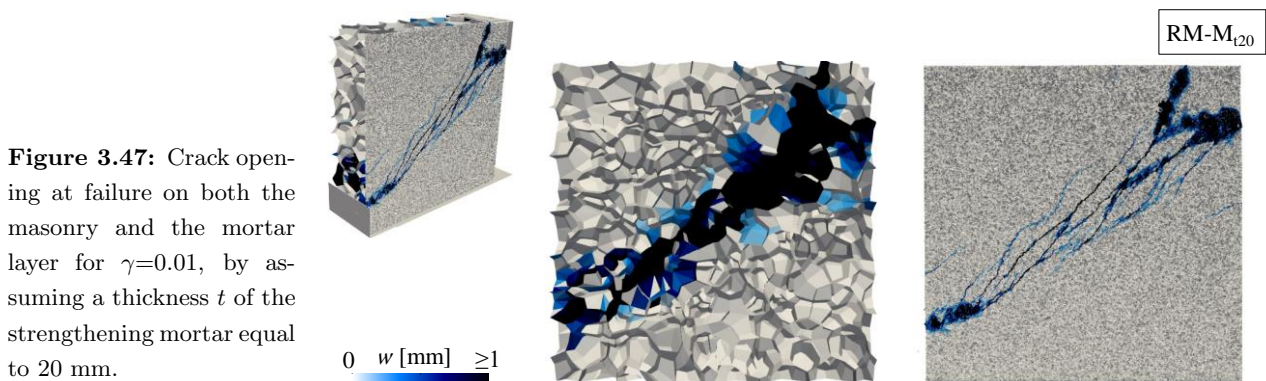
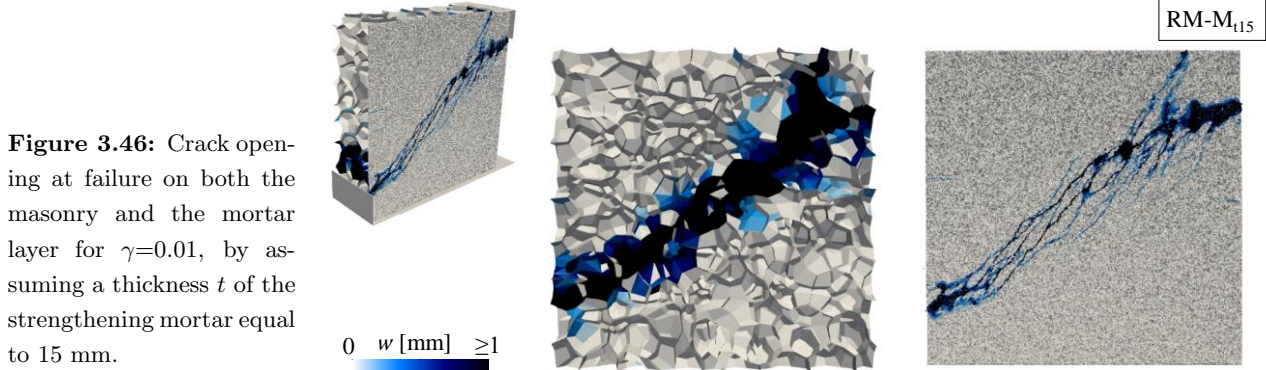
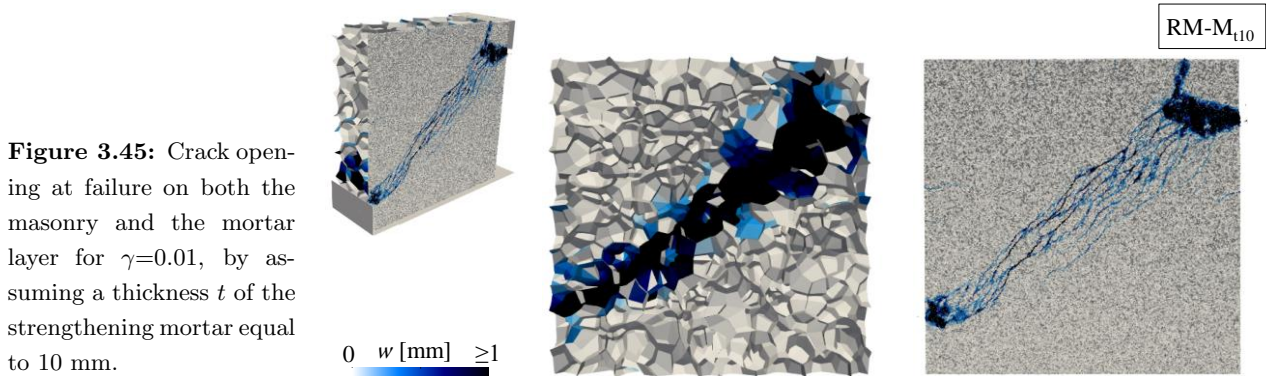
Standard CNR-DT 215/2018 proposes, as a simplification, an amplification coefficient of 1.5 for the mechanical properties of irregular stone masonry walls reinforced by FRCM. However, that coefficient, as highlighted in both experiments and simulations, can be much higher and mainly depends on the thickness of the

reinforcement mortar rather than the fiber characteristics.

A good correlation between the experimental responses and the simulation in terms of strength was observed in the case of mortar thickness  $t=20\text{mm}$ , which was the average mortar thickness applied as reinforcement on the masonry specimens.

Figures 3.45–3.47 shows the cracking opening at the failure for the masonry specimen reinforced by only mortar layers having a thickness  $t$  equal to 10 mm, 15 mm and 20 mm. No clear differences in the fracture propagation can be noticed among the cases.

Definitely, once investigated the influence of the thickness value of the mortar layers, all the following simulations have been carried out assuming  $t=20\text{mm}$ .



### 3.4.2 Bond behavior at the masonry-mortar interfaces

With the aim of investigating the effect of bond behavior at the masonry-mortar interface on the failure behavior of the panels, analyses (Figure 3.48) were conducted assuming two extreme different hypotheses for the bond behavior. First, high values of the static and dynamic friction coefficient,  $f_s = f_k = 0.5$ , were considered to simulate almost perfect bond (PB) condition. Next, small values of the static and dynamic friction coefficients,  $f_s = 0.03$  and  $f_k = 0.0084$ , were assumed (according to [176]) to simulate weak bond (WB) conditions.

Figure 3.48a shows the numerical  $\tau$ - $\gamma$  curves obtained under both the PB and WB hypotheses. In particular, one can see that the bond behavior has no effect in terms of shear modulus  $G$  and has a slight effect on the strength  $\tau_0$ . A difference of about 10% is observed by comparing the strength for the WB case (0.507 MPa) and the strength for the PB case (0.548 MPa). On the contrary, a big difference in terms of load-bearing capacity for large deformation is observed between the WB and the PB cases. Indeed, by measuring  $\tau_{\gamma=0.01}$  one can compute a stress decrease of about 60 % by comparing the PB (0.339 MPa) and WB (0.212 MPa) cases.

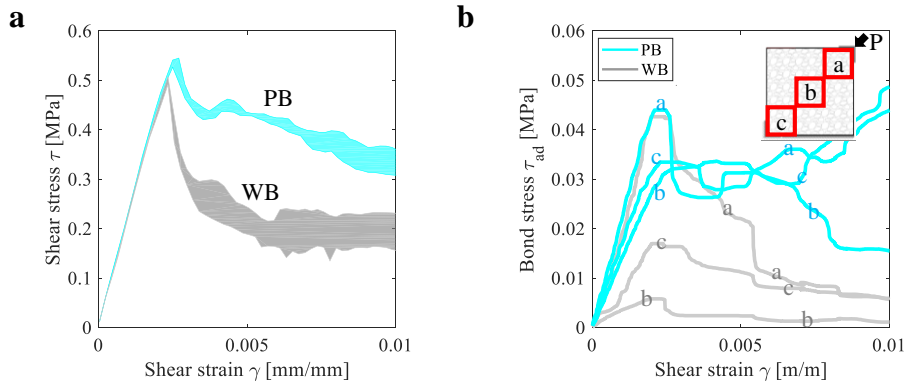


**Figure 3.48:** a) Comparison between Perfect Bond (PB) and Weak Bond (WB) hypotheses at the masonry-mortar interfaces in the case of masonry strengthened only by mortar layers; b) bond stress measured on the three external areas "a", "b" and "c" of the specimen.

Figure 3.48b shows the bond stress  $\tau_{ad} = P/A$  measured on three different square areas (called a, b, and c) at the masonry-mortar interface, where  $P$  is the load applied on the top corner of the masonry sample and  $A$  is the surface area of  $0.4 \text{ m} \times 0.4 \text{ m}$ . The simulation is conducted under both the PB hypothesis and the WB one. In particular, for both the hypotheses one can see that the area closer to the top corner (the so-called "a" in the figure) is characterized by the highest  $\tau_{ad}$ . This result highlights the fact that the reinforcing mortar on the upper corner may be more easily subjected to debonding, as compared to areas far enough from the boundary. On the other hand, the central area (the so-called "c" in the figure) is characterized by the lowest  $\tau_{ad}$ . For all the investigated areas, one can see that a drop in the bond stress was achieved for  $\gamma$  equal to about 0.003, for which the shear strength of the specimens was achieved. At that point,  $\tau_{ad}$  decreases for all

three areas because of the reduction in strength of the masonry panels.

Moreover, one can see that for the "a" area, the maximum value of  $\tau_{ad}$  is almost the same for both the cases, whereas the other areas "b" and "c" are characterized by different values of  $\tau_{ad}$  by comparing the PB case and the WB case. Finally, the plot clearly shows that for the PB case the bond stress-bearing is higher for large deformation, as compared to the WB case.

Figures 3.49–3.50 show the effect of bond behavior on the fracture propagation. Under the PB hypothesis (Figure 3.49) one can observe a more distributed cracking on the mortar surface. On the contrary, under the WB hypothesis (Figure 3.49) damage concentration on the mortar surface is clearly observed.

**Figure 3.49:** Crack opening at failure (masonry on the left and mortar on the right) for  $\gamma=0.005$ , by assuming the PB hypotheses.

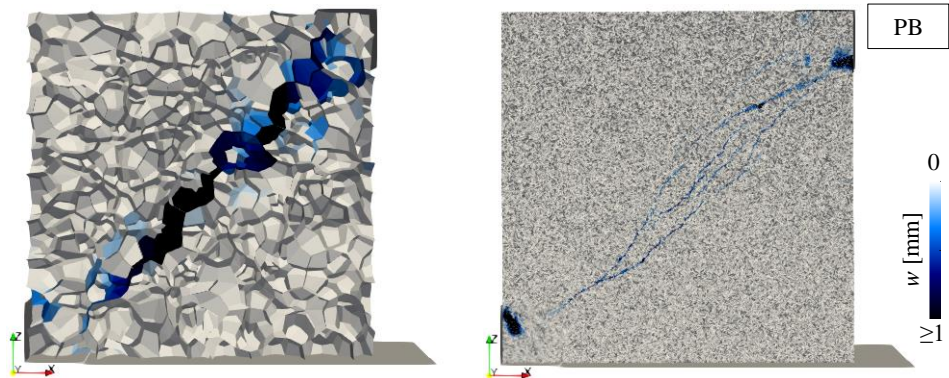
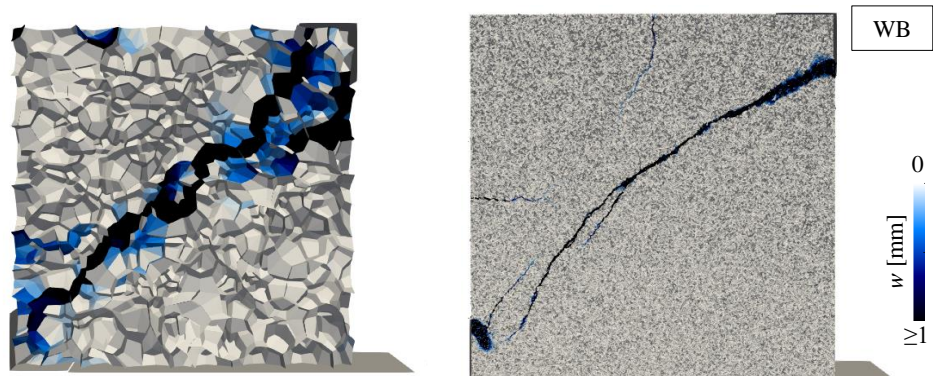


**Figure 3.50:** Crack opening at failure (masonry on the left and mortar on the right) for  $\gamma=0.005$ , by assuming the WB hypotheses.



### 3.4.3 Fiber grid effect

The glass grid consisted of vertical and horizontal fiber strands characterized by equivalent rectangular sections of  $0.1 \text{ mm} \times 10 \text{ mm}$ . The strands were not constrained to each other and, in simplified hypotheses, they were modeled with elastic beam elements ( $E_{fib}=720000 \text{ MPa}$  and  $\nu = 0.22$ ). The fiber strands and the mortar particles were connected via a node-node penalty constraint.

To numerically investigate the effect of the fiber grids on the mechanical properties of the reinforced panels, Figure 3.51a shows the comparison between the LDPM curves carried out by two different strengthening systems applied to the masonry specimens: (1) reinforcement with only mortar layers (RM-M) and (2) reinforcement with both mortar layers and fiber grid (RM-G).

A clear benefit in the ductility of the strengthening system can be attributed to the fiber grids. The increase in load-bearing capacity for large deformations ( $\gamma = 0.01$ ) can be expressed by reinforcement coefficient  $k_\mu$ : one can compute a greater value of  $k_{\mu, RM-G} = 0.523/0.084 = 6.23$  for the RM-G case as compared to the value of  $k_{\mu, RM-M} = 0.343/0.084 = 4.08$  for the RM-M case. Therefore, one can have an increase in load-bearing capacity for large deformations of about 150% by embedding the fiber grids into the mortar layers as compared with the reinforcement system made only by the mortar layers. On the other hand, the results of Figure 3.51a highlight that fiber grids have no effect in terms of both stiffness and shear strength of the specimens. This result appears to contrast with the recommendation of the standards CNR-DT 215/2018 and ACI-549 in which the contribution of the FRCM on the shear capacity of unreinforced panels is attributed to the characteristics of the fibers (geometry and mechanical properties). Simulations showed that fibers have the function to carry tensile stresses (ductility), whereas the reinforcing mortar leads to an increase of shear strength and shear modulus

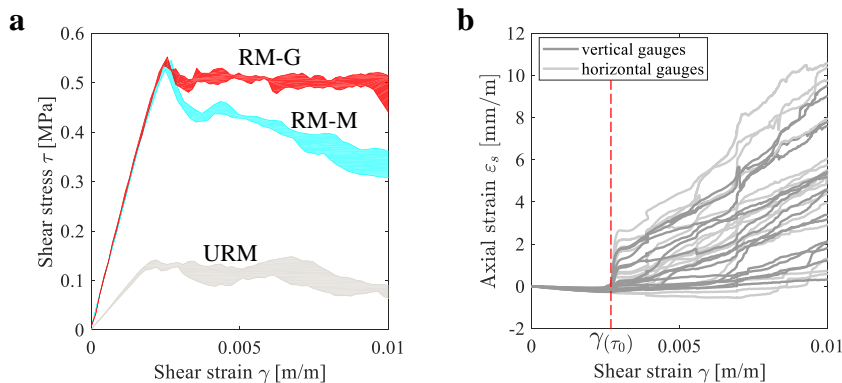
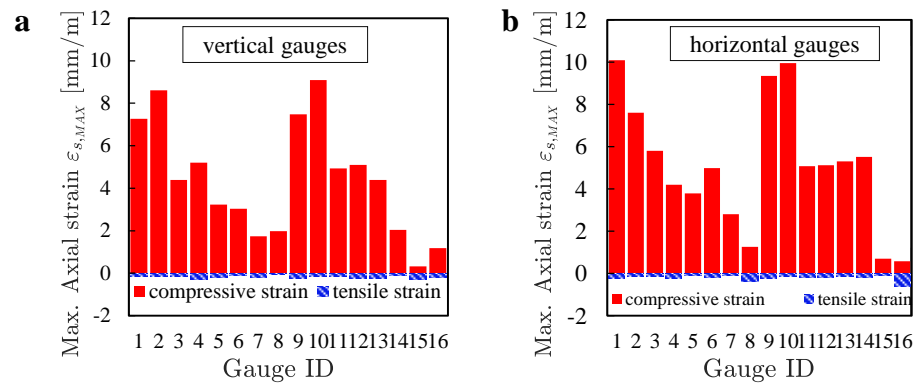


**Figure 3.51:** a) LDPM responses obtained for the URM case, the RM-M case, and the RM-G case (masonry sample strengthened by fiber grids embedded in the mortar layers); b) axial strain of both the vertical and the horizontal gauges Vs shear strain of the masonry panel of the RM-G test.

Figure 3.51b shows the axial strain  $\varepsilon_s$  of both the vertical and horizontal strands of the fiber grids measured during the LDPM simulations. It is worth noting that the axial strain of the horizontal strands was also investigated in the simulation unlike the experimental tests, where only the strain along the vertical strands was measured. In particular,  $\varepsilon_s$  is measured in correspondence to the position of the gauges of the experimental tests. It is worth noting that in Figure 3.51b one can see that the axial strain of the vertical fiber strands has an initial compressive trend (negative value) up to the achievement of the maximum shear stress (dotted line in Figure 3.51b), as already commented in the experimental results.

Figures 3.52a, b show the maximum values of the compressive and tensile axial strain  $\varepsilon_s$  of the vertical and horizontal fiber strands, respectively.

**Figure 3.52:** Maximum values of the axial strain measured along: the vertical fiber strands (a) and the horizontal fiber strands (b).

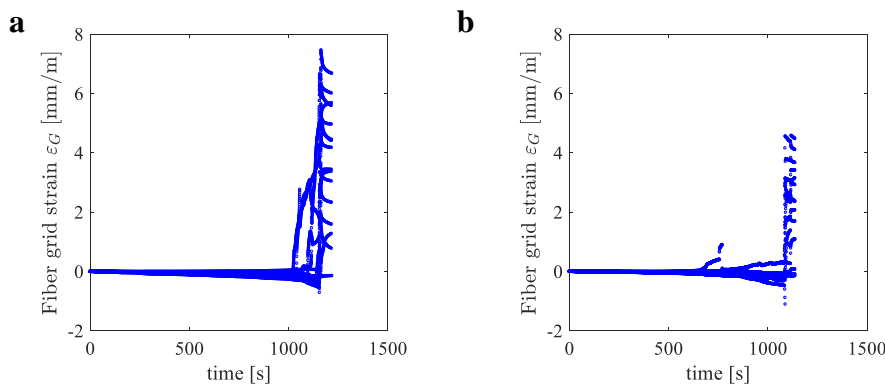


One can see in Figure 3.52a that both the minimum and the maximum values of  $\varepsilon_s$  measured on the vertical gauges are very similar to the experimental ones. In particular, the 1-9 gauge IDs, and the 2-10 ones are characterized by the highest tensile strain values (from about 7 to 9 mm/m). This means that the upper part of the specimens along its compressed diagonal is subjected to the highest crack opening due to the boundary effect, leading to the highest tensile strains of the fiber strands. No strong differences can be instead observed for the compressive strains measured for the gauges. They are almost equal to - 0.4 mm/m for all the gauges. Finally, Fig. 3.52b shows that the tensile strains of the horizontal strands are slightly higher than the ones observed for the vertical strands.

Definitely, one can observe that both the minimum and the maximum values of  $\varepsilon_s$ , measured on the vertical gauges, are really similar to the experimental ones. Indeed, one can see in Figures 3.53a, b the axial strains measured on the fiber grids during the experimental tests. In particular, Figures 3.53a, b have been already shown in Section 2.1.2.3 and are proposed again here for a better comparison with the numerical results. In particular, grids were instrumented with 16 strain gauges (8 strain gauges for each side of the specimen) placed along to the compressed diagonal of the specimen (where the cracking of the panel was expected to take place). These strain gauges recorded the axial strain only of the vertical strands

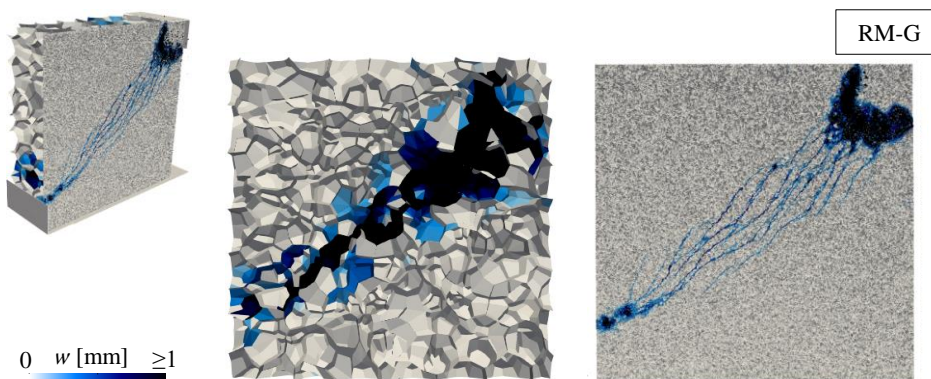
of the grid.

The only differences between numerical (Figures 3.51*b*) and experimental responses (Figures 3.53*a, b*) concerns the way in which the tensile maximum strains were achieved. Indeed, experimental tests were conducted in load-control, whereas the simulations were carried out in displacement-control. Hence, once the maximum resistance of the panel was achieved in the experiments there was an almost instant collapse of the specimens so that also the maximum value of the axial strains of the grids instantly occurred. On the contrary, simulations allowed to obtain similar values of the axial strains, as compared to the experiments, not instantly.



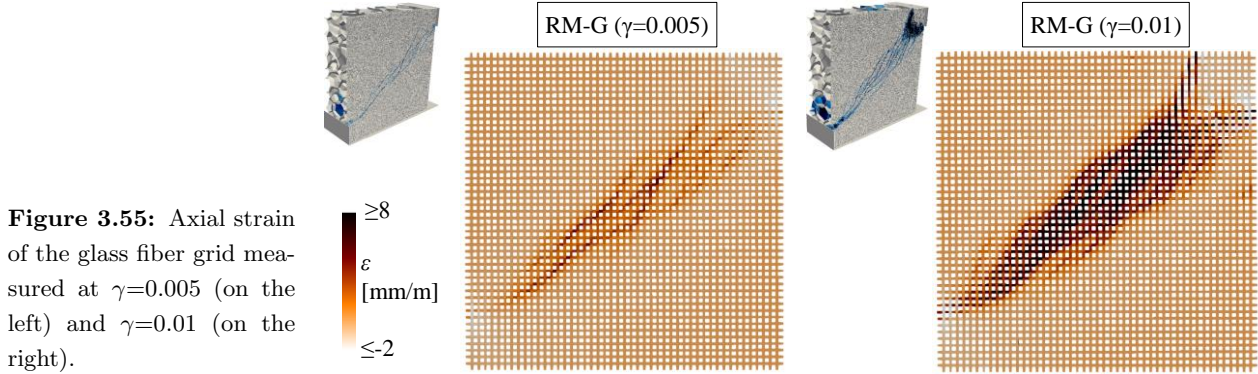
**Figure 3.53:** a,b) Axial strain measured for the vertical stands of the fiber grids during the experimental tests carried out on two masonry panels strengthened by the FRCM.

Figure 3.54 shows the crack opening at failure for the reinforced the specimen reinforced by glass fiber grid embedded in the mortar layer (RM-G). The failure plots correspond to a value of the macroscopic shear strain  $\gamma$  equal to 0.01. By comparing that figure with Figure 3.47 one can observe no strong differences in the fracture propagation. Indeed, the damage that occurred on the masonry wall seems the same, whereas one can observe a more distributed cracking on the mortar surface in Figure 3.54, as compared to Figure 3.47. This highlights the benefit of the grid to reduce crack propagation in masonry panels. That result also explains the higher load-bearing for the masonry specimen reinforced by both mortar and grid (the RM-G case) observed in Figure 3.51, as compared to the RM-M case.



**Figure 3.54:** Crack opening at failure on both the masonry and the mortar layer for  $\gamma=0.01$ , by employing the glass fiber grids embedded in the mortar layers.

Finally, Figure 3.55, shows the evolution of the axial strain of the glass fiber grid measured for different macroscopic shear strain  $\gamma$  equal to 0.005 and 0.01. This figure highlight that concentration of the deformation occurs along the compressed diagonal.



**Figure 3.55:** Axial strain of the glass fiber grid measured at  $\gamma=0.005$  (on the left) and  $\gamma=0.01$  (on the right).

To better understand the effect of the feature fibers on the mechanical properties of the mortar panel as well as the fracture propagation on the panel, a diagonal-compression test was simulated for a  $250 \times 250$  mm mortar specimen with 20 mm in thickness (see Figure 3.56). Two “L-shaped” steel elements, measuring 31.7 mm in length and height were placed at the specimen corners. It is worth noting that both the specimen size and the L-shaped plate sizes proportionally decreased by the factor 3.8 as compared to the sizes suggested by the ASTM standard code for the diagonal compression test of the masonry walls. The reduced size of the specimen ensured a lower computational cost of the simulation. In addition, such a dimension can ensure the chance of spreading this test as an alternative to the classic direct tensile test that is usually performed for the characterization of the FRCM stripes.

A particular constrained system was conceived to avoid instability phenomena for the panel by ensuring an ideal tensile crack along the compressed diagonal of the mortar specimen. That system consisted of two circular steel plates with 100 mm in radius placed at the external surfaces of the mortar panel and were modeled as rigid triangular shell elements (see Figure 3.56). A static friction coefficient  $f_s = 0.1$  and a dynamic friction coefficient  $f_k = 0.0084$  were assumed to simulate the low friction conditions at the plates-specimen interfaces.

The two L-shaped plates were modeled as rigid triangular shell elements and a sliding with ‘stick-slip’ friction constraint between the corner plates and the mortar particle nodes was used under high bond behavior hypotheses ( $f_s = f_k = 0.5$ ).

For this investigation, the mechanical behavior of the fiber strands was characterized by a linear hardening branch up to the fiber strength (equal to 1700 MPa) followed by a nonlinear softening branch (hardening modulus equal to -5000 MPa) to simulate accurately the almost brittle failure of the fiber strands when their

maximum tensile stress is achieved.

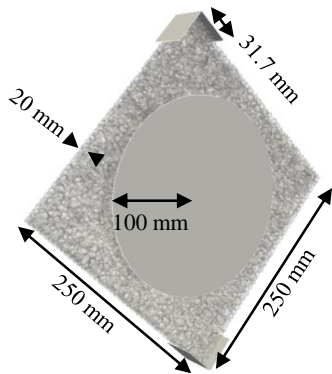


**Figure 3.56:** Simulation of the diagonal compression test for the mortar specimen.

The simulations were performed by assuming different width of the fiber strands (see Figures 3.57a, b) as well as different space gap (see Figures 3.57a, c, d). In particular, the case RP-grid25 (Figure 3.57a) was characterized by fiber strands with 10 mm in width, whereas the case RP-grid25s (Figure 3.57b) was characterized by fiber strands with 5 mm in width. For these two cases, the thickness of the fiber strands and the space gap of the grid were assumed equal to 0.1 mm and 25 mm, respectively.

The case RP-grid25 (Figure 3.57a), the case RP-grid50 (Figure 3.57c), and the case RP-grid100 (Figure 3.57d) were characterized by a space gap of the grid equal to 25 mm, 50 mm and 100 mm, respectively. For these three cases, the thickness and the width of the fiber strands were assumed equal to 0.1 mm and 10 mm, respectively.

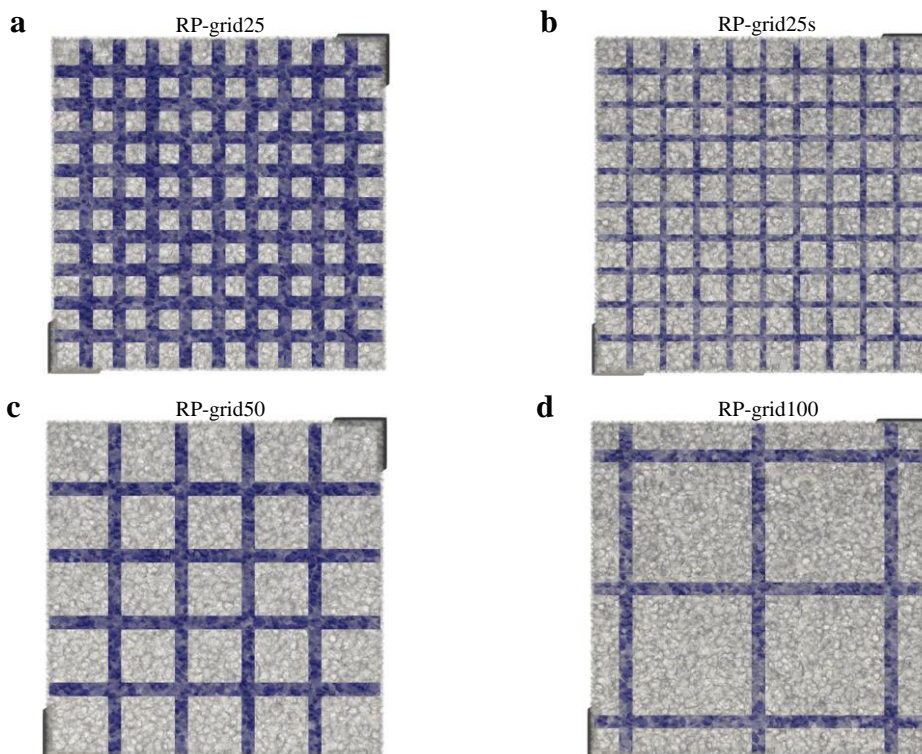
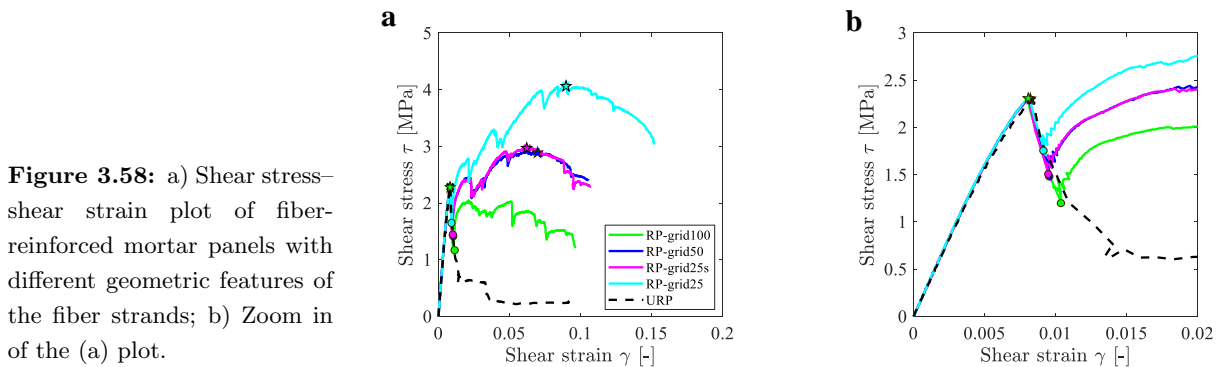


**Figure 3.57:** Mortar square specimen of 250 mm in size and 20 mm in thickness reinforced by fiber grid with different geometrical features: a) Space gap of 25 mm; b) space gap of 25 mm and fiber width of 5 mm; c) space gap of 50 mm; d) space gape of 100. For the cases a, b and c, the fiber width is equal to 10 mm.

Figure 3.58a shows the shear strain - shear stress ( $\gamma$ - $\tau$ ) curves obtained for the unreinforced panel (URP) and the reinforced panels (RPs). In that figure, the achievement of the maximum stress is represented by a star marker, whereas the begin of the re-hardening phase is represented by a circle marker. By observing the curves of Figure 3.58a, one can see that the fiber strand features affect both the strength and the load-bearing capacity of the reinforced panel. In particular, for all the RPs cases an almost sudden drop in the shear stress followed by a re-hardening phenomenon (re-increase of the shear stress) was observed. The sudden decrease in the shear is observed when the failure of the mortar occurred (shear stress almost equal to 2.5 MPa). Only for the RP-grid100 case, the increase in the shear stress is not so consistent to enhance the shear strength of the panel. Indeed, in that case, the shear strength of the reinforced panel is the same of the shear strength computed for the URP case.



A zoom-in of the curves of Figure 3.58a is illustrated in Figure 3.58b. From this figure is clearer the effect of re-hardening of the RPs when the failure of the mortar occurred. In particular, the RP-grid25 case shows the smaller decrease in the shear stress before the begin of the re-hardening phase. On the contrary, the RP-grid100 case shows the higher decrease in the shear stress before the begin of the re-hardening phase.

Results highlighted the differences related to the fiber content in the mechanical behavior of the reinforced panels. In general one can conclude that the higher the fiber content in the FRCM system, the higher the increase in the shear strength of the panel due to the re-hardening phenomenon associated to the fiber as well as the higher ultimate shear strain of the reinforced panel. Furthermore, the higher the fiber content, the lower the drop in the shear stress before the begin of the re-hardening phase.

Figures 3.59a – d show the axial force of the fiber strands related to the shear strain of the panel. The axial forces were measured on the vertical strands placed along the compressed diagonal of the mortar. In particular, for the RP-grid25 case, one can see that the maximum force of the fiber is obtained in correspondence of

$\gamma$  almost equal to 0.1. For the other cases, the the maximum force is achieved for  $\gamma$  almost equal to 0.05.

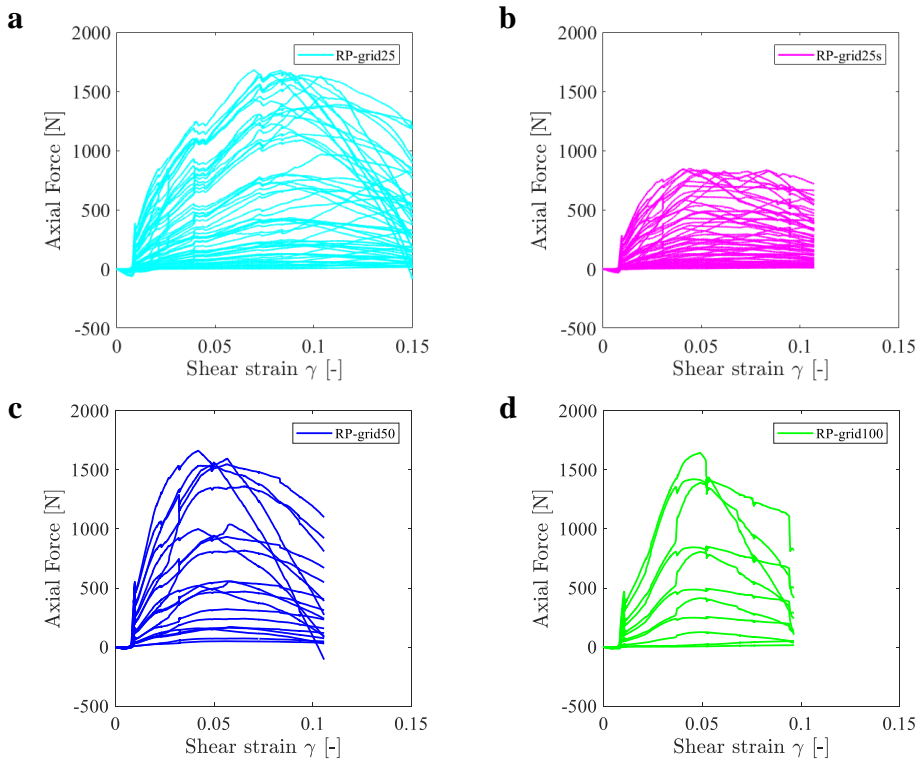


**Figure 3.59:** Axial force measured of the fiber strands as a function of the shear strain of the panel for different cases: (a) RP-grid25; (b) RP-grid25s; (c) RP-grid50; (d) RP-grid100.

Figures 3.60a – d show the strain of the fiber strands related to the shear strain of the reinforced panel.

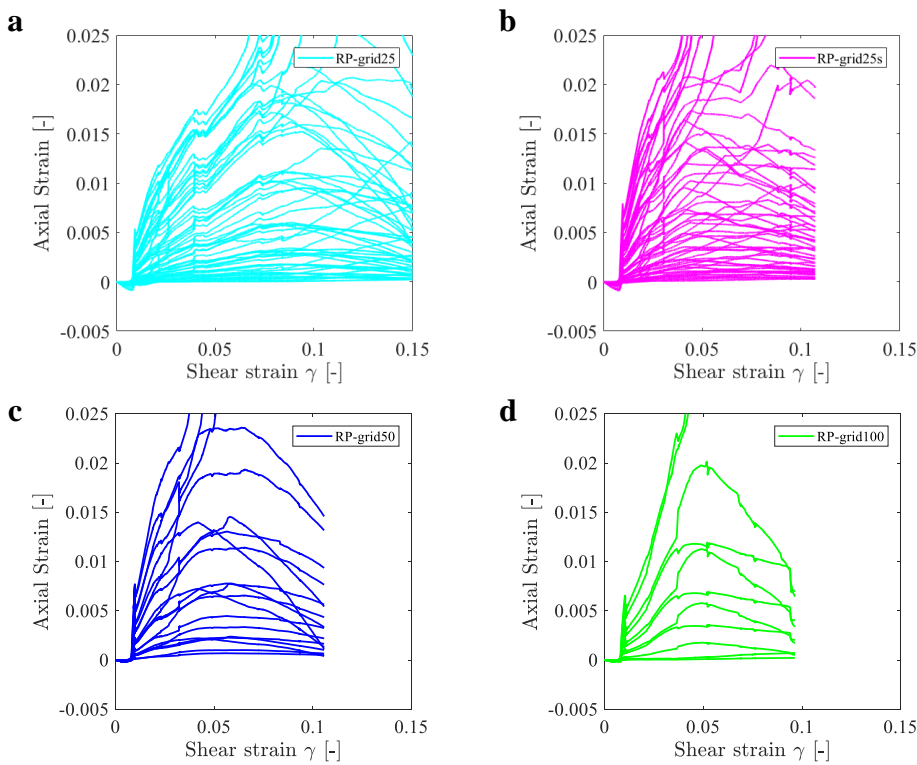


**Figure 3.60:** Axial strain measured of the fiber strands as a function of the shear strain of the panel for different cases: (a) RP-grid25; (b) RP-grid25s; (c) RP-grid50; (d) RP-grid100.

Figures 3.61a – d illustrate the fracture propagation occurred for the FRCM panel by assuming the different features of the fiber. The crack patterns correspond to the same displacement imposed to the specimens. In particular, for all the cases, one can see similar fracture evolution through the mortar, mainly localized along the compressed diagonal and the corners of the specimens. In particular, the RP-grid100 shows a more distributed cracking on the mortar surface, as compared to the other cases. The RP-grid50 and the RP-grid100 cases also show a clear separation of the two portions of the mortar specimen highlighting the lower deformability capacity, as compared to the RP-grid25 and RP-grid25s that are characterized by a lower space gap of the fiber grid (and therefore an higher distribution of the fibers).

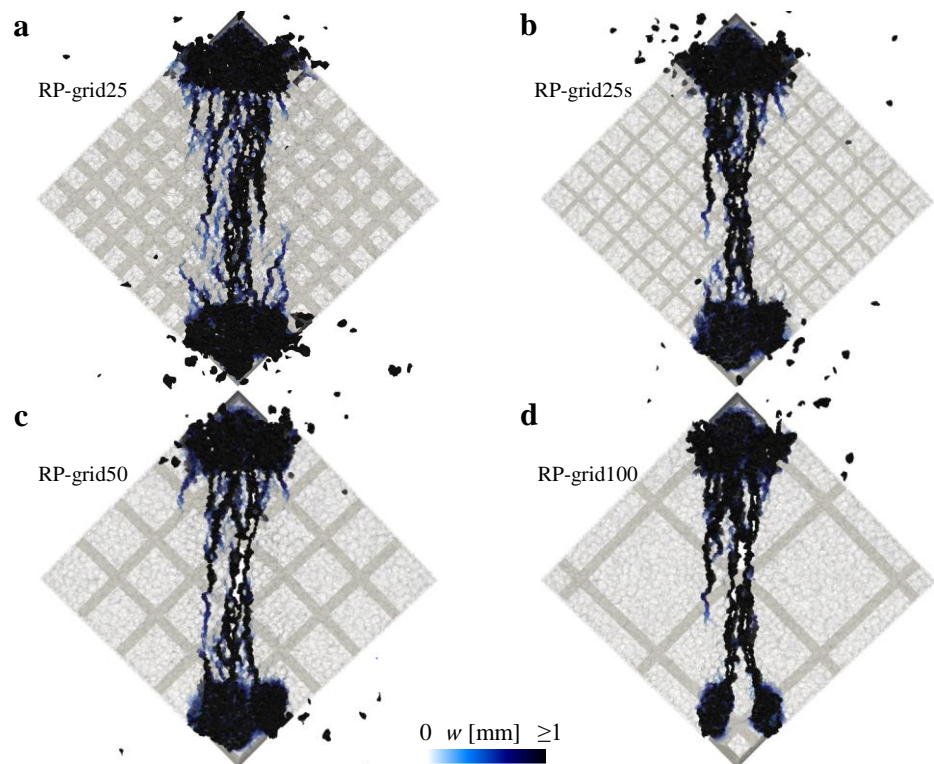


**Figure 3.61:** Crack opening at the failure of the mortar panel by assuming different geometric feature of the fiber strands: (a) RP-grid25 case; (b) RP-grid25s case; (c) RP-grid50 case; (d) RP-grid100 case.

Finally, Figures 3.62a – d and Figures 3.63a – d show the axial force and the axial strain of the fiber strands, respectively. One can see that the higher value of the axial force (1700 MPa) and the axial strain (0.02) of the fiber occur along the compressed diagonal of the mortar panel. This highlights that the fibers are tensed (or strained) where crack opening of the mortar take place.

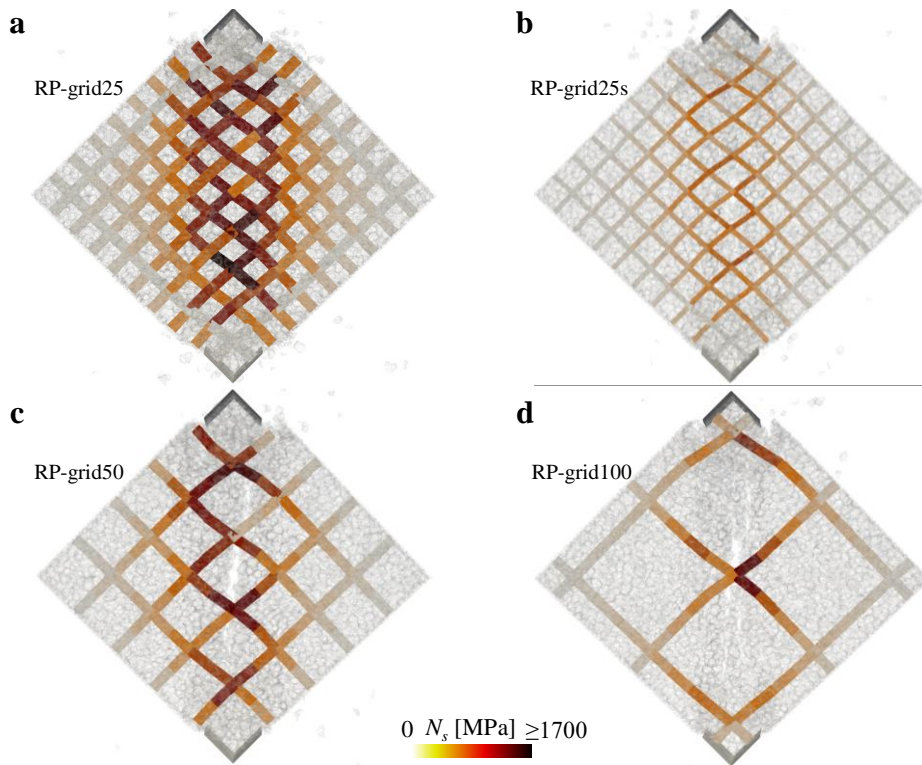


**Figure 3.62:** Axial force of the fiber strands under different geometric feature assumptions: (a) RP-grid25 case; (b) RP-grid25s case; (c) RP-grid50 case; (d) RP-grid100 case.

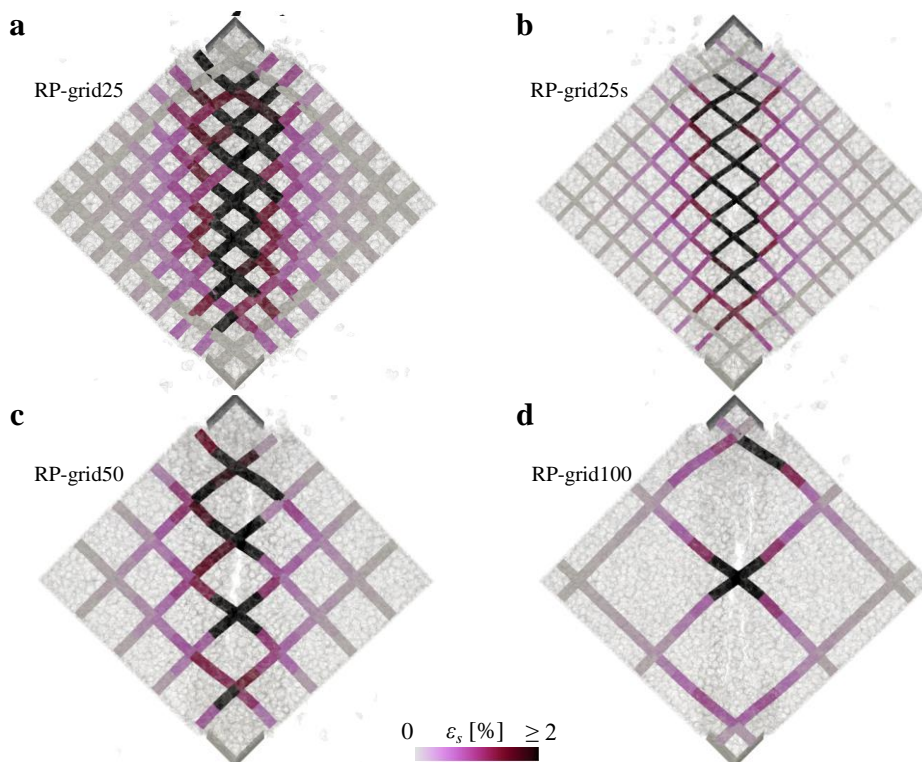


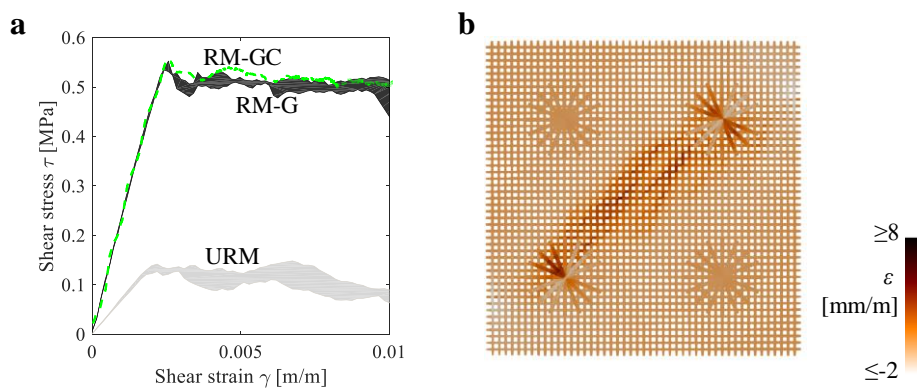
**Figure 3.63:** Axial strain of the fiber strands under different geometric feature assumptions: (a) RP-grid25 case; (b) RP-grid25s case; (c) RP-grid50 case; (d) RP-grid100 case.

### 3.4.4 Fiber anchor effect

With the aim to numerically investigate the effect of the fiber anchors on the mechanical response of the reinforced panels, they have been introduced in the numerical model. In particular, they were modeled with elastic beam elements (Table 3.12) with equivalent rectangular sections of  $0.1 \text{ mm} \times 10 \text{ mm}$ . The fiber anchors were modeled with hexahedral solid elements (Figure 3.43) assuming elastic mechanical properties (Table 3.12). The ends of each anchor were modeled by 16 strands measuring  $14.7 \text{ mm}$  in width,  $0.2 \text{ mm}$  in thickness and  $150 \text{ mm}$  in length. These values were computed by assuming an initial ideal-equivalent circular configuration measuring  $0.1 \text{ mm}$  in thickness and  $150 \text{ mm}$  in radius.

Figure 3.64a shows the LDPM curves obtained for the unreinforced samples (URM) and the reinforced samples obtained by two different strengthening systems: (1) fiber grids and fiber anchors, both embedded in the mortar layers (RM-GC), and (2) only fiber grids embedded in the mortar layers (RM-G). For both reinforced cases, RM-GC and RM-G, one can clearly observe an increase in terms of both the stiffness and shear strength as compared to the URM case. Furthermore, the difference in the mechanical responses between the RM-GC (represented in Figure 3.64a by the average curve of three simulations) and the RM-G cases (represented in Figure 3.64a by the scattering areas between the lower and the upper response curves measured in three simulations) highlights that the fiber anchors have no effect on the mechanical response both in terms of stiffness and strength. One can observe a small contribution (almost negligible) of the fiber anchors only in the load-bearing capacity for large deformation of the masonry sample. This is because fiber anchors are usually introduced in the FRCM system only to improve the out-of-plane mechanical response and they have no strong influence on the in-plane behavior.

**Figure 3.64:** a) Comparison between unreinforced specimens (URM), reinforced panels by both the fiber grids and anchors embedded in the mortar layers (RM-GC), and reinforced panels without fiber anchors (RM-G); b) axial strain of the glass fiber grid and the fiber anchor measured at  $\gamma=0.005$ .



### 3.5 Simulation of the innovative fibrous-mortar

In the last decades the material properties as well as the structural behavior of fiber-reinforced materials have been extensively investigated. In particular, research has expanded in fiber-based composite materials characterized by various fiber materials, sizes, shapes, and fiber content in association with different concrete/mortar compositions, eventually leading to high-performance materials exhibiting strain-hardening behavior accompanied with multiple cracking phenomena at small crack widths [241]. Most of the existing numerical models for the analyses of fiber-reinforced material consist in modifying the post peak behavior of inelastic constitutive models to represent the enhanced ductility of that material [242], (e.g. [243, 244, 245, 246]). These models include the effect of fibers on a phenomenological level. Hence, the increasing in the fracture energy of fibrous material must be determined a priori from experiments resulting in loss of the capacity to predict the effect of specific fiber properties on the the macroscopic behavior of fiber-reinforced material.

For a reliable prediction of the mechanical response of fibrous material, the numerical modeling capabilities should be characterized by the following main features: (i) a realistic, three-dimensional modeling of mortar/concrete mesostructure, including a discrete representation of individual fibers randomly distributed therein; (ii) a multiscale approach in which the effect of embedded fibers on the structural response is based directly on the micromechanics of the fiber-matrix interaction. Obviously, true predictive capability of the model should be demonstrated through a rigorous calibration/validation procedure.

A review of the published literature revealed several notable studies that have some, but not both, of these features. In particular, a sophisticated micro - mechanical model for fiber crack bridging was proposed by Yang [247], who developed earlier work found in [248]. A finite element multiscale (homogenization) approach based on the crack-bridging model was proposed by [249]. A model based on the discretization of fibers, which was randomly distributed in a two-dimensional finite-element model mesh was proposed in [250]. A random distribution of fibers in a 3D FEM to simulate the structural response of direct tension specimens was proposed in [251].

In Schauffert and Cusatis [252, 253], the Lattice Discrete Particle Model was proposed for fibrous concrete. In that study, the LDPM incorporated the effect of the fibers as discrete entities within the mesostructure of the concrete, by modeling individual fibers randomly placed within the framework according to a given fiber volume fraction and fiber geometry. Then, number and orientation of fibers crossing each facet are computed along with the fiber embedment length on each side of

the facet. At facet level, fibers and concrete are assumed to be coupled in parallel; 4) the contribution of each fiber to the facet response is formulated on the basis of the micromechanical analysis that takes into account fiber-matrix debonding, frictional pull-out, scabbing and spalling effects, as well as fiber rupture [252].

The overall pullout behavior is mainly characterized by the debonding and frictional slip phenomena that occur at the fiber-mortar matrix interface. The debonding behavior of fibers strongly affects the properties of fiber-reinforced composite materials. A transition zone between the elastic bonded region and the frictional debonded region may exist [254]. In [255] is well described that the debond mode is determined by the size of this transition zone, in comparison to fiber-embedment length, and the difference in stress distribution between the bonded and debonded regions of the interface. The transition zone size mainly depends on the microstructural size scale of the interphase. Indeed, a material with relatively coarse microstructure is characterized by a larger transition zone as compared to the material with fine grain. Moreover, the debond mode varies with the constituent material involved, such as fibers with different material types or surface treatments, cement matrix with various water/cement ratios or additives, and so on.

When a fiber-reinforced composite material is subjected to tensile load and undergoes fracture failure, the reinforcing fibers may be subjected to various interaction phase with the matrix. First, for a low external load, the fiber-matrix interphase remains well bonded. Then, when the load increases and overcomes the critical interfacial bond properties, a partial debonding occurs. In this phase, the resistance of the applied load comes partly from the elastic bond on the embedded fiber segment and partly from the frictional bond on the debonded fiber segment. When the entire embedment length is completely debonded, the fiber may start to be pulled out. At this final stage, the resistance of the applied load comes entirely from the frictional stress between fiber and matrix. Definitely, prior to a purely frictional pullout phase, a fiber segment embedded in a mortar matrix must completely debond from the surrounding matrix as illustrated in Figure 3.65.

In [255], it was also found that interfacial debonding is dominated by frictional stress which is not dependent on the fiber diameters but only to the material features.

### 3.5.1 Governing equation of the fiber-mortar interaction

The mechanical behavior of the fiber-mortar interaction is governed by the relationship between the pullout load  $P$  and the slippage  $\nu$  at the fiber-matrix interface. In the literature, relationships of this nature have been obtained by various authors, both numerically and analytically, under various simplifying approximations.

To develop the LDPM for fibrous mortar, Schauffert [252, 253] adopted analytical, semi-empirical formulation of Yang et al [247]. This formulation is based on several assumptions, including that the fiber is initially straight, elastic, and has negligible bending stiffness. The developed model, named LDPM-F, was calibrated by carrying out numerical simulations of direct tension and three-point bending tests on fiber reinforced concrete mixes characterized by various fiber volume ratios and volume types. Individual fibers are inserted into the LDPM volume with randomly generated positions and orientations. Hence, the occurrences of fiber-facet intersection are determined by computing the actual locations where fibers cross inter-cell facets. The relative orientation between the fiber and the facet is provided by unit vector  $\mathbf{n}_f$ , whose orientation is based on the local reference system of the particle facet ( $\mathbf{n}$ ,  $\mathbf{m}$ ,  $\mathbf{l}$  described in Section 3.2.2).

The debonding phase can be described as a “tunnel-type” cracking process over the embedment length which is characterized by two fiber-matrix interface parameters [247], namely the debonding fracture energy  $G_d$  and the frictional stress  $\tau_b$ . The slippage has a critical value  $\nu_d$  that represents full debonding. For a generic embedded length  $L_e$ ,  $\nu_d$  can be expressed as [248]:

$$\nu_d = \frac{2\tau_b L_e^2}{E_f d_f} + \left( \frac{8G_d L_e^2}{E_f d_f} \right)^{1/2} \quad (3.12)$$

where  $L_e$  is the embedment length and  $E_f$  is the modulus of elasticity of the fiber.

For the debonding stage ( $\nu < \nu_d$ ), fiber load  $P_{\nu_d}$  is given as [248]:

$$P(\nu) = \left[ \frac{\pi^2 E_f d_f^3}{2} (\tau_b \nu + G_d) \right]^{1/2} \quad (3.13)$$

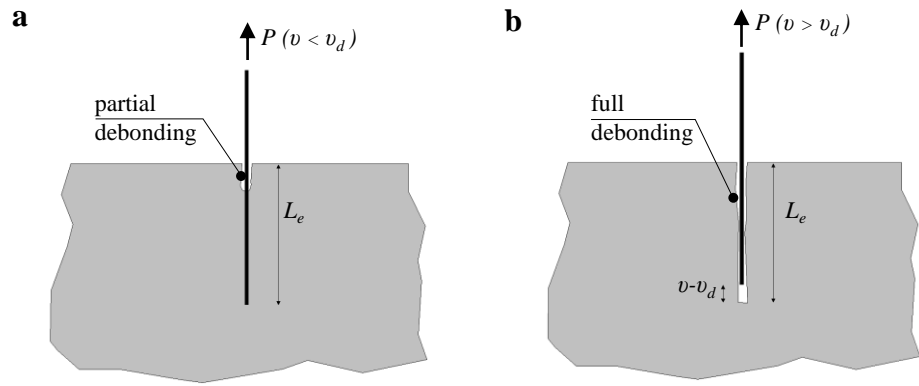
After full debonding ( $\nu > \nu_d$ ), the resistance is entirely frictional and the fiber load  $P_{\nu_d}$  is equal to:

$$P(\nu) = P_0 \left( \frac{1 - \nu - \nu_d}{L_e} \right) \left[ 1 + \frac{\beta(\nu - \nu_d)}{d_f} \right] \quad (3.14)$$

where  $P_0 = \pi L_e d_f \tau_b$ .

The relationship between  $P$  and  $\nu$  is schematically illustrated in Figure 3.65b.

**Figure 3.65:** Single fiber pullout: a) partial debonding; b) full debonding with consequent to frictional slip.



The nature of the frictional interface can vary significantly, and the differences can be accounted for with the dimensionless parameter  $\beta$  [256]. If the interfacial friction is independent of slip distance,  $\beta$  has a value of zero, and the fiber load decays linearly with increasing slippage (see Figure 3.66). When interfacial friction increase with slippage (i.e. slip-hardening) it can be assumed  $\beta > 0$ . On the contrary, for smooth fibers, the literature suggests that interfacial friction typically decreases as pullout progresses (i.e. slip-softening) [257, 258] and it can be accounted for in a simulation by using  $\beta < 0$ .

**Figure 3.66:** Typical load versus slippage relationships for the single fiber pullout.

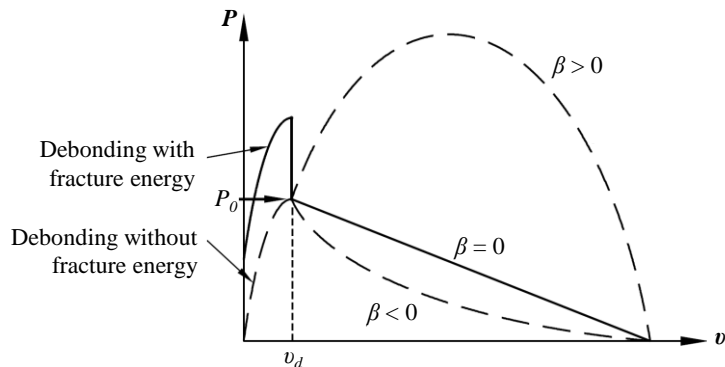
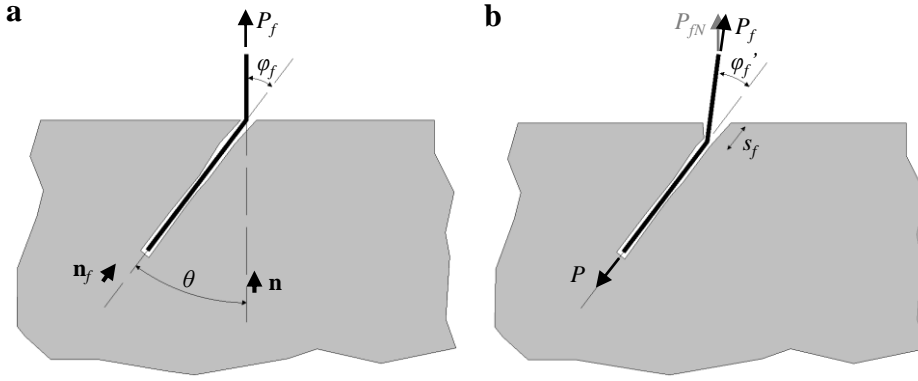


Figure 3.67a shows the general situation where the orientation of the embedded segment and the free (crack-bridging) segment are different. This case can be easily observed for the randomly dispersed fibers that are arranged therein tortuous crack paths generated around concrete particles. However, that phenomenon is lower important to consider for the mortar material due to the absence of aggregates in the matrix. The deflection angle between the two fiber ends is denoted as  $\varphi_f$ . At the point where the fiber exits from the matrix and it changes orientation, a concentration of the stress is created in the matrix.

Here, when this localized stress field reaches a sufficient intensity, localized fracture and spalling occur with a consequent reduction of the embedment length of the fiber, denoted as  $s_f$  that represents the spalling length (see Figure 3.67b). In that case, the deflection angle between the two fiber segments is reduced to a value denoted as  $\varphi'_f$ .



**Figure 3.67:** Single fiber pullout: a) initial condition; b) spalling.

This micromechanism has been well documented in the literature [259], and various models have been proposed for the definition of spalling length  $s_f$  [260, 261, 262]. In the LDPM-F formulation, the spalling length is obtained by the following continuous function of fiber force proposed by [247]:

$$s_f = \frac{P_{fN} \sin(\theta/2)}{k_{sp} \sigma_t d_f \cos^2(\theta/2)} \quad (3.15)$$

In LDPM-F, only the normal component  $P_{fN}$  of the total force  $P_f$  is assumed to contribute to spalling. The angle  $\theta$  then denotes the deflection angle between the embedded fiber segment, with unit orientation vector  $\mathbf{n}_f$ , and the crack face unit normal vector  $\mathbf{n}$ , and is given as  $\theta = \arccos(\mathbf{n}_f^T \mathbf{n})$ . The mesoscale tensile strength of the matrix is represented by  $\sigma_t$ , and  $k_{sp}$  is a dimensionless material parameter that can be calibrated with experimental evidence.

When spalling occur, the crack-bridging fiber segment is collinear with its associated force  $P_f$  (Figure 3.66a). Hence, null shear forces or bending moments occur for it. The fiber must then be assumed to have no bending stiffness (perfectly flexible). Zhang and Li [263] note that, in general, the crack-bridging segment is subject to forces associated with both the pullout resistance of the embedded segments and the bending of the fiber at the point where it exits the matrix. For a very flexible fiber, such as the glass one, the effects of bending are negligible, whereas for fibers that are relatively stiff or brittle, such as steel and carbon fibers, the additional stress generated on the fiber due to bending, in combination with the axial stress, cannot be ignored.

At the point where the fiber exits the tunnel crack (which has been shortened because of spalling), it wraps around the intact matrix in a perfectly flexible manner, especially in the case of flexible synthetic or glass fibers. This phenomenon is denoted as snubbing. The summation of all slip-friction and debonding forces acting parallel to the embedded length is denoted as  $P$ . The additional friction and bearing forces at the exit point imply  $P_f \leq P$ . To quantify this concept, the relationship expressing the change in tensile load for a flexible tendon being pulled

around an unyielding circular surface, which can be expressed as [264]:

$$P_f = P(\nu) \exp(k_{sn}\varphi'_f) \quad (3.16)$$

where the factor  $k_{sn}$  is a fiber-matrix interaction parameter termed the snubbing parameter.

In some studies, the snubbing parameter is described as the basic static coefficient of friction (Coulomb theory) between the two materials of the system [181].

The surface abrasion that may occur along the embedded length during pullout as well as the fiber wraps around the matrix at the exit point, can create localized zones of reduced effective cross-sectional area, with a consequent reduction of the ultimate tensile strength of the fiber. Indeed, single-fiber pullout tests performed for synthetic fibers showed that the higher the values of  $\varphi'_f$ , the lower the rupture loads [259]. The strength reduction relationship adopted for the LDPM-F is expressed in terms of the axial stress in the crack-bridging segment ( $\sigma_f = 4P_f/\pi d_f^2$ ) as follow:

$$\sigma_f \leq \sigma_{uf} \exp(-k_{rup}\varphi'_f) \quad (3.17)$$

where  $k_{rup}$  is a material parameter,  $\sigma_{uf}$  is the fiber ultimate tensile strength.

Consider a fiber, with initial orientation  $\mathbf{n}_f$ , subject to a crack opening of vector  $w$ . The tangential component of  $w$  is defined as  $w_T = (w_M^2 + w_L^2)^{1/2}$ . The crack-bridging segment spans between Points A and B (see Figure 3.68). Assuming that the spalling length  $s_f$  is the same on both sides, the vector for the crack-bridging segment can be computed as  $w' = w + 2s_f\mathbf{n}_f$ . Also, the bridging segment force vector is assumed to be coaxial with the fiber,  $\mathbf{P}_f = P_f\mathbf{n}_f$ , where  $\mathbf{n}_f = \mathbf{w}'/||\mathbf{w}'||$  and the symbol in the double vertical bars, used here and subsequently, represents the Euclidean norm or length of a vector. The frictional pulley model applies equally to both the shorter and longer ends, with initial lengths  $L_s$  and  $L_l$ ; relative slippages  $\nu_s$  and  $\nu_l$ ; and pullout resisting forces  $P_s$  and  $P_l$ , respectively. Equilibrium of the fiber-bridging segment leads to the following expression:

$$P_f = \exp(k_{sn}\varphi'_f)P_s(\nu_s) = \exp(k_{sn}\varphi'_f)P_l(\nu_l) \quad (3.18)$$

In addition, compatibility between the length of the bridging segment and the slippages is enforced, which can be expressed as  $||w'|| = 2s_f + \nu_s + \nu_l$ .

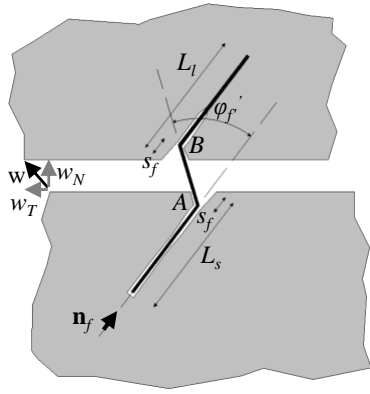


**Figure 3.68:** Crack-bridging fiber with random crack opening orientation.

### 3.5.2 Calibration procedure

Fiber reinforcing geometry is based on a few primary parameters, namely the fiber content  $F$ , fiber equivalent diameter  $d_f$ , length  $L_f$ , and curvature. Fiber curvature can be a fabrication type, such as a hook or bend at the end of steel fiber, or the random tortuosity that may occur when low bending resistance fibers are mixed into the wet mortar. Curvature can be modeled through the assumption that each fiber consists of multiple straight line segments, each with varying orientation. For the present study, fibers were assumed straight to reproduce the real geometry of the two fiber types employed in the experiments (see Figure 2.45).

For the mechanical characterization of the fibers, two fiber material parameters, namely the ultimate tensile strength  $\sigma_{uf}$  and elastic modulus  $E_f$ , are required for the LDPM-F framework. They can be directly assumed from the mechanical properties of the employed fibers, equal to 1700 MPa and 72 GPa, respectively. Moreover, other mechanical parameters are required for the LDPM-F framework, such as the bond fracture energy  $G_d$ , bond frictional stress  $\tau_b$ , slip hardening softening parameter  $\beta$ , spalling parameter  $k_{sp}$ , snubbing parameter  $k_{sn}$ , and fiber strength decay parameter  $k_{rup}$ . These parameters must be performed through indirect parameter identification based on the simulation of the structural response of the specimens tested in the experimental campaign.

The bond fracture energy  $G_d$  between the fiber and matrix can vary widely and it can be determined by a single fiber pullout test. However, that test is really difficult to perform and limited researches are available in the literature. The majority of the experimental test data found in the literature for fiber-reinforced material is based on steel fiber. In the case of synthetic fibers,  $G_d$  is considered to have relatively high bonding due to chemical adhesion and was estimated ranging from 4 to 6 N/m [248]. On the contrary, for the steel/mortar interface, some authors report the bond fracture energy to be relatively low and assume it to be zero [265, 263], whereas other authors [266] reported a  $G_d$  range of 6–12 Nm for smooth steel wire in a conventional cementitious mortar. Also, other studies [261, 257] showed the fiber pullout curves with the characteristic sudden drop of load can be related to a transition from a higher value of debonding friction to a lower value of basic pullout friction, rather than considering it to be a fracturing process governed by fracture energy.

Regarding the basic frictional resistance  $\tau_b$  the reported range is approximately 1.0–4.5 MPa and 2.0–5.0 MPa for smooth steel fibers and synthetic fibers, respectively [253]. Research [266] showed that pullout resistance increases as the fiber content of the mortar specimen increases, though in this study it was assumed to be constant and independent of the fiber content. Also,  $\tau_b$  value can depend on

the uniaxial compression in a direction orthogonal to the pulled fiber. Indeed, a research [267] showed that the initial value of frictional resistance (i.e., immediately after debonding) can increase on the order of 1.5 MPa for each 10 MPa of applied lateral compression. Moreover, another important aspect of the frictional resistance may be related to the additive content employed for the mix design of the composite materials. Indeed, the higher the additive content, the higher the adhesion level at the fiber-mortar interface, and then the higher the  $\tau_b$  value. So, the range of  $\tau_b$  reported in the literature may underestimate the value of  $\tau_b$  when a high content of additive is introduced in the mortar paste.

Similar to debonding, the evolution of the frictional pullout  $\beta$  can vary widely. For synthetic fibers, interfacial friction can increase with slippage; i.e., slip hardening [258]. This is typically attributed to fiber surface abrasion coming into increasing contact with the relatively unyielding surface of the mortar tunnel crack. Hence, the value of  $\beta$  must be calibrated following the experimental evidence.

Finally, since no rupture of the fiber was observed during the experiments for both the type of the fibers, the coefficient  $k_{rup}$  was assumed equal to zero. Furthermore, also the spalling phenomenon was not observed for the mortar specimen during the experiments, so that also the other coefficients  $k_{sp}$  and  $k_{sn}$  were assumed equal to zero. This choice was also in line with the main objective of the present numerical investigation aiming to investigate the main fiber-matrix interaction parameters, namely the bond fracture energy  $G_d$ , the bond friction stress  $\tau_b$ , and the slip-hardening/softening parameter  $\beta$ .

Aiming to reproduce the experimental results obtained for mortar beams under three-point bending tests, a notched mortar sample was modeled with the same geometrical characteristics of the ones tested in the experiments (see Figure 3.69).

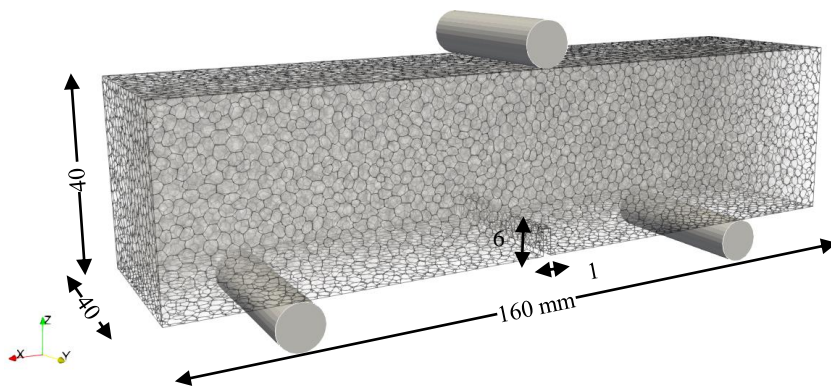


**Figure 3.69:** Notched mortar specimen modeled by using LDPM for the simulation of the experiments performed under 3PBT configuration.

As far as the modeling criteria assumed for the simulations is concerned, the three steel cylinders were modeled as rigid hexahedral solid elements. A penalty constraint with low friction constraint (static friction coefficient  $f_s = 0.1$  and dynamic friction coefficient  $f_k = 0.0084$ ) was used to connect the mortar particles to the cylinders by also assuming a penalty stiffness parameter equal to 100000 N/m

to ensure proper contact between materials.

The LDPM mortar parameters were determined by fitting the experimental response of the unreinforced mortar specimen (fiber content  $F$  equal to 0%). These parameters are listed as follows:  $E_0 = 4000$  MPa,  $\alpha = 0.2$ ,  $\sigma_t = 1.8$  MPa,  $G_t = 100$  N/m,  $n_t = 0.1$ ,  $\sigma_s/\sigma_t = 1.38$ ,  $\sigma_{c0} = 150$  MPa,  $\sigma_{N0} = 600$  MPa,  $H_{c0} = 150$  MPa,  $\mu_0 = 0.2$ ,  $\kappa_{c0} = 1.75$ ,  $\kappa_{c1} = 1.0$ , and  $\kappa_{c2} = 5.0$  (see Section 3.2.2 for the description of these LDPM parameters). The values of mortar particle dimension ranges from  $d_0 = 4$  mm to  $d_a = 4.75$  mm with a Fuller coefficient  $n_F$  equal to 0.6. For the mix design definition, a aggregate-mortar ratio  $a/c = 0.248$ , a water-mortar ratio  $w/c = 0.4$  and an effective binder content parameter  $c = 160$  kg/m<sup>3</sup> were assumed. These parameters were kept fixed for all the simulations.

Hence, short fibers were randomly introduced in the mortar sample according to the given fiber volume ratio and fiber geometry. In particular, the same fiber contents ( $F$  equal to 1.5%, 2.0% and 2.5%) of the experimental cases were assumed for both the fiber type (the HP24 and the 950Y ones), as illustrated in Figures 3.70 and 3.71. As far as the modeling criteria of the fibers is concerned, they were modeled by beam elements, with 24 mm and 13 mm in length as well as with circular equivalent sections of 0.476 mm and 0.316 mm in diameter for the HP24 and the 950Y, respectively.

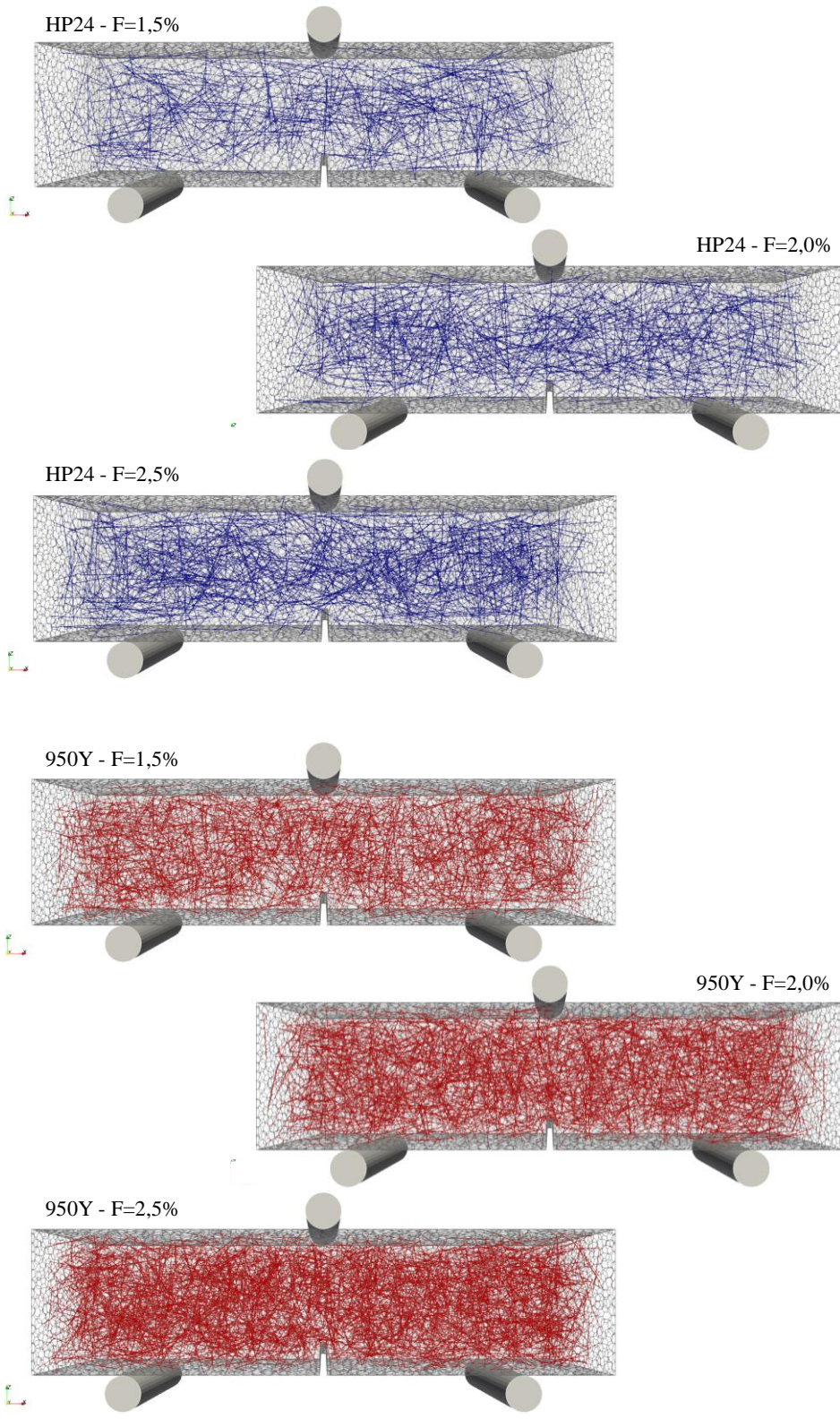


**Figure 3.70:** The HP24 fiber type is chaotically distributed through the mortar matrix by LDPM to simulate the experimental 3PBTs. The fiber content was assumed equal to 1.5%, 2.0% and 2.5%.

**Figure 3.71:** The 950Y fiber type is chaotically distributed through the mortar matrix by LDPM to simulate the experimental 3PBTs. The fiber content was assumed equal to 1.5%, 2.0% and 2.5%.

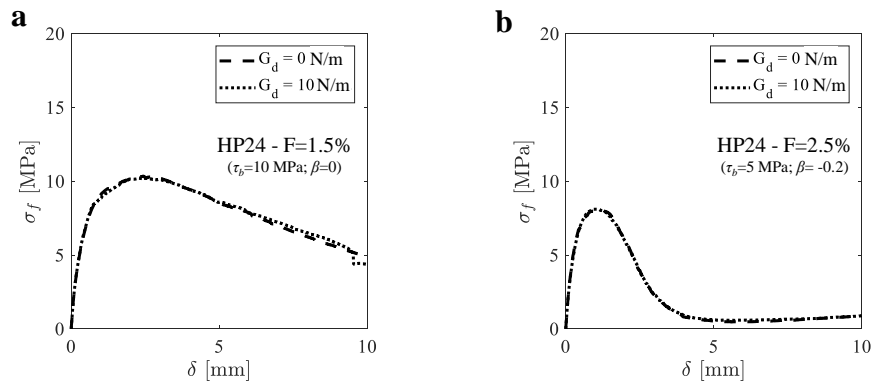
The first aim of the calibration procedure regarded the investigation of the effect of the  $\beta$ ,  $G_d$ , and  $\tau_b$  parameters on the behavior of the fibrous specimen through a sensitivity analyses, as illustrated in Figures 3.72 and 3.73.

In particular, Figure 3.72a shows the mechanical responses obtained for the HP24 fiber with F=2.0% by assuming two values of  $G_d$  (equal to 0 N/m and 10 N/m) and keeping constant the values of  $\tau_b$  (8 MPa) and  $\beta$  (null). One can see that no effect of  $G_d$  on the mechanical response can be noted in both the strength and softening behavior. It worth noting that both the curves of Figure 3.72a were obtained with  $\beta = 0$  hypotheses, which leads to high load-bearing capacity even for a large value of the deflection  $\delta$ .

Figure 3.72b shows the mechanical responses obtained for the fibrous mortar with HP24 fibers and F=1.5% by assuming two values for  $G_d$  (equal to 0 N/m and 10 N/m as in the case illustrated in Figure 3.72a) and keeping constant the values of  $\tau_b$  (5 MPa) and  $\beta$  (-0.2). Even in this case, the variation of  $G_d$  does not affect the mechanical response of the fibrous specimen in both the peak and post-peak behavior. Furthermore, in Figure 3.72b one can observe a higher brittle behavior, as compared to the  $\beta = 0$  case (Figure 3.72a). In particular, one can observe a distinct sudden load drop after the achievement of the flexural strength by assuming a negative value of  $\beta$ . This trend is very similar to the one observed in the experiments.

In general, the results lead to the conclusion that the softening behavior of the fibrous mortar is mainly characterized by the  $\beta$  parameter, since  $G_d$  is almost insensitive to the mechanical response of the sample. This is true in several conditions, namely different  $\beta$  (0 and -0.2),  $\tau_b$  (5 and 8 MPa) and fiber content (1.5% and 2.5%). So that, the value of  $G_d$  was kept constant and equal to 4 N/m (arbitrary value) for the following simulations. Moreover, since a null value of  $\beta$  leads to higher load-bearing capacity, as compared to the experiments, only negative values of  $\beta$  were considered in the simulations.

**Figure 3.72:** Effect of the debonding fracture energy  $G_d$  (assumed equal to 0 N/m and 10 N/m) on the mechanical response of the fibrous mortar specimen by assuming: (a)  $\beta = 0$ ; (b)  $\beta = -0.2$ .



A further sensitivity analyses on the  $\beta$  parameter is illustrated in Figure 3.73a. Results refers to the HP24 fibers with  $F=2.0\%$  by assuming four values for  $\beta$  (equal to 0, -0.1, -0.15 and -0.2) and keeping constant the values of  $\tau_b$  (8 MPa) and  $G$  (4 N/m). In particular, Figure 3.73a shows that the parameter  $\beta$  strongly affect the post-peak behavior and also slightly influence the flexural strength of the specimen. In particular, the higher the (negative) value of  $\beta$ , the higher the brittle behavior of the fibrous mortar specimen.

Figure 3.73b shows a sensitivity analyses carried out for the  $\tau_b$  parameter. Results refers to the HP24 fibers with  $F=2.5\%$  by assuming four different values for  $\tau_b$  (equal to 5, 8, 10, 12 MPa) and keeping constant the values of  $\beta$  (-0.2) and  $G_d$  (4 N/m). The curves show that  $\tau_b$  largely affects the strength of the fibrous mortar specimen. In particular, the strength of the specimen increases more than proportionally with increasing  $\tau_b$ . A slight influence of  $\tau_b$  can be also observed for the load-bearing capacity of the specimen immediately after the achievement of the flexural strength.

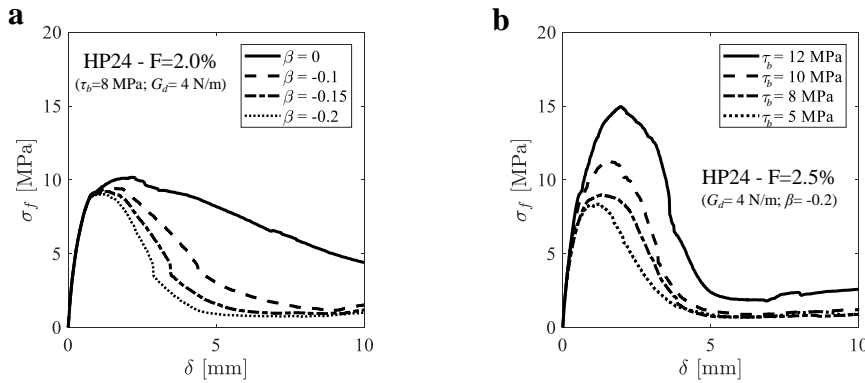
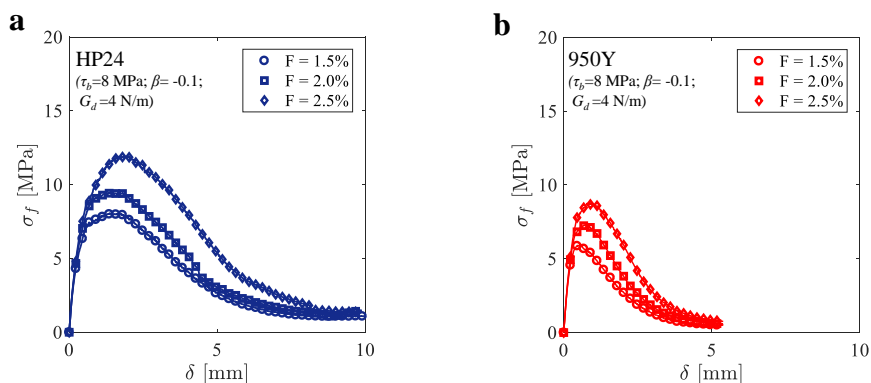


**Figure 3.73:** Effect of the slip-hardening/softening parameter  $\beta$  (a) and the bond friction stress  $\tau_b$  (b) on the mechanical response of the fiber reinforced mortar specimen.

As far as the fiber content  $F$  is concerned, Figures 3.74a, b show the effect of its value on the mechanical response of the fibrous mortar. The curves refers to fixed values of the LDPM parameters ( $\tau_b = 8$  MPa,  $\beta = -0.1$ ,  $G_d = 4$  N/m). In particular, Figure 3.74a shows the curves relative to the HP24 fiber; Figure 3.74b shows the curves relative to the 950Y fiber. One can see that the higher the  $F$ , the higher the flexural strength and the load-bearing capacity of the specimen. This trend can be clearly observed for the two types of fibers (HP24 and 950Y). Moreover, the curves show that the HP24 fiber, which is characterized by a higher fiber length as well as a higher aspect ratio than the 950Y one, ensures the best mechanical performance in terms of both the strength and ductility (fracture energy). On the other hand, also the experimental results showed a higher value of the fracture energy for the HP24. However, in the experiments, the strength measured for the mortar beam with 950Y fiber was slightly higher than the specimen reinforced by the HP24 one. This highlights that different values of  $\tau_0$  and  $\beta$  have to be separately calibrated to fit the experimental curves.

**Figure 3.74:** Effect of the fiber content  $F$  on the mechanical response of the fibrous mortar specimen for: (a) the HP24; (b) the 950Y.



Experimental tests for determining the mechanical behavior of fibrous mortar specimens were characterized by a substantial scatter, also due to the random distribution of the fibers into the mortar matrix. Hence, in order to numerically investigate this phenomenon, a mortar specimen tested under three points bending configuration was analyzed by randomly varying the position of the fibers therein the mortar. To this end, five different random sets of fiber arrangements were employed for the LDPM simulations. Figures 3.75 and 3.76 show the envelopes of the stress vs. deflection curves obtained for the HP24 and the 950Y fiber, respectively. One can see that the mortar sample reinforced by the 950Y fiber is characterized by a lower scattering of the response, as compared to the HP24 one. This is mainly related to the geometry of the fiber. Indeed, the scattering of the results also depends on the level of homogeneity of the material. For the same fiber content, the lower length and aspect ratio of the fiber, the higher the number of the fibers in the mortar matrix and, therefore, the homogeneity of the material. However, is not possible to observe a clear dependence of the response scatter to the fiber content.

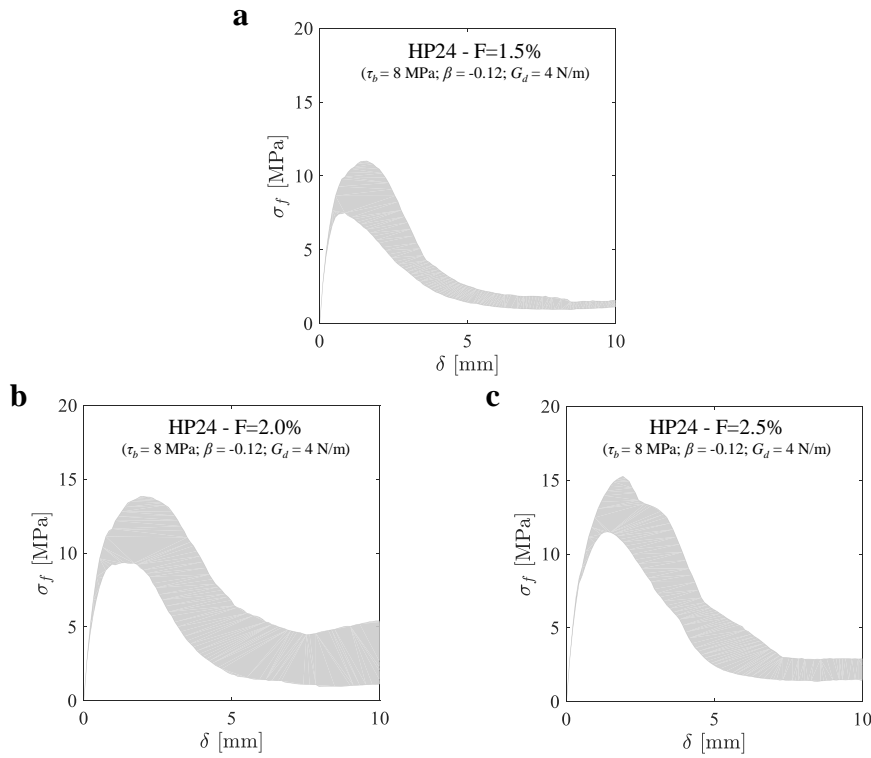


**Figure 3.75:** Variation of the responses due to the the distribution of the fiber through the mortar matrix. Five random distributions of the HP24 fiber for each fiber content (F=1.5%, 2.0% and 2.5%) are considered.

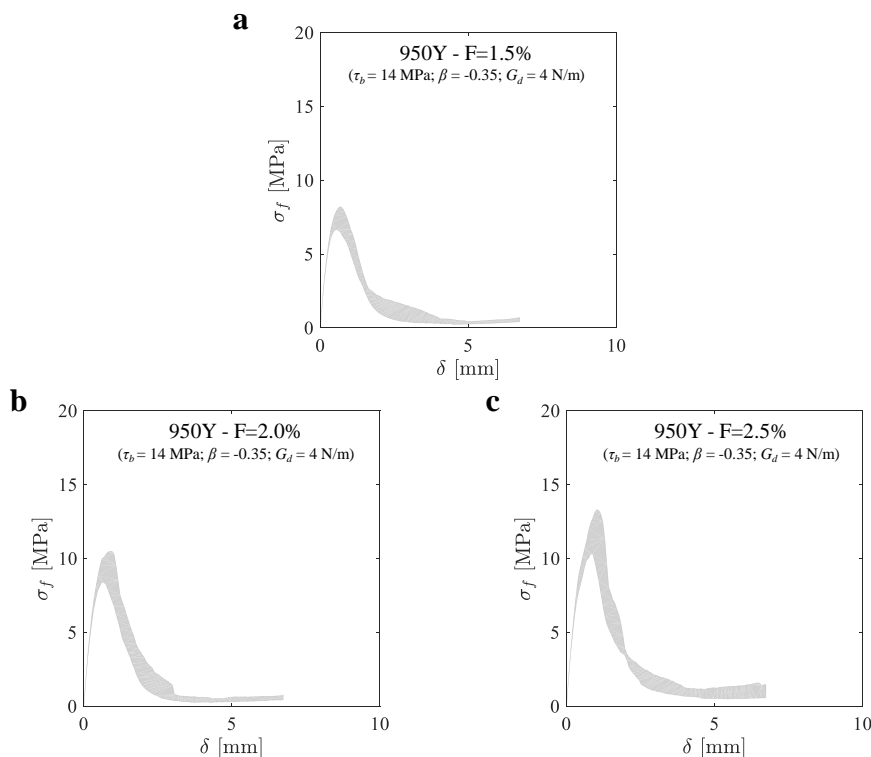


**Figure 3.76:** Variation of the responses due to the the distribution of the fiber through the mortar matrix. Five random distributions of the 950Y fiber for each fiber content (F=1.5%, 2.0% and 2.5%) are considered.

In general, it is worth noting that LDPM allowed obtaining similar trends of the experiments by assuming the literature values of the parameters. However, the parameters  $\tau_b$  and  $\beta$  were individually calibrated for the best fitting of the  $\sigma_f - \delta$  experimental curves based on both the fiber type and fiber content.

It is worth noting that the variability of the experimental responses was inevitably affected by several factors, such as misalignment of the samples with respect to their mid-thickness, small irregularity of the cross-section, the possible presence of micro-cracks, differences in the thickness of the specimen, incorrect casting phase of the product, spatial randomness of material properties, and so on.

On the other hand, for LDPM simulation, only the randomness due to the distribution of both the mortar particles and short fibers was considered. Indeed, the best fitting of the experiments was performed by assuming three different random configurations for both the fiber and mortar particles.

Figures 3.77–3.78 show the comparison between the experimental responses (represented by their envelope) and the numerical simulation carried out for the two fiber types (the HP24 and the 950Y) and three fiber contents ( $F = 1.5\%$ ,  $2.0\%$ , and  $2.5\%$ ). As already mentioned above, numerical curves represent the average of the responses computed for different arrangements of fiber and mortar particles.

In general, experiments indicated a distinct peak followed by an almost sudden load drop (especially for the 950Y case). This was possible to be modeled by assuming a slightly higher value of  $\tau_0$  and a value of  $\beta$  significantly less than zero.

The calibrated LDPM-F parameters are listed in Table 3.13.

**Table 3.13:** LDPM-F mechanical parameter values employed for the fiber material.

Case	$G_d$ [N/m]	$\tau_b$ [MPa]	$\beta$ [-]	$k_{sp}$ [-]	$k_{sn}$ [-]	$k_{rup}$ [-]	$\sigma_{uf}$ [MPa]	$E_f$ [MPa]
HP24-F = 1.5%	4.0	6.5	-0.10	0.0	0.0	0.0	1700	72000
HP24-F = 2.0%	4.0	8.0	-0.12	0.0	0.0	0.0	1700	72000
HP24-F = 2.5%	4.0	14.0	-0.35	0.0	0.0	0.0	1700	72000
950Y-F = 1.5%	4.0	11.5	-0.35	0.0	0.0	0.0	1700	72000
950Y-F = 2.0%	4.0	15	-0.35	0.0	0.0	0.0	1700	72000
950Y-F = 2.5%	4.0	12	-0.35	0.0	0.0	0.0	1700	72000

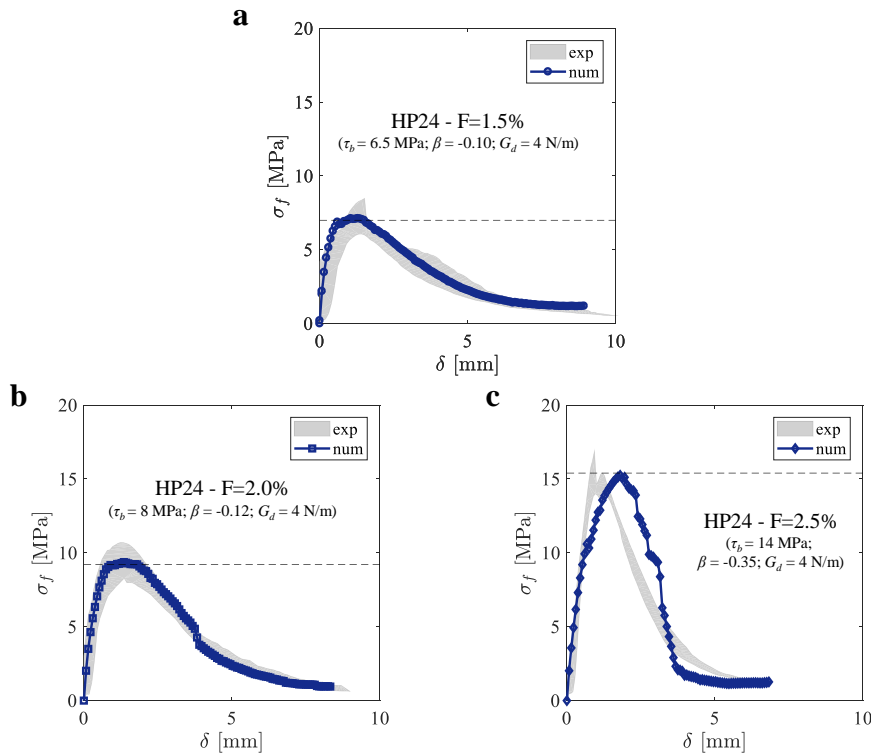


**Figure 3.77:** Comparison between experimental and numerical responses in terms of flexural stress  $\sigma_f$  Vs. vertical displacement  $\delta$  under 3PBT by assuming the HP24 fiber type with different fiber content (F=1.5%, 2.0% and 2.5%).

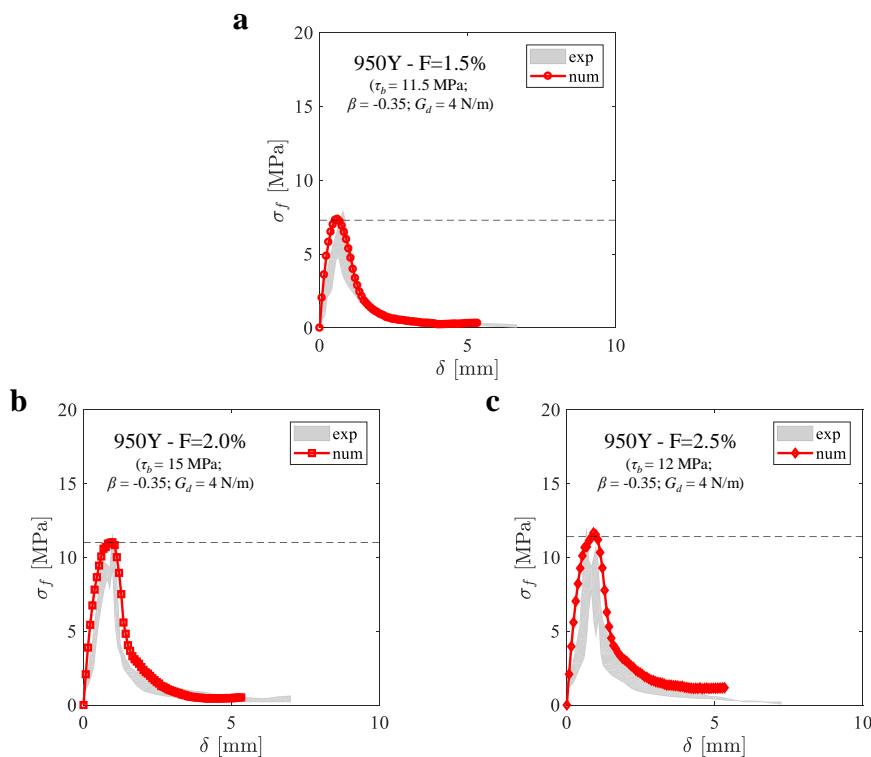


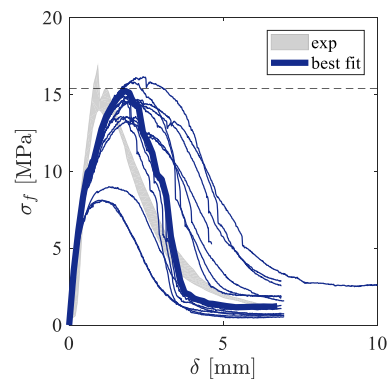
**Figure 3.78:** Comparison between experimental and numerical responses in terms of flexural stress  $\sigma_f$  Vs. vertical displacement  $\delta$  under 3PBT by assuming the HP24 fiber type with different fiber content (F=1.5%, 2.0% and 2.5%).

The mean error, compared with the experimental results, was only a really small percentage at the peak (0.3%) and remained less than 10% also for the fracture energy (see Table 3.14). Only for the HP24-F=2.5% case was not easy to find a proper set of the LDPM parameters to fit the experimental curves. Indeed, although several set of the LDPM parameters was assumed in the calibration procedure (see Figure 3.79), it was not possible to obtain the same stiffness, strength and same softening behavior of the experiments. In particular, the softening branch was characterized by an almost sudden drop in the stress after the peak. This may suggest that the experimental results for the HP24-F=2.5% case were affected by an erroneous small difference in the composition of the mix-design of the mortar. Indeed, experimental results obtained for the HP24-F=2.5% were characterized by a relatively low scatter, meaning that the anomaly in the experimental result was systematic and maybe related to the properties of the mortar rather than the other factors discussed above.

**Table 3.14:** Comparison between the mean mechanical properties computed for the mortar specimens under 3PBT by the experiments and the simulations.

Case	Experiments		Simulations		Error	
	$\sigma_f$ [MPa]	$G_f$ [N/mm]	$\sigma_f$ [MPa]	$G_f$ [N/mm]	$\sigma_f$ [%]	$G_f$ [%]
NF	2.9	0.3	2.9	0.3	0.0	0
HP24-F = 1.5%	7.0	5.0	7	4.5	0.0	-10.0
HP24-F = 2.0%	9.2	6.3	9.4	6.5	-2.2	+3.2
HP24-F = 2.5%	15.4	7.1	15.3	7.6	+0.6	+7.0
950Y-F = 1.5%	7.3	1.9	7.4	1.7	+1.4	+10.5
950Y-F = 2.0%	11.0	2.7	11.0	3.0	0.0	+11.1
950Y-F = 2.5%	11.4	2.9	11.6	3.0	-1.7	+3.4
				mean =	-0.3	+3.6

**Figure 3.79:** Comparison between experimental and numerical responses in terms of flexural stress  $\sigma_f$  Vs. vertical displacement  $\delta$  under 3PBT by assuming the HP24 fiber type with different fiber content (F=1.5%, 2.0% and 2.5%).



Figures 3.80a, b show the trend of the  $\tau_b$  and  $\beta$  parameters, for both the fiber types, as a function of the fiber content F. In particular, in Figure 3.80a one can see that the  $\tau_b$  value is ranging from 11.5 MPa to 15 MPa for the 950Y case, without observing a clear correlation between that parameter and F. On the contrary, one can see that  $\tau_b$  increases for a higher value of F in case of the HP24 fiber. Figure 3.80b shows that the  $\beta$  parameter does not depend on F for the 950Y case. On the contrary, one can see that  $\beta$  increases their (negative) value for the higher value of F in the HP24 case.

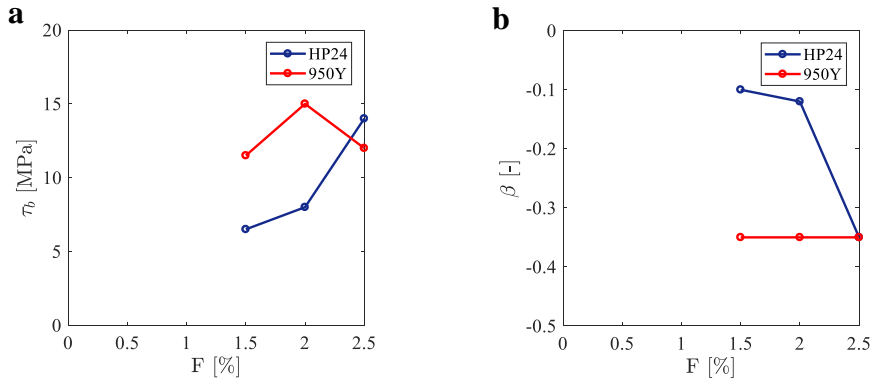


**Figure 3.80:** Trend of  $\tau_b$  (a) and  $\beta$  (b) as function of F for the two different fiber type (HP24 and 950Y).

Finally, Figures 3.81 and 3.82 shows the crack opening at failure for the fibrous specimens at different load steps (deflection  $\delta = 0.75$  mm, 1.5 mm and 4.5 mm). One can see that the main macroscopic crack developed in the vicinity of the notch tip of the mortar specimens because of the associated stress concentration. This crack was the result of a band of mesoscale cracking characterized by a certain width that increases by increasing the deflection value. This highlights that the geometry of the fiber influences the micro-cracks propagation even for low levels of load. Furthermore, one can also see that, for the same fiber type and deflection value, the crack width decrease by increasing the fiber content.

Again, by comparing the crack opening observed for the two fiber types (Figures 3.81–3.82), one can see that the fracture is more and more localized for the 950Y fiber, which is characterized by lower length and aspect ratio values, as compared to the HP24 one.

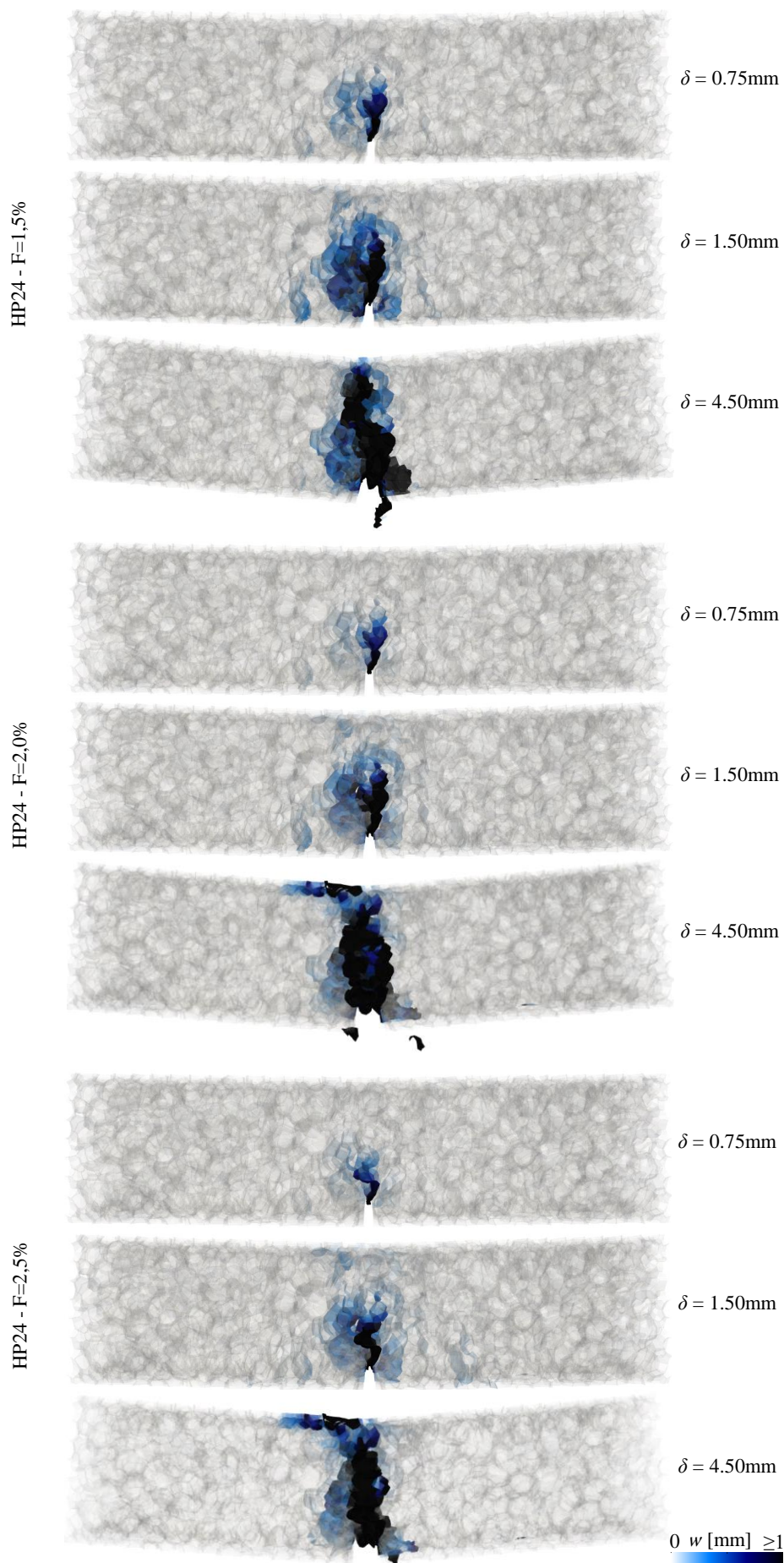


**Figure 3.81:** Mesoscale crack patterns at different values of the deflection  $\delta$  (0.75 mm, 1.5 mm and 4.5 mm) for the mortar specimens reinforced by the HP24 fiber with different fiber content  $F$  (1.5%, 2.0% and 2.5%.)

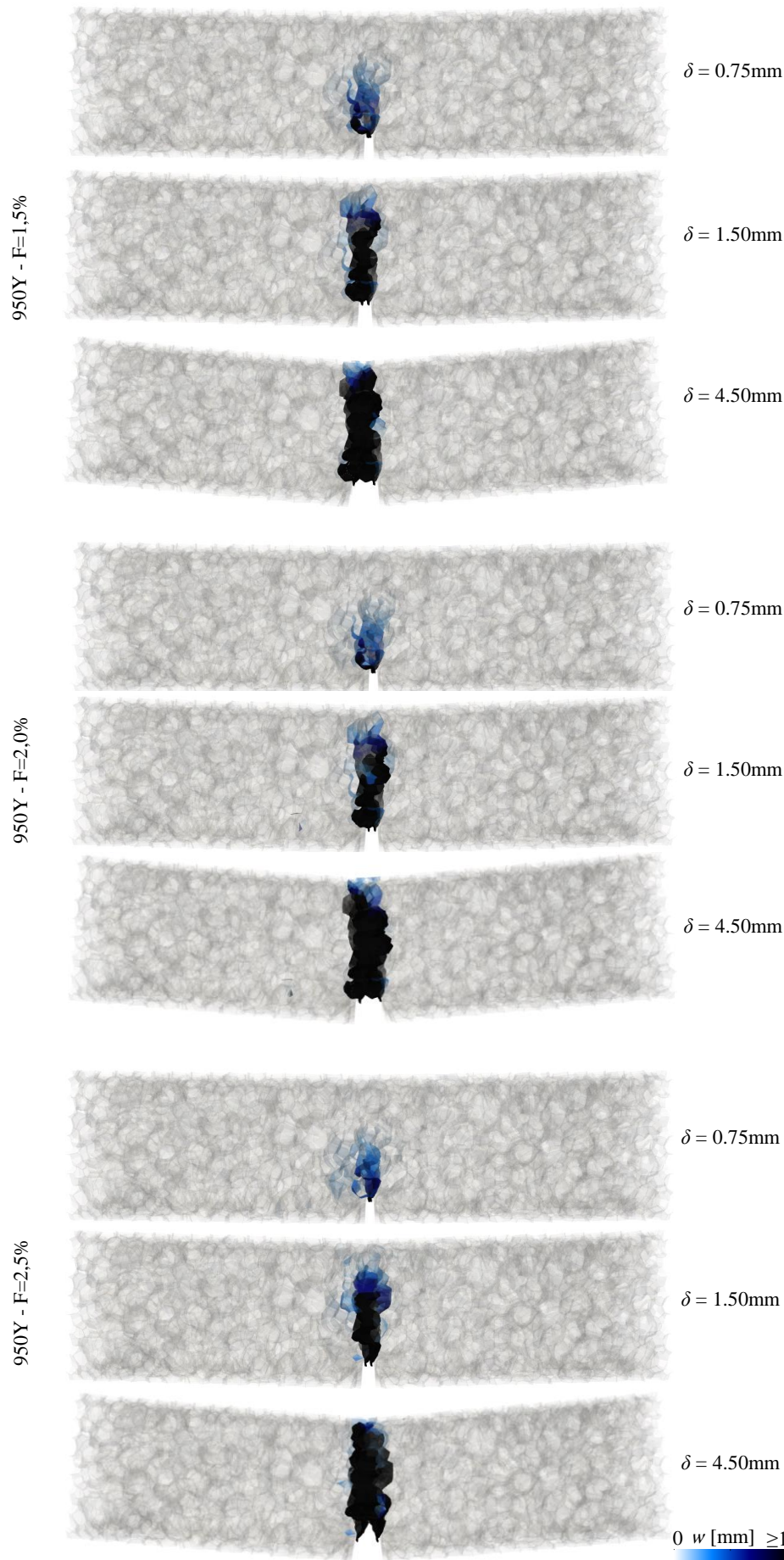


**Figure 3.82:** Mesoscale crack patterns at different values of the deflection  $\delta$  (0.75 mm, 1.5 mm and 4.5 mm) for the mortar specimens reinforced by the 950Y fiber with different fiber content  $F$  (1.5%, 2.0% and 2.5%.)

### 3.6 Comparison between the FRCM and the newly systems

Previous analyses carried out by LDPM showed that this numerical framework can successfully capture the fracture and failure mechanisms in both the irregular stone masonry and mortar as well as coupled construction systems (masonry – FRCM and mortar-short fibers).

Here, a direct approach aiming to estimate the efficiency of the reinforcement type on the mechanical proprieties of the mortar panel was first conducted by simulating the diagonal-compression test for a  $250 \times 250$  mm mortar specimen with 20 mm in thickness (see Figure 3.56). It is worth noting that a particular constrained system was conceived to avoid instability phenomena for the panel by ensuring an ideal tensile crack along the compressed diagonal of the mortar specimen. That system consisted of two fixed circular steel plates with 100 mm in radius placed at the external surfaces of the mortar panel and were modeled as rigid triangular shell elements (see Figure 3.56). A static friction coefficient  $f_s = 0.1$  and a dynamic friction coefficient  $f_k = 0.0084$  were assumed to simulate the low friction conditions at the plates-specimen interfaces.

Three different cases were numerically analyzed: (i) unreinforced mortar specimen (the URP case, see Figure 3.83a); (ii) mortar specimen reinforced by bidirectional fiber fabric embedded in a mortar layer (the RP-FRCM case, see Figure 3.83b); mortar specimen reinforced by short fibers randomly distributed in a mortar layer. In particular, the for latter case, only the HP24 fiber was assumed in the simulations with fiber content  $F$  equal to 1.5%, 2.0% and 2.5% (respectively the RP-SF1.5, the RP-SF2.0 and the RP-SF2.5 cases, see Figures 3.83c, d, e); The 950Y fiber was not investigated in this Section since both experimental and numerical results performed by a three-point bending test (see Sections 2.2.2.2 and 3.5.2) highlighted a significant lower ductility for the mortar reinforced by that type of fiber, as compared to the HP24 one.

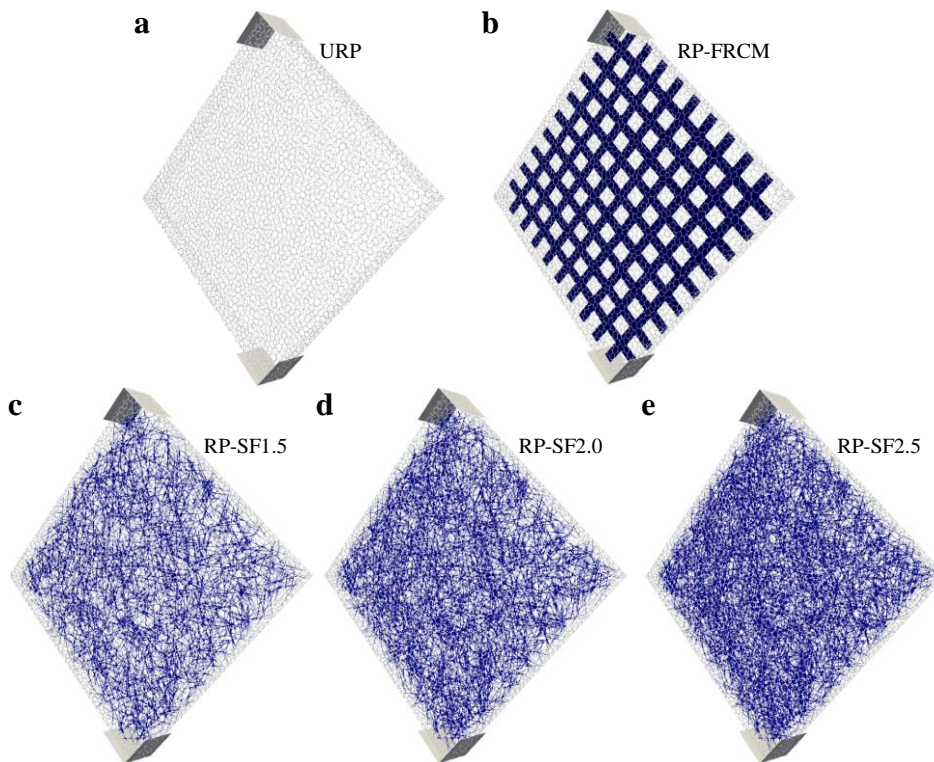


**Figure 3.83:** Simulation of the diagonal compression test performed on mortar specimen of 250x250 mm for several cases: a) the URP; b) the RP-FRCM; c) the RF-SF1.5; d) the RF-SF2.0; e) the RF-SF2.5.

It is worth noting that the same mechanical properties of the mortar were adopted for all the cases. This represented a conservative hypothesis. Indeed, when short fibers are adopted to improve the mechanical properties of the mortar, it is unavoidably uses additives to ensure the proper workability of the fibrous product. These additives also affect the mechanical properties of the product. The higher the additive content, the higher the tensile and compressive strengths of the mortar. However, the main aim of these simulations was to investigate only the effect of the type of reinforcing fiber on the mechanical properties of the irregular stone masonry. Hence, the same LDPM parameters of the mortar were assumed in all the cases (the unreinforced and the reinforced cases). In particular, these LDPM parameters were assumed to be the same as the ones calibrated on the experimental three-point bending test (see Section 3.5.2).

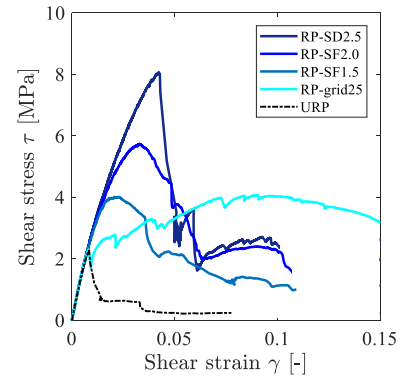
As far as the RP-FRCM case is concerned, the fiber strands were modeled with elastic beam elements (Table 3.12) with equivalent rectangular sections of  $0.1 \text{ mm} \times 10 \text{ mm}$ . A penalty constraint was used to connect the mortar particles to the fiber strands. A penalty stiffness parameter  $k$  was assumed equal to  $m/\Delta_{tp}^2$ , where  $m$  is nodal mass connected to it and  $\Delta_{tp}$  is the penalty time step that is selected to be slightly larger than the simulation minimum time step [268].

Results in Figure 3.84 show the mechanical response of the mortar panels under diagonal compression tests, expressed by the shear stress-shear strain ( $\tau$ - $\gamma$ ) curves. In particular, the RP-FRCM curve represents the case for which the best performance was observed during the investigation of the features of the fiber mesh

(space gap of 25 mm and fiber width of 10 mm, see Section 3.4.3).

As far as the SF cases are concerned, in Figure 3.84 one can see an increase in the shear strength as well as a decrease in the ductile behavior by increasing the fiber content  $F$ . In particular, results show the higher performance obtained in terms of shear strength for the panel reinforced by short fibers with  $F=2.5\%$  (the RP-SF2.5 case). For this case, one can also observe an almost sudden drop of the shear stress. The mechanical responses of the RP-SF2.0 and the RP-SF1.5 cases are characterized by a similar slope of the curves in the post-peak behavior.

**Figure 3.84:** Mechanical responses obtained for the unreinforced panel (URP) and panel reinforced by both the FRCM system (RP-FRCM) and short fibers randomly oriented in the matrix with different fiber content (RP-SF1.5, RP-SF2.0, RP-SF2.5).



Definitively, results of diagonal compression test performed on small mortar panels ( $250 \times 250 \times 20 \text{ mm}^3$ ) showed the enhancement of the shear strength of the mortar by introducing short fiber instead of long fiber. However, the load-bearing capacity of the innovative system is not acceptable if compared to the classic FRCM.

Hence, a combined system was adopted in the follows and consisted of mortar panel reinforced by fiber mesh of 100 mm and short fiber with  $F=2.5\%$ . Results are depicted in Figure 3.85, showing that, despite the use of the mesh fiber for which the worse performance was obtained in the study reported in Section 3.4.3 (i.e. space gap of 100 mm), the load-bearing capacity of the combined system is comparable with the one obtained with only fiber mesh with space gap of 25 mm. Furthermore, by combining short fiber ( $F=2.5\%$ ) and mesh fiber with space gap of 25 mm, one can obtain excellent performance in both shear strength and load-bearing capacity. In the combined system, the short fibers mainly determine the enhancement of the shear strength, whereas the mesh fibers play a role in the load-bearing capacity for high strain value. Obviously, the combined system will lead to the loss of the benefit in using only short fibers, such as the easiness and time application in situ. Furthermore, the cost of the combined reinforcing system will be much higher than that of the reinforcing system characterized by only mesh fiber or short fiber. Its applicability is fairly far to be easily applied in the real cases.

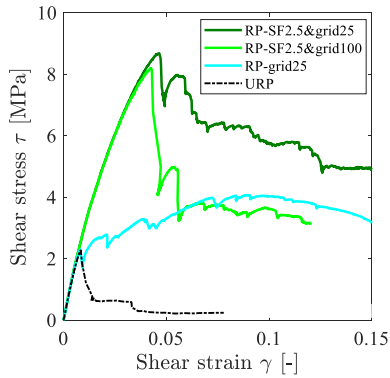


**Figure 3.85:** Shear stress-shear strain curves obtained for the unreinforced panel (URP), panel reinforced by mesh fiber (RP-grid25) and panel reinforced by combined system (short fibers with  $F=2.5\%$  coupled with mesh fiber of 25 mm or 100 mm.)

Figure 3.86 shows the crack opening at failure for the unreinforced mortar panel (URP), the panel reinforced with the FRCM system (RP-FRCM), and the panel reinforced with short fibers (RP-SF1.5, RP-SF2.0, and RP-SF2.5). It is worth noting that the failure plots correspond to the same value of the imposed displacement. Cracks on the unreinforced masonry (Figure 3.86a) occurred along the compressed diagonal, leading to a separation of the two portions of the specimen along the compressed diagonal. This crack pattern highlighted a brittle failure mode for the unreinforced mortar panel. In Figure 3.86b one can see the effect of the fiber mesh on the crack propagation of the specimen. Indeed, band of mesoscale cracking was characterized by a lower width, as compared to the URP case. The fiber grid kept together the two portions of the specimen ensuring a higher load-bearing capacity for the panel. Moreover, the cracks that occurred for the RP-FRCM case were concentrated along the compressed diagonal of the panel, as observed for the URP case.

Figures 3.86a, b, c illustrate the fracture propagation occurred for the specimen reinforced by short fibers. In particular, Figure 3.86a clearly shows a diffuse crack through the mortar specimen for the RP-SF1.5 case. By increasing the fiber content, the cracks width became larger and, at the same time, the crack opening became lower. This trend can be observed by comparing Figures 3.86a, 3.86b and 3.86c obtained for the short fiber reinforcement with  $F$  equal to 1.5%, 2.0% and 2.5% (the RP-SF1.5, the RP-SF2.0 and the RP2.5 cases, respectively).

In general, the crack pattern observed for the mortar specimen reinforced by short fibers randomly oriented in the matrix is much more diffused than the one observed for the FRCM system. This explains the higher ductility of the innovative system, as compared to the FRCM case.

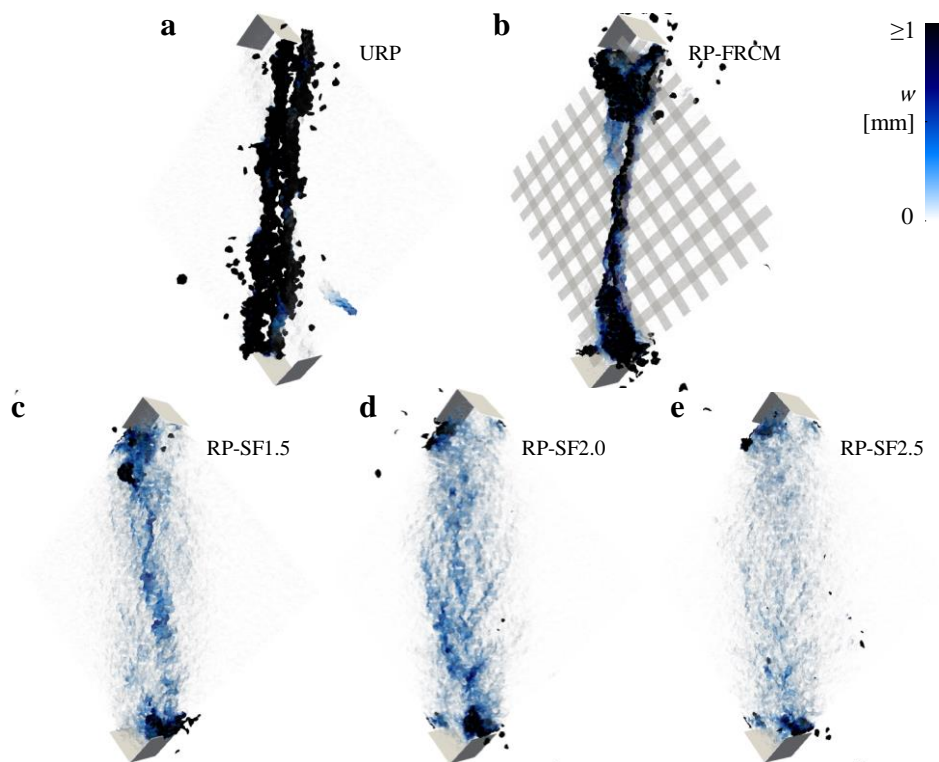


**Figure 3.86:** Crack opening at the failure obtained at the same imposed displacement for different cases: a) the URP; b) the RP-FRCM; c) the RP-SF1.5; d) the RP-SF2.0; e) the RP-SF2.5.

Finally, a simulation of the diagonal-compression test carried out on the stone masonry panel coated by mortar reinforced by short fiber or mesh fiber is presented in the follows. In particular, three different models were analyzed as follows: (i) unreinforced masonry specimen (the NR case); (ii) masonry specimen reinforced by bi-directional fiber fabric embedded in a mortar layer (the RM-FRCM case), as illustrated in Figure 3.87b; masonry specimen reinforced by short fibers randomly distributed in a mortar layer with fiber content equal to 2% (the RM-SFRM case), as illustrated in Figure 3.87c. For both the RM and SFRM, two mortar layers, with 20 mm in thickness, were applied on the surfaces of the masonry specimen.

The reproduction of the diagonal test consisted in the modeling of a square masonry panel of  $1 \times 1 \times 0.3 \text{ m}^3$  subjected to compressive load applied along one of the panel diagonals. As opposed to the diagonal test simulations presented in the Section 3.3 and Section 3.4, in which the size of the square panels was assumed equal to 1.2 m, the simulations presented here were carried out on the smaller panel specimens (i.e. 1 m) due to the high computational effort especially in the SFRM case. A further difference to the tests simulated in the above-mentioned Sections concerns the boundary conditions: for all the three cases, the specimen was assumed to be no supported to a horizontal plate. Indeed, as discussed in Section 3.3.3, the correct evaluation of the shear properties of the masonry walls, especially the ductility, can be influenced by boundary conditions that may affect the propagation of the fracture on the wall and, therefore, its mechanical response. For the LDPM simulations, the two steel plates (L-shape), placed at the specimen

corners, and the horizontal steel plate, placed at the specimen basement, were modeled as rigid triangular shell elements. A sliding with 'stick-slip' friction constraint [212] between the corner plates and the masonry particle nodes was used. That friction constraint is designed to force a set of nodes to move over a frictional surface while the constraint perpendicular to the surface is treated using a master-slave formulation. The simulations used a static friction coefficient  $f_s = 0.5$  and a dynamic friction coefficient  $f_k = 0.5$  to simulate the high friction conditions at the L-shape plates-specimen interfaces. Assuming  $f_s = f_k$  allowed to prevent the reduction of the friction once sliding between surfaces appeared. Moreover, the rotations perpendicular to the normal plate directions were fixed for all particle nodes in contact with the corner plates (L-shape).

The mortar particles were connected to the masonry sample via a frictional penalty constraint;  $f_k = f_s = 0.5$  were assumed to simulate the almost perfect bond (PB) conditions at the masonry-mortar interfaces. That condition can simply be taken into account the effect of the interlock phenomenon between materials. The interface between stone particles and reinforcement mortar particles was simplistically assumed to be flat.

In the FRCM case, the fiber strands were modeled with elastic beam elements (Table 3.12) with equivalent rectangular sections of  $0.1 \text{ mm} \times 10 \text{ mm}$ . A penalty constraint was used to connect the mortar particles to the fiber strands. A penalty stiffness parameter  $k$  was assumed equal to  $m/\Delta_{tp}^2$ , where  $m$  is nodal mass connected to it and  $\Delta_{tp}$  is the penalty time step that is selected to be slightly larger

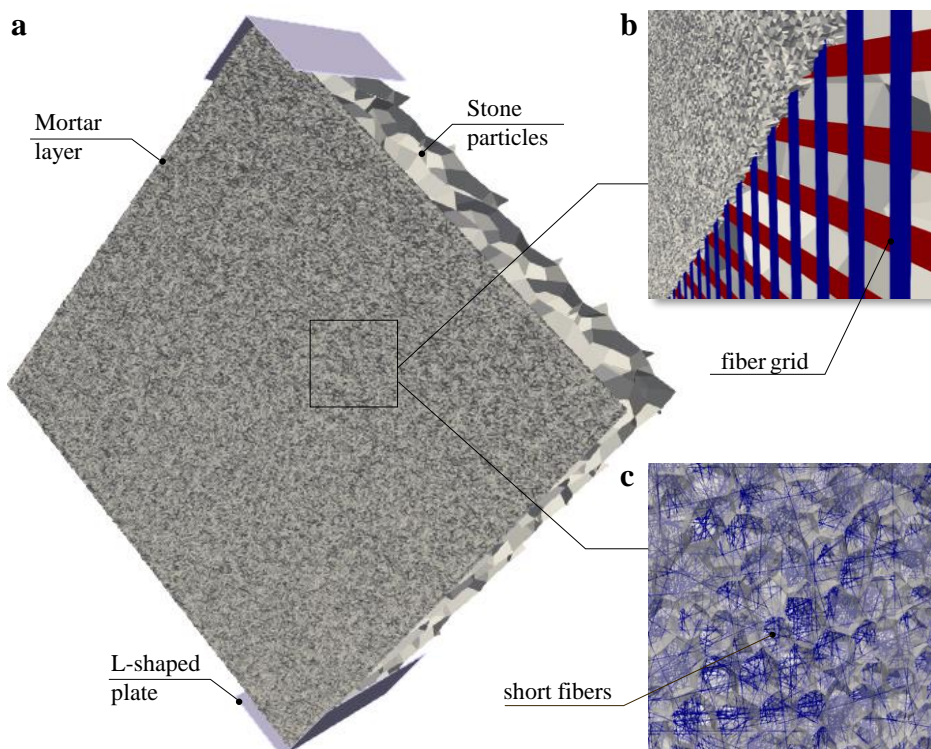


Figure 3.87

than the simulation minimum time step [268].

Furthermore, since results presented in Section 3.4.4 have shown that the influence of the fiber anchors is negligible in the enhancement of the in-plane mechanical properties of the walls, they were not introduced in the models.

In Section 3.3.1 have been shown that the mechanical response is highly affected by the distribution of the stone through the masonry specimen, here the same arrangement of the stones was assumed for the three cases. Moreover, for the two reinforced cases, also the arrangement of the mortar particles was fixed.

The mechanical parameters of the masonry, reinforcing mortar and bi-directional fiber fabric as well as the mechanical parameters of short fibers assumed in the following simulation have been described in Sections 3.3.1 and 3.5.2, respectively.

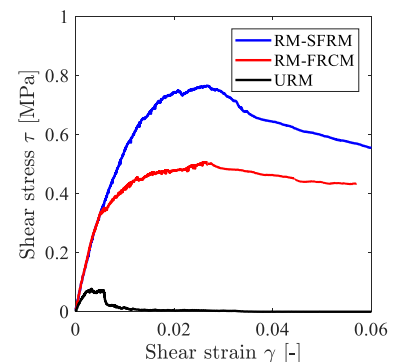
It is worth noting that the same mechanical properties of the reinforcing mortar were adopted for the RM-FRCM and RM-SFRM cases. This represented a conservative hypothesis, as already discussed for the simulations of the single mortar panel of 250x250x20 mm reinforced by a bi-directional fiber fabric and short fibers.

Results in Figure 3.88 show the mechanical response of the unreinforced and reinforced stone masonry panels under diagonal compression tests, expressed by the shear stress and shear strain ( $\tau$ - $\gamma$ ) curves. In particular, one can see that the shear strength of the masonry increase of about 800% and 530% for the RM-SFRM and RM-FRCM cases, respectively, as compared to the unreinforced masonry. Hence, the RM-SFRM ensures a higher shear strength of about 50%, as compared to the RM-FRCM. This result is in line with previous results carried out on a single panel of mortar reinforced by bi-directional fabric and short fibers. In that case, the increment ensured by the short fibers was about 100%. Hence, when the new mortar is coupled to the masonry reduces his efficiency in terms of shear strength, as compared to the analyses carried out on the single panels of 250×250×20 mm<sup>3</sup>.

No difference in terms of the shear modulus  $G$  was observed for the two reinforcement systems. Indeed, for both the cases  $G$  increased of about 2.2 times the shear modulus computed for the unreinforced masonry.

As far as the ductility is concerned, one can compute the  $\mu_{80\%}$  coefficient equal

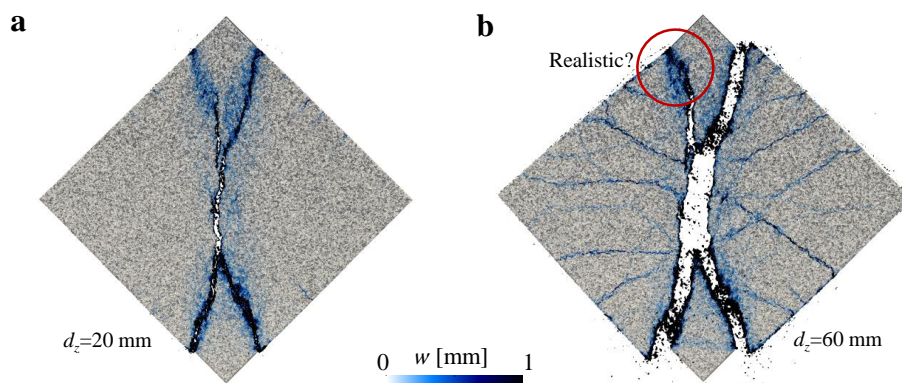
**Figure 3.88:** a) Reinforced stone masonry specimen tested under diagonal compression; b) detail of the fiber strands embedded in the mortar matrix (the RM-FRCM case); c) detail of the short fibers embedded in the mortar matrix (the RM-SFRM case).



to 1.75 and 2.30 for the RM-SFRM and RM-FRCM cases, respectively. Hence, the FRCM ensures a higher load-bearing capacity than the SFRM. However, this parameter is not satisfactory to characterize the softening behavior of the reinforcements. Indeed, assuming that the fracture energy is proportional to the area under the  $\tau$ - $\gamma$  curves, one can compute an increase of the fracture energy of 35% for the RM-SFRM, as compared to the RM-FRCM case.

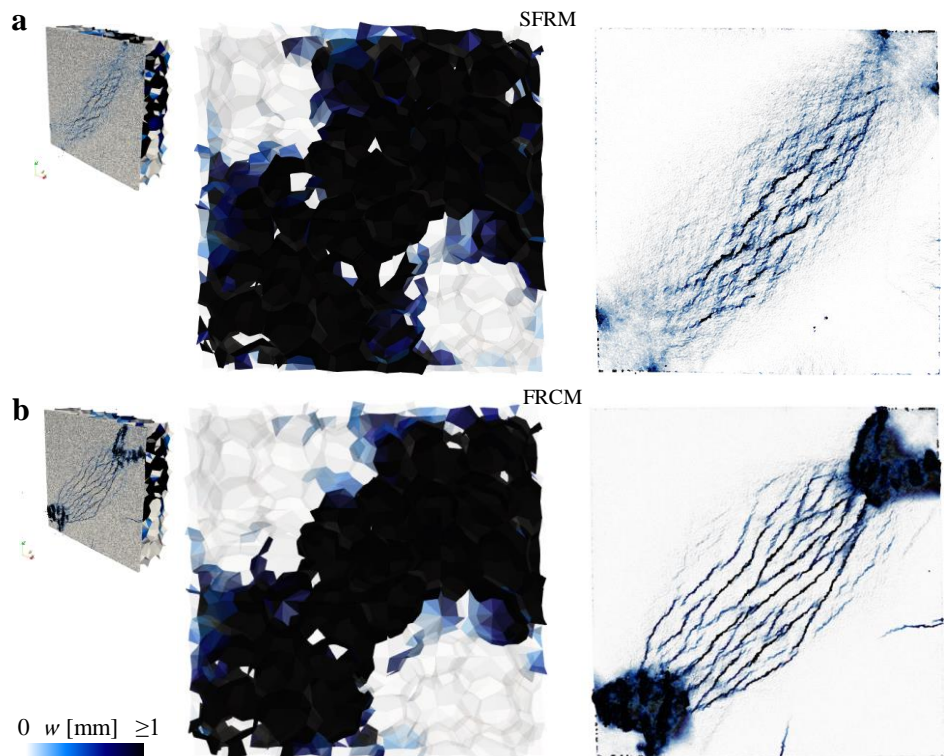
Unfortunately, it was not possible to properly investigate the numerical responses of both the reinforcement system for larger deformations due to the high computational cost. It suffices to see that masonry and the reinforcement mortar were discretized in almost 150 and 5800 particles, respectively. Instead, fiber strands were represented by 1560 beam elements connected to each other along the direction of the fiber strands. Short fibers were individually represented by 7500 beam elements. Despite the higher number of beams elements generated for the short fibers, the computation cost required for the FRCM was much higher. This was due to the continuous interaction between the beam nodes of the fiber strands and the facets of the mortar particles, for all the duration of the simulation. After the optimization of the analyses (necessary to reduce the time of the simulation and, at the same time, ensuring the convergence of the analysis) the simulations of the RM-FRCM case required 48 processors and 120 computational hours performed by a high performance computing cluster (Quest) of Northwestern University.

Figure 3.89 shows the crack opening at the failure for the external reinforcing layer of fibrous mortar. In particular, two steps were plotted and corresponding to an imposed vertical displacement of 20 mm ( $\gamma$  of about 0.035) and 60 mm ( $\gamma$  of about 0.06). For large displacements one cannot observe a failure of the specimens, as instead was expected, since the upper portion of the mortar layer carries the bottom part. However, despite the effort in trying to understand the reliability of this behavior, it is not possible to assume with certain that the softening of the masonry coated by SFRLM is realistic.



**Figure 3.89:** Crack opening at the failure for the only coating mortar layer ( $F=2.0\%$ ) occurred at the applied vertical displacements  $d_z$  of 20 mm (a) and 60 mm (b)

Figure 3.90 shows the crack opening at the failure for the masonry specimen reinforced by the SFRM system (Figure 3.90a) and the FRCM system (Figure 3.90b). The failure plots correspond to a value of the shear strain  $\gamma = 0.025$ , for which the maximum shear stress was achieved for both the reinforced panels. In particular, one can see that the masonry panel is slightly more damaged for the SFRM case rather than the FRCM case. This is because the SFRM is subjected to higher shear stress (0.77 MPa), as compared to the FRCM case (0.54 MPa). Furthermore, by comparing the fracture propagation on the mortar panels, one can see that the crack band for the SFRM is more diffused, as compared to the FRCM case. In addition, the FRCM leads to a concentration of the damage at the corners of the panel.



**Figure 3.90:** Crack opening at the failure for stone masonry reinforced by: a) the new fibrous lime-mortar; b) the FRCM. Plots correspond to a shear strain  $\gamma$  equal to 0.025.

### 3.7 Chapter conclusions

The Fiber Reinforced Cementitious Matrix (FRCM) system consisting of a glass fiber grid embedded into a lime-based mortar, used for the strengthening of historical stone masonry walls, is investigated in the present work. First, the paper presents experimental diagonal compression tests carried out on both unreinforced and reinforced panels. Second, the tests are numerically simulated by the Lattice Discrete Particle Model (LDPM) which is able to model the heterogeneous character of masonry walls by modeling stone particles interacting with each other.

In particular, experimental tests show that the FRCM systems applied as a coating to the masonry walls provide a significant increase both in shear modulus and shear strength (620% and 390% respectively).

Furthermore, the numerical simulations show that the LDPM can predict the mechanical response of stone masonry material and it can be useful for studying the behavior of alternative strengthening systems, especially for the post-peak mechanical behavior that is usually difficult to investigate by experimental tests. In particular, by comparing perfect and weak bond behavior at the mortar-masonry interface, numerical results highlight that bond behavior has a strong effect (up to 60%) on the load-bearing capacity for very large displacements. Instead, the bond behavior has a slight effect in terms of strength (up to 10%) and no influence in terms of stiffness.

The numerical results also highlight the need to combine both the mortar layers and the fiber grids in the strengthening system. Indeed, the strength of the reinforced masonry specimens is mainly due to the thickness of the mortar layers applied on the side of the walls: the larger the thickness, the larger the maximum shear stress. However, the load-bearing capacity for large deformations depends significantly on the fiber grid embedded in the mortar layers. By comparing the reinforced panels with the unreinforced ones, one can observe an increase in load-bearing capacity for very large displacements of up to about 400% for the reinforced system without fiber grid and 600% for the one with fiber grid.

Only a slight increase in the load-bearing capacity for large displacements can be obtained by introducing fiber anchors (placed across the thickness of the masonry wall) in the strengthening system, which are commonly used with the primary goal of improving the out-plane mechanical response of masonry buildings.

Based on the results discussed in this paper, the conclusion can be made that the LDPM approach can be reliably employed to help reduce the number of experimental tests when designing strengthening alternatives for historical masonry. This leads to a reduction in both cost and investigation time.

Definitively, the good agreement between experimental results and numerical

predictions confirmed the high reliability of LDPM to simulate the mechanical behavior of masonry material both for unreinforced and reinforced cases.

Contrarily to most (if not all) computational methods available in the literature that provide a deterministic numerical prediction of the mechanical performance of masonry structures, the LDPM-based approach allows stochastic predictions for the failure of such structures. LDPM simulated the behavior of irregular masonry structures accurately and captured the effect of different stone size distributions as well as size effect. Moreover, LDPM captured accurately the initiation and subsequent localization of damage in irregular masonry structures. More specifically, it simulated well the evolution of the fracture process zone during fracture propagation and failure.

Due to the ability to simulate size effect, LDPM predicts the difference between the strength and ductility of laboratory samples versus actual masonry walls. Results show that tests on laboratory samples overestimate by 50% the strength of real structures. Results show also that despite certain ductility shown by laboratory samples, real masonry structures should be considered perfectly brittle. Hence the customary plastic analysis approach used in many design guidelines is not warranted. The stone distribution does not influence strongly the strength and shear modulus (variation within 10% for different stone configurations). On the contrary, it affects significantly the ductility (up to 40% variation).

The statistical scatter in the LDPM results depends on the level of homogeneity of the masonry samples: the larger the sample, the lower is the effect of material heterogeneity leading to a smaller coefficient of variation of the response in terms of strength and shear modulus. The trend is different for the coefficient of variation of the ductility due to damage localization and size effect. Furthermore, the scatter of the predicted ductility depends on the level of stress for which it is computed. The scatter increases for stress levels deep into the post-peak.

Another important aspect analyzed in the simulation concerned the effect of different configurations of the diagonal compression test on the evaluation of the mechanical properties of masonry walls. By keeping the specimen in a horizontal configuration and using a basement to support it, one can overestimate the ductility of the panel of almost 2 times as well as reduce of about 20% the stiffness of the wall, as compared to the configuration in which the specimen is rotated of  $45^\circ$ . The latter configuration, although recommended by the standard codes, is almost never adopted especially in the experimental test carried out in situ (and also at the laboratory), due to the brittleness of the masonry panels and to reduce the risk of damaging the panels during the handling.

As far as the simulation of the fibrous mortar material is concerned, reproduced well the experiments. In particular, a proper investigation of the main fiber-

matrix interaction parameters (the bond fracture energy, the bond friction stress, and the slip-hardening/softening coefficient) were carried out for the simulation of the three-point bending test. In particular, these parameters showed different sensitivity to the mechanical behavior of the fibrous-mortar. The bond friction stress mainly affected the flexural strength of the fibrous-mortar specimen and increases by increasing the fiber content in the case of longer fibers (24 mm), as compared to the smaller ones (13 mm). The slip-hardening/softening coefficient strongly affects the post-peak behavior, much more than the bond fracture energy, and depends on the geometrical feature of the fiber. In particular, for the smaller fiber (13 mm) the value of that parameter was constant. On the contrary, for longer fiber (24 mm), it showed an increase in its (negative) value by increasing the fiber content.

Simulation carried out by LDPM on a  $250 \times 250 \times 20$  mm fiber-reinforced mortar specimen tested in diagonal compression showed that the FRCM system can be affected by the re-hardening phenomena, which ensure higher shear strength of the composite material, as compared to the strength of the unreinforced panel. However, that phenomena is sensitive to the features of the fiber strands (space gap and geometry) as well as the boundary condition of the test. The best performance of the FRCM system was obtained for the glass fiber grid with 25 mm in space gap of, 10 mm width and 0.1 mm in thickness. In general, results showed that the higher fiber fiber content, the higher the shear strength. The same trend was observed also in terms of the fracture energy, which increases for higher fiber content. However, for the case of fiber content equal to 1.5%, an almost sudden drop in the shear stress was observed. This suggests using a minimum fiber content equal to 2% to ensure ductility properties as well as load-bearing capacity even for large deformation. By assuming a fiber content equal to 2%, the same stress reduction (30%) as the case of the unidirectional long fiber of the FRCM was observed.

A final comparison between the classic reinforcement system (the FRCM) and the new proposed in this research (the short fiber reinforced mortar SFRM) was presented at the end of the chapter. In particular, simulation of the diagonal-compression test carried out on the stone masonry panel was proposed by adopting the two different reinforcement systems applied as a coating on the masonry surfaces. Results highlighted that the new composite material enhanced the shear strength of the masonry about 800% and 50%, as compared to the unreinforced masonry and the reinforced masonry with FRCM, respectively. Also, promising results in terms of ductility of the panel were observed for the new strengthening system. In particular, although the load-bearing capacity of the FRCM was higher of about 30% than the SFRM case, the fracture energy ensured by the

FRCM system was about 30% lower than the SFRM case.

The excellent ductility capacity of the new composite material was related to its fracture propagation that it was more and more diffused, as compared to the FRCM case. Indeed, the FRCM showed a more localized fracture along the compressed diagonal as well as a higher concentration of the damage at the corners of the compressed diagonal of the masonry panel, as compared to the SFRM case.

# TECHNICAL DIRECTION

---

## Abstract

The present Chapter provides technical information for the characterization of the shear strength of the masonry walls reinforced by Fiber Reinforced Mortar coating system. Based on the numerical and experimental results discussed in the present thesis, an analytical formulation was proposed for the estimation of the shear strength of the reinforced masonry merely based on the properties of the unreinforced masonry and the reinforcing mortar of the FRM. That formulation was validated on a consistent number of experimental data, concerning also tests on stone masonry collected in the literature. Technical indications on the geometrical features of the fiber are also provided for both uni/bi-directional fiber and short fibers.



# Technical direction

---

## Abstract in italiano

Il seguente capitolo ha lo scopo di fornire alcune indicazioni tecniche per la caratterizzazione meccanica dei sistemi FRCM o più in generale, sui sistemi di rinforzo caratterizzati dall'applicazione di uno strato di malta (rinforzate con fibre lunghe o corte) sulle superfici murarie. Infatti, anche se negli ultimi anni l'applicazione dei sistemi FRCM per le murature storiche è considerevolmente aumentata, il comportamento meccanico di tale sistema accoppiato a pareti murarie non è ancora completamente caratterizzato. Questo a causa della mancanza di dati sperimentali esaustivi e di modelli matematici affidabili. In particolare, gli studi sull'applicazione degli FRCM sono più numerosi per le strutture in calcestruzzo che per le strutture in muratura. Solo negli ultimi anni, sono state proposte linee guida e codici per la caratterizzazione e la progettazione di sistemi FRCM, che nonostante l'enorme lavoro scientifico, non possono essere definite del tutto complete. I risultati sperimentali e numerici discussi nei precedenti capitoli hanno permesso di individuare una semplice formulazione analitica per la stima delle proprietà meccaniche delle murature rinforzate. Tale formulazione permette di stimare qualitativamente l'efficienza dei sistemi di rinforzo ad intonaco utilizzando solamente le principali informazioni della muratura non rinforzata e della malta di rinforzo applicata superficialmente. La relazione si basa sul fatto che il sistema FRCM, in una configurazione di compressione, deve il suo incremento prestazionale in termini di resistenza a taglio principalmente alle proprietà meccaniche e allo spessore del muro non rinforzato e della malta di rinforzo. Le fibre lunghe uni- o bi-direzionali disposte nel sistema FRCM hanno invece la principale funzione di incrementare la capacità di mantenimento del carico per grandi spostamenti/deformazioni e non forniscono un contributo nell'incremento della resistenza a taglio delle murature.

The knowledge of the mechanical behavior of composite materials is very important for their use as rehabilitation/strengthening systems. This chapter aims to provide guidance in technical and content matters for the evaluation of the shear strength of masonry panel coated by layers of reinforcement mortar. In particular, a simplified formulation is proposed. That relation can be applied to summarily compute the enhancement of the FRCM system or, more generally, of coating (jacketing) systems consisted of mortar/concrete material reinforced by element with negligible resistance in compression, such as the fiber.

Indeed, although the FRCM began to be widely applied to the masonry construction, its mechanical behavior is still not completely characterized due to a lack of exhaustive experimental data and reliable mathematical models for the investigation of the mechanics behind the complex coupled resistance system made of the masonry wall and the FRCM.

The number of studies on the use of FRCM for masonry is much lower than the number of studies on concrete structures. Only a few years ago, guidelines and codes for characterization and design of FRCM systems were proposed. However, they are limited and not entirely satisfactory to design such a reinforcing system.

Standards CNR-DT 215/2018 and ACI-549 [95] defines that the contribution of the FRCM on the shear capacity of unreinforced panels is attributed to the characteristics of the fibers (geometry and mechanical properties). Furthermore, Standard CNR-DT 215/2018 proposes, as a simplification, an amplification coefficient of 1.5 for the mechanical properties of irregular stone masonry walls reinforced by FRCM.

However, by observing both experiments and simulations, a general opinion on the mechanical behavior of the FRCM system has been conceived. In particular, the efficiency of the FRCM in terms of shear strength is mainly related to the thickness of the unreinforced masonry wall. The higher the masonry wall thickness, the lower the efficiency of the FRCM in terms of shear strength, end vice-versa.

Furthermore, has highlighted in the simulations, also the thickness of the reinforcement mortar layer strongly affects the shear strength of the reinforced masonry.

Standards define a specific range value for the mortar layer thickness (5–20 mm). However, during the application of the mortar layer, it is difficult to ensure a uniform thickness for it due to the asperity of the masonry surface (especially the irregular one). Standard suggests measuring the mortar thickness from the protruding stones leaving aside to consider the depths mortar joints or the irregularity of the surface. However, this assumption can strongly affect the enhancement of the shear behavior of masonry. It suffices to see that the asperity of the surface of irregular stone masonry is about a few centimeters.

Hence, the amplification coefficients proposed by Standard CNR-DT 215 and NTC18 (equal to 1.5 and 2.5, respectively), for the design of the mechanical properties of stone masonry strengthened by FRCM in absence of experimental investigation appears not consistent. That coefficient can be much higher (or lower) and mainly depends on the thickness of both the masonry wall and reinforcement mortar as well as the boundary condition at the reinforcement mortar-masonry interface.

Moreover, another incongruity with Standards CNR-DT 215/2018 and ACI-549 [95] concerns the effect of the fiber on the mechanical behavior of the FRCM. In particular, Standards define that the contribution of the FRCM on the shear capacity of unreinforced panels is attributed to the characteristics of the fibers (geometry and mechanical properties). Simulations showed that, in the case of compressed FRCM, fibers have only the function to carry tensile stresses (load-bearing capacity), whereas both the shear strength and shear modulus of the FRCM are related to the mortar. In particular, for all of the geometrical features of the fiber grid analyzed in the simulations, the re-hardening phase has not to lead to an increase in the shear strength of the panel. Indeed, the shear strength of the FRCM was achieved when the failure of the mortar occurred. After that, an almost sudden drop in the shear stress followed by a re-hardening phenomenon (re-increase of the shear stress) was observed. However, the stress increment due to the re-hardening was not so consistent to enhance the shear strength of the panel.

Standards may have adopted a relation between shear strength and characteristics of the fibers only based on the mechanical behavior of the FRCM tested under tensile configuration. Indeed, when a FRCM specimen is subject to a tensile test, the matrix undergoes a multi-cracking process resulting in the transfer of stresses from the matrix to the fibers. Then, an increase in the tensile stress (rehardening phase) of the composite material can be observed up the failure (rupture) of the fiber fabric. In that case, the tensile strength of the FRCM mainly depends on the characteristics of the fiber, which is characterized by really high resistance in the axial direction of the fibers.

However, it is worth noting that fibers present negligible resistance in the other directions. Hence, when a FRCM-reinforced masonry wall is subjected to diagonal compression (typical action induced by earthquakes), the overall behavior of the coupled system, based on the results of the numerical simulations, can be differentiated in three phases: i) the load is carried mainly by the mortar matrix until cracking; ii) the matrix undergoes a multi-cracking process resulting in the transfer of stresses from the matrix to the fibers; iii) the load is carried almost exclusively by the fabric.

Collapse mechanics observed for masonry structure during seismic action highlights that the tensile test, which represents the main test for the characterization of the FRCM, may not be representative to characterize the mechanics of the coupled FRCM-masonry system under seismic action. The compressive test may be more appropriated.

The in-plane shear capacity of strengthened walls can be defined as the sum of the contribution of masonry (minimum between the shear sliding, shear friction, diagonal tension, and compression failures) and the FRCM reinforcement, where the effectiveness of FRCM is considered only after occurrence of masonry cracking [53, 269, 94, 58, 270]. From ACI 549, the FRCM contribution is calculated as  $2nA_fLf_{fv}$ , where  $A_f$ ,  $n$ ,  $L$  are the area of the fabric reinforcement by unit width, the number of layers of fabric, and the length of the masonry, respectively. The tensile strength of the FRCM ( $f_{fv}$ ) is equal to  $E_f\varepsilon_{fv}$ , being  $\varepsilon_{fv}$  the FRCM tensile strain ( $\leq 0.004$ ). Indeed, from tests on clay brick masonry reinforced by (i) near-surface mounted (NSM) glass FRP bars externally bonded, (ii) glass/carbon FRP laminates, and (iii) glass FRP grid reinforced polyurea [53], it was observed that the experimental shear strength of the URM increases proportionally to the so-called “calibrated reinforcement ratio index” ( $\eta$ ) computed as  $\eta = \rho E_f/E_m$ , where  $\rho$  is the ratio between the area of reinforcement and net area of URM walls, whereas  $E_f$  and  $E_m$  are the elastic modulus of cracked reinforcement and URM wall, respectively. That study concluded that that formulation could be applied for both the FRCM and FRP strengthening technologies, assumed as similar reinforcing systems. However, it is worth mentioning that, for the FRCM and differently from the FRP, recent study [79] experimentally demonstrated the negligible contribution of the fiber on the RM strength, as confirmed by simulation presented in this thesis. For the FRCM, the main contribution to the RM strength is mainly given by the mortar

Hence, an analytical relation needed to be found to estimate the strength of the reinforced masonry merely based on the mechanical and geometrical properties of both the unreinforced masonry (URM) and the FRCM.

The behavior of the coupled system composed of stone masonry and FRCM external layers may be approximately assimilated to the behavior of three-leaf masonry under compression that is described in [271]. Indeed, for the three-leaves masonry, the mechanical properties of the external leaves are significantly higher than that of the internal one (the filling). Therefore, the external leaves carry a bigger percentage of the applied load. Here, the internal filling and the external leaves of the three-leaves masonry can be assumed as the FRCM reinforcing layer and the unreinforced stone masonry, respectively. Indeed, the coating mortar of the FRCM carries the bigger percentage of the load with respect to URM wall.

Based on that simplified assumption, the estimated shear strength of the RM ( $\tau_{0,RM}^*$ ) can be obtained by the following formulation:

$$\tau_{0,RM}^* = (V_{URM}/V)\tau_{0,URM} + (V_{FRCM}/V)f_{tc,m} \quad (4.1)$$

where  $(V_{URM}/V)$  and  $(V_{FRCM}/V)$  are the volumetric ratios of the URM and FRCM, respectively. Since the surface area of both the URM and FRCM is the same (equal to almost 1.2 m×1.2 m for the analyzed cases), Eq. 4.1 can be simplified as follows:

$$\tau_{0,RM}^* = \lambda_b \frac{(t_{RM} - t_m) \tau_{0,URM} + t_m f_{tc,m}}{t_{RM}} \quad (4.2)$$

where  $t_{RM}$  and  $t_{URM}$  are the thickness of the reinforced and unreinforced masonry, respectively, whereas  $t_m$  is the total thickness of the FRCM. The corrective factor  $\lambda_b$  was introduced to taking into account the effect of the bond behavior at the FRCM mortar-masonry interface. Indeed, simulations [84] showed that the shear strength increases of about 20% by assuming high bond behavior instead of weak bond (static friction at the reinforcing mortar-masonry interface equal to 0.5 and 0.03, respectively). In that study, the interface between stone particles and reinforcement mortar particles was simplistically assumed to be flat. For irregular stone masonry, it is presumable that the effect of the bond behavior could be even higher of 20% because of the interlocking effect.

To validate that relation, both experimental and numerical results were processed. Here, the results derived from other research programs (in addition the the experiments described in this thesis) are summarized. All of them were performed on irregular stone masonry panels, with single and/or multi-leaf cross sections, strengthened by FRCM. Only tests performed by diagonal compression configuration were selected. The benchmark results are presented in detail in [79, 65, 79, 81, 82, 78] and partially reported here.

Results presented in [78] regards on-site tests performed on four panels 0.48–0.57 mm thick isolated from a historic building located in Umbria (Italy) and five tests on stone-wall panels of a historic building of L'Aquila made of double-leaf wall with a thickness between 0.58 m and 0.61 m. The strengthening system comprises glass-FRCM 30 mm tick and five connectors consisted of two unidirectional fiberglass L-shaped bars. These tests are labeled as S2.

In [79] were presented results of different masonry types reinforced by FRP with various features. Here, only rubble stone masonry was considered for the comparison. The walls were prepared in laboratory and had a cross-sectional thickness of 0.40 m and 0.70 m. The strengthening technique consisted of the application on both faces of glass-FRCM layer of about 30 to 45 mm in thickness

as well as five L-shaped glass-FRP connectors through the thickness of the walls. The L2 labels are used for these tests.

From a vast experimental campaign presented in [65], a total of twelve tests on rubble stones masonry samples (4 URMs and 8 RMs) with 0.4 m in thickness were considered. The panels were built in laboratory by using two different poor infill mortar that can be typically found in two-leaf masonry of ancient buildings. Reinforcing system consisted of glass FRP meshes (with different features) embedded in a 30 mm thick mortar coating as well as six L-shaped glass-FRP connectors. These tests are labeled as L3.

Two tests (1URM and 1RM) were considered from [80]. A further test available from that research program was not taken into account, as concerned a hybrid reinforcement (reticolatus and glass-FRCM). The double leaf rubble masonries had 0.40 m in thickness. The reinforcement consisted of glass-FRCM thick 30 mm and six L-shaped glass-FRP connectors. Tests are labeled as L4.

From the extensive experimental campaign presented in [81], nine tests (3 URMs and 6 RMs) were considered. Half of the RM specimens were reinforced only on one side. No anchors were adopted for all the specimens. Tests are labeled as L5.

Five tests (1 URM and 4 RMs) were considered from [82]. In that research, limestone masonry panels were built aiming to reproduce the typical existing building in the area of L'Aquila (Italy). Both basalt-FRCM and glass-FRCM were adopted without using connectors. Tests are labeled as L6.

Table 4.1 lists the main geometrical and mechanical properties of the URM and RM walls as well as the FRCM features. In particular, since authors of the different research programs adopted various criteria to compute the shear strength of the walls, it was decided to normalize the data by adopting a unique criterion (defined by the ASTM code, and by re-computing  $\tau_0$ , when necessary, from the peak load and wall cross-section data. Furthermore, also the tensile strength data of the reinforcing mortar were computed by authors adopting different methods. Here, it was decided to normalize them by assuming the tensile strength  $f_{tc,m}$  given by the splitting test instead of the three-points bending test. When necessary, it was assumed the equation  $f_{tc,m} = 0.56f_{c,m}^{0.5}$  (ACI 318/98), being  $f_{c,m}$  the compression strength of the reinforcing mortar.

From the sixty tests reported in Table 4.1 (19 URMs and 41 RMs), one can compute the mean value of  $\tau_{0,RM}$  of 0.536 MPa (CoV=0.315) and the mean value of  $\tau_{0,URM}$  of 0.202 MPa (CoV=0.596). The mean value of the efficiency  $\beta$  is 3.23 (CoV=0.681). In particular, on-site experiments (S) lab-tests (L) and numerical tests (N) without reference were presented and commented in Sections 2.1.1-2.1.2 and Section 3.4.1, respectively.

Finally, Figure 4.1 shows the relation between the real shear strength  $\tau_{0,FRCM}^*$  and the estimated shear strength  $\tau_{0,FRCM}$ , which is evaluated by using the Eq.(4.2). The predictive formulation highlighted a good agreement with the experimental data. From Eq. (4.1) it was possible to calibrate the value of  $\lambda_b$  for which the estimated and the measured shear were equal to 1.56 (assumed constant for all the experimental data). For the numerical results,  $\lambda_b = 1.2$  was assumed. Obviously, the proposed analytical formulation is purely indicative and does not aspire to exactly estimates the shear strength of the masonry reinforced by FRCM, as many variables can affect its prediction (exact estimation of the thicknesses of the coating mortar due to the irregularity of the stone masonry surface, intrinsic variability of the mechanical properties of the URM that are strongly related to the quality and integrity of the wall, etc.). Anyway, although the simplicity of the proposed relation, one can have a good estimation of the shear strength of the reinforced masonry by using Eq. (4.2). Indeed, the best fitting between the measured shear strengths of the RM ( $\tau_{0,RM}$ ) and the estimated ones ( $\tau_{0,RM}^*$ ) was calibrated for  $\lambda_b$  equal to 1.56. The efficiency of the predictive analytical formulation can be observed in Fig. 4.1, in which an almost linear relation was found.

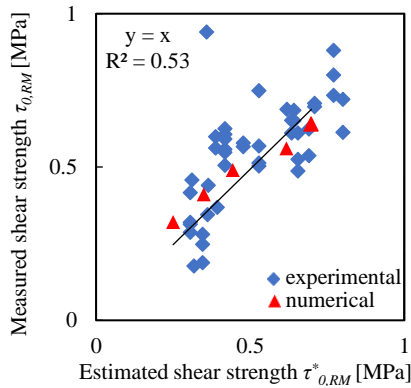


**Figure 4.1:** Relation between the real shear strength (in both experiments and simulations) the estimated shear strength (by eq.4.2) for the estimation of the shear strength of the coupled system ( $\tau_{0,FRCM}$ ). The  $\tau_{0,FRCM}^*$  parameter is the real shear strength.

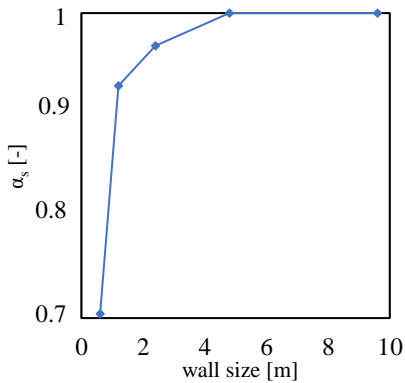


**Figure 4.2:** Trend of the corrective coefficient  $\alpha_s$  as a function of the wall size.

**Table 4.1:** Geometrical and mechanical properties of the unreinforced masonry and the reinforcement mortar (N=Numerical test, S=experimental on-site test, L=experimental lab-test).

Ref	ID	$t_{URM}$ [mm]	$\tau_{0,URM}$ [MPa]	$t_{RM}$ [mm]	$t_m$ [mm]	$f_{c,m}$ [MPa]	$f_{tc,m}$ [MPa]	SG	C	$\tau_{0,RM}$ [MPa]	$\beta$ -
-	S1-1	545	0.127	750	40	15.0	2.2	25	C-5	0.280	2.2
-	S1-2	545	0.127	565	40	15.0	2.2	25	C-5	0.368	2.9
-	L1-1	340	0.138	340	40	15.0	2.2	25	G-4	0.749	5.4
-	L1-2	340	0.138	340	40	15.0	2.2	25	-	0.513	3.7
-	L1-3	340	0.138	340	40	15.0	2.2	25	G-4	0.503	3.7
-	L1-4	340	0.138	340	40	15.0	2.2	25	-	0.569	4.1
-	N-1	340	0.120	340	20	15.0	3.2	25	-	0.320	2.7
-	N-2	340	0.120	340	30	15.0	3.2	25	-	0.410	3.4
-	N-3	340	0.120	340	40	15.0	3.2	25	-	0.490	3.8
-	N-4	340	0.120	340	50	15.0	3.2	25	-	0.560	4.6
-	N-5	340	0.120	340	60	15.0	3.2	25	-	0.640	5.3
[78]	S2-1	620	0.050	720	60	21.4	2.1	66	G-5	0.177	3.5
[78]	S2-2	620	0.050	640	60	21.4	2.1	66	G-5	0.248	4.9
[78]	S2-3	620	0.050	640	60	21.4	2.1	66	G-5	0.188	3.7
[78]	S2-4	540	0.041	570	60	21.4	2.1	66	G-5	0.345	8.4
[78]	S2-5	540	0.041	565	60	21.4	2.1	66	G-5	0.440	10.8
[78]	S2-6	540	0.041	700	60	21.4	2.1	66	G-5	0.458	11.2
[79]	L2-1	400	0.364	400	75	4.7	0.8	66	G-5	0.652	1.8
[79]	L2-2	400	0.364	400	75	4.7	0.8	66	G-5	0.685	1.9
[79]	L2-3	400	0.364	400	75	7.4	1.1	66	G-5	0.708	1.9
[79]	L2-4	400	0.364	400	75	7.4	1.1	66	G-5	0.697	1.9
[79]	L2-5	400	0.364	400	75	11.7	1.4	66	G-5	0.721	2.0
[79]	L2-6	400	0.364	400	75	11.7	1.4	66	G-5	0.614	1.7
[79]	L2-7	400	0.180	400	75	7.4	1.1	66	G-5	0.578	3.2
[79]	L2-8	400	0.180	400	75	7.4	1.1	66	G-5	0.566	3.1
[79]	L2-9	400	0.180	400	75	3.6	0.6	66	G-5	0.941	5.2
[79]	L2-10	400	0.180	400	75	3.6	0.6	66	G-5	1.093	6.1
[79]	L2-11	700	0.355	700	75	7.4	1.1	66	G-5	0.611	1.7
[79]	L2-12	700	0.355	700	75	7.4	1.1	66	G-5	0.653	1.8
[79]	L2-13	700	0.355	700	75	11.7	1.4	66	G-5	0.538	1.5
[79]	L2-14	700	0.355	700	75	11.7	1.4	66	G-5	0.624	1.8
[65]	L3-1	400	0.200	400	60	6.7	0.8	33	G-6	0.591	3.0
[65]	L3-2	400	0.200	400	60	6.7	0.8	33	G-6	0.548	2.7
[65]	L3-3	400	0.200	400	60	6.7	0.8	66	G-6	0.506	2.5
[65]	L3-4	400	0.200	400	60	6.7	0.8	66	G-6	0.558	2.8
[65]	L3-5	400	0.200	400	60	6.7	0.8	66	G-6	0.626	3.1
[65]	L3-6	400	0.200	400	60	6.7	0.8	66	G-6	0.607	3.0
[65]	L3-7	400	0.177	400	60	6.7	0.8	66	G-6	0.562	3.2
[65]	L3-8	400	0.177	400	60	6.7	0.8	66	G-6	0.599	3.4
[80]	L4-1	400	0.174	400	60	-	2.0*	66	G-6	0.689	4.0
[81]	L4-1	300	0.351	300	30	14.5	2.1	25	-	0.800	2.3
[81]	L4-2	300	0.351	300	30	14.5	2.1	25	-	0.881	2.5
[81]	L4-3	300	0.351	300	30	14.5	2.1	25	-	0.734	2.1
[81]	L4-4	300	0.351	300	15	14.5	2.1	25	-	0.487	1.4
[81]	L4-5	300	0.351	300	15	14.5	2.1	25	-	0.611	1.7
[81]	L4-6	300	0.351	300	15	14.5	2.1	25	-	0.525	1.5
[82]	L5-1	250	0.122	250	24	3.5	1.0	22	-	0.319	2.6
[82]	L5-2	250	0.122	250	24	3.5	1.0	22	-	0.416	3.4
[82]	L5-3	250	0.122	250	24	3.5	1.0	22	-	0.313	2.6
[82]	L5-4	250	0.122	250	24	3.5	1.0	22	-	0.287	2.4

Since numerical simulation showed the effect of the size-effect on the wall size, a multiplicative parameter  $\alpha_s$  can be applied to Eq. (4.2) aiming to extend results of test performed on specimen of a certain size to the actual dimension of the walls of the real structure. That coefficient can vary from 0.7 (for specimen sizing 0.6 m) to 1 (for wall sizing more than 5 m). and can be estimated by observing the trend of Figure 4.2. It is worth noting that in the case of specimen sizing 1.2 m, this coefficient can be assumed equal to 0.9 to extend the results to huge masonry walls.

In general, the investigation of the geometrical feature of the fiber employed for the FRCM system can affect the load-bearing capacity of the mortar panel as well as the fracture propagation. Results showed that the best performance was obtained for the glass fiber grid with a space gap of 25 mm and a width of 10 mm. Similar results, in terms of load-bearing capacity for large deformation, was also observed for fiber grid with space gap of 50 mm and width of 10 mm. However, in the latter case, it was observed a more localized fracture of the mortar along the compressed diagonal.

As far as the mechanical behavior of the new composite material is concerned, results showed that glass fiber with length equal to 13 mm, despite the good enhancement of the tensile, flexural, and compressive strengths, provided unsatisfactory ductility for the material. On the other and, glass fiber with length equal to 24 mm, ensured excellent fracture energy values as well as high load-bearing capacity. A recommendation on the fiber content almost equal to 2% of the total weight of the product (1.3% of the total volume of the product) can be provided. This value may ensure high ductility for the material even for large deformation. Other recommendations on the mix-design of the fibrous lime-mortar cannot be provided since representing the know-how of the company Aquilaprem (the industrial partner of the present research) and cannot be revealed to their competitors.



# CONCLUSIONS

---

## Abstract

The present Chapter focuses on conclusive critical assessments made on different fiber-reinforcement systems, based on the results obtained in both the experiments and numerical simulations (by using the Lattice Discrete Particle Model). The ability of LDPM in capturing the fracture and failure mechanisms in the quasi-brittle material, combined with the vast experimental campaign, allowed the understanding of the mechanics behind the complex behavior of the irregular stone masonry, the FRCM, and the newly developed fibrous lime-mortar material. Hence, a detailed description of the mechanical behavior of the FRCM system is described, defining the effect of both the fiber and mortar features on the shear mechanical parameters. Final considerations on the new composite material developed and investigated in this research are presented.



# Conclusions

---

## Abstract in italiano

Il seguente capitolo è incentrato su alcune valutazioni critiche effettuate sui diversi sistemi di rinforzo in fibra, sulla base dei risultati ottenuti sia in ambito sperimentale e sia numerico (questi ultimi attraverso il framework computazionale Lattice Discrete Particle Model). In particolare, il capitolo propone un'ampia discussione del comportamento meccanico dei rinforzi FRCM accoppiati a pareti murarie, evidenziando la limitazione di alcune indicazioni fornite da codici Normativi per la stima della resistenza a taglio di tali sistemi compositi. Per quanto riguarda il materiale innovativo sviluppato in questa ricerca, basato su una malta a base-calce rinforzata con fibre corte diffuse caoticamente nell'impasto, i risultati sperimentali e numerici hanno sottolineato le grandi potenzialità di tale materiale in termini di incremento di duttilità, trazione e compressione. Tali prestazioni sono essenzialmente legate all'effetto di confinamento e di cucitura che le fibre corte svolgono nei confronti dei grani della malta. Infatti, è stato possibile osservare come i campioni di materiale composito innovativo sono caratterizzati da una propagazione della frattura molto più diffusa rispetto ai sistemi FRCM, caratterizzati invece da una rottura localizzata. La capacità di mantenimento del carico per grandi spostamenti del sistema innovativo rimane ancora non del tutto soddisfacente. Tale aspetto è quello più critico da analizzare in quanto, rispetto alle fibre lunghe uni- o bi-direzionali degli FRCM, le fibre corte hanno una inevitabile maggiore capacità di scorrimento legata alla lunghezza di ancoraggio con la malta. Ulteriori sperimentazioni sono quindi necessarie e fibre con tipologia di forma differente potrebbero essere utilizzate per tale scopo. Infine, altre importanti considerazioni sono state effettuate sulla variabilità delle proprietà meccaniche dei paramenti murari non rinforzati in funzione della distribuzione granulometrica delle pietre e dell'effetto scala dei pannelli. In particolare, si è osservato che i risultati ottenuti su pannelli di dimensione standard sovrastimano la resistenza di taglio e duttilità delle reali strutture murarie.

Here, some general remarks and final observations arising from the experimental work and numerical analyses are drawn. The research aimed at deepening the knowledge of the mechanical behavior of existing technology based on the fiber-reinforced systems. In particular, consistent experimental results were presented for the mechanical characterization of the Fiber Reinforced Cementitious Matrix (FRCM) system. That system consisted of a glass fiber grid embedded into a lime-based mortar applied as a coating to the masonry surface. Furthermore, the research also regarded the experimental development of new composite material for the conservation and the retrofitting of the vast historical and architectural heritage. That material consisted of a lime-based mortar reinforced by randomly oriented short fibers. All the experiments were interpreted by a sophisticated numerical framework, based on the Lattice Discrete Particle Model. The ability of LDPM in capturing the fracture and failure mechanisms in the quasi-brittle material allowed the understanding of the mechanics behind the complex behavior of the irregular stone masonry, the FRCM, and the newly developed fibrous lime-mortar material.

The experimental campaign carried out on the FRCM-masonry system consisted of diagonal compression tests performed on both the unreinforced and reinforced stone masonry specimens. This test allowed the evaluation of the main mechanical properties of the masonry, namely the shear strength, the shear modulus, and the deformability of the panel. Some of the masonry specimens adopted in the experiments were isolated from the original walls of a historical building of L'Aquila. Other samples were prepared at the laboratory LPMS of the University of L'Aquila according to the ancient constructive technique featured in the historic buildings by using: (i) stone elements taken from the debris of buildings collapsed during L'Aquila 2009 earthquake; (ii) poor mortar developed with the same feature of the historical one. The difference between the two conditions regarded the thickness of the panels. Indeed, while historical panels ranged from 500 mm to 750 mm, the reproduced panels were approximately 340 mm.

Results highlighted that the shear strength obtained for the specimens prepared at the laboratory (0.137 MPa) was almost the same as the one computed for the panel isolated from the existing building (0.118 MPa). In particular, the difference between experiments was relatively small (less than 10%). This difference can be considered negligible, given the nature of the heterogeneous character and the quasi-brittle behavior of the material. This encouraging result validated the possibility to obtain reliable results when investigating irregular stone masonry prepared in the laboratory, at the condition that the latter is strictly built in line

with features of the existing buildings.

Furthermore, results showed that the FRCM system enhanced the shear strength of about 240% and 310% for the historical walls and the reproduced walls, respectively. This variance may be mainly related to the difference in the thickness of the panels. Moreover, the different efficiency of the FRCM was also due to the inevitably non-uniform thickness of the reinforcement mortar layer given by the strong asperity of the masonry substrate.

In general, it is easy to think that the higher the masonry wall thickness, the lower the efficiency of the FRCM in terms of shear strength. The higher the reinforcing mortar layer, the higher efficiency of the FRCM in terms of shear strength. This initial hypothesis was then confirmed by the simulations carried out by the Lattice Discrete Particle Model. Furthermore, the shear capacity of unreinforced panels cannot be attributed to the characteristics of the fibers (geometry and mechanical properties) as fibers have mainly the function to carry tensile stresses (load-bearing capacity). Shear strength is instead strongly related to the characteristics of the reinforcement mortar (geometry and mechanical properties). In particular, simulations showed that the re-hardening phase observed for the FRCM is lower when applied to the masonry wall, differently from the test performed on individual FRCM sample. Such phenomenon is even null when masonry walls are supported on a basement in the diagonal compression test configuration (typically adopted especially for onsite tests).

For the latter case, the shear strength of the FRCM was achieved when the failure of the mortar occurred. After that, an almost sudden drop in the shear stress was observed. Then, a re-hardening phenomenon led to an increase in the shear stress. However, this increment was not so consistent to enhance the shear strength of the panel.

Hence, based on the results, a simplified analytical formulation aiming to estimate the shear strength of the masonry panel strengthened by the FRCM system was proposed. In particular, a comparison between predicted and actual shear strengths showed a good agreement. The validation of the formulation regarded also experiments on stone masonry collected in other researches (total number of 60 tests). In that formulation, a corrective factor assumed to depend from the bond behavior at the masonry-FRCM interfaces was introduced. Also another corrective factor was proposed aiming to extend the result given from masonry walls of certain size to that obtainable with the actual size of walls.

In general, the results of the experimental campaign conducted on the FRCM showed that the reinforcement system is effective in improving the in-plane mechanical behavior of the stone masonries in terms of tensile strength, stiffness, and deformability. Moreover, good bond behavior of the FRCM system was observed

even for large deformation of the masonry. This result was also related to the interlocking between materials. Indeed, for stone masonry structures, one can observe high roughness of the masonry surface that enhances the bond behavior at the masonry – reinforcing mortar interface.

A key aspect of the experimental campaign conducted in situ highlighted the propensity of the historical walls of stones to modify their mechanical behavior during the loading. The result highlighted the “disaggregation” phenomenon concerning the total loss of cohesion between the stone elements. This aspect was also observed in the numerical simulations. In particular, it was shown that both the shear modulus and shear strain of the unreinforced panels are strongly reduced even for a low value of the load. This reduction (especially for the shear modulus) is less evident for the masonry reinforced by FRCM.

As far as the new fibrous lime-mortar is concerned, experimental results showed that the contribution of diffuse short fibers greatly increased the mechanical properties of the mortar as a function of both the geometry and content of the fiber. In particular, the fracture energy increase up to about 2500% with short-fibers, as compared to the unreinforced case. Then, the maximum increase in the flexural strength was about 450%. The maximum increment of the tensile strength values was about 100%. Finally, the mechanical property less affected by the fiber contribution was the compressive strength. In this case, the maximum increase was about 50%. In general, results showed that, although the fibers characterized by a shorter length may lead to slightly higher tensile strength, they are less capable to ensure proper ductility to the mortar. Indeed, only the fiber characterized by the longer length (24 mm) led to a significant increase in the fracture energy of the mortar (up to 2500%). Furthermore, as expected, the higher the fiber content, the higher the fracture energy. A similar trend was also observed for the other mechanical properties, namely flexural, tensile, and compressive strengths albeit they were more scattered as compared to the fracture energy.

Since the long unidirectional fiber strands used in the FRCM system have only the function to carry tensile stresses and do not improve the tensile strength of the masonry specimens, the results obtained for the innovative composite material are important. Indeed, when it is applied to the masonry wall, it can significantly increase both the strength and ductility of the quasi-brittle masonry specimens. Moreover, the enhancement in the mechanical properties due to the FRCM system is strongly related to the direction of the applied force, in contrast to the reinforcing composite material developed in this thesis.

Simulation carried out by LDPM on a 250×250×20 mm fibrous mortar specimen tested in diagonal compression showed that the shear strength of that material is much higher than the FRCM even for the lower fiber content assumed (1.5%

of the mortar weight). In particular, the higher the fiber content, the higher the shear strength. However, despite the benefit in terms of the shear strength for low fiber content, a minimum fiber content equal to 2% is recommended to ensure even higher ductility properties, as compared to the FRCM. It is worth noting that despite short fibers that may be easily subjected to the slippage phenomena, the new composite material showed the same stress reduction (30%) for large deformation (shear strain equal to 0.4), as the case of the unidirectional long fiber of the FRCM. This was the most important aspect to analyze.

However, the innovative composite material showed higher stress reduction for large deformation, as compared to the FRCM system. This was due to the slippage phenomenon that occurs for the short fibers.

A final comparison between the classic reinforcement system (the FRCM) and the new proposed in this research (the short fiber reinforced mortar SFRM) was performed by simulating the diagonal-compression test on stone masonry wall reinforced by the two systems applied as a coating on the masonry surfaces. Results highlighted that the new composite material enhanced the shear strength of the masonry about 800% and 50%, as compared to the unreinforced masonry and the reinforced masonry with FRCM, respectively. Results in terms of ductility should be better investigated also by experimental tests, which was unfortunately was possible to perform. The new composite material was characterized by higher propagation of fracture. By increasing the fiber content, the crack width became larger and, at the same time, the crack opening became lower. On the other hand, FRCM showed a more localized fracture along the compressed diagonal. The fiber grid kept together the two portions of the specimen, ensuring the load-bearing capacity of the panel.

As mentioned above, the Lattice Discrete Particle Model was employed to simulate the experimental test performed for: (i) the irregular stone masonry; (ii) the coupled system masonry-FRCM system; (iii) the fibrous lime-mortar material. In general, LDPM captures accurately the initiation and subsequent localization of damage in the materials. More specifically, it simulates well the evolution of the fracture process zone during fracture propagation and failure.

Furthermore, the numerical model was adopted to investigate the effect of different stone size distributions as well as the size effect.

In particular, by assuming randomly arrangement of the stones and different stone size distribution, it was possible to statistically investigate the main mechanical properties of masonry panels tested in diagonal compression.

Results showed that the stone distribution does not influence strongly the strength and the shear modulus, showing a variation within 10% for different stone configurations. This may suggest that large variation of these mechanical

properties, typically observed in the experimental tests, is instead due to the large variability of the mechanical properties of the constituent materials, especially of the mortar joint material, which mainly governs the failure process in stone masonry structures. On the contrary, the stone distribution affects significantly the ductility (up to 40% variation). In particular, the variation in the shear strength and shear modulus depends on the fact that the granulometric distribution influences the micro-cracks propagation even for low levels of the load producing a variation of the wall stiffness. The homogeneity of the masonry samples also affected the statistical scatter in the strength and shear modulus: the higher the homogeneity, the lower the scattering of both the mechanical properties. This trend is true regardless of the size of the specimen.

On the other hand, the level of ductility of stone masonry panels may depend on the homogeneity level of the stone. For panel sizing 1.2 m, the higher the homogeneity, the higher the mean value of the ductility and the lower scattering of the result. Indeed, the higher homogeneity level corresponds to a higher number of stones generated through the specimen volume and, then, a higher connection number between stone particles. A number of stones (sizing 50 mm - 250 mm) into a volume of a square panel of dimension equal to 1.2 m is not very high. Hence, for a higher range of stone size and/or lower specimen thickness (low homogeneity level) there is a sudden drop in the load-bearing capacity because the applied load cannot be redistributed, and vice-versa. However, this trend is not true (and completely opposed) for larger specimen, as discussed later in the results of the size-effect of the wall. Hence, the estimation of the ductility value on small specimens can be inaccurate and it cannot be assumed for huge structures, that must be considered almost perfectly-brittle.

Moreover, the scatter of the predicted ductility depended on the level of stress for which it is computed. Indeed, the ductility parameter is defined as the ratio between the shear strain at the shear strength and the shear strain corresponding to a certain percentage of the stress (considered in the post-peak behavior). The variability of the ductility value increases more than proportionally by computing it in correspondence of the 80%, 70%, or 60% of the maximum shear stress in the post-peak. In other words, the scatter increases for stress levels deep into the post-peak. Anyhow, in the general case, the ductility is very low, almost corresponding to the case of perfectly brittle behavior. Hence the customary plastic analysis approach used in many design guidelines is not warranted.

Furthermore, since there is a significant lack of information relevant to the stone masonry size effect, which is the dependence of mechanical properties on structural size, an LDPM investigation was presented in this research. This was obtained by simulating the shear behavior of geometrically similar samples of different sizes.

The simulations demonstrate that increasing structural size leads to a significant reduction of both structural strength and structural ductility. The magnitude of the predicted size effect suggested that, contrarily to typical experimental results on reduced size samples, real irregular masonry structures must be considered as perfectly brittle. Indeed, results showed that the larger the masonry specimen size, the more brittle the material behaves and, in particular, for large sizes of the wall ( $> 1.2$  m) the behavior transitions to purely brittle behavior. Furthermore, results showed that tests on laboratory samples (1.2 m) may overestimate by 50% the strength of real structures. As also observed for concrete materials, it is well known that quasi-brittle structures become more brittle as their size increases. This phenomenon is related to fracture energy dissipation, which varies with the width of the Fracture Process Zone (FPZ). By increasing the specimen size, the dissipated fracture energy decreases due to the decrease of the FPZ.

As far as the fibrous mortar material is concerned, simulations reproduced well the experiments. In particular, a proper investigation of the main fiber-matrix interaction parameters (the bond fracture energy, the bond friction stress, and the slip-hardening/softening coefficient) were carried out for the simulation of the three-point bending test. These parameters showed different sensitivity to the mechanical behavior of the fibrous-mortar. The bond friction stress mainly affected the flexural strength of the fibrous-mortar specimen and increases by increasing the fiber content in the case of longer fibers (24 mm), as compared to the smaller ones (13 mm). The slip-hardening/softening coefficient strongly affects the post-peak behavior, much more than the bond fracture energy, and depends on the geometrical feature of the fiber. In particular, for the smaller fiber (13 mm) the value of that parameter was constant. On the contrary, for longer fiber (24 mm), it showed an increase in its (negative) value by increasing the fiber content.

Definitely, this dissertation validated the efficiency of the new composite material for the preservation and the strengthening of historic structures as well as characterized the complex mechanical behavior of the FRCM coupled to the masonry structure. Valuable information was also provided for the size-effect of the wall panel on the main shear mechanical properties as well as the variability of the results for different stone and size distributions.

This dissertation can be also considered as a starting point for additional researches of several fields. In particular, based on the results obtained, further development for the new composite material is more than desirable. It will be interesting to experimentally analyze the enhancement of the mechanical properties of short-fiber-reinforced masonry panel in both the coating and the structural repointing technique, also using short-fiber of different natures, geometries, and shapes aiming to improve the load-bearing capacity of the system.

Moreover, a delicate aspect related to the efficiency of the fiber-based strengthening systems (both the FRCM and the new fibrous lime mortar) for high temperatures will be interesting to analyze. Indeed, it often happens that wildfires develop as a consequence of seismic actions. Although fibers are embedded in the mortar matrix, which protects the fibers from direct contact with flames, high temperatures may strongly reduce the mechanical properties of the fiber and therefore the efficiency of the reinforcement system for large deformations.

Furthermore, it is worth pointing out that this research numerically investigated only the randomness due to the variable stone size and distribution. Spatial randomness of material properties and consequently the resulting statistical effects (including size-effect) were not taken into account. These aspects will be considered in future work.

# Bibliography

- [1] Rui A Silva, Paul Jaquin, Daniel V Oliveira, Tiago F Miranda, Luc Schuermans, and Nuno Cristelo. Conservation and new construction solutions in rammed earth. In *Structural rehabilitation of old buildings*, pages 77–108. Springer, 2014.
- [2] The margherita palace of l’aquila. <https://www.ilcapoluogo.it/2016/11/07/palazzo-margherita-rinascere/>, 2020. [Online; accessed 2-March-2020].
- [3] I Calì, M Marletta, and B Pantò. A simplified model for the evaluation of the seismic behaviour of masonry buildings. In *Proceedings of the 10th international conference on civil, structural and environmental engineering computing*. Stirlingshire, UK: Civil-Comp Press, Paper, volume 195, 2005.
- [4] Siro Casolo. Modelling in-plane micro-structure of masonry walls by rigid elements. *International Journal of Solids and Structures*, 41(13):3625–3641, 2004.
- [5] Michele Angiolilli, Amedeo Gregori, and Massimo Fragiaco. Studies for the definition of seismic input for non-structural elements inside historical buildings (in italian). *Proceedings of the 18th Italian National Association of Earthquake Engineering - ANIDIS*, pages 116–126, 2019.
- [6] ISO3374. Reinforcing products – mats and fabrics – determination of mass per unit area. In *ISO3374*. International Organization for Standardization, 2000.
- [7] ISO4606. Textile glass – woven fabric – determination of tensile breaking force and elongation at break by the strip method. In *ISO4606*. International Organization for Standardization, 1995.
- [8] ISO12390. Testing hardened concrete - part 11: Determination of the chloride resistance of concrete, unidirectional diffusion. In *ISO12390*. International Organization for Standardization, 2015.
- [9] EN1015-11. Methods of test for mortar for masonry - part 11: Determination of flexural and compressive strength of hardened mortar. In *EN1015-11*. 2015.
- [10] Santiago Huerta. Galileo was wrong: the geometrical design of masonry arches. *Nexus Network Journal*, 8(2):25–52, 2006.
- [11] Subhamoy Bhattacharya, Sanket Nayak, and Sekhar Chandra Dutta. A critical review of retrofitting methods for unreinforced masonry structures. *International Journal of Disaster Risk Reduction*, 7:51–67, 2014.

- [12] Junji Kiyono and Afshin Kalantari. Collapse mechanism of adobe and masonry structures during the 2003 iran bam earthquake. *Bull. Earthq. Res. Inst. Univ. Tokyo*, 79(157):161, 2004.
- [13] T Rossetto and N Peiris. Observations of damage due to the kashmir earthquake of october 8, 2005 and study of current seismic provisions for buildings in pakistan. *Bulletin of Earthquake Engineering*, 7(3):681–699, 2009.
- [14] Giuseppe Brandonisio, Giuseppe Lucibello, Elena Mele, and Antonello De Luca. Damage and performance evaluation of masonry churches in the 2009 l’aquila earthquake. *Engineering Failure Analysis*, 34:693–714, 2013.
- [15] Gabriele Milani and Marco Valente. Failure analysis of seven masonry churches severely damaged during the 2012 emilia-romagna (italy) earthquake: non-linear dynamic analyses vs conventional static approaches. *Engineering Failure Analysis*, 54:13–56, 2015.
- [16] Raffaele Azzaro, Andrea Tertulliani, Filippo Bernardini, Romano Camassi, Sergio Del Mese, Emanuela Ercolani, Laura Graziani, Mario Locati, Alessandra Maramai, Vera Pessina, et al. The 24 august 2016 amatrice earthquake: macroseismic survey in the damage area and ems intensity assessment. *Annals of Geophysics*, 2016.
- [17] Elisa Tinti, Laura Scognamiglio, Alberto Michellini, and Massimo Cocco. Slip heterogeneity and directivity of the ml 6.0, 2016, amatrice earthquake estimated with rapid finite-fault inversion. *Geophysical Research Letters*, 43(20), 2016.
- [18] Andrea Penna, Chiara Calderini, Luigi Sorrentino, Caterina F Carocci, Elvis Cescatti, Romina Sisti, Antonio Borri, Claudio Modena, and Andrea Prota. Damage to churches in the 2016 central italy earthquakes. *Bulletin of Earthquake Engineering*, pages 1–28, 2019.
- [19] Dmytro Dizhur, Jason Ingham, Lisa Moon, Mike Griffith, Arturo Schultz, Ilaria Senaldi, Guido Magenes, Jocelyn Dickie, Shelley Lissel, Jose Centeno, et al. Performance of masonry buildings and churches in the 22 february 2011 christchurch earthquake. *Bulletin of the New Zealand Society for Earthquake Engineering*, 44(4):279–296, 2011.
- [20] Jason Ingham and Michael Griffith. Performance of unreinforced masonry buildings during the 2010 darfield (christchurch, nz) earthquake. *Australian Journal of Structural Engineering*, 11(3):207–224, 2010.
- [21] Dina D’Ayala and Gianmario Benzoni. Historic and traditional structures during the 2010 chile earthquake: observations, codes, and conservation strategies. *Earthquake Spectra*, 28(S1):S425–S451, 2012.
- [22] Revathy M Parameswaran, Thulasiraman Natarajan, Kusala Rajendran, CP Rajendran, Rishav Mallick, Matthew Wood, and Harish C Likhak. Seismotectonics of the april–may 2015 nepal earthquakes: An assessment based on the aftershock patterns, surface effects and deformational characteristics. *Journal of Asian Earth Sciences*, 111:161–174, 2015.
- [23] V Bosiljkov, A Page, and BOSILJKOV V BOKAN. Performance based studies of in-plane loaded unreinforced masonry walls. 2003.
- [24] G Vasconcelos and PB Lourenço. Experimental characterization of stone masonry in shear and compression. *Construction and Building Materials*, 23(11):3337–3345, 2009.

- [25] Antonino Giuffrè. *Sicurezza e conservazione dei centri storici: il caso Ortigia: codice di pratica per gli interventi antisismici nel centro storico*. Laterza, 2000.
- [26] Luigia Binda, Giuliana Cardani, and Antonella Saisi. A classification of structures and masonries for the adequate choice of repair. In *Proc. International RILEM Workshop on Repair for Historic Masonry, Delft*, volume 2005, pages 20–34, 2005.
- [27] Antonio Borri, Marco Corradi, Giulio Castori, and Alessandro De Maria. A method for the analysis and classification of historic masonry. *Bulletin of Earthquake Engineering*, 13(9):2647–2665, 2015.
- [28] Antonio Borri and Alessandro De Maria. Il metodo iqm per la stima delle caratteristiche meccaniche delle murature: allineamento alla circolare n. 7/2019. *Il metodo IQM per la stima delle caratteristiche meccaniche delle murature: allineamento alla circolare n. 7/2019*, pages 2–21, 2019.
- [29] Panagiotis Asteris and Vagelis Plevris. *Handbook of Research on Seismic Assessment and Rehabilitation of Historic Structures (2 Volumes)*. 07 2015.
- [30] Jukka Jokilehto. The context of the venice charter (1964). *Conservation and management of archaeological sites*, 2(4):229–233, 1998.
- [31] Michael Petzet. Principles of preservation: an introduction to the international charters for conservation and restoration 40 years after the venice charter. 2004.
- [32] Anna Di Nucci. *L'arte di costruire in Abruzzo: tecniche murarie nel territorio della diocesi di Valva e Sulmona*. Gangemi Editore spa, 2011.
- [33] Giovanni Carbonara. *Trattato di restauro architettonico*. Utet, 1997.
- [34] Antonino Giuffrè. *Lecture sulla meccanica delle murature storiche*. 1991.
- [35] S Abbaneo, Anna Anzani, and Luigia Binda. Il rilievo delle sezioni e il comportamento meccanico delle murature. 1996.
- [36] L Binda, G Baronio, D Penazzi, M Palma, and C Tiraboschi. Caratterizzazione di murature in pietra in zona sismica: data-base sulle sezioni murarie e indagini sui materiali. In *proceedings of the ninth conference in earthquake engineering in Italy, Turin, Italy*, 1999.
- [37] Giuliana Cardani. La vulnerabilità sismica dei centri storici: il caso di campi alto di norcia, linee guida per la diagnosi finalizzata alla scelta delle tecniche di intervento per la prevenzione dei danni. 2004.
- [38] L Binda, A Fontana, and G Mirabella. Mechanical behavior and stress distribution in multiple-leaf stone walls. In *Proceedings of 10th international brick block masonry conference, Calgary, Canada*, volume 45, 1994.
- [39] L Binda, A Anzani, and A Fontana. Mechanical behaviour of multiple-leaf stone masonry: experimental research. In *Int. Conf. Structural Faults & Repair*, 2003.
- [40] Angelo Aloisio, Massimo Fragiaco, and Gianfranco D'Alò. The 18th-century baraccato of l'aquila. *International Journal of Architectural Heritage*, pages 1–15, 2019.

- [41] Angelo Aloisio, Massimo Fragiaco, and Gianfranco D'Alò. Traditional masonries in the city centre of l'aquila—the baraccato aquilano. *International Journal of Architectural Heritage*, pages 1–18, 2019.
- [42] Federica Ottoni and Eva Coisson. Nuovi materiali per il restauro strutturale: una questione antica. *ArcHistoR*, (4):92–117, 2015.
- [43] M Tomažević. The computer program por. *Report ZRMK*, 1978.
- [44] Elizabeth Vintzileou and Theodoros P Tassios. Three-leaf stone masonry strengthened by injecting cement grouts. *Journal of Structural Engineering*, 121(5):848–856, 1995.
- [45] J Gustavo Tumialan, Francesco Micelli, and Antonio Nanni. Strengthening of masonry structures with frp composites. In *Structures 2001: A Structural Engineering Odyssey*, pages 1–8. 2001.
- [46] MR Valluzzi. Strengthening of masonry structures with fibre reinforced plastics: from modern conception to historical building preservation. In *Structural Analysis of Historic Construction: Preserving Safety and Significance, Two Volume Set*, pages 53–66. CRC Press, 2008.
- [47] G Schwegler. Strengthening of masonry in seismic regions using frp. *Empa report N*, 1995.
- [48] Juan Ignacio Velazquez-Dimas. Out-of-plane cyclic behavior of urm walls retrofitted with fiber composites. 1998.
- [49] Yasser Korany and Robert Drysdale. Rehabilitation of masonry walls using unobtrusive frp techniques for enhanced out-of-plane seismic resistance. *Journal of Composites for Construction*, 10(3):213–222, 2006.
- [50] C Oswald and K Chang. Shock tube testing on masonry walls strengthened with kevlar. In *10th Int. Symp. on Interaction of Effects of Munitions with Structures*, pages 7–11, 2001.
- [51] K Roko, TE Boothby, and CE Bakis. Failure modes of sheet bonded fiber reinforced polymer applied to brick masonry. *Special Publication*, 188:305–312, 1999.
- [52] Leonidas Alexandros S Kouris and Thanasis C Triantafillou. State-of-the-art on strengthening of masonry structures with textile reinforced mortar (trm). *Construction and Building Materials*, 188:1221–1233, 2018.
- [53] Saman Babaeidarabad, Francisco De Caso, and Antonio Nanni. Urm walls strengthened with fabric-reinforced cementitious matrix composite subjected to diagonal compression. *Journal of Composites for Construction*, 18(2):04013045, 2014.
- [54] Thanasis C Triantafillou and Catherine G Papanicolaou. Shear strengthening of reinforced concrete members with textile reinforced mortar (trm) jackets. *Materials and structures*, 39(1):93–103, 2006.
- [55] Catherine G Papanicolaou, Thanasis C Triantafillou, Kyriakos Karlos, and Myrto Papathanasiou. Textile-reinforced mortar (trm) versus frp as strengthening material of urm walls: in-plane cyclic loading. *Materials and structures*, 40(10):1081–1097, 2007.

- [56] Catherine G Papanicolaou, Thanasis C Triantafyllou, Myrto Papathanasiou, and Kyriakos Karlos. Textile reinforced mortar (trm) versus frp as strengthening material of urm walls: out-of-plane cyclic loading. *Materials and structures*, 41(1):143–157, 2008.
- [57] Yousef A Al-Salloum, Hussein M Elsanadedy, Saleh H Alsayed, and Rizwan A Iqbal. Experimental and numerical study for the shear strengthening of reinforced concrete beams using textile-reinforced mortar. *Journal of Composites for Construction*, 16(1):74–90, 2012.
- [58] American Concrete Institute (ACI). Guide for the design and construction of externally bonded fiber-reinforced polymer systems for strengthening unreinforced masonry structures. 2010.
- [59] ICOMOS/Iscarsah Committee et al. Recommendations for the analysis, conservation and structural restoration of architectural heritage. See *www.icomos.org*, 2005.
- [60] Antonio De Luca. Frcm systems. *STRUCTURE*, 23, 2014.
- [61] Catherine Papanicolaou, Thanasis Triantafyllou, and Maria Lekka. Externally bonded grids as strengthening and seismic retrofitting materials of masonry panels. *Construction and Building Materials*, 25(2):504–514, 2011.
- [62] Miha Tomažević, Matija Gams, and Thierry Berset. Seismic strengthening of stone masonry walls with polymer coating. In *Proc., 15th World Conference on Earthquake Engineering (15 WCEE), Lisbon, Portugal*, pages 24–28, 2012.
- [63] Ahmet Murat Türk. Seismic response analysis of masonry minaret and possible strengthening by fiber reinforced cementitious matrix (frcm) materials. 2013.
- [64] Saman Babaeidarabad, Diana Arboleda, Giovanni Loreto, and Antonio Nanni. Shear strengthening of un-reinforced concrete masonry walls with fabric-reinforced-cementitious-matrix. *Construction and Building Materials*, 65:243–253, 2014.
- [65] Natalino Gattesco, Ingrid Boem, and Allen Dudine. Diagonal compression tests on masonry walls strengthened with a gfrp mesh reinforced mortar coating. *Bulletin of Earthquake Engineering*, 13(6):1703–1726, 2015.
- [66] Marcos Venicius Pereira, Roberto Fujiyama, Fathi Darwish, and Gilvania Tertto Alves. On the strengthening of cement mortar by natural fibers. *Materials Research*, 18(1):177–183, 2015.
- [67] Giancarlo Marcari, Michela Basili, and Fabrizio Vestroni. Experimental investigation of tuff masonry panels reinforced with surface bonded basalt textile-reinforced mortar. *Composites Part B: Engineering*, 108:131–142, 2017.
- [68] Amedeo Gregori, Gabriele Marchini, Daniele Martini, and Michele Angiolilli. Experimental characterization of frcm systems for conservative and strengthening intervention on monumental real estate heritage. In *Atti del XVII Convegno ANIDIS L'ingegneria Sismica in Italia*, pages 116–126. Pisa University Press, 2017.

- [69] Francesca Giulia Carozzi, Alessandro Bellini, Tommaso D'Antino, Gianmarco de Felice, Francesco Focacci, Lukasz Hojdys, Luca Laghi, Emma Lanoye, Francesco Micelli, Matteo Panizza, et al. Experimental investigation of tensile and bond properties of carbon-frcm composites for strengthening masonry elements. *Composites Part B: Engineering*, 128:100–119, 2017.
- [70] Jacopo Donnini, Giovanni Lancioni, and Valeria Corinaldesi. Failure modes in frcm systems with dry and pre-impregnated carbon yarns: Experiments and modeling. *Composites Part B: Engineering*, 140:57–67, 2018.
- [71] Najif Ismail and Jason M Ingham. Polymer textiles as a retrofit material for masonry walls. *Proceedings of the Institution of Civil Engineers-Structures and Buildings*, 167(1):15–25, 2014.
- [72] Paolo Morandi, Luca Albanesi, Francesco Graziotti, T Li Piani, A Penna, and G Magenes. Development of a dataset on the in-plane experimental response of urm piers with bricks and blocks. *Construction and Building Materials*, 190:593–611, 2018.
- [73] Tommaso D'Antino, Francesca Giulia Carozzi, and Carlo Poggi. Diagonal shear behavior of historic walls strengthened with composite reinforced mortar (crm). *Materials and Structures*, 52(6):114, 2019.
- [74] A Prota, G Marcari, Giovanni Fabbrocino, G Manfredi, and C Aldea. Experimental in-plane behavior of tuff masonry strengthened with cementitious matrix-grid composites. *Journal of Composites for Construction*, 10(3):223–233, 2006.
- [75] Fulvio Parisi, Ivano Iovinella, Alberto Balsamo, Nicola Augenti, and Andrea Prota. In-plane behaviour of tuff masonry strengthened with inorganic matrix-grid composites. *Composites Part B: Engineering*, 45(1):1657–1666, 2013.
- [76] Ciro Faella, Enzo Martinelli, Emidio Nigro, and Sergio Paciello. Shear capacity of masonry walls externally strengthened by a cement-based composite material: An experimental campaign. *Construction and Building Materials*, 24(1):84–93, 2010.
- [77] Marta Del Zoppo, Marco Di Ludovico, and Andrea Prota. Analysis of frcm and crm parameters for the in-plane shear strengthening of different urm types. *Composites Part B: Engineering*, 171:20–33, 2019.
- [78] Marco Corradi, Antonio Borri, Giulio Castori, and Romina Sisti. Shear strengthening of wall panels through jacketing with cement mortar reinforced by gfrp grids. *Composites Part B: Eng.*, 64:33–42, 2014.
- [79] Natalino Gattesco and Ingrid Boem. Experimental and analytical study to evaluate the effectiveness of an in-plane reinforcement for masonry walls using gfrp meshes. *Construction and Building Materials*, 88:94–104, 2015.
- [80] Natalino Gattesco, Claudio Amadio, and Chiara Bedon. Experimental and numerical study on the shear behavior of stone masonry walls strengthened with gfrp reinforced mortar coating and steel-cord reinforced repointing. *Engineering Structures*, 90:143–157, 2015.
- [81] Marta Del Zoppo, Marco Di Ludovico, Alberto Balsamo, and Andrea Prota. Diagonal compression testing of masonry panels with irregular texture strengthened with inorganic composites. *Materials and Structures*, 53(4):1–17, 2020.

- [82] A Balsamo, I Iovinella, and G Morandini. Frg strengthening systems for masonry building. In *NZSEE Conference*, 2014.
- [83] Marta Del Zoppo, Marco Di Ludovico, Alberto Balsamo, and Andrea Prota. Experimental in-plane shear capacity of clay brick masonry panels strengthened with frcm and frcm composites. *Journal of Composites for Construction*, 23(5):04019038, 2019.
- [84] Michele Angiolilli, Amedeo Gregori, Madura Pathirage, and Gianluca Cusatis. Fiber reinforced cementitious matrix (frcm) for strengthening historical stone masonry structures: experiments and computations. *Engineering Structures*, 2020.
- [85] Alessio Cascardi, Marianovella Leone, and Maria Antonietta Aiello. Transversal joining of multi-leaf masonry through different types of connector: Experimental and theoretical investigation. *Construction and Building Materials*, 265:120733, 2020.
- [86] Antonio Borri, Marco Corradi, Emanuela Speranzini, and Andrea Giannantoni. Reinforcement of historic masonry with high strength steel cords. *Masonry International*, 23(3):79–90, 2010.
- [87] Antonio Borri, Giulio Castori, Marco Corradi, and Emanuela Speranzini. Shear behavior of unreinforced and reinforced masonry panels subjected to in situ diagonal compression tests. *Construction and Building Materials*, 25(12):4403–4414, 2011.
- [88] Antonio Borri, Giulio Castori, Marco Corradi, and Romina Sisti. Masonry wall panels with gfrp and steel-cord strengthening subjected to cyclic shear: An experimental study. *Construction and Building Materials*, 56:63–73, 2014.
- [89] Ali Abbass, Paulo B Lourenço, and Daniel V Oliveira. The use of natural fibers in repairing and strengthening of cultural heritage buildings. *Materials Today: Proceedings*, 2020.
- [90] Arnon Bentur and Sidney Mindess. *Fibre reinforced cementitious composites*. Crc Press, 2006.
- [91] HR Pakravan, M Latifi, and M Jamshidi. Hybrid short fiber reinforcement system in concrete: A review. *Construction and building materials*, 142:280–294, 2017.
- [92] CNR DT200 et al. Guide for the design and construction of an externally bonded frp system for strengthening existing structures. *Technical document*, (200), 2004.
- [93] CNR DT215 et al. Istruzioni per la progettazione, l'esecuzione ed il controllo di interventi di consolidamento statico mediante l'utilizzo di compositi fibrorinforzati a matrice inorganica. *Technical document*, (215), 2015.
- [94] ICC AC434. Acceptance criteria for masonry and concrete strengthening using fiber-reinforced cementitious matrix (frcm) composite systems. *ICC-Evaluation Service, Whittier, CA*, 2013.
- [95] ACI (American Concrete Institute). Guide to design and construction of externally bonded fabric-reinforced cementitious matrix (frcm) systems for repair and strengthening concrete and masonry structures. 2013.

- [96] Michele Angiolilli, Amedeo Gregori, Madura Pathirage, and Gianluca Cusatis. Fiber reinforced cementitious matrix (frcm) for strengthening historical stone masonry structures: experiments and computations. *Engineering Structures*, 2020.
- [97] Patrick Degryse, Jan Elsen, and Marc Waelkens. Study of ancient mortars from sagalassos (turkey) in view of their conservation. *Cement and concrete research*, 32(9):1457–1463, 2002.
- [98] A Moropoulou, AS Cakmak, G Biscontin, A Bakolas, and E Zendri. Advanced byzantine cement based composites resisting earthquake stresses: the crushed brick/lime mortars of justinian’s hagia sophia. *Construction and Building Materials*, 16(8):543–552, 2002.
- [99] Javier Lanás and José I Alvarez-Galindo. Masonry repair lime-based mortars: factors affecting the mechanical behavior. *Cement and concrete research*, 33(11):1867–1876, 2003.
- [100] National Research Council et al. Cnr-dt 200. *R1: Istruzioni per la Progettazione, l’Esecuzione ed il Controllo di Interventi di Consolidamento Statico mediante l’utilizzo di Compositi Fibrorinforzati*, 2013.
- [101] MIBAC. Linee guida per la valutazione e riduzione del rischio sismico del patrimonio culturale allineate alle nuove norme tecniche per le costruzioni (d.m. 14 gennaio 2008). 2011.
- [102] Valerio Alecci, Mario De Stefano, Francesco Focacci, Raimondo Luciano, Luisa Rovero, and Gianfranco Stipo. Strengthening masonry arches with lime-based mortar composite. *Buildings*, 7(2):49, 2017.
- [103] Michele Angiolilli, Amedeo Gregori, and Daniele Martini. Mechanical characterization of the cyclic behavior of historic masonry panels reinforced by frcm system subject to diagonal compression tests (in italian). *Proceedings of the 18th Italian National Association of Earthquake Engineering - ANIDIS*, pages 116–126, 2019.
- [104] Gian Paolo Cimellaro, IP Christovasilis, Andrei M Reinhorn, Alessandro De Stefano, and Tatiana Kirova. L’aquila earthquake of april 6th, 2009 in italy: rebuilding a resilient city to multiple hazard. *MCEER Technical Rep.—MCEER-10*, 10, 2010.
- [105] H Salem, A Gregori, H Helmy, K Fassieh, and H Tagel-Din. Seismic assessment of damaged margherita palace using applied element method. In *16th World Conference on Earthquake Engineering, 16WCEE*, 2017.
- [106] Gian Paolo Cimellaro, S Piantà, and A De Stefano. Output-only modal identification of ancient l’aquila city hall and civic tower. *Journal of structural engineering*, 138(4):481–491, 2012.
- [107] ASTM. Standard e 519, standard test method for diagonal tension (shear) in masonry assemblages. 2010.
- [108] Marco Corradi, Antonio Borri, and Andrea Vignoli. Experimental study on the determination of strength of masonry walls. *Construction and building materials*, 17(5):325–337, 2003.
- [109] A Borri. Costruzioni storiche e qualità muraria: problematiche e possibili interventi di consolidamento. *Atti del Convegno “Sicurezza e Conservazione nel Recupero dei Beni Culturali Colpiti da Sisma”*, Venezia, pages 8–9, 2010.

- [110] Luigi Sorrentino, Serena Cattari, Francesca da Porto, Guido Magenes, and Andrea Penna. Seismic behaviour of ordinary masonry buildings during the 2016 central italy earthquakes. *Bulletin of Earthquake Engineering*, 17(10):5583–5607, 2019.
- [111] The aqmesh 240v glass fiber of aquilaprem s.r.l. <https://www.aquilaprem.it/aqmesh-reti-in-fibra/>, 2019. [Online; accessed 30-October-2019].
- [112] The ch15 mortar of aquilaprem s.r.l. <https://www.aquilaprem.it/calce-idraulica-naturale/ch-15-malta-strutturale/>, 2019. [Online; accessed 30-October-2019].
- [113] Circolare applicativa delle NTC08. Circolare del ministero delle infrastrutture e dei trasporti 2 febbraio 2009, n617 recante istruzioni per l'applicazione delle nuove norme tecniche per le costruzioni di cui al decreto ministeriale 14 gennaio 2008. *Suppl ord*, (27), 2009.
- [114] G Magenes, A Penna, A Galasco, and M Rota. Experimental characterisation of stone masonry mechanical properties. In *Proceedings of the 8th International Masonry Conference*, 2010.
- [115] Anna Brignola, Sara Frumento, Sergio Lagomarsino, and Stefano Podesta. Identification of shear parameters of masonry panels through the in-situ diagonal compression test. *International Journal of Architectural Heritage*, 3(1):52–73, 2008.
- [116] EN UNI. 1015-11. 2007. *Methods of test for mortar for masonry—Part, 11*.
- [117] Bryant Mather and Hamdi Celik Ozyildirim. Concrete primer. American Concrete Institute, 2002.
- [118] ARNE Hillerborg. Concrete fracture energy tests performed by 9 laboratories according to a draft rilem recommendation. *Report to RILEM TC50-FMC, Report TVBM-3015, Lund, Sweden*, 1983.
- [119] Zdenek P Bazant and Phillip A Pfeiffer. Determination of fracture energy from size effect and brittleness number. *ACI Materials Journal*, 84(6):463–480, 1987.
- [120] Zdeněk P Bažant and Feng-Bao Lin. Nonlocal smeared cracking model for concrete fracture. *Journal of Structural Engineering*, 114(11):2493–2510, 1988.
- [121] Arne Hillerborg. Results of three comparative test series for determining the fracture energy  $f$  of concrete. *Materials and Structures*, 18(5):407–413, 1985.
- [122] K Duan, XZ Hu, and FH Wittmann. Boundary effect on concrete fracture induced by non-constant fracture energy distribution. *Fracture Mechanics of Concrete Structures (R. de Borst, J. Mazars, G. Pijaudier-Cabot and JGM Van Mier (Eds)), Proc FRAMCOS-4, Balkema, Rotterdam*, pages 49–55, 2001.
- [123] Kai Duan, Xiaozhi Hu, and Folker H Wittmann. Boundary effect on concrete fracture and non-constant fracture energy distribution. *Engineering Fracture Mechanics*, 70(16):2257–2268, 2003.

- [124] RILEM Draft Recommendation. Determination of the fracture energy of mortar and concrete by means of three-point bend tests on notched beams. *Materials and structures*, 18(106):285–290, 1985.
- [125] TC RILEM. 187-soc. *Experimental determination of the stress-crack opening curve for concrete in tension*”, *Final report*, 2007.
- [126] Zdenek P Bazant and Jaime Planas. *Fracture and size effect in concrete and other quasibrittle materials*, volume 16. CRC press, 1997.
- [127] Fanlu Min, Zhanhu Yao, and Teng Jiang. Experimental and numerical study on tensile strength of concrete under different strain rates. *The Scientific World Journal*, 2014, 2014.
- [128] Joshua Martin, John Stanton, Nilanjan Mitra, and Laura N Lowes. Experimental testing to determine concrete fracture energy using simple laboratory test setup. *ACI Materials Journal*, 104(6):575, 2007.
- [129] C Rocco, GV Guinea, J Planas, and M Elices. Review of the splitting-test standards from a fracture mechanics point of view. *Cement and concrete research*, 31(1):73–82, 2001.
- [130] AA Griffith. The phenomena of rupture and flow in solids (philosophical transactions/royal society of london ser. a, v. 221). 1920.
- [131] Víctor J García, Carmen O Márquez, Alonso R Zúñiga-Suárez, Berenice C Zúñiga-Torres, and Luis J Villalta-Granda. Brazilian test of concrete specimens subjected to different loading geometries: review and new insights. *International Journal of Concrete Structures and Materials*, 11(2):343–363, 2017.
- [132] Panagiotis G Asteris and Vagelis Plevis. *Handbook of research on seismic assessment and rehabilitation of historic structures*, volume 2. IGI Global, 2015.
- [133] Pere Roca, Miguel Cervera, Giuseppe Gariup, et al. Structural analysis of masonry historical constructions. classical and advanced approaches. *Archives of Computational Methods in Engineering*, 17(3):299–325, 2010.
- [134] Paulo B Lourenço, Jan G Rots, and Johan Blaauwendraad. Continuum model for masonry: parameter estimation and validation. *Journal of structural engineering*, 124(6):642–652, 1998.
- [135] Rui Manuel Carvalho Marques de Faria. Avaliação do comportamento sísmico de barragens de betão através de um modelo de dano contínuo. 1994.
- [136] R Faria, J Oliver, and M Cervera. A strain-based plastic viscous-damage model for massive concrete structures. *International journal of solids and structures*, 35(14):1533–1558, 1998.
- [137] Bruno Silva, João M Guedes, António Arêde, and Aníbal Costa. Calibration and application of a continuum damage model on the simulation of stone masonry structures: Gondar church as a case study. *Bulletin of Earthquake Engineering*, 10(1):211–234, 2012.
- [138] Ernesto Grande, Maura Imbimbo, and Elio Sacco. A beam finite element for nonlinear analysis of masonry elements with or without fiber-reinforced plastic (frp) reinforcements. *International Journal of Architectural Heritage*, 5(6):693–716, 2011.

- [139] Laurent Pasticier, Claudio Amadio, and Massimo Fragiaco. Non-linear seismic analysis and vulnerability evaluation of a masonry building by means of the sap2000 v. 10 code. *Earthquake engineering & structural dynamics*, 37(3):467–485, 2008.
- [140] Sergio Lagomarsino, Andrea Penna, Alessandro Galasco, and Serena Cattari. Tremuri program: an equivalent frame model for the nonlinear seismic analysis of masonry buildings. *Engineering structures*, 56:1787–1799, 2013.
- [141] Ivo Caliò, Massimo Marletta, and Bartolomeo Pantò. A new discrete element model for the evaluation of the seismic behaviour of unreinforced masonry buildings. *Engineering Structures*, 40:327–338, 2012.
- [142] Ivo Caliò, Francesco Cannizzaro, and Massimo Marletta. A discrete element for modeling masonry vaults. In *Advanced materials research*, volume 133, pages 447–452. Trans Tech Publ, 2010.
- [143] Hamid R Lotfi and P Benson Shing. Interface model applied to fracture of masonry structures. *Journal of structural engineering*, 120(1):63–80, 1994.
- [144] Luca Pelà, Miguel Cervera, and Pere Roca. An orthotropic damage model for the analysis of masonry structures. *Construction and Building Materials*, 41:957–967, 2013.
- [145] Nicola Tarque, Guido Camata, Enrico Spacone, Humberto Varum, and Marcial Blondet. Nonlinear dynamic analysis of a full-scale unreinforced adobe model. *Earthquake Spectra*, 30(4):1643–1661, 2014.
- [146] V Gattulli, E Lofrano, A Paolone, and G Pirolli. Performances of frp reinforcements on masonry buildings evaluated by fragility curves. *Computers & Structures*, 190:150–161, 2017.
- [147] Vincenzo Gattulli, Gianluca Lampis, Giancarlo Marcari, and Achille Paolone. Simulations of frp reinforcement in masonry panels and application to a historic facade. *Engineering Structures*, 75:604–618, 2014.
- [148] Gaetano Manfredi, Gian Piero Lignola, and Simona Voto. Military quarters in nola, italy—caserma principe amedeo: Damage assessment and reconstruction of a partially collapsed xviii century complex. *International Journal of Architectural Heritage*, 7(2):225–246, 2013.
- [149] Francesca da Porto, Giovanni Guidi, Enrico Garbin, and Claudio Modena. In-plane behavior of clay masonry walls: experimental testing and finite-element modeling. *Journal of structural engineering*, 136(11):1379–1392, 2010.
- [150] Bahman Ghiassi, Daniel V Oliveira, Paulo B Lourenço, and Giancarlo Marcari. Numerical study of the role of mortar joints in the bond behavior of frp-strengthened masonry. *Composites Part B: Engineering*, 46:21–30, 2013.
- [151] Francesco Clementi, Valentina Gazzani, Marina Poiani, Pardo Antonio Mezzapelle, and Stefano Lenci. Seismic assessment of a monumental building through nonlinear analyses of a 3d solid model. *Journal of Earthquake Engineering*, 22(sup1):35–61, 2018.
- [152] Alexandre A Costa, António Arêde, Aníbal Costa, João Guedes, and Bruno Silva. Experimental testing, numerical modelling and seismic strengthening of traditional stone masonry: comprehensive study of a real azorian pier. *Bulletin of Earthquake Engineering*, 10(1):135–159, 2012.

- [153] PAULO B Lourenço. A user/programmer guide for the micro-modeling of masonry structures. *Report*, 3(1.31):35, 1996.
- [154] Paulo B Lourenço and Jan G Rots. Multisurface interface model for analysis of masonry structures. *Journal of engineering mechanics*, 123(7):660–668, 1997.
- [155] Mohammad Bolhassani, Ahmad A Hamid, Alan CW Lau, and Franklin Moon. Simplified micro modeling of partially grouted masonry assemblages. *Construction and Building Materials*, 83:159–173, 2015.
- [156] Melbourne Gilbert and C Melbourne. Rigid-block analysis of masonry structures. *Structural engineer*, 72(21), 1994.
- [157] M Gilbert. Limit analysis applied to masonry arch bridges: state-of-the-art and recent developments. In *5th International arch bridges conference*, pages 13–28, 2007.
- [158] Paulo B Lourenço, Daniel V Oliveira, Pere Roca, and Agustín Orduña. Dry joint stone masonry walls subjected to in-plane combined loading. *Journal of Structural Engineering*, 131(11):1665–1673, 2005.
- [159] DJ Sutcliffe, HS Yu, and AW Page. Lower bound limit analysis of unreinforced masonry shear walls. *Computers & Structures*, 79(14):1295–1312, 2001.
- [160] PG Asteris and AD Tzamtzis. Nonlinear seismic response analysis of realistic gravity dam-reservoir systems. *International Journal of Nonlinear Sciences and Numerical Simulation*, 4(4):329–338, 2003.
- [161] Michele Angiolilli and Amedeo Gregori. Triplet test on rubble stone masonry: Numerical assessment of the shear mechanical parameters. *Buildings*, 10:49, 03 2020.
- [162] Simona Di Nino and Angelo Luongo. A simple homogenized orthotropic model for in-plane analysis of regular masonry walls. *International Journal of Solids and Structures*, 167:156–169, 2019.
- [163] Jean-Baptiste Colliat, Martin Hautefeuille, Adnan Ibrahimbegovic, and Hermann G Matthies. Stochastic approach to size effect in quasi-brittle materials. *Comptes Rendus Mécanique*, 335(8):430–435, 2007.
- [164] J Armesto, Javier Roca-Pardiñas, H Lorenzo, and P Arias. Modelling masonry arches shape using terrestrial laser scanning data and nonparametric methods. *Engineering Structures*, 32(2):607–615, 2010.
- [165] Bora Pulatsu, Eduardo M Bretas, and Paulo B Lourenco. Discrete element modeling of masonry structures: Validation and application. *Earthquakes and Structures*, 11(4):563–582, 2016.
- [166] Axel Roland Tóth, Zoltán Orbán, and Katalin Bagi. Discrete element analysis of a stone masonry arch. *Mechanics Research Communications*, 36(4):469–480, 2009.
- [167] José V Lemos. Discrete element modeling of masonry structures. *International Journal of Architectural Heritage*, 1(2):190–213, 2007.
- [168] V Giamundo, Vasilis Sarhosis, GP Lignola, Y Sheng, and G Manfredi. Evaluation of different computational modelling strategies for the analysis of low strength masonry structures. *Engineering Structures*, 73:160–169, 2014.

- [169] Vinh Phu Nguyen, Martijn Stroeven, and Lambertus Johannes Sluys. Multiscale continuous and discontinuous modeling of heterogeneous materials: a review on recent developments. *Journal of Multiscale Modelling*, 3(04):229–270, 2011.
- [170] Petr Havlásek, Peter Grassl, and Milan Jirásek. Analysis of size effect on strength of quasi-brittle materials using integral-type nonlocal models. *Engineering Fracture Mechanics*, 157:72–85, 2016.
- [171] G Cusatis and X Zhou. High-order microplane theory for elasticity and softening of quasi-brittle materials.
- [172] Zdeněk P Bažant, Mazen R Tabbara, Mohammad T Kazemi, and Gilles Pijaudier-Cabot. Random particle model for fracture of aggregate or fiber composites. *Journal of engineering mechanics*, 116(8):1686–1705, 1990.
- [173] Gianluca Cusatis, Zdeněk P Bažant, and Luigi Cedolin. Confinement-shear lattice model for concrete damage in tension and compression: I. theory. *Journal of Engineering Mechanics*, 129(12):1439–1448, 2003.
- [174] Gianluca Cusatis, Zdeněk P Bažant, and Luigi Cedolin. Confinement-shear lattice csl model for fracture propagation in concrete. *Computer methods in applied mechanics and engineering*, 195(52):7154–7171, 2006.
- [175] Gianluca Cusatis, Daniele Pelessone, and Andrea Mencarelli. Lattice discrete particle model (ldpm) for failure behavior of concrete. i: Theory. *Cement and Concrete Composites*, 33(9):881–890, 2011.
- [176] Gianluca Cusatis, Andrea Mencarelli, Daniele Pelessone, and James Baylot. Lattice discrete particle model (ldpm) for failure behavior of concrete. ii: Calibration and validation. *Cement and Concrete composites*, 33(9):891–905, 2011.
- [177] Mohammed Alnaggar, Daniele Pelessone, and Gianluca Cusatis. Lattice discrete particle modeling of reinforced concrete flexural behavior. *Journal of Structural Engineering*, 145(1):04018231, 2019.
- [178] Erol Lale, Roozbeh Rezakhani, Mohammed Alnaggar, and Gianluca Cusatis. Homogenization coarse graining (hcg) of the lattice discrete particle model (ldpm) for the analysis of reinforced concrete structures. *Engineering Fracture Mechanics*, 197:259–277, 2018.
- [179] Weixin Li, Roozbeh Rezakhani, Congrui Jin, Xinwei Zhou, and Gianluca Cusatis. A multiscale framework for the simulation of the anisotropic mechanical behavior of shale. *International Journal for Numerical and Analytical Methods in Geomechanics*, 41(14):1494–1522, 2017.
- [180] Weixin Li, Xinwei Zhou, J William Carey, Luke P Frash, and Gianluca Cusatis. Multiphysics lattice discrete particle modeling (m-ldpm) for the simulation of shale fracture permeability. *Rock Mechanics and Rock Engineering*, 51(12):3963–3981, 2018.
- [181] Edward A Schaufert, Gianluca Cusatis, Daniele Pelessone, James L O’Daniel, and James T Baylot. Lattice discrete particle model for fiber-reinforced concrete. ii: Tensile fracture and multiaxial loading behavior. *Journal of engineering mechanics*, 138(7):834–841, 2011.

- [182] Jovanca Smith, Gianluca Cusatis, Daniele Pelessone, Eric Landis, James O’Daniel, and James Baylot. Discrete modeling of ultra-high-performance concrete with application to projectile penetration. *International Journal of Impact Engineering*, 65:13–32, 2014.
- [183] Congrui Jin, Nicola Buratti, Marco Stacchini, Marco Savoia, and Gianluca Cusatis. Lattice discrete particle modeling of fiber reinforced concrete: Experiments and simulations. *European Journal of Mechanics-A/Solids*, 57:85–107, 2016.
- [184] Jovanca Smith and Gianluca Cusatis. Numerical analysis of projectile penetration and perforation of plain and fiber reinforced concrete slabs. *International Journal for Numerical and Analytical Methods in Geomechanics*, 41(3):315–337, 2017.
- [185] M Pathirage, F Bousikhane, M D’Ambrosia, M Alnaggar, and G Cusatis. Effect of alkali silica reaction on the mechanical properties of aging mortar bars: Experiments and numerical modeling. *International Journal of Damage Mechanics*, 2018.
- [186] Mohammed Alnaggar, Gianluca Cusatis, and Giovanni Di Luzio. Lattice discrete particle modeling (ldpm) of alkali silica reaction (asr) deterioration of concrete structures. *Cement and Concrete Composites*, 41:45–59, 2013.
- [187] Lin Wan, Roman Wendner, Benliang Liang, and Gianluca Cusatis. Analysis of the behavior of ultra high performance concrete at early age. *Cement and Concrete Composites*, 74:120–135, 2016.
- [188] Lin Wan-Wendner, Roman Wan-Wendner, and Gianluca Cusatis. Age-dependent size effect and fracture characteristics of ultra-high performance concrete. *Cement and Concrete Composites*, 85:67–82, 2018.
- [189] Mohammed Alnaggar, Giovanni Di Luzio, and Gianluca Cusatis. Modeling time-dependent behavior of concrete affected by alkali silica reaction in variable environmental conditions. *Materials*, 10(5):471, 2017.
- [190] M Pathirage, DP Bentz, G Di Luzio, E Masoero, and Gianluca Cusatis. The onix model: a parameter-free multiscale framework for the prediction of self-desiccation in concrete. *Cement and Concrete Composites*, 103:36–48, 2019.
- [191] Roozbeh Rezakhani, Mohammed Alnaggar, and Gianluca Cusatis. Multi-scale homogenization analysis of alkali-silica reaction (asr) effect in concrete. *Engineering*, 2019.
- [192] Lei Shen, Weixin Li, Xinwei Zhou, Jun Feng, Giovanni Di Luzio, Qingwen Ren, and Gianluca Cusatis. Multiphysics lattice discrete particle model for the simulation of concrete thermal spalling. *Cement and Concrete Composites*, 106:103457, 2020.
- [193] Giovanni Di Luzio and Gianluca Cusatis. Hygro-thermo-chemical modeling of high performance concrete. i: Theory. *Cement and Concrete composites*, 31(5):301–308, 2009.
- [194] Giovanni Di Luzio and Gianluca Cusatis. Hygro-thermo-chemical modeling of high-performance concrete. ii: Numerical implementation, calibration, and validation. *Cement and Concrete composites*, 31(5):309–324, 2009.

- [195] Paulo José Brandão Barbosa Lourenço. Computational strategies for masonry structures. 1997.
- [196] Franco Di Fabio, Amedeo Gregori, and Matteo Totani. Experimental and numerical investigations on historical masonry wall specimens tested in shear-compression configuration. *Engineering Structures and Technologies*, 7(4):177–188, 2015.
- [197] Amedeo Gregori and Michele Angiolilli. Simulating shear-compression mechanical behavior of historical masonry panels: sensitivity of 3d numerical models to input parameters. 2017.
- [198] EI Dolinsky, AM Mukhamedzhanov, et al. Bull. acad. sci. ussr, phys. ser. 41, 55 (1977). *Bull. Acad. Sci. USSR, Phys. Ser.*, 41:55, 1977.
- [199] C Bradford Barber, David P Dobkin, and Hannu Huhdanpaa. The quickhull algorithm for convex hulls. *ACM Transactions on Mathematical Software (TOMS)*, 22(4):469–483, 1996.
- [200] Christophe Geuzaine and Jean-François Remacle. Gmsh: A 3-d finite element mesh generator with built-in pre-and post-processing facilities. *International journal for numerical methods in engineering*, 79(11):1309–1331, 2009.
- [201] Kristin Bunte and Steven R Abt. Sampling surface and subsurface particle-size distributions in wadable gravel-and cobble-bed streams for analyses in sediment transport, hydraulics, and streambed monitoring. *Gen. Tech. Rep. RMRS-GTR-74. Fort Collins, CO: US Department of Agriculture, Forest Service, Rocky Mountain Research Station. 428 p.*, 74, 2001.
- [202] G Cusatis and E Schaufert. Discontinuous cell method (dcm) for cohesive fracture propagation. In *Proceedings of the 7th international conference on fracture mechanics of concrete and concrete structures (FraMCoS 7)*, pages 23–28, 2010.
- [203] Gianluca Cusatis and Xinwei Zhou. High-order microplane theory for quasi-brittle materials with multiple characteristic lengths. *Journal of Engineering Mechanics*, 140(7):04014046, 2013.
- [204] Erol Lale, Xinwei Zhou, and Gianluca Cusatis. Isogeometric implementation of high-order microplane model for the simulation of high-order elasticity, softening, and localization. *Journal of Applied Mechanics*, 84(1):011005, 2017.
- [205] Gianluca Cusatis, Roozbeh Rezakhani, and Edward A Schaufert. Discontinuous cell method (dcm) for the simulation of cohesive fracture and fragmentation of continuous media. *Engineering Fracture Mechanics*, 170:1–22, 2017.
- [206] Chiara Calderini, Serena Cattari, and Sergio Lagomarsino. The use of the diagonal compression test to identify the shear mechanical parameters of masonry. *Constr. and build. mater.*, 24(5):677–685, 2010.
- [207] Jelena Milosevic, António Sousa Gago, Mário Lopes, and Rita Bento. Experimental assessment of shear strength parameters on rubble stone masonry specimens. *Construction and Building Materials*, 47:1372–1380, 2013.

- [208] Marco Corradi, Antonio Borri, and Andrea Vignoli. Experimental evaluation of in-plane shear behaviour of masonry walls retrofitted using conventional and innovative methods. *Masonry International*, 21(1):29, 2008.
- [209] M Tomazevic, M Lutman, P Weiss, and T Velechovsky. The influence of rigidity of floors on the seismic resistance of old masonry buildings: shaking-table tests of stone-masonry houses: summary report. *ZRMK Report, 117p, Ljubljana*, 1992.
- [210] C. Modena and C. Bettio. Experimental characterisation and modelling of injected and jacketed masonry walls. In *Proceedings of Italian-French Symposium Strengthening and Repair of Structures in Seismic Area, Nizza, France*, page 273–282, 1994.
- [211] C Modena. Interpretazione dei risultati ottenuti dalle prove in sito nell’ambito delle tre convenzioni con gli istituti di ricerca di firenze e milano e modellazione del comportamento strutturale dei componenti rinforzati. *Convenzione di ricerca tra la Regione Toscana e il Dipartimento di Costruzioni e Trasporti dell’Università degli Studi di Padova*, 1999.
- [212] Dean Karnopp et al. Computer simulation of stick-slip friction in mechanical dynamic systems. *J. Dyn. Syst. Meas. Control.*, 107(1):100–103, 1985.
- [213] Zdenek P Bazant. *Fracture and size effect in concrete and other quasibrittle materials*. Routledge, 2019.
- [214] MF Kaplan. Crack propagation and the fracture of concrete. In *Journal Proceedings*, volume 58, pages 591–610, 1961.
- [215] Clyde E Kesler, Dan J Naus, and James L Lott. Fracture mechanics-its applicability to concrete. In *Proceedings of the Society of Materials Science Conference on the Mechanical Behavior of Materials.*, number Conf Paper, 1972.
- [216] PF Walsh. Crack initiation in plain concrete. *Magazine of Concrete Research*, 28(94):37–41, 1976.
- [217] Arne Hillerborg, Mats Mod er, and P-E Petersson. Analysis of crack formation and crack growth in concrete by means of fracture mechanics and finite elements. *Cement and concrete research*, 6(6):773–781, 1976.
- [218] Alberto Carpinteri, Bernardino Chiaia, and Kamran M Nemati. Complex fracture energy dissipation in concrete under different loading conditions. *Mechanics of Materials*, 26(2):93–108, 1997.
- [219] Alberto Carpinteri, Pietro Cornetti, Fabrizio Barpi, and Silvio Valente. Cohesive crack model description of ductile to brittle size-scale transition: dimensional analysis vs. renormalization group theory. *Engineering fracture mechanics*, 70(14):1809–1839, 2003.
- [220] Zdeněk P Bažant. Concrete fracture models: testing and practice. *Engineering fracture mechanics*, 69(2):165–205, 2002.
- [221] G Appa Rao and BK Raghun Prasad. Fracture process zone in high strength concrete. In *Fourth International Conference on Fracture Mechanics of Concrete and Concrete Structures*, pages 327–332, 2001.
- [222] Zdeněk P Bažant and Byung H Oh. Crack band theory for fracture of concrete. *Matériaux et construction*, 16(3):155–177, 1983.

- [223] Zdeněk P Bažant and Milan Jirásek. Nonlocal integral formulations of plasticity and damage: survey of progress. *Journal of engineering mechanics*, 128(11):1119–1149, 2002.
- [224] Ignacio Carol, Carlos M López, and Olga Roa. Micromechanical analysis of quasi-brittle materials using fracture-based interface elements. *International Journal for Numerical Methods in Engineering*, 52(1-2):193–215, 2001.
- [225] A Caballero, CM López, and I Carol. 3d meso-structural analysis of concrete specimens under uniaxial tension. *Computer methods in applied mechanics and engineering*, 195(52):7182–7195, 2006.
- [226] John E Bolander and N Sukumar. Irregular lattice model for quasistatic crack propagation. *Physical Review B*, 71(9):094106, 2005.
- [227] Zdeněk P Bažant and Siddik Şener. Size effect in torsional failure of concrete beams. *Journal of Structural Engineering*, 113(10):2125–2136, 1987.
- [228] Zdeněk P Bažant and Pere C Prat. Measurement of mode iii fracture energy of concrete. *Nuclear Engineering and Design*, 106(1):1–8, 1988.
- [229] Pietro Bocca, Alberto Carpinteri, and Silvio Valente. Fracture mechanics of brick masonry: size effects and snap-back analysis. *Materials and Structures*, 22(5):364–373, 1989.
- [230] R Ince and E Arici. Size effect in bearing strength of concrete cubes. *Construction and Building Materials*, 18(8):603–609, 2004.
- [231] X-Z Hu and FH Wittmann. Fracture energy and fracture process zone. *Materials and Structures*, 25(6):319–326, 1992.
- [232] Giovanni Di Luzio and Gianluca Cusatis. Cohesive crack analysis of size effect for samples with blunt notches and generalized size effect curve for quasi-brittle materials. *Engineering Fracture Mechanics*, 204:15–28, 2018.
- [233] Roozbeh Reza khani and Gianluca Cusatis. Asymptotic expansion homogenization of discrete fine-scale models with rotational degrees of freedom for the simulation of quasi-brittle materials. *Journal of the Mechanics and Physics of Solids*, 88:320–345, 2016.
- [234] Zdeněk P Bažant and Qiang Yu. Universal size effect law and effect of crack depth on quasi-brittle structure strength. *Journal of engineering mechanics*, 135(2):78–84, 2009.
- [235] Marco Corradi, Antonio Borri, and Andrea Vignoli. Strengthening techniques tested on masonry structures struck by the umbria–marche earthquake of 1997–1998. *Construction and building materials*, 16(4):229–239, 2002.
- [236] Bruno Silva, Massimo Dalla Benetta, Francesca da Porto, and Claudio Modena. Experimental assessment of in-plane behaviour of three-leaf stone masonry walls. *Constr. and Build. Mater.*, 53:149–161, 2014.
- [237] Bruno Quelhas Silva, Athanasios Pappas, João Miranda Guedes, Francesca Da Porto, and Claudio Modena. Numerical analysis of the in-plane behaviour of three-leaf stone masonry panels consolidated with grout injection. *Bulletin of Earthquake Engineering*, 15(1):357–383, 2017.

- [238] Italian Code-NTC08. Norme tecniche per le costruzioni in zone sismiche. *Ministerial Decree DM*, 14(08):9–04, 2008.
- [239] Comité Européen de Normalisation et al. Eurocode 6: Design of masonry structures—part 1-1: General rules for reinforced and unreinforced masonry structures. *Comité Européen de Normalisation: Brussels, Belgium*, 2005.
- [240] Miha Tomazevic. The influence of rigidity of floors on the seismic resistance of old masonry buildings: shaking-table tests of stone-masonry houses : summary report. 1992.
- [241] Daniel M Moreno, William Trono, Gabriel Jen, Claudia Ostertag, and Sarah L Billington. Tension stiffening in reinforced high performance fiber reinforced cement-based composites. *Cement and Concrete Composites*, 50:36–46, 2014.
- [242] Y Zhan and G Meschke. Multilevel computational model for failure analysis of steel-fiber-reinforced concrete structures. *Journal of Engineering Mechanics*, 142(11):04016090, 2016.
- [243] Petr Jun and Viktor Mechtcherine. Behaviour of strain-hardening cement-based composites (shcc) under monotonic and cyclic tensile loading: part 1—experimental investigations. *Cement and Concrete Composites*, 32(10):801–809, 2010.
- [244] Ferhun C Caner, Zdeněk P Bažant, and Roman Wendner. Microplane model m7f for fiber reinforced concrete. *Engineering fracture mechanics*, 105:41–57, 2013.
- [245] Jean-Louis Tailhan, Pierre Rossi, and Dominic Daviau-Desnoyers. Probabilistic numerical modelling of cracking in steel fibre reinforced concretes (sfrc) structures. *Cement and Concrete Composites*, 55:315–321, 2015.
- [246] Erik Denneman, Rongzong Wu, Elsabe P Kearsley, and Alex T Visser. Discrete fracture in high performance fibre reinforced concrete materials. *Engineering Fracture Mechanics*, 78(10):2235–2245, 2011.
- [247] En-Hua Yang, Shuxin Wang, Yingzi Yang, and Victor C Li. Fiber-bridging constitutive law of engineered cementitious composites. *Journal of advanced concrete technology*, 6(1):181–193, 2008.
- [248] Z Lin, T Kanda, and Victor C Li. On interface property characterization and performance of fiber reinforced cementitious composites. 1999.
- [249] Petr Kabele. Multiscale framework for modeling of fracture in high performance fiber reinforced cementitious composites. *Engineering Fracture Mechanics*, 74(1-2):194–209, 2007.
- [250] FKF Radtke, A Simone, and LJ Sluys. A computational model for failure analysis of fibre reinforced concrete with discrete treatment of fibres. *Engineering fracture mechanics*, 77(4):597–620, 2010.
- [251] Vitor MCF Cunha, Joaquim AO Barros, and JM Sena-Cruz. An integrated approach for modelling the tensile behaviour of steel fibre reinforced self-compacting concrete. *Cement and Concrete Research*, 41(1):64–76, 2011.
- [252] Edward A Schaufert, Gianluca Cusatis, Daniele Pelessone, James L O’Daniel, and James T Baylot. Lattice discrete particle model for fiber-reinforced concrete. ii: Tensile fracture and multiaxial loading behavior. *Journal of engineering mechanics*, 138(7):834–841, 2012.

- [253] Edward A Schaufert, Gianluca Cusatis, Daniele Pelessone, James L O'Daniel, and James T Baylot. Lattice discrete particle model for fiber-reinforced concrete. ii: Tensile fracture and multiaxial loading behavior. *Journal of engineering mechanics*, 138(7):834–841, 2012.
- [254] Christopher KY Leung and Victor C Li. Strength-based and fracture-based approaches in the analysis of fibre debonding. 1990.
- [255] Jill K Morrison, Surendra P Shah, and Yeou-Shang Jenq. Analysis of fiber debonding and pullout in composites. *Journal of engineering mechanics*, 114(2):277–294, 1988.
- [256] Zhong Lin and Victor C Li. Crack bridging in fiber reinforced cementitious composites with slip-hardening interfaces. *Journal of the Mechanics and Physics of Solids*, 45(5):763–787, 1997.
- [257] Antoine E Naaman and Husamuddin Najm. Bond-slip mechanisms of steel fibers in concrete. *Materials Journal*, 88(2):135–145, 1991.
- [258] Youjiang Wang, Victor C Li, and Stanley Backer. Modelling of fibre pull-out from a cement matrix. *International Journal of Cement Composites and Lightweight Concrete*, 10(3):143–149, 1988.
- [259] Tetsushi Kanda and Victor C Li. Interface property and apparent strength of high-strength hydrophilic fiber in cement matrix. *Journal of materials in civil engineering*, 10(1):5–13, 1998.
- [260] Emmanuel Cailleux, Thierry Cutard, and Gérard Bernhart. Pullout of steel fibres from a refractory castable: experiment and modelling. *Mechanics of materials*, 37(4):427–445, 2005.
- [261] Christopher KY Leung and Victor C Li. Effect of fiber inclination on crack bridging stress in brittle fiber reinforced brittle matrix composites. *Journal of the Mechanics and Physics of Solids*, 40(6):1333–1362, 1992.
- [262] Xiao Dong Hu, Robert Day, and Peter Dux. Micro-mechanical approximation to the stress field around an inclined fiber of frcc. *Mechanics Research Communications*, 29(1):27–34, 2002.
- [263] Jun Zhang and Victor C Li. Effect of inclination angle on fiber rupture load in fiber reinforced cementitious composites. *Composites Science and Technology*, 62(6):775–781, 2002.
- [264] Victor C Li, Youjiang Wang, and Stanley Backer. Effect of inclining angle, bundling, and surface treatment on synthetic fiber pull-out from a cement matrix. 1990.
- [265] Christopher KY Leung and Y Philip Geng. Micromechanical modeling of softening behavior in steel fiber reinforced cementitious composites. *International journal of solids and structures*, 35(31-32):4205–4222, 1998.
- [266] M Jamal Shannag, Rune Brincker, and Will Hansen. Pullout behavior of steel fibers from cement-based composites. *Cement and Concrete Research*, 27(6):925–936, 1997.
- [267] Christopher KY Leung and Yiping Geng. Effect of lateral stresses on fiber debonding/pull-out. *Composites Engineering*, 5(10-11):1331–1348, 1995.

- [268] Mohammed Alnaggar, Minghe Liu, Jianmin Qu, and Gianluca Cusatis. Lattice discrete particle modeling of acoustic nonlinearity change in accelerated alkali silica reaction (asr) tests. *Materials and Structures*, 49(9):3523–3545, 2016.
- [269] Tong Li, Nestore Galati, J Gustavo Tumialan, and Antonio Nanni. Analysis of unreinforced masonry concrete walls strengthened with glass fiber-reinforced polymer bars. *ACI structural journal*, 102(4):569, 2005.
- [270] ACI (American Concrete Institute). Design and construction guide of externally bonded frcm systems for concrete and masonry repair and strengthening. 2013.
- [271] George G Penelis and Gregory G Penelis. *Structural Restoration of Masonry Monuments: Arches, Domes and Walls*. CRC Press, 2020.

# Appendix A

## A1 List of publications during the Ph.D.

The following papers are indexed on ISI/Scopus and/or of A level in ANVUR ranking.

- **M. Angiolilli** and A. Gregori. Triplet Test on Rubble Stone Masonry: Numerical Assessment of the Shear Mechanical Parameters. *Buildings*: 10(3), 49, 2020. doi:10.3390/buildings10030049.
- **M. Angiolilli**, A. Gregori, M. Parithage and G. Cusatis. Fiber Reinforced Cementitious Matrix (FRCM) for strengthening historical stone masonry structures: experiments and computations. *Engineering Structures*: 224, 111102, 2020. doi:10.1016/j.engstruct.2020.111102
- **M. Angiolilli**, A. Gregori, M. Vailati. Lime-based mortar reinforced by randomly oriented short fibers for the retrofitting of the historical masonry structure. *Materials*: 13(16), 3462, 2020. doi:10.3390/ma13163462
- A. Gregori, C. Castoro, M. Mercuri, **M. Angiolilli**. Modeling the Mechanical Response of Rubberised Concrete. *In Developments and Novel Approaches in Biomechanics and Metamaterials*, Springer, Cham: 2020, pp. 341-352. doi:10.1007/978-3-030-50464-9\_19
- A. Gregori, C. Castoro, M. Mercuri, **M. Angiolilli**. Numerical modelling of the mechanical behaviour of rubbercrete. *Computers and Structures*: 242, 106393, 2021. doi:10.1016/j.compstruc.2020.106393
- **M. Angiolilli**, M. Parithage, A. Gregori, G. Cusatis. The Lattice Discrete Particle Model for the simulation of irregular stone masonry. *Journal of Structural Engineering* accepted on November 12, 2020
- **M. Angiolilli**, A. Gregori. Experimental investigation of the FRCM effect on the mechanical behavior of ancient stone masonry building tested under cyclic diagonal compression. Submitted to *Journal of Composites for Construction*

## A2 International and national conference papers

- **M. Angiolilli**, A. Gregori, M. Fragiaco. Studies for the definition of seismic input for non-structural elements inside historical buildings. *Conference proceedings ANIDIS*, 2019, SS04-2, Ascoli Piceno (Italy)
- **M. Angiolilli**, A. Gregori, G. Cusatis. Lattice discrete particle model (LDPM) for the tensile behaviour characterization of historical stone masonries. *Conference proceedings ANIDIS*, 2019, SG06-40, Ascoli Piceno (Italy)
- **M. Angiolilli**, A. Gregori, D. Martini. Mechanical characterization of the cyclic behavior of historic masonry panels reinforced by FRCM system subject to diagonal compression tests. *Conference proceedings ANIDIS*, 2019, SG06-116, Ascoli Piceno (Italy)
- V. Rinaldi, M. Sciomenta, **M. Angiolilli**, M. Fragiaco. Numerical evaluation of the carbonation effect on the seismic vulnerability of a RC plane frame. *Conference proceedings ANIDIS*, 2019, SG05-53, Ascoli Piceno (Italy)
- E. Marino, F. Barbagallo, **M. Angiolilli**, B. Belletti, G. Camata, C. Delapina, M. Di Domenico, G. Fiorentino, A. Gregori, D. Lavorato, C. Lima, E. Martinelli, A. Rasulo, P. Ricci, S. Ruggieri, E. Spacone, M. Terrenzi, G. Uva, G. Verderame. Influence of nonlinear modeling on capacity assessment of RC framed structures. *7th ECCOMAS Computational Methods in Structural Dynamics and Earthquake Engineering, COMPDYN*, 2019, Crete (Greece)
- A. Gregori, **M. Angiolilli**, C. Castoro, M. Mercuri. Comparing deterministic and reliability method for the seismic vulnerability assessment of an existing RC building. *13th Conf. Conference in the Computational Structures Technology*, 2018, Barcelona (Spain)
- A. Gregori, **M. Angiolilli**, C. Castoro, M. Mercuri. Simulating shear-compression behavior of historical masonry panels: sensitivity of 2D-3D FE Models to input parameters. *13th Conference in the Computational Structures Technology*, 2018, Barcelona (Spain)
- C. Lima, **M. Angiolilli**, F. Barbagallo, B. Belletti, A. V. Bergami, G. Camata, C. Cantagallo, M. Di Domenico, G. Fiorentino, A. Ghersi, A. Gregori, D. Lavorato, R. Luciano, E.M. Marino, E. Martinelli, C. Nuti, P. Ricci, L. Rosati, S. Ruggieri, S. Sessa, E. Spacone, M. Terrenzi, G. Uva, F. Vecchi, G.M. Verderame. Nonlinear modeling approaches for existing RC buildings: the case study of De Gasperi-Battaglia school building in Norcia. *Italian Concrete Days*, 2018, Lecco (Italy)
- A. Gregori, G. Marchini, D. Martini, **M. Angiolilli**. Caratterizzazione Sperimentale di FRCM per la Conservazione ed il Rafforzamento Sismico del Patrimonio Edilizio Monumentale e Storico. *Conference proceeding ANIDIS*, 2017, n.3108, SG03-116
- A. Gregori, **M. Angiolilli**. Sensitività ai parametri di modelli numerici 3D per la simulazione della risposta di pannelli di muratura storica provati a taglio-compressione. *Conference Proceeding ANIDIS*, 2017, n.3100, SG03-111
- A. Gregori, **M. Angiolilli** (2017). Valutazione affidabilistica della vulnerabilità sismica di un edificio strategico esistente in calcestruzzo armato. *Conference proceeding ANIDIS*, 2017, n.3095, SG03-221

# Appendix B

## B1 Nomenclature

3PBT	Three-Point Bending Test
950Y	Glass fiber with 13 mm in length and 0.316 mm in diameter
BT	Brazilian Test
CT	Compression Test
DEM	Discrete Element Model
FEM	Finite Element Model
FPZ	Fracture Propagation Zone
FRCM	Fiber Reinforced Cementitious Matrix
HP24	Glass fiber with 24 mm in length and 0.476 mm in diameter
IP	In Plane
LDPM	Lattice Discrete Particle Model
OOP	Out Of Plane
RM	Reinforced Masonry
TRC	Textile Reinforced Concrete
TRM	Textile Reinforced Mortar
URM	UnReinforced Masonry
URP	UnReinforced mortar Panel



La borsa di dottorato è stata cofinanziata con risorse del Programma Operativo Nazionale 2014-2020 (CCI 2014IT16M2OP005), Fondo Sociale Europeo, Azione I.1 “Dottorati Innovativi con caratterizzazione industriale”



UNIONE EUROPEA  
Fondo Sociale Europeo



*Ministero dell'Università  
e della Ricerca*

